INSTRUMENTAL MODELLING AND NOISE REDUCTION ALGORITHMS FOR THE LASER INTERFEROMETER SPACE ANTENNA

Von der Fakultät für Mathematik und Physik
der Gottfried Wilhelm Leibniz Universität Hannover

zur Erlangung des akademischen Grades
Doktor der Naturwissenschaften

– Dr. rer. nat. –

genehmigte Dissertation von

M. Sc. Olaf Hartwig

2021

Referent:	apl. Prof. Dr. Gerhard Heinzel
Korreferent:	Maître de Conférences Dr. Antoine Petiteau
Korreferent:	Prof. Dr. Guido Müller
Tag der Promotion:	17.09.2021

On two occasions I have been asked, "Pray, Mr. Babbage, if you put into the machine wrong figures, will the right answers come out?" ...

I am not able rightly to apprehend the kind of confusion of ideas that could provoke such a question.

– Charles Babbage, Passages from the Life of a Philosopher

ABSTRACT

The Laser Interferometer Space Antenna (LISA) is a large ("L-Class") European Space Agency (ESA) mission, scheduled to fly in the mid 2030s. LISA is a constellation of three satellites designed to detect gravitational waves (GWs) using laser interferometry. GWs will cause µcycle phase fluctuations in the MHz interferometric beatnotes. Tracking the beatnotes to this precision would require equally precise onboard clocks, which unfortunately do not exist. Instead, LISA will use additional interferometric measurements of the differential errors between the spacecraft clocks to correct any clock errors in post-processing.

This correction has to be performed alongside the main noise suppression step for LISA, an algorithm called time-delay interferometry (TDI). TDI is designed to suppress fluctuations in the laser frequencies, which would otherwise exceed the expected GW signal by more than 8 orders of magnitude. Both TDI and clock correction are part of the so-called initial noise-reduction pipeline (INREP) of LISA.

In this thesis, we will review the principles behind gravitational wave detectors and the operating principle of LISA, including a technical overview of the main components of the LISA measurement chain. This serves as a basis for developing a detailed simulation model for the main interferometric measurements produced by LISA. In particular, we include in this model large frequency offsets of the laser beams, which are affected by Doppler shifts during the propagation, as well laser frequency locking control loops, which were neglected in previous studies. A particular focus is put on modelling the three independent spacecraft clocks, and the additional measurements used to correct for their timing jitters. We also show results of numerical simulations based on this model, and discuss the noise sources limiting these raw measurements.

Finally, we study one possible realization of the INREP. We show that we are able to suppress all primary noise sources included in our simulation, and provide models for the residual noise levels. We also review the basics of TDI, and reproduce a numerical search for possible TDI combinations, finding additional noise suppressing signal combinations previously missed in the literature. We study the relationships between these combinations, and identify how they relate to a basic set of generators. We conclude by discussing different approaches how the un-synchronized spacecraft clocks can be corrected for as part of TDI, and show analytical and numerical results regarding the correction performance.

Keywords: Gravitational waves, LISA, Time-Delay Interferometry

KURZZUSAMMENFASSUNG

Die Laser Interferometer Space Antenna (LISA) ist eine große ("L-Class") ESA-Mission, die Mitte der 2030er Jahre starten soll. LISA ist eine Konstellation aus drei Satelliten, die Gravitationswellen (GW) mit Hilfe von Laserinterferometrie detektieren soll. GW erzeugen µcycle Phasenschwankungen in den interferometrischen MHz Signalen. Solch eine präzise Phasenmessung würde ebenso präzise Referenzuhren auf den Satelliten erfordern, die leider nicht existieren. Stattdessen wird LISA zusätzliche interferometrische Messungen der relativen Fehler zwischen den Uhren der Satelliten verwenden um deren Fehler im Nachhinein zu korrigieren.

Diese Korrektur muss zusäztlich zu dem Hauptschritt der Rauschunterdrückung für LISA durchgeführt werden, einem Algorithmus namens TDI. TDI wurde entwickelt, um Fluktuationen in den Laserfrequenzen zu unterdrücken, die ansonsten das erwartete GW-Signal um mehr als 8 Größenordnungen übersteigen würden. Sowohl TDI als auch die Uhrenkorrektur sind Teil der sogenannten initial noise-reduction pipeline (INREP) für LISA.

Wir werden die Prinzipien hinter GW-Detektoren und das Funktionsprinzip von LISA diskutieren, inklusive eines technischen Überblick über die Hauptkomponenten der LISA-Messkette. Dies dient als Grundlage für die Entwicklung eines detaillierten Simulationsmodells für die interferometrischen Messungen, die von LISA erzeugt werden. Insbesondere beziehen wir in dieses Modell große Frequenz-Offsets der Laserstrahlen ein, die durch Doppler-Verschiebungen während der Ausbreitung beeinflusst werden, sowie Regelkreise zur Laserfrequenzkontrolle, die in früheren Studien vernachlässigt wurden. Ein besonderer Schwerpunkt liegt auf der Modellierung der drei unabhängigen Satellitenuhren und den zusätzlichen Messungen, die zu ihrer Korrektur verwendet werden. Wir präsentieren Simulationsergebnisse und diskutieren welche Rauschquellen die Rohmessdaten limitieren.

Schließlich untersuchen wir eine mögliche Implementierung der INREP. Wir zeigen, dass wir in der Lage sind, alle primären Rauschquellen, die in unserer Simulation enthalten sind, zu unterdrücken, und liefern Modelle für die verbleibenden Rauschquellen. Wir besprechen die Grundlagen von TDI und reproduzieren eine numerische Suche nach möglichen TDI-Kombinationen, wobei wir zusätzliche rauschunterdrückende Signalkombinationen finden, die bisher in der Literatur übersehen wurden. Wir untersuchen die Beziehungen zwischen diesen Kombinationen und stellen fest, wie sie sich auf eine Grundmenge von Generatoren beziehen. Abschließend diskutieren wir verschiedene Ansätze, wie die desynchronisierten Uhren der 3 Satelliten als Teil von TDI korrigiert werden können, und zeigen analytische und numerische Ergebnisse hinsichtlich der Korrekturleistung.

Schlagwörter: Gravitationswellen, LISA, Time-Delay Interferometry

CONTENTS

ACRONYMS

ACES Atomic Clock Ensemble in Space.
ADC analog-to-digital converter.
AEI Albert Einstein Institute.
AFS atomic frequency standard.
aLIGO advanced Laser Interferometer Gravitational-Wave Observatory.
ASD amplitude spectral density.

BCRS Barycentric Celestial Reference System.

CBE current best estimate.
CDF Concurrent Design Facility.
CSD cross spectral density.

DAC digital-to-analog converter.
DFACS drag-free attitude control system.
DLL delay-locked loop.
DPLL digital phase-locked loop.
DUT device under test.
DWS differential wavefront sensing.

EKF extended Kalman filter.
EM electro-magnetic.
EMRI Extreme Mass Ratio Inspiral.
EOM electro-optical modulator.
ESA European Space Agency.
ESTRACK European Space Tracking.

FDS frequency distribution system.
FIR finite impulse response.

GAIA Global Astrometric Interferometer for Astrophysics.
GFZ Deutsches GeoForschungsZentrum.
GLONASS Globalnaja nawigazionnaja sputnikowaja sistema.
GNSS Global Navigation(al) Satellite System.
GPS Global Positioning System.
GR general relativity.
GRACE-FO Gravity Recovery and Climate Experiment-Follow-On.
GRS gravitational reference sensor.
GW gravitational wave.

INREP initial noise-reduction pipeline.
ISC inter-spacecraft.
ISS International Space Station.

L0 level 0.
L1 level 1.

LDC LISA data challenge.
LDPG LISA data-processing group.
LFN laser frequency noise.
LISA Laser Interferometer Space Antenna.
LO local oscillator.
LPSD log-scale power spectral density.
LUT look-up table.

MOSA movable optical sub-assembly.
MPR measured pseudo-range.

NCO numerically controlled oscillator.

OB optical bench.
OCXO oven controlled crystal oscillator.
OMS optical metrology system.

PA phase accumulator.
PIR phase increment register.
PLL phase-locked loop.
PPR proper pseudo-range.
PRN pseudo random noise.
PSD power spectral density.
PTA Pulsar Timing Array.

QPD quadrant photo diode.

REF reference.
RIN relative intensity noise.

TCB Barycentric Coordinate Time.
TCXO temperature compensated crystal oscillator.
TDI time-delay interferometry.
TDI-R time-delay interferometric ranging.
THE on-board clock time.
TM test-mass.
TPS spacecraft proper time.
TT transverse-traceless.
TTL tilt-to-length.

USO ultra-stable oscillator.

VCXO voltage controlled crystal oscillator.

WG working group.

XO crystal oscillator.

LIST OF FIGURES

LIST OF TABLES

Part I

INTRODUCTION

1

OVERVIEW

This thesis is organized in three parts.

Part i gives an introduction to the topic. We first review the principle behind gravitational waves and their detection in chapter 2, and summarize the observations to date, as well as which sources we expect to find with different proposed detectors. Chapter 3 then focuses on LISA, where we review the mission architecture and introduce most of the instrumental systems modelled in the later parts of the thesis.

A large part of this thesis work was the development of a more realistic model for LISA instrumental simulations, presented in part ii.

Chapter 4 explains the context in which this work was performed, and introduces the basic model used to represent the information content of laser beams in our simulation. We then present the model for the optical simulation in chapter 5, where we derive equations for modelling the phase and frequency of all laser beams, how they are propagated between the spacecraft and what signals are generated by their interference. We choose here a formulation which is compatible with general relativity (GR), in the sense that all signals onboard a single spacecraft are expressed in that spacecrafts proper time, while relativistic effects are only relevant for the propagation of these signals between the spacecraft.

Chapter 6 is concerned with modelling the different timing signals present on each LISA satellite, and how clock errors couple in to the measurements. This includes the additional clock-derived signals used for on-ground calibration and absolute ranging. This is followed by chapter 7, where we further discuss how to model the last stage of the on-board anti-aliasing filters, and give the final phasemeter equations describing the interferometric measurements. This includes a model for the laser-locking control loops, which relate all six lasers to one primary laser and ensure that all beatnote frequencies in the constellation fall within a pre-determined frequency range.

We conclude part ii by presenting simulation results in chapter 8, based on instrumental model previously presented. We discuss the limiting noise sources appearing in the different interferometers, and how the raw measurements are impacted by the laser locking scheme.

Part iii then presents a version of the initial noise-reduction pipeline (INREP), which consists of a chain of processing elements designed to remove all primary noise sources.

We start this part with chapter 9, where we review the processing elements in the full pipeline, and give simulation results showing that all primary

noise sources included in the simulation presented in part ii indeed can be succesfully suppressed below the level of secondary noises.

We then introduce the basic principles behind the main noise suppression step, TDI, in chapter 10. This is followed by a review of the numerical search algorithms for finding so-called 2nd generation combinations known from the literature, which we reproduced with the result of finding additional 14 link combinations previously missed, in chapter 11. We also review there how these combinations are related to the 4 basic generators of first generation TDI.

We then introduce the so-called intermediary TDI variables in chapter 12, and derive how different noise sources couple into the final TDI variable. For this, we include the effect of laser locking, which affects the level of residual laser noise, but not those of secondary noises. In this chapter, we also derive how TDI has to be adopted for data given in units of frequency in order to achieve the same levels of laser noise reduction achievable by the usual formulation in phase.

Finally, we review in chapter 13 how the three independent spacecraft clocks can be corrected for in TDI. First, we discuss how the clocks can in principle already be corrected for while building the TDI combinations. We then discuss how this is affected by the choice of different units, in particular when using the total phase or frequency, or just phase or frequency fluctuations remaining after a polynomial trend has been subtracted from the data. The latter case requires an additional clock correction algortihm to be applied to the data, for which we present a general formulation applicable to almost any TDI variable. We also present both analytically and numerically that both laser and clock noise can be reduced below the level of secondary noises, even in the presence of large offsets and drifts of all three spacecraft clocks and stochastic ranging noise. We then conclude with an outlook for how to synchronize the final TDI variables to a common global time frame, such as Barycentric Coordinate Time (TCB), and briefly discuss the alternative approach to first synchronizing all raw measurements to Barycentric Coordinate Time (TCB) before constructing the TDI variables.

The appendix is located in part iv. It contains an overview of the common conventions and notations used in parts ii and iii, which we summarize in appendix A. Furthermore, we review how Lagrange interpolation can be used to apply fractional delays to data given at discrete sampling times, and present a model for the errors in these interpolations, in appendix B.

Appendix C contains an overview over the different quantities used to describe frequency stability of oscillators, both in the time- and frequency domain, as well as a short catalogue of the typical frequency stability of different kinds of oscillators.

Finally, we list the noise models used for the instrument simulation in appendix D.

2

GRAVITATIONAL WAVE ASTRONOMY

Going back to A. Einstein [33], a GW propagating through spacetime sufficiently far away from its source can be described as a small pertubation on an otherwise flat spacetime metric. It is shown there that these metric fluctuations carry energy, which indicates that they are a real physical effect and not just an artifact of the mathematical framework used to describe general relativity.

GWs are arguably one of the most extreme observable quantities in modern physics, in multiple respects. As we will discuss in section 2.1, the energy emitted in gravitational radiation by merging black holes can outshine the rest of the visible universe by some orders of magnitude. Despite this large luminosity, it still takes extremely precise equipment to directly detect any trace of them. The reason for this disparity is that the interaction of GWs with matter is an extremely weak one. Still, GW observatories are now regularly detecting signals from merging binary systems (cf. section 2.3), opening a new window for observing our universe.

Compared to electro-magnetic (EM) observations, GWs allow studies of a completely new class of astrophysical objects, which by themselves do not emit any EM radiation, such as black holes. In addition, they can support EM observatories by giving alerts to extreme events such as the merging of neutron stars or super novae. And last but not least, they allow unique tests of the fundamental theory of gravity, general relativity (GR).

In this chapter, we will first focus on the amount of energy emitted in binary systems in the form of GWs in section 2.1. This is sufficient to sketch the principle behind the first indirect detection of GWs, as well as to highlight why it is infeasible to generate detectable GWs in a laboratory.

We then review the basic toolset of GR in section 2.2, which allows us to understand how GWs interact with matter, and how they can be measured directly.

Consequently, we describe the principle behind the detectors which allowed the first direct detection of GWs in section 2.3, and conclude with an overview over the current and planned GW observatories, as well as the sources they will observe, in section 2.4.

2.1 GRAVITATIONAL WAVE LUMINOSITY AND INDIRECT DETECTION

GWs arise when matter is accelerated. This is not unlike the case for EM radiation, which is generated by accelerating charged particles. Contrary to EM radiation, however, there are no dipole GWs [73].

Instead, the simplest possible GWs are created as quadropole radiation, that is, from a constellation of matter for which the second time-derivative of the quadrupolemoment is non-vanishing.

Already in [33], Einstein provided a formula for the amount of energy radiated by such a system.

In this section, we provide a short review of these fundamentals, following closely the formulation presented in [38]. There, this formula is applied to the case of a body rotating around one of its main axes of inertia with an (almost) constant angular velocity Ω. The radiated energy per unit time is called the luminosity, and in this case is given by

$$L_{GW} = \frac{32}{5} \cdot \frac{G}{c^5} \cdot \Omega^6 \cdot (I_1 - I_2)^2 \,. \tag{2.1}$$

Here, G is the gravitational constant, c the speed of light in a vacuum, and I_1, I_2 are the moments of inertia along the axis prependicular to the rotation axis.

2.1.1 *Gravitational waves from binary systems*

A likely candidate to produce measurable amounts of gravitational radiation is a gravitationally bound system. Inspecting eq. (2.1), we observe that to maximize the amount of gravitational radiation being emitted from a system, it should be rotating with a large angular velocity, Ω, while having a large moment of inertia along one axis. The ratio between these two quantities is governed by orbital mechanics in this case.

We can consider two equal point masses orbiting each other at a separation D. In this scenario, we simply get $I_1 = \frac{1}{2}MD^2$ and $I_2 = 0$. Equation (2.1) becomes

$$L_{GW} = \frac{8}{5} \cdot \frac{G}{c^5} \cdot \Omega^6 \cdot M^2 D^4 \,. \tag{2.2}$$

Neglecting relativistic effects for the moment, we can use Kepler's third law to compute the angular velocity based on the masses and separation, to get

$$\Omega^2 = \frac{2GM}{D^3} \,. \tag{2.3}$$

Inserting this into eq. (2.2), yields

$$L_{GW} = \frac{64}{5} \cdot \frac{G}{c^5} \cdot G^3 \frac{M^5}{D^5} \,. \tag{2.4}$$

The only free parameters are the masses of the two test masses and their separation. To maximize the amount of GWs, we are looking for massive objects on tight orbits. This implies that these objects should not only be massive, but also compact, such that they are able to closely orbit each other without colliding or being ripped apart from tidal effects. Possible candidates could therefore be the remnants of collapsed stars, such as white dwarfs, neutron stars or black holes.

A useful parameter to study such compact objects is the Schwarzschild radius,

$$R_S = \frac{2MG}{c^2}\,, \tag{2.5}$$

which defines the radius of the event horizon of a black hole of the given mass.

Inserting this expression into eq. (2.2) gives

$$\begin{aligned} L_{GW} &= \frac{2}{5} \cdot \frac{c^5}{G} \cdot \left(\frac{R_S}{D}\right)^5 \\ &\approx 10^{52}\,\mathrm{W} \cdot \left(\frac{R_S}{D}\right)^5 . \end{aligned} \tag{2.6}$$

Note that the result is given as the ratio between the Schwarzschield radius and the separation to the fifth power, amplified by $\frac{c^5}{G} \approx 3.6 \times 10^{52}\,\mathrm{W}$. This means that compact, tightly orbiting binaries, for which the ratio R_S/D is within a few orders of magnitude of 1, could indeed emit large amounts gravitational radiation.

As an upper bound for the most luminous events we can expect, we can consider two black holes immediately before merger, such that their event horizons are almost touching. In this extreme limit we would simply have $R_S \approx D$, and the power of the gravitational radiation would be $10^{52}\,\mathrm{W}$.

Note that some assumptions we made – such as the application of Kepler's law – are certainly invalid in this scenario. Still, the calculated value is within a few orders of magnitude of what has been observed using direct detection of GWs, see section 2.3.

It is not easy to put this number into context. For example, a typical star like our sun has a luminosity of 'just' $10^{26}\,\mathrm{W}$. One of the most luminous stars observed to date, RMC 136a1, radiates $2.3 \times 10^{33}\,\mathrm{W}$ [25], still far below the energy emitted in a black hole merger. It is estimated that there are around 10^{22}-10^{24} stars in the observable universe[1], such that at least for the short time at which the two black holes are merging, they would emit more energy in GW radiation than all stars combined emit as EM radiation[2].

However, as we will see in section 2.2, despite the large amount of gravitational radiation emitted in such events, the interaction of GWs with matter is so weak that it is still extremely hard to detect them directly.

Instead, the first detections of gravitational waves were indirect, and relied on continous observation of systems which also emit electromagnetic radiation.

1 This estimate is given on `http://www.esa.int/Science_Exploration/Space_Science/Herschel/How_many_stars_are_there_in_the_Universe`.

2 Stars can have luminosities ranging from 10^{-5} to 10^{6} that of our sun, as visible on a Hertzsprung-Russell Diagram (e.g., see `https://www.eso.org/public/austria/images/eso0728c/`). We assumed for this estimate that the average star emits around $10^{26}\,\mathrm{W}$.

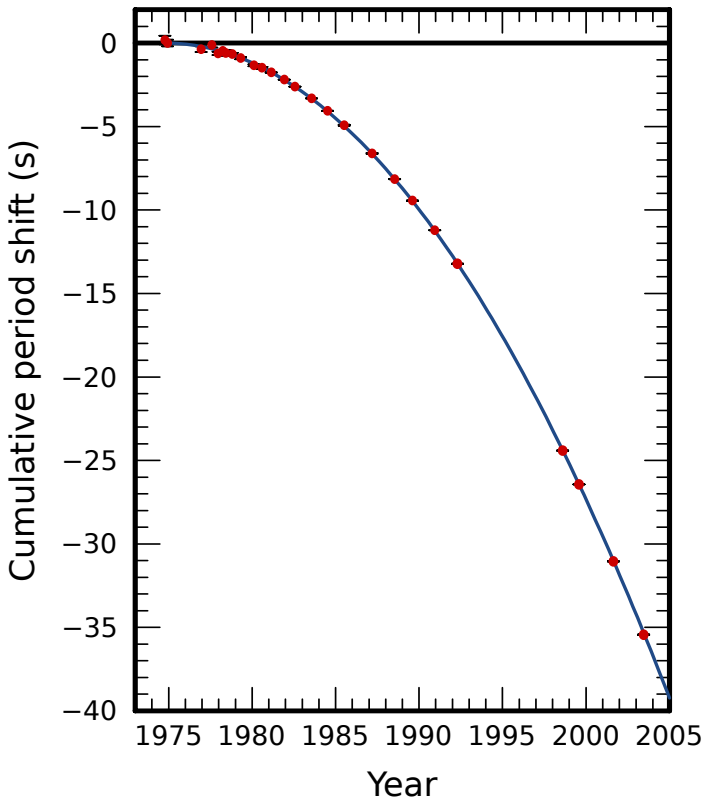

FIGURE 2.1: Observed change in the orbital period of the Hulse-Taylor binary compared to the prediction from general relativity. Figure from [91], itself based on data from [98].

2.1.2 *Indirect detection*

As discussed above, compact binary systems can emit significant amounts of energy in the form of gravitational radiation. This energy is not created out of nothing, but instead converted from the kinetic energy and mass of the binary. Therefore, the orbital period of such a system will not be constant, but will slowly decrease with time as the two stars radiate away their kinetic energy and get closer together.

This phenomenon was first observed in the Hulse-Taylor binary, which consists of a neutron star and a pulsar [99]. Pulsars are rapidly rotating, highly magnetized neutron stars which emit large amounts of electromagnetic radiation with each rotation. In the case of the Hulse-Taylor binary, the pulsar was rotating 17 times per second. In the case of this pulsar, they could observe periodic variations in the arrival time of those pulses, and could conclude that these are caused by a non-pulsing companion star, with an orbital period of 7.75 hours.

Pulsars are usually highly stable in their rotational period. This allows observation of fluctuations in the orbital period of this binary star system over long timescales. And indeed, over 3 decades of observations, the Hulse-Taylor binary has been slowing down at a rate almost perfectly predicted by GR [98], see fig. 2.1.

The two neutron stars are believed to be of almost equal mass of $1.4\,M_\odot$, and follow a highly eccentric orbit with an eccentricity of ≈ 0.6 and a semi-major axis of 1 950 100 km. Due to this high eccentricity, we would not expect our

simplified eq. (2.2), which is based on a circular orbit, to produce accurate results. Still, it's interesting to compare how close we can get with such a simple model. Putting in the masses of the two binaries and assuming we can use the semi-major axis as our separation yields a luminosity of

$$L_{GW} \approx 6.2 \times 10^{23}\,\mathrm{W}\,. \tag{2.7}$$

This falls short by about one order of magnitude from the real value $7.35 \times 10^{24}\,\mathrm{W}$ computed from a full relativistic treatment, see for example [101].

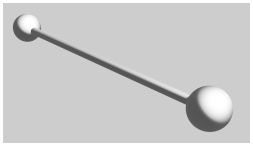

FIGURE 2.2: A naive gravitational wave generator: two test-masses connected by a thin rod or cable. In principle, this setup will emit gravitational waves when rotated – however, as explained in the text, the amount of radiation is incredibly small.

2.1.3 *Gravitational waves from the laboratory*

It would be interesting if we could study GWs by directly generating them in a laboratory here on earth. The problem in generating GWs in a laboratory is the extremely small scaling factor $G/c^5 \approx 2.7 \times 10^{-53}\,\mathrm{W}^{-1}$ appearing in eq. (2.1). This factor must be overcome by $\Omega^6 \cdot (I_1 - I_2)^2$.

To get an idea of the orders of magnitude involved, we make a simplified thought experiment: We consider two massive spheres, which we will again model as point masses with mass M_S. While the binary in the previous example was held together by gravity, we instead link our two spheres by a cable of radius r and length L. For simplicity, we will work under the assumption that we have a thin cable with $r \ll L$. As before, the whole setup is rotated around the spheres' common center of mass (see fig. 2.2).

The moments of inertia along the non-rotating axes are then $I_1 \approx \frac{1}{12}(M_C + 6M_S)L^2$ and $I_2 \approx 0$, with M_C as the mass of the cable. Inserting this into eq. (2.1) gives

$$L_{GW} = \frac{2}{45} \cdot \frac{G}{c^5} \cdot \Omega^6 \cdot (M_C + 6M_S)^2 L^4\,. \tag{2.8}$$

Even if we assume that our idealized system does not lose kinetic energy by any other means, it should eventually slow down due to the energy lost by gravitational radiation.

A possible laboratory experiment to prove the existence of gravitational waves could therefore be to put such a setup into a frictionless environment, bring it to rotation around its center of mass, and observe the rate at which it slows down. Observing that the angular velocity Ω enters eq. (2.8) to the sixth power, we want to rotate our system as fast as possible to maximize the amount of radiated GWs.

The speed at which we can rotate this system will be limited by the cables ultimate tensile strength, S_{max}, which has to counteract the centrifugal force pulling the system apart.

The tension acting on the cable is highest at it's center, where it is given as the sum of the centrifugal force due to the cable itself and the test mass, divided by the cross sectional area, A, of the cable. We get

$$S = \frac{L\Omega^2}{8A}(4M_S + AL\rho)\,, \tag{2.9}$$

with ρ as the density of the cable.

This means the highest angular velocity we can achieve before the cable breaks is given by

$$\Omega^2 = \frac{8AS_{max}}{L(4M_s + AL\rho)}\,. \tag{2.10}$$

Inserting this into eq. (2.8), and replacing the mass of the cable by $M_C = \rho AL$ gives

$$L_{GW} = \frac{1024}{45} \cdot \frac{G}{c^5} \cdot A^3 L S_{max}^3 \cdot \frac{(6M_S + AL\rho)^2}{(4M_S + AL\rho)^3}\,. \tag{2.11}$$

We observe that M_S appears to the third order in the denominator, but only up to the second order in the numerator. This means that mounting heavy masses at the end of the cable actually *decreases* the amount of gravitational radiation. This tells us it is better to remove the spheres and rotate just the cable, which allows us to achieve a higher angular velocity.

This can be modelled by replacing $M_S \to 0$ in the previous equations, which leads to the same simplified formula given in [38],

$$L_{GW} = \frac{1024}{45} \cdot \frac{G}{c^5} \cdot \frac{A^2 S_{max}^3}{\rho}\,. \tag{2.12}$$

The parameters we can adjust to construct our experiment are the cross-sectional area, A, and the material properties, S_{max} and ρ. Ideally, we would need a material with high tensile strength and low density, i.e., a material of high specific strength. $A = \pi r^2$ can in principle be made arbitrarily large. However, for these equations to remain valid, we have to stay within the assumption that the cable is indeed thin, i.e., that $L^2 \gg r^2$.

The commercially available materials with the highest specific strength are carbon fibres, with an extremely high tensile strength of up to $S_{max} = 7000\,\mathrm{MPa}$ combined with a comparatively low density of $\rho = 1.79\,\mathrm{g\,cm^{-3}}$ [88]. Typically, carbon fibres are very thin, with diameters of the order of a few µm. For the sake of argument, we will assume that it is possible to create a composite cable out of these carbon fibres with $A = 1\,\mathrm{cm}^2$ while preserving the same specific strength. Assuming this cable has a length of $L = 1\,\mathrm{m}$, eq. (2.10) tells us that we could spin it up to a frequency of more than 5 kHz before it breaks. Inserting these values into eq. (2.12) gives a maximum luminosity of $10^{-33}\,\mathrm{W}$. By comparison, the total kinetic energy of the rotating cable would be given as

Given as $\nu = 2\pi\Omega$.

$$E_{kin} = \frac{1}{2} I_1 \Omega^2 \approx 2 \times 10^5\,\mathrm{J}\,. \tag{2.13}$$

This means that even if we started our experiment at the dawn of time, it would only have radiated a factor 2×10^{-21} of it's total energy.

Assuming an age of the universe of 13.8 billion years.

This is obviously far below any observable power level.

Theoretically, novel materials such as colossal carbon tubes could achieve similar tensile strengths of $S_{max} = 6.9\,\mathrm{GPa}$, but with densities as low as

$\rho = 0.116\,\mathrm{g\,cm^{-3}}$ [65]. However, such numbers are currently not achievable on scales usable for our experiment. If we assume for the sake of curiosity that we could construct a cable with the same dimensions as before out of these colossal carbon tubes, we could theoretically spin it up to more than 20 kHz - it would still only radiate 10^{-32} W in gravitational radiation.

This highlights the complete infeasability of producing any measurable amount of GW power in such a laboratory experiment any time in the foreseeable future.

2.2 A SHORT REVIEW OF GENERAL RELATIVITY

So far, we have only computed the amount of energy radiated by GWs. Now, we want to sketch how they interact with matter, and how they can be detected directly. We will first review the basic mathematical toolset used to describe GR, give the Einstein field equations as well as their approximate wave solution, and finally discuss the principle behind the direct GW detections up to this date.

All material presented in this section is adapted from the literature, in particular using [37], [73] and [58]. See there for a much more detailed treatment, as well as proofs which are omitted here.

2.2.1 *Introduction*

A guiding principle in modern physics is that of general covariance. Simply put, it means that our description of physics should not depend on our choice of coordinates. In Special Relativity, this principle is only fulfilled for coordinate transformations between *inertial* reference frames. Extending it to allow invariance of the physical laws under *any* differentiable coordinate transformation ultimately lead to the discovery of the general theory of relativity.

Contrary to classical mechanics - where space is seen as isomorphic to the three dimensional flat space with time as an absolute parameter governing the laws of physics - space and time are seen as coordinates of a 4-dimensional space-time $\mathcal{M}$. The points of this spacetime are called *events* - they uniquely identify a time and place.

Mathematically, $\mathcal{M}$ can be described using the tool-set of pseudo-Riemannian geometry. The central object in this theory is a so called manifold, which can be any set of points, $\mathcal{M}$, which are locally equivalent to pseudo-Euclidean space. Formally, this means $\mathcal{M}$ must be equipped with a set of local maps $x : \mathcal{M} \to \mathbb{R}^4$ which give a one-to-one correspondence of the area around any point $r \in \mathcal{M}$ to the usual vector space $\mathbb{R}^4$. These allow us to - at least locally - define coordinates in the familiar $\mathbb{R}^4$ to mathematically describe physics in a curved space. We consider only differantiable manifolds, for which any

There are some additional technical restricitions these have to fulfill, which are not relevant here.

two maps x, y around the same point p are compatible in such a way that $x \circ y^{-1} : \mathbb{R}^4 \to \mathbb{R}^4$ is infinitely differentiable.

The coordinates of any spacetime event p in a given map x are therefore specified by four numbers, which we indicate by $x^0(p)$, $x^1(p)$, $x^2(p)$, $x^3(p)$. We will use greek indices to denote any of these 4 coordinates. Latin indices denote just the spatial components $x^1(p), x^2(p), x^3(p)$, while the temporal coordinate is identified with $x^0(p)$. Furthermore, we will usually drop the explicit dependence on the spacetime event p, and just write the coordinates as x^μ.

Practically, this abstract structure of a manifold equipped with maps allows us to define quantities on $\mathcal{M}$ itself, which are independent of the choice of coordinates, thus fullfilling the principle of general covariance.

2.2.2 *Vectors, co-vectors and tensors*

One common example of such a quantity is a vector field. Given any coordinate chart x around a point p, we can define a basis of the *tangent space* $T_p\mathcal{M}$ in that point as

$$\left.\frac{\partial}{\partial x^\mu}\right|_p = \left.\frac{\mathrm{d}}{\mathrm{d}\lambda} x^{-1}\big(x(p) + \lambda e_\mu\big)\right|_{\lambda=0}, \tag{2.14}$$

where e_μ is an element of the standard basis of $\mathbb{R}^n$. Any member $v(p)$ of the tangent space can then be written as

$$v(p) = \sum_{\mu=0}^{3} v^\mu(p) \left.\frac{\partial}{\partial x_\mu}\right|_p = v^\mu(p) \left.\frac{\partial}{\partial x_\mu}\right|_p, \tag{2.15}$$

$T\mathcal{M}$ (without the subscript p) is the **tangent bundle**. It can be defined as the set of all vector fields on $\mathcal{M}$.

where we introduce the Einstein sum convention - repeated identical indices of upper and lower indices are to be summed. A vector field is then a map $v : \mathcal{M} \to T\mathcal{M}$, which assigns a vector in $T_p\mathcal{M}$ for each point, p, in the manifold. Since our manifold represents 4 dimensional space-time, we call members of its tangent space 4-vectors, to distinguish them from the 3 component vectors used in classical physics.

Another way to look at vectors in the point p is to interpret them as the derivative along a curve $\gamma : \mathbb{R} \to \mathcal{M}$ with $\gamma(0) = p$. Such a curve could, for example, describe the trajectory of a particle moving through spacetime. In that case, it is also called a world line of that particle.

Meaning that $f \circ x^{-1} : \mathbb{R}^n \to \mathbb{R}$ is differentiable in the usual sense for any map x.

Given a differentiable function $f : \mathcal{M} \to \mathbb{R}$, we can define its derivative along the curve γ in the point p as

$$\dot{\gamma}_p(f) = \left.\frac{\mathrm{d}}{\mathrm{d}\lambda} f \circ \gamma(\lambda)\right|_{\lambda=0} \equiv \dot{\gamma}^\mu(0) \left.\frac{\partial}{\partial x^\mu}\right|_p f, \tag{2.16}$$

where the last equality relates to the previous definition of a vector using the definitions

See [37] for a detailed derivation.

$$\dot{\gamma}^\mu(\lambda) = \frac{\mathrm{d}}{\mathrm{d}\lambda'} x^\mu \circ \gamma(\lambda') \Big|_{\lambda'=\lambda} , \tag{2.17a}$$

$$\frac{\partial}{\partial x^\mu}\Big|_p f = \frac{\mathrm{d}}{\mathrm{d}\lambda} f \circ x^{-1}\big(x(p) + \lambda e_\mu\big)\Big|_{\lambda=0} . \tag{2.17b}$$

If the curve γ describes the world line of a particle parametrized by its proper time, it's derivative $\dot{\gamma}$ with components $\dot{\gamma}^\mu$ is called the 4-velocity of the particle.

The **proper time** of a particle is the time shown by a perfect clock comoving with it.

Closely related to the tangent space is the *co-tangent space* $T_p^*\mathcal{M}$, which is defined as the space of linear functions $\eta : T_p\mathcal{M} \to \mathbb{R}$, or dual space of $T_p\mathcal{M}$. It is also a vector space, and we can define a basis $\mathrm{d}x^\mu\big|_p$ by demanding

$$\mathrm{d}x^\mu\Big|_p \left(\frac{\partial}{\partial x^\nu}\Big|_p \right) = \delta^\nu_\mu , \tag{2.18}$$

where δ^ν_μ is the Kronecker delta. Consequently, we can define a general co-vector in the point p as

$$k(p) = k_\mu(p)\, \mathrm{d}x^\mu\Big|_p . \tag{2.19}$$

Similar to a vector field, a co-vector field is then a map $k : \mathcal{M} \to T^*\mathcal{M}$ which assigns a co-vector in $T_p^*\mathcal{M}$ to each point p of the manifold. In the following, we will drop the explicit mention of the event p for vectors, co-vectors and the more general tensors defined below.

Similarly to $T\mathcal{M}$, $T^*\mathcal{M}$ is the **Cotangent bundle**, the set of all co-vector fields on $\mathcal{M}$.

A co-vector's action on a vector v can simply be computed as

$$k(v) = k_\mu v^\mu , \tag{2.20}$$

to be evaluated for each point of the manifold.

We can use vector and co-vector fields to construct more general fields of (m,n) tensors $T \in T^n_m\mathcal{M}$, which can be written as

$$T = T^{\beta_1\dots\beta_n}_{\alpha_1\dots\alpha_m} \frac{\partial}{\partial x^{\beta_1}} \otimes \dots \frac{\partial}{\partial x^{\beta_n}} \otimes \mathrm{d}x^{\alpha_1} \otimes \dots \mathrm{d}x^{\alpha_m} . \tag{2.21}$$

Employing the sum convention, each index α_i, β_i takes 4 different values, so this equation has a total of $4^{(m+n)}$ summands.

Such a (m,n) tensor can be thought of as a function attached to each point of the manifold which maps m vectors $v_1, \dots, v_m$ and n co-vectors $k^1, \dots, k^n$ to one real number:

$$T(k^1, \dots, k^n, v_1, \dots, v_m) = T^{\beta_1\dots\beta_n}_{\alpha_1\dots\alpha_m} \cdot k^1_{\beta_1} \dots k^n_{\beta_n} \cdot v_1^{\alpha_1} \dots v_m^{\alpha_m} . \tag{2.22}$$

2.2.3 *The metric tensor*

2.2.3.1 *Measuring distances*

By definition, each pseudo-Riemannian manifold is equipped with a *metric tensor* $g \in T^0_2\mathcal{M}$, defining a scalar product at each point. Physically, it can be

used to define distances between events in the curved spacetime. As described above, since it is a tensor, we can always write its action on two vectors v, w as

$$g(v, w) = g_{\mu\nu} v^\mu w^\nu \,, \tag{2.23}$$

such that it is convenient to write its coefficients, $g_{\mu\nu}$, as a matrix.

Contrary to massive particles, light-like particles don't have a proper time one could use to parametrize the world line, and λ is just a mathematical parameter without physical significance. Consequently, $\dot{\gamma}(\lambda)$ is not a 4-velocity.

The two vectors could represent the derivative, $\dot{\gamma}(\lambda)$, along the worldline of a photon. Photons follow null-geodesics[3], fulfilling

$$g(\dot{\gamma}(\lambda), \dot{\gamma}(\lambda)) = 0 \qquad \forall \lambda \,. \tag{2.24}$$

One important example of a metric is the Minkowski metric tensor, $\eta_{\mu\nu}$, of special relativity, which can be written globally in an inertial frame as

$$\eta = \begin{pmatrix} -1 & 0 & 0 & 0 \\ 0 & 1 & 0 & 0 \\ 0 & 0 & 1 & 0 \\ 0 & 0 & 0 & 1 \end{pmatrix} . \tag{2.25}$$

This means that in an inertial frame in a flat spacetime, eq. (2.24) simply becomes

$$\left(\dot{\gamma}^0(\lambda)\right)^2 = \delta_{ij} \dot{\gamma}^i(\lambda) \dot{\gamma}^j(\lambda) \,, \tag{2.26}$$

where we used the definitions in eqs. (2.16), (2.17a) and (2.18).

We can integrate the square root of this expression between two events A and B to represent a macroscopic spacetime interval:

$$\Delta t = \int_{\lambda_A}^{\lambda_B} \mathrm{d}\lambda \, \dot{\gamma}^0(\lambda) = \int_{\lambda_A}^{\lambda_B} \mathrm{d}\lambda \, \sqrt{\delta_{ij} \dot{\gamma}^i(\lambda) \dot{\gamma}^j(\lambda)} = L \,. \tag{2.27}$$

Note that while eq. (2.24) is valid in any reference frame, the values of $\dot{\gamma}^\mu$ are coordinate dependent! Therefore, the computed values for Δt and ΔL will depend on the chosen reference frame.

The left-hand side is then the coordinate time difference between the events, while the right-hand side is the spatial distance between them. This means we can measure spatial distances by tracking the time of flight of photons, which is the basic principle behind interferometric distance measurements.

2.2.3.2 *Converting vectors to co-vectors*

We can use a metric to convert a vector v into a co-vector $v^\flat$ by defining

$$v^\flat = g(v, \cdot) = \underbrace{g_{\mu\nu} v^\mu}_{= v_\nu} \mathrm{d}x^\nu \,. \tag{2.28}$$

Conversely, we can use the dual of the metric, defined via

$$g_{\mu\alpha} (g^{-1})^{\alpha\nu} = \delta^\nu_\mu, \tag{2.29}$$

3 This is an additional property in addition to the geodesic equation, see section 2.2.4 below.

to convert a co-vector k into a vector $k^\sharp$,

$$k^\sharp = g^{-1}(k, \cdot) = \underbrace{(g^{-1})^{\mu\nu} k_\mu}_{=k^\nu} \frac{\partial}{\partial x^\nu} . \tag{2.30}$$

These rules can directly be generalized to pull any numer of indices of a general tensor up or down, by applying the same rule for each index.

Note that using eqs. (2.29) and (2.30), we get

$$g^{\mu\nu} = (g^{-1})^{\mu\alpha} (g^{-1})^{\nu\beta} g_{\alpha\beta} = (g^{-1})^{\mu\nu} . \tag{2.31}$$

This means the components of g^{-1} are exactly given by those of g with the indices pulled up, such that we will use the same symbol for g and g^{-1}.

2.2.4 *Derivatives and geodesics*

We need a structure on the spacetime manifold to allow us to take derivatives of tensor fields. There are different ways to define such a derivative, but the most prevelant one used in GR is the *covariant derivative* or more general a connection. The covariant derivative ∇ of a general tensor $T \in T^n_m \mathcal{M}$ along a vector $v = v^\mu \frac{\partial}{\partial x^\mu}$ can be defined as

We consider here only a special case called the **Levi-Civita connection**.

$$\nabla_v T = v^\mu \left(\nabla_\mu T^{\beta_1 \dots \beta_n}_{\alpha_1 \dots \alpha_m} \right) \frac{\partial}{\partial x^{\beta_1}} \otimes \dots \frac{\partial}{\partial x^{\beta_n}} \otimes \mathrm{d}x^{\alpha_1} \otimes \dots \mathrm{d}x^{\alpha_m} , \tag{2.32}$$

where

$$\begin{aligned} \nabla_\mu T^{\beta_1 \dots \beta_n}_{\alpha_1 \dots \alpha_m} = \frac{\partial}{\partial x^\mu} \left(T^{\beta_1 \dots \beta_n}_{\alpha_1 \dots \alpha_m} \right) + \Gamma^{\beta_1}_{\mu\nu} T^{\nu \beta_2 \dots \beta_n}_{\alpha_1 \dots \alpha_m} + \dots + \Gamma^{\beta_n}_{\mu\nu} T^{\beta_1 \dots \beta_{n-1} \nu}_{\alpha_1 \dots \alpha_m} \\ - \Gamma^{\nu}_{\mu\alpha_1} T^{\beta_1 \dots \beta_n}_{\nu \alpha_2 \dots \alpha_m} - \dots - \Gamma^{\nu}_{\mu\alpha_m} T^{\beta_1 \dots \beta_n}_{\alpha_1 \dots \alpha_{m-1} \nu} . \end{aligned} \tag{2.33}$$

The symbols $\Gamma^\mu_{\nu\kappa}$ are called the Christoffel symbols (or more generally, the connection components). For the Levi-Civita connection, they can be computed from the metric coefficients:

$$\Gamma^\mu_{\nu\kappa} = \frac{1}{2} g^{\mu\delta} \left(-\frac{\partial}{\partial x^\delta} g_{\nu\kappa} + \frac{\partial}{\partial x^\nu} g_{\kappa\delta} + \frac{\partial}{\partial x^\kappa} g_{\delta\nu} \right) . \tag{2.34}$$

We can use the covariant derivative to define a condition for free-falling particles. A free-falling particle's world line is a curve γ which naturally follows the background spacetimes curvature. In other words, the particles 4-velocity does not change along this trajectory, meaning that there is no acceleration acting on it.

As mentioned above, light-like particles do not have a 4-velocity. But they do have tangent vectors to their world lines, which can be used in the geodesic equation instead.

Formally, this means that

$$\nabla_{\dot\gamma} \dot\gamma = 0 . \tag{2.35}$$

Such a curve is called a *geodesic*.

2.2.5 *Curvature and the Einstein field equations*

The metric alone is not sufficient to judge if spacetime is curved at a particular point or not. Instead, one has to compute the Riemann curvature tensor $\mathrm{Riem} \in T^1_3\mathcal{M}$, whose components in a given basis are

$$\mathrm{Riem}^{\mu}{}_{\nu\alpha\beta} = \frac{\partial}{\partial x^{\alpha}}\Gamma^{\mu}_{\beta\nu} - \frac{\partial}{\partial x^{\beta}}\Gamma^{\mu}_{\alpha\nu} + \Gamma^{\mu}_{\alpha\gamma}\Gamma^{\gamma}_{\beta\nu} - \Gamma^{\mu}_{\beta\gamma}\Gamma^{\gamma}_{\alpha\nu}\,. \tag{2.36}$$

A spacetime $\mathcal{M}$ is considered flat if $\mathrm{Riem} = 0$ globally. The contraction

$$\mathrm{Ric}_{\mu\nu} = \mathrm{Riem}^{\gamma}{}_{\mu\gamma\nu} \tag{2.37}$$

is called the Ricci tensor, and it's contraction

$$R = \mathrm{Ric}^{\mu}_{\mu} \tag{2.38}$$

is called the Ricci scalar.

Utilizing these quantities, we can write down the *Einstein field equations*,

$$\mathrm{Ric}_{\mu\nu} - \left(\frac{1}{2}R + \Lambda\right)g_{\mu\nu} = \kappa T_{\mu\nu}\,. \tag{2.39}$$

At first glance, these appear to be 16 equations, since both μ and ν can take on 4 values. This reduces to 10 equations since all tensors appearing here are symmetric.

These are the 10 fundamental equations which relate the spacetime geometry to the matter content encoded in the stress-energy tensor $T_{\mu\nu}$, which appears scaled by the Einstein gravitational constant κ. Λ is a free parameter, the cosmological constant, which can be related to the rate of expansion of the universe.

Note that this is a system of non-linear differential equations for the spacetime metric $g_{\mu\nu}$, since the curvature terms $\mathrm{Ric}_{\mu\nu}$ and R contain derivatives of the Christoffel symbols $\Gamma^{\alpha}_{\mu\nu}$, which themselves contain derivatives of the metric $g_{\mu\nu}$.

Note that in order to conserve general covariance, any field equation for the metric has to leave 4 of it's 10 degrees of freedom un-constraint.

2.2.6 *Gravitational waves as weak-field solutions*

Solving the full Einstein field equations is a significant challenge. This remains true even when considering special cases, such as vacuum solutions satisfying $T_{\mu\nu} = 0$.

Exact analytical solutions do exist, for example the famous Schwarzschild metric describing a non-rotating spherical black hole, but are relatively rare. In addition, it is possible to numerically solve the equations, which allows accurate modelling of the gravitational waveforms generated by events involving strong gravitational fields, such as the merging of two black holes.

This decomposition is not valid under arbitrary coordinate transformation, but only under a subset of so-called **gauge transformations**, see [58].

For describing the action of GWs far away from their generating source, however, it has proven more succesful to consider them as a small pertubation $h_{\mu\nu}$ of the metric tensor on a flat background spacetime:

$$g_{\mu\nu} = \eta_{\mu\nu} + h_{\mu\nu}\,, \tag{2.40}$$

where $\eta_{\mu\nu}$ is the Minkowski tensor of special relativity. As shown in e.g. [58], one can define a special coordinate system called the transverse-traceless (TT) gauge in which the $h_{\mu\nu}$ fulfill

$$h_{\mu 0} = 0, \quad \frac{\partial}{\partial x^j} h_{kj} = 0, \quad \sum_{k=1}^{3} h_{kk} = 0\,. \tag{2.41}$$

In this case, it can be shown that the vacuum Einstein field equations simplify significantly to just ordinary wave equations,

$$\Box h_{kj} = 0\,, \tag{2.42}$$

where $\Box$ is the D'Alambertian operator of special relativity.

These linearized equations are identical in form to the usual wave equations appearing in, for example, electromagnetism. Therefore, eq. (2.42) allows simple monochromatic plane-wave solutions. Due to the additional gauge constraints given in eq. (2.41), the solutions of eq. (2.42) have only two degrees of freedom.

For example, we can consider a plane wave propagating in the x^3 direction. This solution is given in the TT gauge by

$$h_{\mu\nu} = \cos\big(\omega(x^0 - x^3)\big) \cdot \begin{pmatrix} 0 & 0 & 0 & 0 \\ 0 & h_+ & h_\times & 0 \\ 0 & h_\times & -h_+ & 0 \\ 0 & 0 & 0 & 0 \end{pmatrix}, \tag{2.43}$$

In GR, these are the only two valid GW polarizations. Some alternative gravitational theories allow up to 6 different polarizations, see e.g. [102].

with h_+ and $h_\times$ describing the amplitude of the so-called plus and cross polarizations of the gravitational wave.

The full metric is therefore given by

$$g_{\mu\nu} = \begin{pmatrix} -1 & 0 & 0 & 0 \\ 0 & 1 + h_+ \cos\big(\omega(x^0 - x^3)\big) & 1 + h_\times \cos\big(\omega(x^0 - x^3)\big) & 0 \\ 0 & 1 + h_\times \cos\big(\omega(x^0 - x^3)\big) & 1 - h_+ \cos\big(\omega(x^0 - x^3)\big) & 0 \\ 0 & 0 & 0 & 1 \end{pmatrix}. \tag{2.44}$$

For the moment, we focus on just the h_+ polarization. If we remember that the metric determines distances between spacetime events, we see that a h_+ polarized GW periodically stretches and contracts the x^1 direction, while having an equal but opposite effect on the x^2 direction.

There are other kinds of GW detectors. One example are **bar detectors**, which are designed to amplify the effect of a passing GW using mechanical resonance. However, these have not succeeded to detect any GWs to date.

In principle, this distortion can be measured by two observers $\mathcal{A}$ and $\mathcal{B}$, which, in the absence of a GW, are at rest in the given coordinate system and seperated by the flat-spacetime distance L, both equipped with a perfect clock. $\mathcal{A}$ can encode the time shown by his clock on an electromagnetic signal, for example by modulating a laser beam, and send it to $\mathcal{B}$. On reception, $\mathcal{B}$ can then recover the encoded time, and compare it to the time shown by his own clock to determine the coordinate time difference between the event the beam was emitted and the event he received it.

As we saw in section 2.2.3.1, in the absence of GWs, this time difference will directly yield the unperturbed spatial distance, L.

In a first approximation, assuming that the photon path connecting $\mathcal{A}$ and $\mathcal{B}$ is aligned with the x^1 axis and that L is small compared to the GW wavelength, the GW will cause a change ΔL in the propagation time proportional to the undisturbed separation L [73],

$$\Delta L \approx h_+ \cos\big(\omega(x^0 - x^3)\big) L\,. \tag{2.45}$$

$\mathcal{B}$ will therefore see a periodic variation in the emission times of the signals received from $\mathcal{A}$, from which they can deduce the properties of the GW. The same principle can be applied to measure $h_\times$, which acts similarly on the diagonal between x^1 and x^2.

Although conceptually simple, such a light-time GW detector is difficult to realize in practice. Typical GW amplitudes observable on earth are of the order $h_{+/\times} < 10^{-20}$, such that both observers $\mathcal{A}$ and $\mathcal{B}$ need extremely precise clocks[4] to actually be able to distinguish the small fluctuations ΔL caused by GWs from the intrinsic imperfections of their reference clocks.

2.3 DIRECT GRAVITATIONAL WAVE DETECTION

We discussed in the previous section that the effect of gravitational waves can be measured by tracking the time of flight of electromagnetic signals between free-falling observers. One technical challenge in designing such a light time gravitational wave detector is that the time of flight fluctuations must be measured with extreme precision, which requires very stable clocks at both ends of the detector. A way around this is to use only a single timing reference, typically in the form of a laser source of coherent light, which is split into two seperate, orthogonal paths, reflected at mirrors acting as test-masses and then recombined at the point of origin. Such a differential detector is called a Michelson interferometer, and is depicted in fig. 2.3. Since the light output from the laser comes from the same origin and travels almost equal paths, any fluctuations in the lasers frequency are heavily suppressed at the output port of this configuration. This allows us to measure relative distance fluctuations between the two arms with the required precision to detect GWs. For example, the advanced Laser Interferometer Gravitational-Wave Observatory (aLIGO) [3] can resolve relative changes in its 4 km arms to better than a factor 10^{-23}, which corresponds to an absolute distance change of less than 4×10^{-20} m. For comparison, this is roughly a hundred-thousand times smaller than the charge radius of a proton [60].

The **charge radius** is a measure of the size of an atomic nucleus, and is determined by scattering electrons around it.

4 And/or be seperated by extremely large distances. In addition, any matter between the observers can affect the light propagation time as well, potentially further limiting the achievable performance [73].

2.3.1 *Principle of a Michelson interferometer*

We formulate here the basic operating principle of a Michelson interferometer, as depicted in fig. 2.3. A single laser beam is split at a central beam splitter. The two resulting beams are send along two seperate arms, reflected off of mirrors at the end and finally recombined at the same beam splitter. Since the two arms differ in length, the two recombined beams have a relative phase shift and interfere. The resulting interferometric signal can be read out using a photo diode.

Formally, the electrical field of the laser before the beam is split can be written as

$$E(t) = 2A\cos(\Phi(t)) = 2A\cos(\omega t + \phi(t))\,, \tag{2.46}$$

where we assume the amplitude A to be constant while $\phi(t)$ accounts for any intrinsic imperfections in the lasers phase. We assume the two arms to be of unequal length, such that the light travel time for one round-trip is given as $\tau + \delta\tau_N$ for the north arm and $\tau + \delta\tau_E$ for the east arm. Therefore, the two arms differ in round trip time by $\Delta\tau = \delta\tau_E - \delta\tau_N$.

The electrical field after recombining the two beams after each round trip is then given as a superposition of the two recombined beams,

We ignore here any other phase shifts of the beams, for example due to interaction with the mirror surfaces.

$$E_{BS}(t) = A(\cos(\Phi(t-\tau_N)) + \cos(\Phi(t-\tau_E)))\,. \tag{2.47}$$

The photodiode detects a signal proportional to the time averaged squared magnitude of the electrical field:

$$\begin{aligned} P &= \langle |E_{BS}|^2 \rangle \\ &= A^2(1 + \cos(\Phi(t-\tau_N) - \Phi(t-\tau_E)))\,. \\ &= A^2(1 + \cos(\omega\Delta\tau + \phi(t-\tau_N) - \phi(t-\tau_E)))\,. \end{aligned} \tag{2.48}$$

Ground-based Michelson interferometers such as aLIGO are usually designed such that the nominal $\Delta\tau$ is constant. Note that the cosine in eq. (2.48) can take values between 1 and -1, such that the overall detected power at the photodiode can take any value between $2A^2$ and 0. By intentionally moving one of the mirrors, it is possible to adjust $\Delta\tau$ in such a way that the interferometer is tuned to a nominal operating point. In the case of aLIGO, this operating point is close to the dark fringe, at which no light arrives at the photodiode. This ultimately allows a readout of the phase fluctuations [44],

Interferometers with a nominally constant readout signal are called **homodyne interferometers**.

$$\omega\Delta\tau + \phi(t-\tau_N) - \phi(t-\tau_E)\,. \tag{2.49}$$

Assuming that the arm length mismatch $\Delta\tau$ is small, we can write

'Small' means here that $f_{max} \ll 1/\Delta\tau$, with f_{max} as the highest signal frequency we want to measure.

$$\begin{aligned} \phi(t-\tau_N) - \phi(t-\tau_E) &= \phi(t-\tau_E+\Delta\tau) - \phi(t-\tau_E) \\ &\approx \Delta\tau\dot{\phi}(t-\tau_E) \\ &= 2\pi\Delta\tau\nu(t-\tau_E) \end{aligned} \tag{2.50}$$

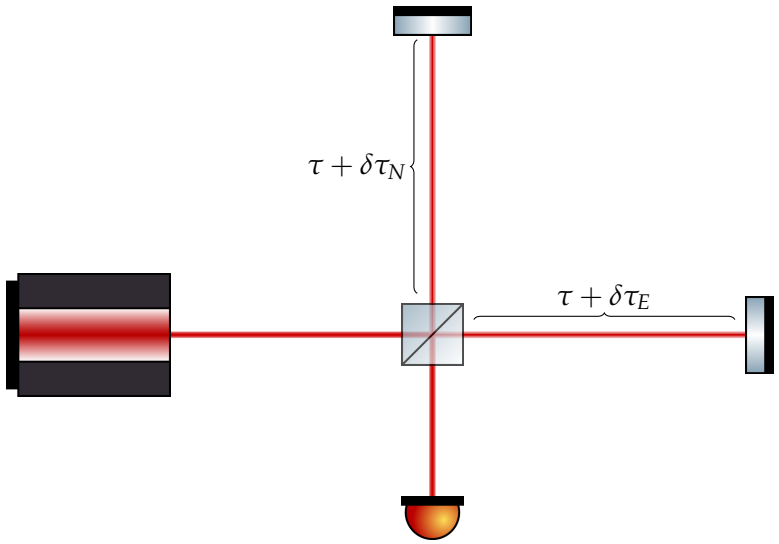

FIGURE 2.3: A simple Michelson interferometer. A single laser beam is split up at a beam splitter, send to two mirrors, reflected, and recombined at the same beam splitter. Any pathlength fluctuations in either of the two arms creates a phase difference between the two beams, which creates the interferometric signal.

for the terms related to the inherent laser instability. Here, we used $\nu(t) = \frac{1}{2\pi}\dot{\phi}(t)$ for the lasers frequency fluctuations. These directly couple into the phase readout of a Michelson interferometer. Since they enter scaled by the armlength mismatch, a Michelson interferometer with perfectly equal arms is completely insensitive to laser frequency noise.

On the other hand, the term $\omega\Delta\tau$ means that Michelson interferometers are very sensitive to differential changes in the arm length, which makes them ideal gravitational wave detectors. As discussed in section 2.2.6, a plus polarized monochromatic GW propagating in the x^3 direction periodically changes relative distances in the x^1 and x^2 directions, with opposing signs. If our Michelson interferometer is oriented in such a way that the north arm is aligned with x^1 direction and the east arm is aligned with the x^2 direction the effect of the gravitational wave directly translates into a differential armlength change.

Keeping the same orientation, a cross-polarized wave, on the other hand, doesn't create any differential armlength change, such that the interferometer is insensitive to it. It is therefore possible to determine the polarization of a passing GW by utilizing multiple detectors with different orientations.

Multiple detectors working in tandem have a number of additional benefits. For one, they allow discrimination of instrumental glitches by rejecting signals which are only visible in one detector at a time. In addition, since GWs propagate at the speed of light, multiple detectors can triangulate the direction the wave is coming from, since the same signal will be seen in different detectors with a small time delay.

2.3.2 *First detections*

On the 14th of September 2015, aLIGO made the first direct detection of a gravitational wave signal [5]. They observed the merging of two black holes

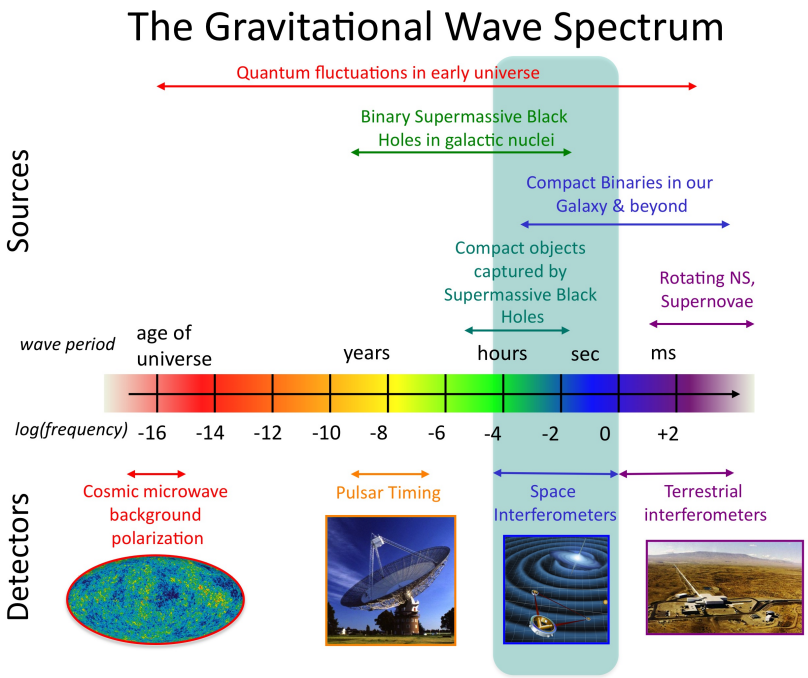

FIGURE 2.4: The gravitational wave spectrum. Image from [27]

of approximately 36 and 29 solar masses, with the final black hole having only a mass of approximately 62 solar masses. About 3 solar masses worth of energy were radiated in form of gravitational waves in this event, with a peak gravitational luminosity of 3.6×10^{49} W.

The two aLIGO detectors are working in tandem with the European Virgo detector, with more gravitational wave observatories being planned to join in a global network of detectors [6], which promises an exciting future of ground based gravitational wave observations.

Indeed, within the first half year of observation, the LIGO-VIRGO collaboration already detected three binary black hole mergers, followed by the detection of a binary neutron star merger and seven additional binary black hole mergers in the second observation run [7]. Including the latest catalogue of the first half of the third observation run [8], this collaboration reported a total of 50 individual detections.

2.4 GRAVITATIONAL WAVE SPECTRUM

The growing network of ground based detectors are remarkable instruments, but they can only observe a limited part of the gravitational universe. In particular, they are severly limited at low frequencies, mainly due to the impact of seismic and newtonian noise.

Newtonian noise is caused by gravitational attraction of moving masses in the environment, for example due atmospheric variations.

However, it is exactly at these low frequencies were we expect a large catalogue of astrophysical GW sources [28]. This is not surprising, since the prime target for GW detection are binary systems of compact objects, most notably of black holes, neutron stars and white dwarfs. Due to the large mass and scale of

these systems, they move comparatively slowly; consequently, their emitted GW radiation is also at low frequencies, especially while they are far away from their merger.

Figure 2.4, provided by [27], shows an overview of the different sources we expect in different frequency ranges. We summarize here the main sources expected in some present and future GW observatories.

2.4.1 *High frequency sources*

Following [27], ground based interferometers such as aLIGO and Virgo cover only the very high part of the expected frequency spectrum, with GW periods of less than 1 second.

The main sources in that range are merging compact binaries, as those already observed by aLIGO and Virgo. The ground based observatories typically only see the very last few seconds of such a merger, when the two compact objects get close together, resulting in a large peak in amplitude as well as a shift to higher frequency.

Violent events such as supernovae also involve large mass redistributions, and could therefore also generate GW in this frequency range. As of the writing of this thesis, however, there have been no detections [4].

In addition to these transient signals, rapidly rotating neutron stars could generate continous GW signals provided that they have some non-axisymmetric deformations. Even though the amplitude of these sources is expected to be much smaller than that of the transient signals, the fact that they are theorized to be stable over very long time scales allows statistical analysis of data from multiple observation runs. So far, no continous wave detection has been confirmed, but this might change when more data becomes available. See [31, 80] for more information.

2.4.2 *Mid frequency sources*

Space-based observatories will be able to observe signals with GW periods ranging from seconds to hours. The most developed mission of this kind is LISA [10], planned to fly in the 2030s, which aims to measure gravitational waves in the frequency band from 1×10^{-4} Hz to 1 Hz.

Contrary to ground based detectors, which are mostly noise dominated with occasional loud transient sources, LISA will most likely be signal dominated.

Similar to ground based detectors, LISA will also be able to observe compact binaries such as those responsible for all direct detections up to date. However, we will be able to see them long before the merger, where the two components of the binary are still widely seperated on relatively stable orbits. This means that these sources will be present as quasi-monochromatic sources, which

slowly increase in frequency as the binary radiates away its kinetic energy. This could allow accurate predictions of the actual time and sky position of the merger, as described in [75], which both EM observatories and ground-based GW observatories could use as early warning to prepare for observation.

In addition to black hole and neutron star binaries, LISA will also be able to observe millions of white dwarf binaries in our own galaxy. EM observations already confirmed the existence of some of those white dwarf binary systems, which should produce continous GWs right in this frequency range. This will allow immediate verification of the measurement chain, since we know that these sources have to be in the data, with a predictable amplitude.

But not all of these will be resolvable as individual sources, such that we expect a stochastic gravitational wave background ever present in the signal. This stochastic background might also have components which can be linked to a cosmological origin, and might give insight into the physics of the very young universe, shortly after the big bang.

Besides these stellar mass sources, LISA will also be able to observe mergers of supermassive black holes expected in the centers of most galaxies, which are millions of times more massive than those visible in ground based observatories.

And a related class of signal are the so-called Extreme Mass Ratio Inspirals (EMRIs), which appear when a relatively small object, such as a stellar mass black hole, merges into a supermassive blackhole. These have a relatively complicated waveform, and allow a unique test of the predictions of GR.

In general, space based observatories such as LISA are projected to have some signals with very high signal to noise ratio. This will allow precision tests of the predictions made by GR, which could constrain the validity of alternative theories of gravity.

In addition, these GW observations can be used to get a completely independent estimate of the expansion rate of the universe.

2.4.3 *Low frequency sources*

We hinted in section 2.3 that one of the primary challenges of constructing a light time GW detector is the requirement of having extremely stable clocks to measure fluctuations in the light travel time of the electromagnetic signals.

Pulsars are a special case of neutron stars from which we can observe periodical electromagnetic pulses with very high timing stability. Indeed, these pulses should be stable enough to in principle allow GW detection by ground based observation with radio telescopes. The actual measurement principle relies on measurements of the arrival time of pulses from multiple pulsars, which are then searched for correlations which can hint at the presence of a GW signal. Such a collection of observatories is called a Pulsar Timing Array (PTA), and is only sensitive to very low frequencies. Possible sources

are for example super massive black hole binaries at the center of galaxies, with orbital periods of months to years. See for example [13] for more information.

Finally, it is possible that GWs from the very early universe might have imprinted on the cosmic microwave background and could be discerned from EM observations of it. To date, this only lead to upper limits of such an effect, see e.g. [71] for more details.

3

THE LASER INTERFEROMETER SPACE ANTENNA

LISA is a large ESA mission, scheduled to fly in the mid 2030s. It's operating principle is similar to that of the ground based observatories, in that LISA also aims to detect gravitational waves using laser interferometry. However, there are some very significant design differences, and therefore unique technical challenges.

In this chapter, we give a brief overview of the LISA mission, with a particular emphasis on the technical details which are relevant to the research presented in this thesis.

In the following, we first describe the LISA constellation and orbits in section 3.1. The orbital dynamics have important implications for the achievable laser noise reduction, which we discuss in section 3.2. In addition, as we will discuss in section 3.3, the large inter-spacecraft velocities require a heterodyne detection scheme, in which the on-board reference clocks become a significant performance limitation.

We then present an overview of the scientific payload in section 3.4, describing the overall optical layout and the available interferometers on each satellite. The main phase readout mechanism is then described in section 3.5.

Finally, we describe further auxilliary functions related to the phasemeter and give an overview of the frequency distribution system in sections 3.6 and 3.7.

3.1 THE LISA CONSTELLATION AND ORBITS

LISA isn't just a single Michelson interferometer, but consists of 3 seperate spacecraft which all follow their individual orbits. The spacecraft exchange laser beams between them, tracking distance fluctuations to the level required for GW detection. The orbits are chosen in such a way that the overall constellation of the three spacecraft forms an almost equilateral triangle.

The iconic triangle configuration is achieved by positioning the three spacecraft in a plane which is tilted by 60 degrees with respect to the ecliptic plane, with the center of mass of all 3 spacecraft trailing earth on its orbit by about 20 degrees, or roughly 50 million km [10], see fig. 3.2. Each individual spacecraft is therefore on a slightly eccentric orbit, where it moves faster when close to the sun and slower when further away. The result is that the overall constellation performs a cartwheel motion around the sun, with the rotation direction of the spacecraft around their center of mass opposite to that of constellation as a whole, see fig. 3.1.

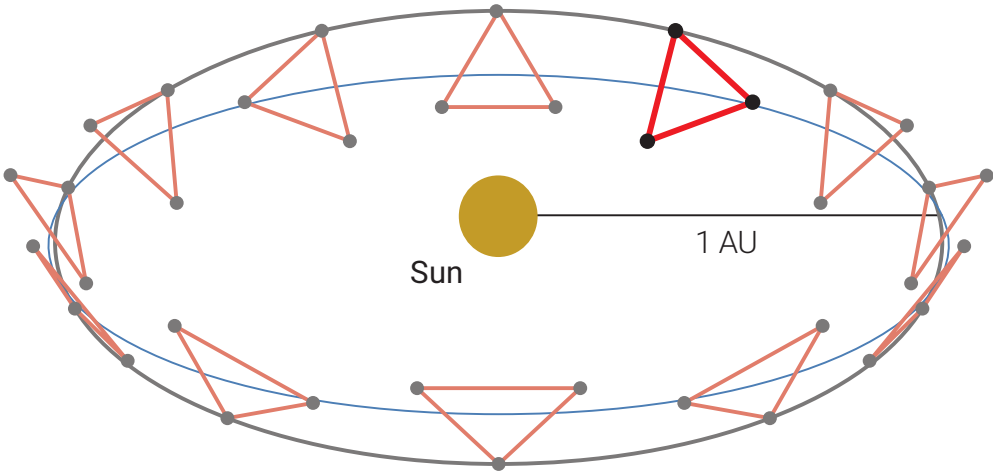

FIGURE 3.1: The LISA orbits, from [10]. All three spacecraft follow their individual trajectory around the sun, such that the constellation as a whole performs a cart-wheel like motion.

These kinds of orbits can be constructed for a wide range of spacecraft seperations [68]. As we saw in section 2.2, GWs create *relative* distance fluctuations, such that large armlengths are desirable, since they yield a stronger signal. However, this is only true up to a certain point: if the arms are too long with respect to the GW wavelength, multiple periods of the GW can partly cancel their effect during a single roundtrip time [10].

In addition, making the arms too long brings a number of technical challenges. For example, even though the laser beams which leave the spacecraft are highly collimated, they will diverge during the propagation, such that only a fraction of the power will actually reach the far spacecraft. In the far field, the intensity of a gaussian laser beam in a given area evolves with the distance squared. Therefore, an increase in the arm length needs to be compensated by either larger telescopes, which would decrease the beam divergence while simultaneously increasing the reception area, or by using higher power lasers. Therefore, a tradeoff between technical challenges and ideal detector sensitivity must be found, balancing cost with scientific performance.

For LISA, the current baseline foresees arm lengths of 2.5×10^9 m, which should allow fulfillment of all science objectives outlined in [10].

3.2 LASER NOISE SUPPRESSION IN LISA

A first approach to construct an analogon to the ground based Michelson interferometers in space would be to use two of the spacecraft as retroreflectors for beams emitted from the remaining spacecraft. We label the emitting spacecraft with the index 1, and the other two by the indices 2 and 3.

Just as we saw in section 2.3, a single laser source on spacecraft 1 would generate light which is sent on two different paths, reflected, and recombined at spacecraft 1.

A first technical problem is that, as discussed in section 3.1, the laser beams lose a very significant amount of their power when propagating between the spacecraft. As a result, the spacecraft cannot act as simple passive retro-

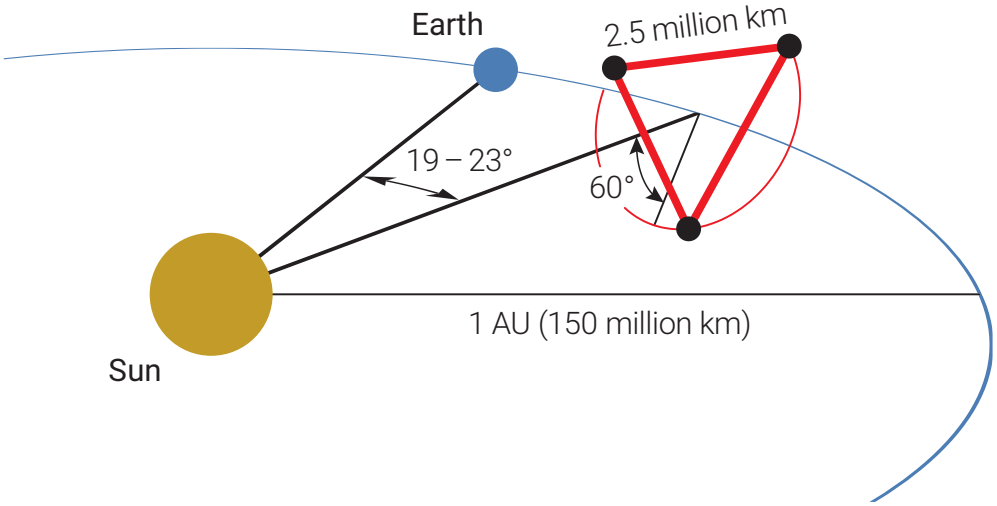

FIGURE 3.2: The LISA constellation, from [10]. The triangular constellation trails earth by 20° and is tilted by 60° with respect to the ecliptic plane.

reflectors, but must amplify the incoming signal before reflecting it back to the sending spacecraft. This can be achieved by using a control loop to phase-lock the lasers on spacecraft 2 and 3 to the incoming light from spacecraft 1. This allows the spacecraft to act as active retro-reflectors, such that the beams being returned from spacecrafts 2 and 3 are transmitted at full power.

Such control loops are required in any case, to ensure that all beatnotes fall within the photoreceivers detection bandwidth, as discussed in section 3.6.2.

This is similar to the situation in the satellite mission Gravity Recovery and Climate Experiment-Follow-On (GRACE-FO), which uses laser interferometry to track the seperation of two satellites in orbit to determine mass distributions below them. GRACE-FO has comparable laser intensities at the receiving spacecraft and uses a similar active transponder scheme, demonstrating its feasability [9].

A more serious problem with this approach is that, different from the ground based detectors, the arms in LISA are not perfectly equal, and thus laser frequency noise (LFN) is not perfectly suppressed.

Figure 3.3 shows a numerical simulation of the light travel times between the spacecraft for realistic orbits[1]. It shows that even though the constellation is quite stable, the arm lengths still fluctuate by about 1 percent over the course of a year. In absolute terms, this can correspond to an armlength mismatch of about 30 000 km.

As we will show in part ii of the thesis, the resulting non-suppressed LFN due to this mismatch is several orders of magnitude above the level required for GW detection. This is sketched in fig. 3.4, where we depict the residual laser noise level assuming the armlengths shown in fig. 3.3 at the beginning of the mission. The top curve of the figure shows the typical laser noise of a cavity stablized space qualified laser, here assumed to be at $30\,\mathrm{Hz}/\sqrt{\mathrm{Hz}}$, as described in appendix D.1. The standard Michelson retains a high laser noise level due to the large armlength mismatch of 0.22 s, as shown by the orange curve. This is to be compared to the dotted curve, which corresponds

1 Orbit from numerical simulations performed at the ESA Concurrent Design Facility (CDF), data provided by D. Escorial Olmos.

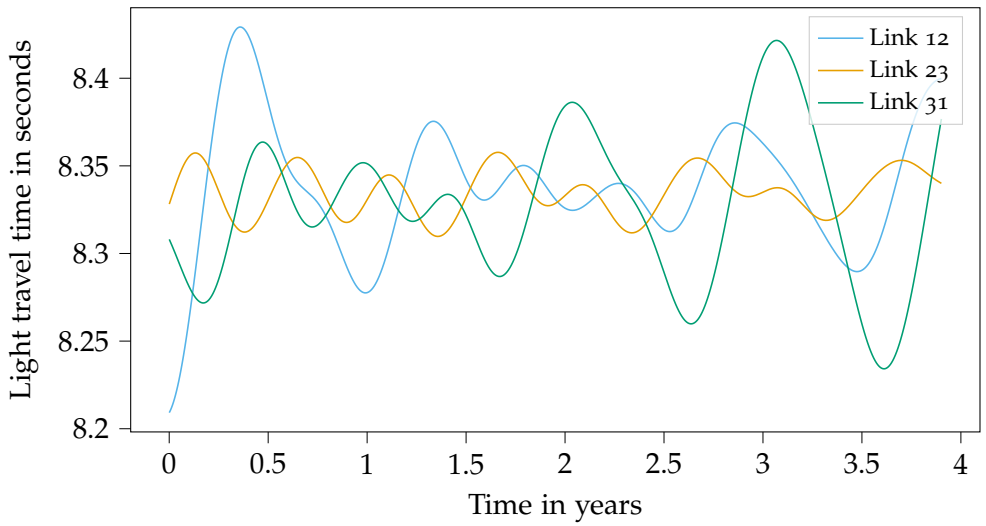

FIGURE 3.3: Light travel times along the links between spacecraft 1, 2 and 3. Computed using [19] based on orbits provided by ESA.

to a typical LISA noise allocation for a single noise source of $1\,\mathrm{pm}/\sqrt{\mathrm{Hz}}$ [10][2].

The proposed solution to this problem is a post-processing algorithm called time-delay interferometry (TDI), which we study in detail in part iii of the thesis. In summary, TDI time shifts and combines multiple inter-spacecraft phase measurements to construct *virtual* interferometers with almost equal arms, in which LFN is naturally suppressed.

The original, first generation combinations were designed to cancel laser noise exactly under the assumption that the arm lengths are unequal, but constant and symmetric under an exchange of the sending and receiving spacecraft [82]. Using realistic orbits, the cancellation will no longer be exact, as depicted by the blue solid line in fig. 3.4. The equivalent interferometer has an armlength mismatch of just $10^{-7}\,\mathrm{s}$, reducing LFN by over six orders of magnitude compared to the standard Michelson.

This can be further improved upon by utilizing so-called second generation combinations [85], which take the time evolution of the arm lengths into account. As can be seen by the dark green bottom curve in fig. 3.4, the resulting combinations have an armlength mismatch of just $10^{-11}\,\mathrm{s}$, suppressing laser noise far below the level required for GW detection. We omit here for clarity that constructing these TDI combinations also affects the signal and other secondary noise levels, such that in principle, their residual laser noise level should be compared to a different requirement curve. However, this does not invalidate the points made above, as we will see in part iii.

2 The overall suggested noise allocation for the optical metrology in LISA is $10\,\mathrm{pm}/\sqrt{\mathrm{Hz}}$ [10]. We plot an allocation a factor of 10 below this, since laser noise is only a single contribution to the overall noise budget. In addition, we neglect for the moment the usual relaxation towards lower frequency (cf. [10], pg. 17) for clarity. This simplification will be dropped in the more detailed analysis in parts ii and iii.

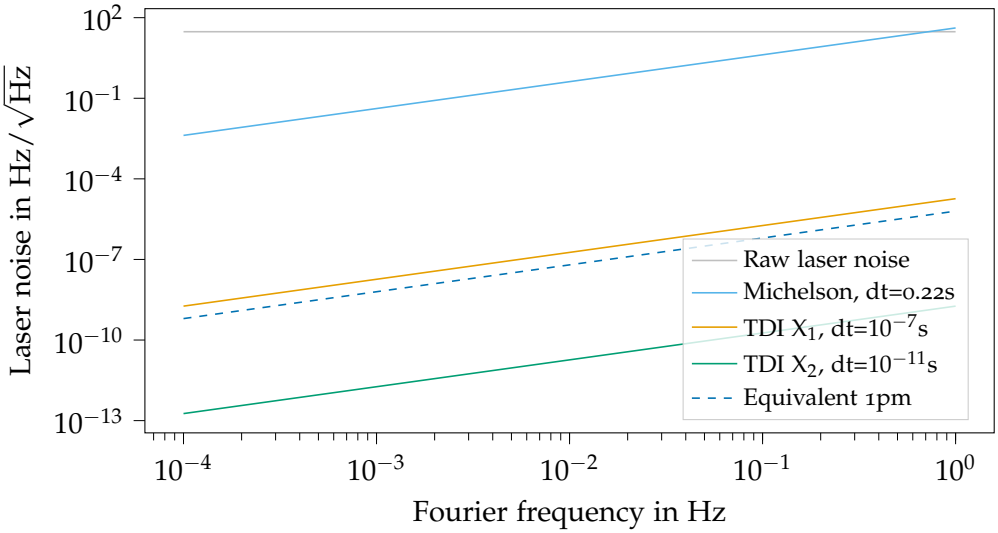

FIGURE 3.4: Residual laser noise in a simple Michelson vs. first and second generation Michelson combinations. Noise shape function and TDI transfer functions omitted for clarity, see section 3.2 for more details.

3.3 HETERODYNE DETECTION AND CLOCK NOISE

Another consequence of the dynamics of the LISA orbits is that the spacecraft are moving with high relative velocities of several $\mathrm{m\,s^{-1}}$ along the line of sight. This causes large Doppler shifts of the laser beams being exchanged, such that the beams entering the intererometers differ in frequency by several MHz. GWs cause tiny fluctuations in the arrival time of the incoming beams, which cause a small phase fluctuation. Therefore, LISA uses a heterodyne detection scheme, in which the phase evolution of the MHz beatnotes is tracked with µcycle precision [15]. The GW signal is then recovered from the recorded phase as small fluctuations around the nominal frequency.

Tracking the phase of such a high frequency signal to this precision requires an equally precise local timing reference. In LISA, each spacecraft will be equipped with a local clock, typically a temperature stabilized quartz oscillator, also called an ultra-stable oscillator (USO). Appendix C contains an overview of the performance of different kinds of oscillators. As explained there, currently available space qualified clocks do not fulfill the stringent timing requirements required for the interferometric readout.

This will be compensated by a sophisticated frequency distribution scheme, in which the signals generated by each clock are distributed throughout the whole constellation. This allows a differential measurement between the different clocks, which ultimately allows suppression of these clock errors in the final TDI data streams.

We will summarize the hardware involved in this frequency distribution in section 3.7, describe the resulting signals in part ii and finally propose an actual noise subtraction algorithm in part iii.

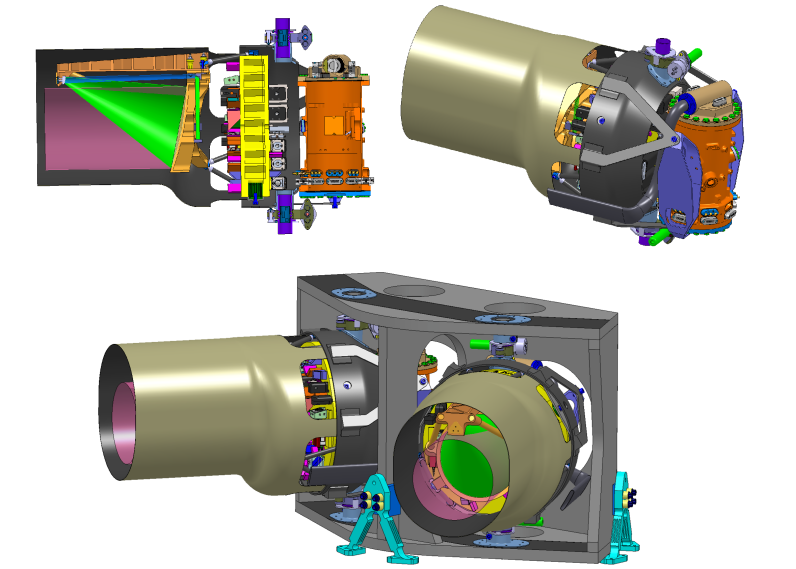

FIGURE 3.5: Payload conceptual design, from [10]. Two MOSAs are mounted at a 60° angle. Each of them houses a telescope, an optical bench and a GRS.

3.4 PAYLOAD OVERVIEW

3.4.1 *Movable optical sub-assemblies*

We show in fig. 3.5 an overview of the LISA payload. Each satellite carries two MOSAs, which are mounted with a roughly 60° angle, each pointing towards one of the other two spacecraft (bottom of fig. 3.5). This angle is adjustable by about 2° to allow compensations for deviations from a perfect triangular constellation due to orbital mechanics [10].

Each MOSA is a rigid structure connecting the optical bench (OB) with a telescope and a gravitational reference sensor (GRS) (top-left of fig. 3.5). The telescope (left) is used for light transmission and reception towards the distant spacecraft, while the GRS (right) houses the test-mass. The OB is mounted in-between telescope and GRS, and carries the optical components needed for interferometry.

3.4.2 *Gravitational reference sensors*

We described in section 2.2 that a GW creates a periodic modulation of the light travel time between two test masses. This result is only valid under the condition that the test-masses are actually free-falling, i.e., that no non-gravitational forces are acting on them.

Although the spacecraft themselves are on nominally free-falling orbits around the sun, they are in reality un-shielded from the influence of, e.g., solar winds and micro-meteorites. As has been confirmed by LISA-Pathfinder, these effects create jitters of the spacecraft position at a level which would spoil our GW measurements [12].

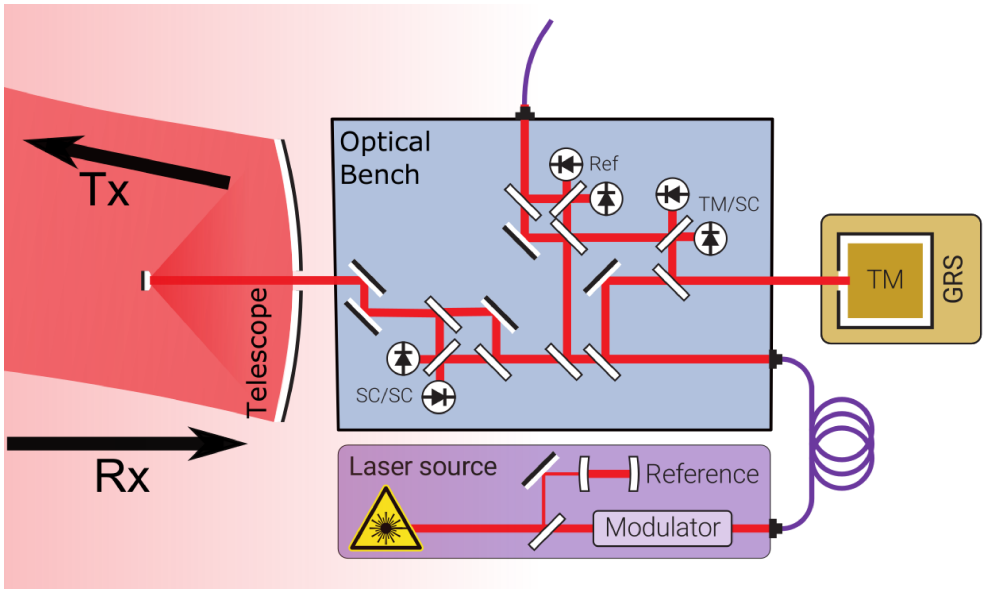

FIGURE 3.6: Sketch of the LISA optical layout, from [55]. Each optical bench carries three interferometers, allowing a readout of the inter-spacecraft and spacecraft-testmass seperation, as well as a reference measurement between the two lasers on the spacecraft.

A solution, which was also demonstrated by LISA pathfinder, is that each spacecraft will house two small cubic test-masses which act as gravitational reference points for the measurements. Their position relative to the spacecraft will be read out using dedicated interferometers.

The test-masses themselves are housed in a gravitational reference sensor (GRS). It is responsible for most functionality regarding the test mass. In particular, each GRS has to be able to securely hold the test-mass during launch, before releasing it into free-fall for science operations. The test-mass then stays enclosed inside the GRS, where it is shielded from external influences and controlled along the non-sensitive degrees of freedom to avoid collisions with the spacecraft [10]. Along the sensitive direction, the test-masses are 'drag-free', meaning that the spacecraft follows the test-mass motion instead, as described in section 3.4.4.

3.4.3 *Optical layout and split interferometry*

The overall optical layout for each LISA satellite is outlined in fig. 3.6.

Each OB has an associated local laser. In addition, the two OBs on each spacecraft are inter-connected by an optical fibre, such that a total of 3 different laser beams are available on each OB:

- The local beam, which is being emitted towards the far spacecraft and the adjacent optical bench,
- the distant beam, incoming from the distant spacecraft through the telescope, which carries the GW signal, and
- the adjacent beam, incoming from the adjacent OB on the same spacecraft, which is used as a local reference.

These are used to construct three different interferometers:

- The ISC interferometer[3], which beats the distant beam against the local one,
- the reference interferometer, which beats the adjacent beam against the local one,
- and the test-mass interferometer, which also beats the adjacent beam against the local one, but includes an additional reflection off the local test mass.

Most noise sources, such as LFN, are common in the reference and test-mass interferometer. Thus, we can combine the measurements from these two interferometers to cancel this common noise and get a high-precision readout of the seperation between test-mass and the local optical bench.

This information can be used in conjunction with the ISC interferometer, which measures the seperation between the local and distant optical bench, to synthesize a high-precision readout of the seperation between the two test-masses at the ends of one LISA link.

In addition, the reference interferometer readout can also be used to remove LFN of one of the two lasers on each spacecraft.

This concept is called split-interferometry, and the actual signal combinations are computed on-ground out of the individual interferometric readouts. We discuss this in detail in chapter 12.

3.4.4 *DFACS*

In addition, the DFACS also uses capacitative readouts of the test-mass orientation provided by the GRS [10].

In addition to allowing a post-processing correction for jitters of the spacecraft, the interferometric readout of the test-mass position will also be used in the drag-free attitude control system (DFACS) to adjust the spacecraft trajectories such that they follow the test-masses on their free-fall trajectory. Since there are two test-masses, the spacecraft can't follow both of them in all degrees of freedom. Instead, each of the test-masses is only free-falling along some degrees of freedom, including the sensitive axes connecting to the distant spacecraft, while their position in the other ones is controlled by electro-static actuators. The DFACS then only ensures drag-free control of the spacecraft positions along three translational degrees of freedom [10].

As experimentally demonstrated in LISA-Pathfinder [12], the DFACS is not perfect[4], such that although the spacecraft tries to follow the test-mass motion in the sensitive direction, there is still a significant amount of residual spacecraft displacement noise in the inter-spacecraft interferometer carrying the gravitational wave signal. This will be compensated in a post-processing step, as described in section 3.4.3.

3 This interferometer is sometimes also called the 'long-arm interferometer' or 'science interferometer'.

4 The main noise sources limiting the DFACS performance are thruster noise and the finite gain of the DFACS control loops (G. Heinzel, personal communication, 2021).

3.5 PHASE READOUT

3.5.1 *Overview*

As mentioned above, the phase of the MHz interferometric beatnotes is tracked and recorded with µcycle precision. The device responsible for this measurement is called the phasemeter. At its core, this phasemeter will rely on a device called a digital phase-locked loop (DPLL). In general, a phase-locked loop (PLL) is a device or algorithm which takes as input an oscillating signal and produces as output another signal which has a stable phase relationship to the input signal. In a DPLL, this allows to create a digital replica of the analog input signal, of which the phase and frequency are directly accesible.

Note that although in the case of the LISA phasemeter both input and output signal have the same frequency, this is in general not required for a PLL.

The full LISA measurement chain is sketched in fig. 3.11, with the parts directly related to the phasemeter to the bottom left of the picture. The input signal is generated by interference of the beams in the different interferometers. This signal is first converted from a fluctuating intensity of the EM field of the laser beam to a proportional voltage using a photoreceiver, and then digitized using an analog-to-digital converter (ADC). The ADC records samples of the input signal at a high sampling rate of around 80 MHz. In addition, all input signals are overlayed with a so-called pilot tone at 75 MHz, which is directly derived from the USO and acts as timing reference for all phasemeter measurements. This allows correction of timing jitters of the ADC and the phasemeter clock, see section 3.6.3. Any imperfections in the pilot tone itself still couple into the digitized signal, and need to be corrected in a post-processing step. We will derive a detailed model for this coupling of clock errors in chapter 6, and discuss its correction in chapter 13.

A **photoreceiver** consists of a photodetector (e.g., a photodiode) and the associated electronics needed to create a voltage output, such as an amplifier.

The phasemeter uses a DPLL running at a clock rate of 80 MHz to determine the phase and frequency of the input signal. The measured phase or beatnote frequency is then filtered and downsampled to a much lower sampling rate of around 4 Hz before being transmitted to earth. Signals sampled at intermediary frequencies can also be provided and used as input to, for example, the DFACS [47].

A prototype of this phasemeter design is explained in detail in [36].

3.5.2 *Digital phase locked loop*

The core of the phasemeter is a DPLL, sketched in fig. 3.7. It creates a digital replica of the input signal, within a device called a numerically controlled oscillator (NCO), of which the phase and frequency are directly accessible.

The NCO consists of a phase increment register (PIR), a phase accumulator (PA) and a sine and cosine look-up table (LUT). The PA represents the total phase of the oscillator, and gets incremented at each time step by the value of the PIR, which therefore represents its instantaneous frequency. The

See appendix C.1.2 for the exact definition of these quantities.

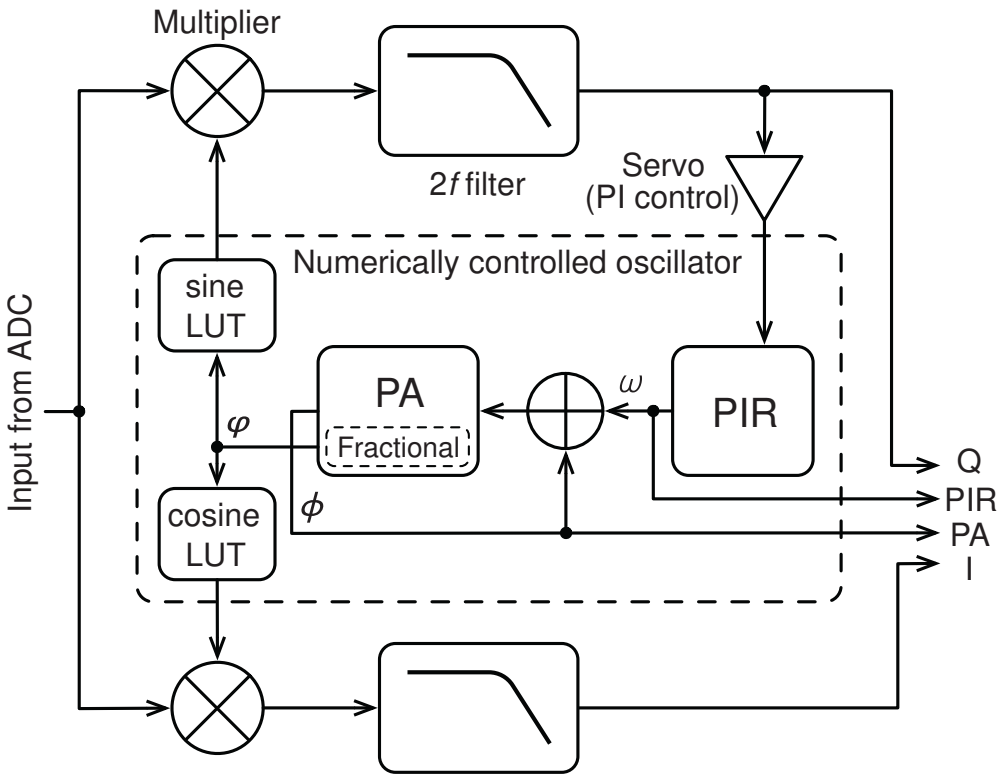

FIGURE 3.7: Schematic overview of a DPLL, from [48]. See section 3.5.2 for full description of the algorithm.

fractional part of the PA, corresponding to up to one cycle of the oscillator, is used as input to the LUTs to produce quantized values of a sine and cosine function.

The digital input signal coming from the ADC is given as

$$V(t) = A\cos(\omega t + \phi_s(t))\,, \tag{3.1}$$

and gets multiplied by these digital sine and cosine signals provided by the NCO. This is followed by a low-pass filter, to get the in-phase signal,

$$\begin{aligned} I(t) &= \langle V(t)\cdot\cos(\omega t + \phi_n(t))\rangle \\ &= \frac{A}{2}\cos(\phi_n(t) - \phi_s(t)) \\ &\approx \frac{A}{2}\,, \end{aligned} \tag{3.2}$$

and the quadrature signal,

$$\begin{aligned} Q(t) &= \langle V(t)\cdot\sin(\omega t + \phi(t))\rangle \\ &= \frac{A}{2}\sin(\phi_n(t) - \phi_s(t)) \\ &\approx \frac{A}{2}(\phi_n(t) - \phi_s(t))\,. \end{aligned} \tag{3.3}$$

Here, we assumed that the NCO is already locked to the input signal, such that $\phi_n(t) - \phi_s(t) \ll 1$. Q then gives a direct readout of the phase fluctuations, which can be used as error signal in a controller to adjust the PIR of the NCO and keep it locked to the input signal. Both the PIR and PA are available as output, and get further low-pass filtered and decimated to a frequency suitable

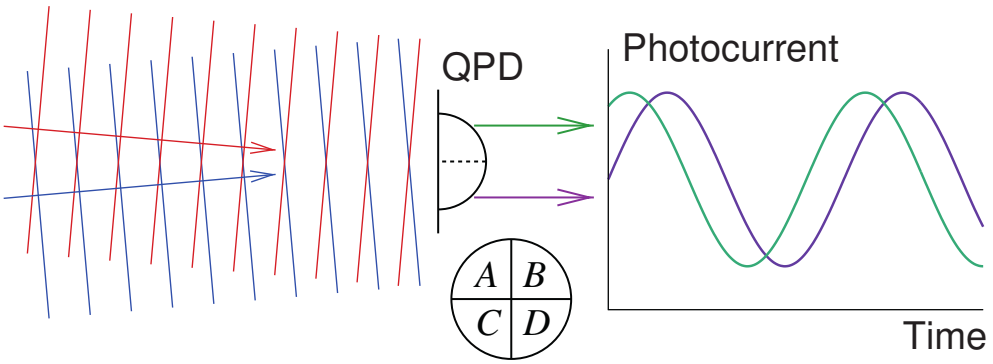

FIGURE 3.8: Sketch of the principle behind DWS, from [48]. A tilt of the incoming beams causes a small phase shift between the signals in the upper and lower quadrants, which can be readout using DPLLs.

for transmission to earth in multiple steps. See [36] for more information on DPLLs and related functionality of the phasemeter.

Note that the PIR and PA represent the full dynamic range of the input signal, including the MHz offsets in the frequency and corresponding phase ramps of millions of cycles per second. The desired gravitational wave signals cause µcycle phase fluctuations in these signals, which need to be recovered in further processing steps on ground, see chapter 8 for more details.

3.6 AUXILLIARY PHASEMETER FUNCTIONS

In addition to the main phase readout, the phasemeter will provide a number of additional auxilliary functions and measurements.

3.6.1 *Differential wavefront sensing*

The main purpose of the LISA phase measurement is to determine the longitudinal pathlength change between the test masses located in the local and distant spacecraft.

In addition, it will also provide a precise measurement of the angles between the local and incoming beams, using a method called differential wavefront sensing (DWS). See fig. 3.8 for a schematic overview.

Instead of using a single photodiode at each interferometer output, this method uses a so-called quadrant photo diode (QPD), whose sensitive area is split into 4 quadrants of equal area.

Any tilt between the phase front of the incoming beam and that of the local beam will create a slight phase shift in the signals recorded in the different quadrants. By tracking the phase of each quadrant individually, using one DPLL for each of them, it is possible to reconstruct the tilt of the incoming wavefronts from the relative phase between the four readouts. [48] contains a good summary of this method, as well as an efficient algorithm of combining the signals from the different quadrants to recover both the relative beam tilts as well as the longitudinal signal.

This readout will be used as input to the DFACS, as well as for on-ground calibrations which compensate for residual tilt-to-length (TTL) couplings.

3.6.2 *Laser locking and frequency planning*

The overall available bandwidth for tracking the different interferometers will be limited to a range of approximately[5] 5 MHz to 25 MHz. Therefore, we must ensure that any two lasers entering into an interferometer must have a frequency difference within this range.

This can be achieved by offset-frequency locking all lasers in the constellation to one primary laser used as reference, utilizing additional control loops. Each of them uses the frequency output of the DPLL as error signal to adjust the frequency of one of the lasers entering the interferometer. The result is that the locked laser's frequency is adjusted in such a way that the measured beatnote is at exactly the desired value.

As described above, each spacecraft carries two local lasers and receives light from two remote spacecraft. In principle, either of the local lasers could therefore be locked to:

(a) The adjacent beam,

(b) the distant beam arriving on the same optical bench, or

(c) the distant beam arriving on the adjacent optical bench.

Mixing options (a) and (c) is referred to as 'frequency-swap', and not considered as the LISA baseline. Therefore, each laser will be locked using either (a) or (b), utilizing an interferometric readout of the optical bench on which it acts as local laser. See [46] for further information.

The set of offset frequencies of all locked lasers for the whole mission duration is called a frequency plan, and its computation is non-trivial. We can count the number of frequencies we have to determine: All reference and test-mass interferometers on the same spacecraft use the same two laser beams, thus they end up at the same frequency. So there are a total of three reference interferometer beatnote frequencies for the three spacecraft. In addition, each ISC interferometer uses a different set of beams, giving an additional 6 beatnote frequencies. Therefore, we have to find as set of 5 offsets for the 5 locked lasers to control the value of 9 different beatnote frequencies.

We will later introduce a sign convention such that the two reference beatnotes on the same spacecraft have opposite signs, cf. section 5.4.2.

This is further complicated by the fact that the laser beams pick up Doppler shifts during propagation between the spacecraft, such that the frequency plan has to adjust over time to compensate for changes in the orbits. In addition, to avoid cross-talk between different interferometer channels, no two frequencies on the same spacecraft should have the same value at the

5 For example, the photoreceivers only have a limited bandwidth which limits at high frequencies, while some noise sources like relative intensity noise (RIN) are expected to become limiting at low frequencies. In addition, the aliased pilot tone will appear at 5 MHz, such that all other signals should be above this frequency.

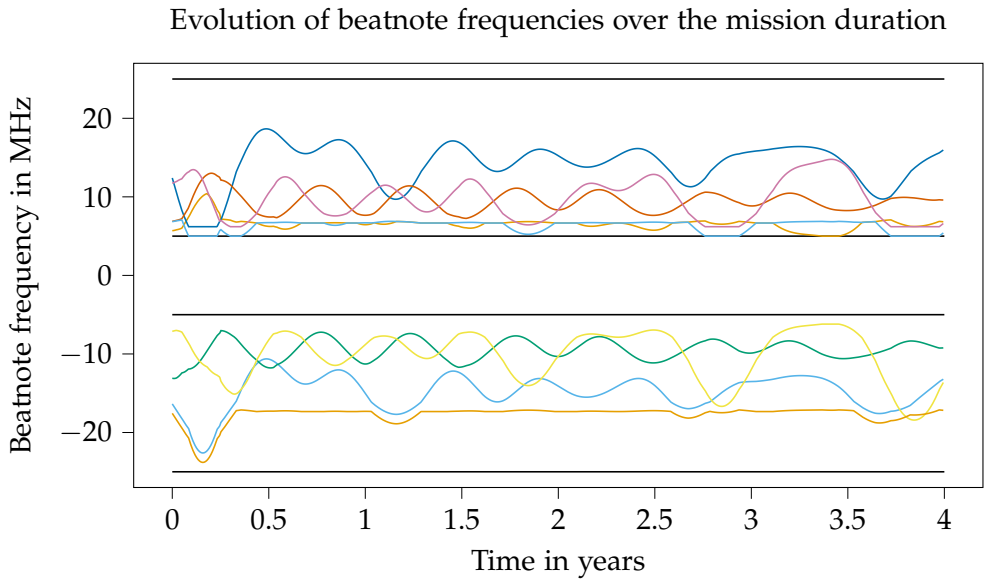

FIGURE 3.9: Example frequency plan for four years, data provided by G. Heinzel. 5 laser offset frequencies are controlled such that all 9 beatnotes fall within a range of ±5 MHz to ±25 MHz, indicated by black lines. We plot all 9 beatnote frequencies, legend omitted for clarity.

same time - including some margin to account for the additional sideband beatnotes required for the clock correction (cf. section 3.7).

This topic, in particular the computation of a frequency plan given a set of constraints on the beatnote frequencies, can be solved exactly, as discussed in detail in [46]. An example frequency plan is depicted in fig. 3.9, showing that it is possible to control all frequencies to fall within the desired range. This frequency plan is provided by G. Heinzel and based on the same orbits used for the illustration in fig. 3.3.

We will include a model for laser locking as well as an overview of the different possible locking configurations first presented in [46] in our simulation model, see section 7.3. In addition, we will study the impact laser locking has on the INREP in section 12.2.

3.6.3 *Pilot tone correction*

As described above, the analog photoreceiver signal is digitized at the input to the phasemeter, using an ADC. This ADC uses the on-board USO as timing reference, therefore inheriting its timing jitters. However, the ADC itself will also contribute its own timing jitter on top of those of the sampling clock, at a level incompatible with the stringent noise requirements.

The planned solution is to superimpose a copy of the pilot tone on each ADC channel. The phase of this pilot tone gets tracked with a dedicated DPLL. Since the pilot tone is very stable and at a well known frequency, we can predict it's phase evolution. Comparing the recovered phase of the pilot tone with its expected phase then allows an accurate measurement[6] of

6 The pilot tone is intentionally generated at a relatively high frequency of 75 MHz to be more sensitive to timing jitter of the ADC. This is above the phasemeters Nyquist frequency of 40 MHz, such that the pilot tone appears as a signal aliased to 5 MHz.

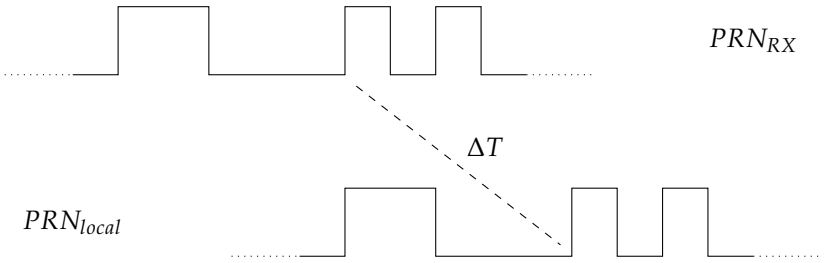

FIGURE 3.10: Principle of the pseudo-ranging measurement via PRN codes. The received code from the distant spacecraft is correlated with a local copy, allowing a measurement of the time delay ΔT.

the additional ADC jitter, up to errors in the pilot tone itself. This phase measurement can then be used to correct for the ADC jitter in all other DPLLs which are processing the same time series. Therefore, the pilot tone should be seen as the clock defining the onboard time for the phasemeter measurements.

These are typically tracking one carrier and two sideband beatnotes.

3.6.4 *Absolute ranging*

As discussed above, the LISA metrology system will be able to measure relative distance fluctuations at pm precision over timescales of about 1 s to 1000 s. Constructing the laser-noise-suppressing TDI combinations out of the raw phase measurements, however, needs additional information on the absolute separation between the spacecraft. More precisely, as we will discuss in chapter 13, the application of TDI requires knowledge of a combination of the physical light travel time and of the desynchronization between the 3 independent spacecraft clocks.

This is realized using a low-power phase modulation, cf. [34] and [15] for more technical details.

This information can be obtained by imprinting a unique pseudo random noise (PRN) code on each laser beam. On the one hand, these binary codes are perfectly pre-determined - they are generated from a fixed sequence of ones and zeros which is known on each spacecraft. On the other hand, they are 'random' in the sense that their auto-correlation function approximates a delta distribution. In addition, they are orthogonal, meaning that the cross-correlation between any two of these codes is vanishing.

The absolute ranging measurement relies on these correlation properties to determine the delays experienced by the beams as they propagate between the spacecraft. When the beam is sent, the sending laser's PRN code is imprinted on it. This requires a conversion from the digital code to an analog signal, which in turn requires referencing to the local clock. Therefore, the PRN code that is actually imprinted on the laser will inherit any timing errors of the sending spacecraft's clock.

The beam then propagates to the distant spacecraft, where it is received with a time delay. The local phasemeter on the receiving spacecraft records the phase difference between the incoming and the local beam, in which the PRN code is visible as a step-wise modulation. This modulation pattern is correlated to a local copy of the code in a delay-locked loop (DLL). Any errors of the receiving spacecrafts USO will now also affect this correlation, since the phasemeter uses it as timing reference.

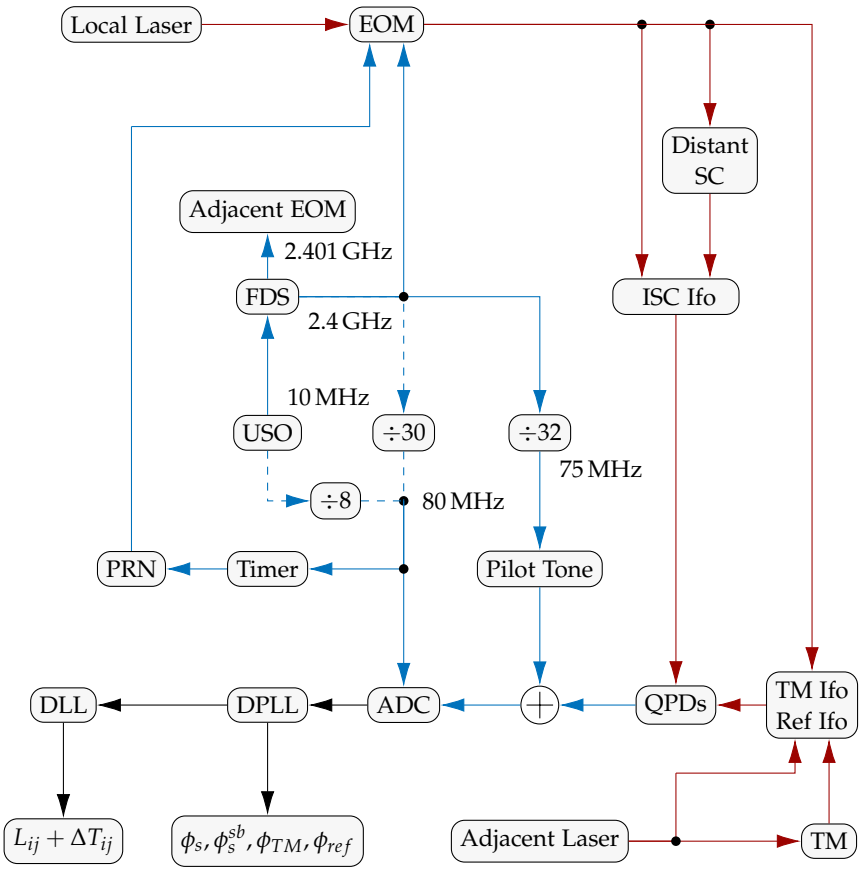

FIGURE 3.11: Overview over USO frequency distribution and measurements on one optical bench. Red lines represent laser links, blue lines are electrical signals and black lines are digital. Not depicted is a possible electrical comparison between the 2.4 GHz and 2.401 GHz modulation signal. The 80 MHz phasemeter clock can be either generated from the 2.4 GHz signal or from the 10 MHz USO (see section 6.1.2). See section 3.7 for a detailed description of this diagram.

Overall, the time-correlation of the received code with the local copy allows a measurement of the receiver's clock time at the event of reception of the modulated beam versus the emitter's clock time at the event of emission, as sketched in fig. 3.10. This quantity is called a pseudo-range, which depends on both the actual distance of the satellites and the errors in the satellite clocks.

Note that the PRN code has a finite length, and simply repeats itself after a certain timespan. In the case of LISA, this repetition period is significantly shorter than the overall light travel time between the spacecraft [34]. The PRN measurement therefore only determines the pseudo-range up to a constant offset.

The code repetition period is expected to correspond to a few 100 km.

This ambiguity can be resolved by combining the PRN measurement with ground-based obervations from the ESA tracking stations, which are accurate enough to determine which repetition of the PRN is actually received.

3.7 FREQUENCY DISTRIBUTION SYSTEM

As sketched in section 3.3, the clocks available for LISA are not precise enough to allow GW detection without any correction. We outline here the hardware involved in generating and distributing the different timing signals needed to suppress clock errors below the requirements. The most relevant signals

are then modelled in chapter 6, while the actual clock correction algorithm is given in chapter 13.

Figure 3.11 summarizes the main electrical, optical and digital signal paths on one optical bench, with a particular focus on the clock signals generated by the frequency distribution system (FDS). The figure is based on the much more detailed description in [14] and [15]. All shown frequencies should be seen as placeholder values and are subject to change.

The USO provides a timing signal, which we assume to be at 10 MHz. This signal is up-converted to generate two electrical signals, one at 2.4 GHz and one at 2.401 GHz. These are used to drive the electro-optical modulator (EOM) on the left-hand and right-hand optical bench, respectively.

The EOMs convert this electrical signal into a phase modulation of the local laser beam. We will model this modulation in section 5.2.2. In summary, this can be described by adding two sidebands which are seperated from the main carrier frequency by the modulation frequency, as shown in fig. 3.12 below.

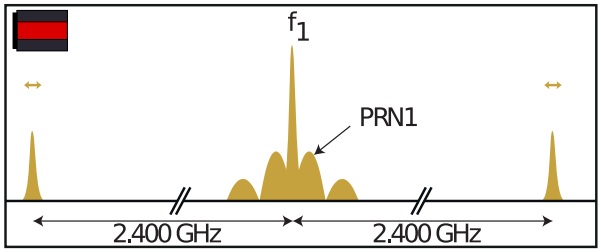

FIGURE 3.12: Spectrum of the modulated laser beam, from [55]. The PRN code is visible as modulation around the carrier. The two clock sidebands are seperated from the carrier by 2.4 GHz.

Note that all interferometers always interfere beams from a left-handed optical bench with those from a right-handed optical bench. In addition, the sidebands on the left- and right-handed optical benches are seperated by 1 MHz, which will ensure that the resulting sideband-sideband beatnotes will be offset from the carrier-carrier beatnote by 1 MHz[7]. This allows the phasemeter to track both sideband and carrier beatnotes independently. The spectrum of the beatnote is shown in fig. 3.13.

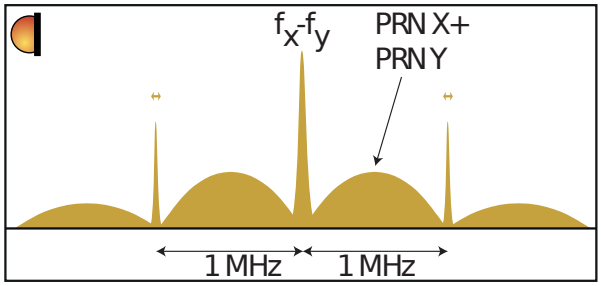

FIGURE 3.13: Spectrum of the recorded beatnote, from [55]. Two sideband-beatnotes appear seperated by 1 MHz from the carrier beatnote. Both local and received PRN codes are visible in the spectrum.

In addition to producing the sideband, the 2.4 GHz signal is also used as timing reference from which other signals are derived. Most notably the 80 MHz phasemeter clock[8] and the 75 MHz pilot tone signal, both of which can be generated by integer frequency dividers by 30 and 32, respectively. The

7 This 1 MHz offset has to be taken into account as margin around each beatnote frequency when designing the frequency plan, cf. section 3.6.2

8 Since the phasemeter clock is not performance critical, it could also be directly synthesized from the 10 MHz USO signal.

80 MHz signal is used to drive most onboard processing of the phasemeter. This includes the field programmable gate array (FPGA) clock used for digital signal processing (DSP) algorithms, the ADC used to sample the beatnotes, counters used to generate the PRN modulation signal as well as a timer providing timestamps for all phasemeter measurements.

The 75 MHz pilot tone, on the other hand, is the primary timing reference to which all interferometric measurements on one spacecraft are referred, as explained in section 3.6.3. The conversion chain from the 2.4 GHz sideband to the 75 MHz pilot tone is therefore performance-critical: the pilot tone represents the clock to which our measurements are ultimately referred, while the sidebands are the only measurements we can use to correct errors in it.

Conversely, the 2.401 GHz sideband does not need to be perfectly stable with respect to the pilot tone. Instead, it can be referred to the 2.4 GHz signal by utilizing either the sideband-sideband beatnotes in the reference interferometers, or even a dedicated electrical measurement between the 2.4 GHz and the 2.401 GHz signals (not depicted in fig. 3.11).

Part II

LISA INSTRUMENTAL MODELLING AND SIMULATIONS

4

INTRODUCTION

4.1 SIMULATIONS FOR LISA

LISA is a complex instrument, which combines highly precise on-board measurements with sophisticated on-ground processing algorithms to achieve the required precision to detect GWs in space. Some aspects of the full LISA signal chain – such as the propagation of laser beams through 2.5×10^6 km of free space – are very challenging to accurately reproduce in ground based experiments.

Still, numerous ground based verifications of different aspects of the LISA measurement chain exist, including verifications of the working principles of TDI [30, 54, 59, 74, 79]. The development of TDI and the associated noise reduction algorithms, however, relies heavily on analytical studies, guided and verified by numerical experiments.

One main aspect of this thesis work was to develop a more accurate physical model for the simulated data streams of LISA.

In particular, this applies to

- accounting for large frequency offsets in the modelling of beams,
- simulation of Doppler frequency shifts during beam propagation,
- inclusion of laser frequency locking in the simulation, and
- proper modelling and simulation of different clocks and their impact on the signal chain.

Besides allowing the development and testing of noise suppression algorithms, as discussed in part iii, these simulated data sets also allow studies on the expected LISA performance [39], as well as provide a more realistic basis for other consortium activities, such as the LISA data challenges (LDCs).

See `lisa-ldc.lal.in2p3.fr` for more information on the LDC!

This simulation model uses the index and notation conventions summarized in appendix A.

This activity was performed in the context LISA data-processing group (LDPG) working group (WG) 7 of the LISA consortium. As such, most of the modelling presented in this part of the thesis (chapter 4 to chapter 8) was developed in close collaboration with other members of the LISA consortium, in particular J.-B. Bayle, and is based on a technical note published internally as [16].

4.2 SIMULATION TOOLS

Besides the modelling efforts, the author was also heavily involved in implementing most of these models into the LISA consortiums instrument simulator prototype `LISANode` [18], as well as its spin-off project `LISA Instrument`. We will present results of these simulations in chapter 8.

`LISANode` is a simulation framework designed to allow the user to build modular simulation graphs out of atomic computational units, called nodes. This is realized using a mix of python and C++, where the python code is responsible for defining the graph structure and interconnecting the different nodes. The nodes themselves are instead implemented in C++, such that the final executable is a C++ command line program.

This has the advantage that we can make use of C++ compiler optimizations to produce a fast executable, as well as make use of legacy code from previous LISA simulators such as LISACode [66].

The basis of the `LISANode` was originally developed by J.-B. Bayle, and is well documented in [20]. It has now become a large software project with close collaboration of multiple contributors from all over the world.

Besides `LISANode`, the very same simulation model is also the basis for a new entirely python based simulator called `LISA Instrument` [17]. The code base was again developed by J.-B. Bayle, with regular exchange with and input from the author of this thesis (among others). It is designed to facilitate fast explorative studies. All intermediary variables computed during a simulation with `LISA Instrument` are directly accessible after the simulation is completed, which is useful for debugging. In addition, `LISA Instrument` relies strongly on the numpy framework, which includes fast optimized functions for handling these large arrays of data.

A downside of this approach is that with increasing simulation length, memory becomes a bottleneck. `LISANode`, on the other hand, is designed to compute new simulated samples on the fly, keeping only the data in memory which is required for the current and future samples. This way, the memory requirements are significantly less sensitive to the length of the simulation, allowing longer simulation runs on memory constrained machines.

Both `LISA Instrument` and `LISANode` are rapidly evolving projects. In this thesis, we focus on the description of the physical model, and refer to the extensive in-code documentation for the actual technical implementation.

4.3 SIMULATION OVERVIEW

We aim to derive a model for the main interferometric measurements of LISA. The model should capture the most significant performance impacting effects, while being able to simulate around ten years of data. In addition, we want to test a wide variety of mission parameters, such that simulation has to be

able to produce data at a much faster rate than 'real-time' in order to allow testing of different scenarios.

Most derivations for this model are performed in continuous time. Actual numerical simulations rely on a discrete time grid, whose sampling rate f_s^{phy} has to be chosen in such a way that all signals we are interested in can be properly represented, and any numerical processing artifacts during the physics simulation occur outside the LISA measurement band between 10^{-4} Hz and 1 Hz.

As described in section 7.1, we will also model some of the on-board processing. In particular, we will include a down-sampling step to go from f_s^{phy} to a lower measurement sampling rate f_s^{meas}, which represents the rate of actual phasemeter data which is ultimately telemetered down to earth. In addition, the sampling rate f_s^{phy} can be chosen to directly represent one of the higher sampling rates present in the real phasemeter, such as the input data for the DFACS. Besides facilitating easier integration of a dynamics simulation, this will also allow us to use the same filters in the simulation which are used in the final stages of the hardware phasemeter prototypes.

Recent investigation [47] have revealed that these sampling rates cannot be chosen arbitrarily for the real mission, due to constraints of the timing signal conversion chain inside the phasemeter. A final baseline has not been decided yet, but we will assume values of

$$f_s^{\text{phy}} = 16\,\text{Hz} \quad \text{and} \quad f_s^{\text{meas}} = 4\,\text{Hz} \tag{4.1}$$

for the purpose of our simulations. These are compatible with the options proposed in [47], and allow simulations at much higher rate than real-time.

Note that f_s^{phy} is much lower than the phasemeter sampling rate (about 80 MHz [15]), and even more significantly lower than the rate which would be required to represent the actual EM field of the laser beams, which oscillates at $\nu_0 = 281.6\,\text{THz}$.

Assuming a laser wavelength of $\lambda = 1064\,\text{nm}$, as proposed for LISA [10]

As such, we neither simulate the full EM field of the beam itself, nor the full range of the interferometric beatnote.

Instead, we simulate variables representing the information content of the beams as well as the final measurements produced by the phasemeter. This means that most of the physics as well as the phasemeter algorithms, such as the DPLL described in section 3.5, have to be described by a high-level model capturing the most significant effects.

4.3.1 *Phase vs. Frequency*

We want to simulate the information content of a laser beam, which is encoded in its total phase $\Phi(\tau)$ or the equivalent instantaneous frequency $\nu(\tau)$. These quantities are defined for our beam model in chapter 5. Their relationship to each other is explored in detail in appendix C.

As shown in fig. C.1, the total phase of a periodic function increases quickly with time. This makes using it challenging for numerical simulations, since any variable representing the total phase will either numerically overflow when using fixed point arithmetic, or eventually suffer an unacceptable loss of precision when using floating-point arithmetic.

To avoid these issues, we simulate frequencies instead of phases. Indeed, as visible in fig. 3.9, the frequencies observed in LISA are controlled to remain at the same order of magnitude during the whole mission duration.

However, modelling the propagation of laser beams is often easier in phase. Therefore, we will derive most of the equations in part ii of this thesis both in units of phase and frequency.

4.3.2 *Two-variable representation*

In LISA, we will have effects at completely different timescales and dynamic ranges affecting our signals in various ways.

On the one hand, there are effects which modulate the frequency of our beams on a time scale of the orbital revolution around the sun, which lies well outside our measurement band. In addition, these effects tend to have large dynamic ranges. The Doppler shifts caused by the relative spacecraft velocities, for example, can fluctuate by several MHz over the mission duration.

On the other hand, we want to track precisely the small phase fluctuations within our measurement band, which are caused by GWs and instrumental noises. These have a much smaller magnitude, with the LFN being the dominant effect at $30\,\mathrm{Hz}/\sqrt{\mathrm{Hz}}$, while GWs typically cause frequency shift of a few hundred nHz [10].

To account for this discrepancy, we model these different effects independently. We decompose the total laser frequency into one constant ν_0 and two variables,

$$\nu(\tau) = \nu_0 + \nu^o(\tau) + \nu^\epsilon(\tau)\,. \tag{4.2}$$

The constant central laser frequency $\nu_0 = 281.6\,\mathrm{THz}$ is identical for all laser beams, and saved as a separate parameter. In this simulation model, a simple laser beam would therefore be entirely represented by the couple

$$(\nu^o(\tau), \nu^\epsilon(\tau))\,, \tag{4.3}$$

where we express both the frequency offsets $\nu^o(\tau)$ and the frequency fluctuations $\nu^\epsilon(\tau)$ in units of Hz.

The large frequency offset $\nu^o(\tau)$ will be used to represent frequency plan offsets and Doppler shifts (both on the order of MHz), as well as the GHz sidebands. The small frequency fluctuations $\nu^\epsilon(\tau)$, on the other hand, are used to describe GW signals and noises, the largest of which are the laser frequency noise at $30\,\mathrm{Hz}/\sqrt{\mathrm{Hz}}$.

Alternatively, we can express eq. (4.2) in phase units by writing the total phase as

$$\Phi(\tau) = \nu_0 \tau + \phi^o(\tau) + \phi^\epsilon(\tau)\,, \tag{4.4}$$

where the definitions of large phase drifts $\phi^o(\tau)$ and small phase fluctuations $\phi^\epsilon(\tau)$ follow from eq. (C.2),

As described in appendix C, we express phase in unit of cycles, not radian.

$$\nu^o(\tau) = \dot{\phi}^o(\tau) \quad \text{and} \quad \nu^\epsilon(\tau) = \dot{\phi}^\epsilon(\tau)\,. \tag{4.5}$$

4.3.3 *Usage of the two variables*

It is important to stress that this decomposition into two variables is entirely artificial, and in the real mission, we will only have access to the total phase or the total frequency. Therefore, to produce data representative of the real instrument telemetry, we have to always consider the *sum* of the two variables as the final simulation output. This might raise the question of why we go to the effort of seperating the whole model in two variables in the first place. The answer is twofold.

First, we observe that our beatnote frequencies are limited to up to 25 MHz. Therefore, assuming we use double precision variables, we expect a numerical noise floor around $10^{-16} \times 25\,\text{MHz} \approx 2.5\,\text{nHz}$, which is below the noise level allocated for the mission (see chapters 8 and 9 for simulation results verifying this). This means a double precision variable containing the total frequency should be sufficient to do the GW data analysis. However, we also want to study sub-dominant noises - and their residual noise levels are often far below 2.5 nHz, as demonstrated in chapters 12 and 13.

Secondly, though we only get the total phase/frequency as raw data from the instrument, we can still decompose this data into two variables in a post-processing step, as described in chapter 8 and section 9.1. This is not strictly required, but will ease the stringent processing requirements of TDI, see chapter 13.

Therefore, we can actually bypass the computation of the total frequency to generate data under the *assumption* that we can perfectly decompose our signals into deterministic out-of-band and stochastic and in-band effects. This allows us to achieve a much lower numerical noise floor when studying small noise residuals, and identify effects which would normally be buried under the quantization noise of the MHz beatnotes.

We can (and do) still compute the total frequency as the sum of the two variables, and apply all simulated on-board processing steps to it to generate more realistic data, as described in chapter 7.

5

OPTICAL SIMULATION

In this chapter, we derive a model for the generation and propagation of the laser beams in LISA, as well as their interference at the photodiodes. It is structured as follows.

We first review the optical bench design of LISA in section 5.1, and introduce the notation used to identify the different signals present on each optical bench.

We then define our basic model of a laser beam in section 5.2, including a model for the sideband modulation. While this description is general, we give explicit definitions for the laser beams generated by the laser source in section 5.3. These beams are interfered at the photodiodes, and we model this interference in section 5.4. Before interference, the beams need to be propagated from the laser sources to the photodiodes, as described in section 5.5.

Finally, we summarize all photodiode signals observed on a single optical bench in section 5.6.

5.1 OPTICAL BENCH OVERVIEW

As described in section 3.4, each spacecraft hosts two optical benches, each of them associated with a laser source and a GRS containing a test mass. Our goal in this chapter is to derive expressions representing the main signals observed in the three interferometers on each OB.

In reality, each single interferometer output is implemented using redundant balanced detection with four QPDs, c.f. [55]. We do not simulate balanced detection, and only consider a single data stream for each interferometer. Additional readouts related to the laser beams alignment, such as the DWS described in section 3.6.1, are not included in the model presented here. We plan to include them in a future version of the simulation by propagating additional independent variables representing the different beam tilts.

In addition, we neglect most phase shifts of the beams due to interaction with optical components.

Figure 5.1 gives an overview of the optical bench, as well as the notation used for the different signals in our model.

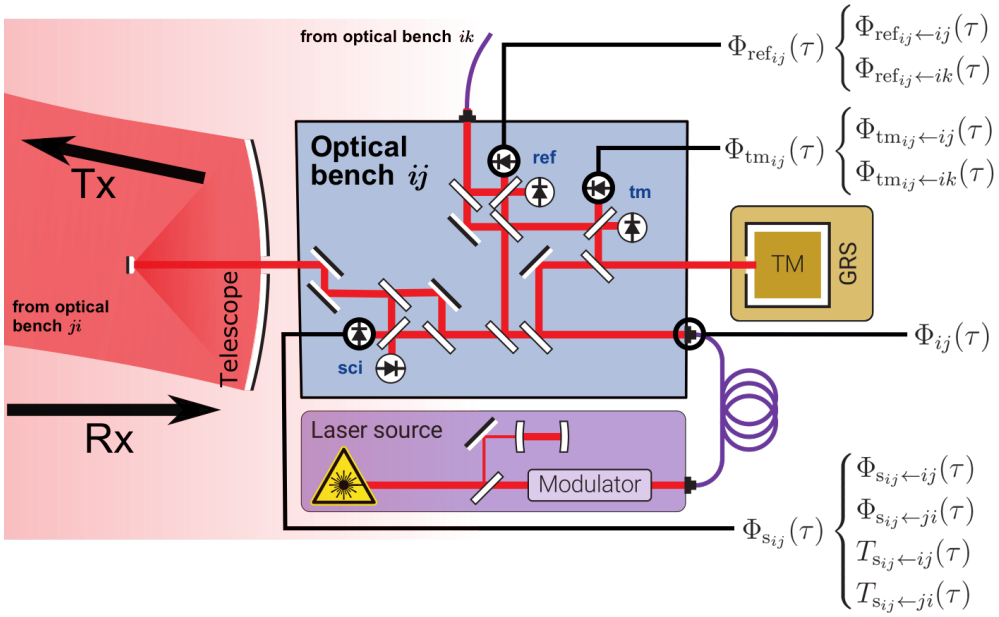

FIGURE 5.1: Schematics of the optical design along with notations for the laser beam and beatnote total phases, here for MOSA ij. Adapted from [55].

Laser beams at the exit of the laser source[1] ij are expressed in terms of quantities derived from its total phase $\Phi_{ij}(\tau)$. We will first present our general model to represent these modulated laser beams in section 5.2, and apply it to the actual beams produced in LISA in section 5.3.

We will then model the interference of two modulated beams in section 5.4, again in general terms. To apply the resulting expressions to the final photodiode signal, we first need to derive expressions for propagating the beams from the laser source to the respective photodiode in section 5.5.

We will give there expressions which enable us to compute the total phase and frequency of all beams arriving at the photodiodes on optical bench ij, all implicitly expressed in terms of the associated spacecraft proper time (TPS) τ_i:

See appendix A.3 for the definition of the different time frames used in the simulation, and the associated notation.

- $\Phi_{\mathrm{isc}_{ij}\leftarrow ij}(\tau)$, the total phase of laser ij after propagation to the photodiode of the inter-spacecraft interferometer isc_{ij};
- $\Phi_{\mathrm{ref}_{ij}\leftarrow ij}(\tau)$, the total phase of laser ij after propagation to the photodiode of the reference interferometer ref_{ij};
- $\Phi_{\mathrm{tm}_{ij}\leftarrow ij}(\tau)$, the total phase of laser ij after propagation to the photodiode of the test-mass interferometer tm_{ij};
- $\Phi_{\mathrm{isc}_{ij}\leftarrow ji}(\tau)$, the total phase of laser ji after propagation to the photodiode of the inter-spacecraft interferometer isc_{ij};
- $\Phi_{\mathrm{ref}_{ij}\leftarrow ik}(\tau)$, the total phase of laser ik after propagation to the photodiode of the reference interferometer ref_{ij};

1 As discussed in detail in appendix A, we label all elements uniquely associated to a MOSA using two indices. The first index corresponds to the spacecraft the MOSA is mounted on, while the second index corresponds to the spacecraft the MOSA sends to and receives light from. For example, the laser 12 is used as local laser for the optical bench on MOSA 12, which itself is mounted on spacecraft 1 and points to spacecraft 2.

- $\Phi_{\mathrm{tm}_{ij} \leftarrow ik}(\tau)$, the total phase of laser *ik* after propagation to the photodiode of the test-mass interferometer isc_{ij}.

Any quantities derived from the total phase follow the same notation, with braces around the inner symbols carrying the indices. For example, $\nu^{o}_{ij,c}(\tau)$ is the frequency offset of the carrier virtual local beam at the laser source ij (cf. section 5.2.4), while $(\nu_{\mathrm{ref}_{ij} \leftarrow ij})^{o}_{c}(\tau)$ is the same quantity after it has propagated to the reference interferometer photodiode.

Finally, we list the available interferometric readouts in section 5.6.

5.2 LASER BEAM SIMULATION

5.2.1 *Laser beam model*

We want to model the information content of the EM field of a laser beam. In all generality, the EM field can be modelled by two three-dimensional vector fields, the electrical field and the magnetic field. For our simulation modelling, however, we will operate under a number of simplifications.

Or alternatively, it could be described in all generality by the antisymmetric EM field tensor $F_{\mu\nu}$.

We work in the plane wave approximation, and assume that any effects due to wavefront imperfections can be modeled as equivalent longitudinal pathlength variations. In addition, we neglect effects related to the fields polarization, consider the waves to propagate in a perfect vacuum and only model the scalar electric field amplitude[2].

This allows us to use a simple model for the electrical field of our laser beam. At any fixed point inside a spacecraft, its amplitude can be written as

$$E(\tau) = E_0(\tau)\cos(2\pi\Phi(\tau))\,, \tag{5.1}$$

using the time coordinates associated with a reference frame at rest for this point.

In practice, it is often more useful to use a complex representation of such a signal,

$$\mathrm{E}(\tau) = E_0(\tau)e^{i2\pi\Phi(\tau)}\,, \tag{5.2}$$

with i as the unit imaginary number.

The physical electrical field amplitude is then given as the real part of the complex signal,

$$E(\tau) = \Re[\mathrm{E}(\tau)]\,. \tag{5.3}$$

2 We don't need to model the magnetic field amplitude, as it is also determined by the electrical field amplitude [103].

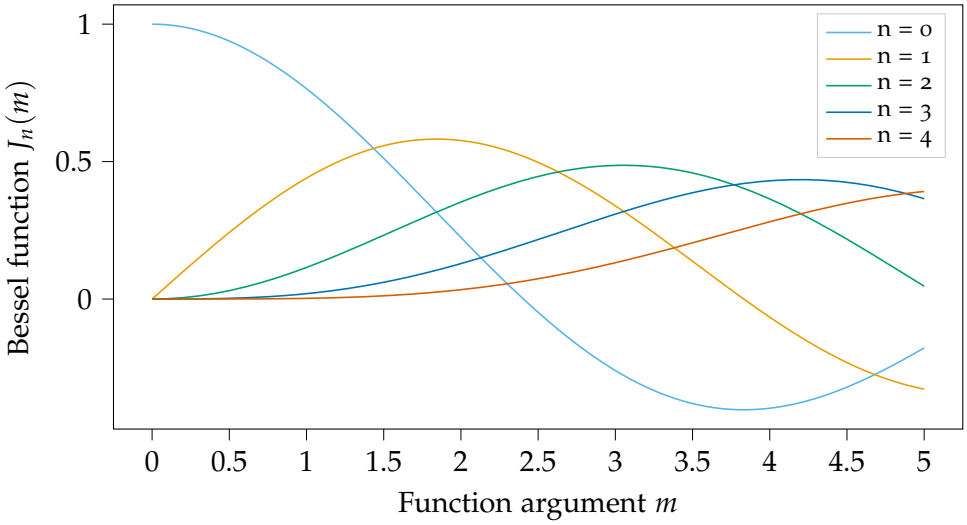

FIGURE 5.2: Bessel functions of the first kind.

5.2.2 *Sideband modulation*

As discussed in section 3.7, the laser beams in LISA will be modulated using a GHz signal derived from the local clock.

This signal is imprinted on the outgoing laser beam using an EOM, which creates a phase modulation. The electric field then reads

$$\mathrm{E}(\tau) = E_0 e^{i2\pi\Phi_c(\tau)} e^{im\cos(2\pi\Phi_m(\tau))}\,, \tag{5.4}$$

where m is the modulation depth, $\Phi_c(\tau)$ is the total phase of the carrier, and $\Phi_m(\tau)$ is the total phase of the modulating signal, both expressed in cycles.

Following [44], the term $e^{im\cos(2\pi\Phi_m(\tau))}$ in the resulting electric field can be expanding using the Bessel functions of the first kind J_n. This is known as the Jacobi-Anger expansion [100], given as

$$e^{im\cos(\Theta)} = \sum_{n=-\infty}^{\infty} i^n J_n(m) e^{in\theta}\,. \tag{5.5}$$

We expect that $m \approx 0.15$ [64].

If the modulation depth m is not too large, we can further expand the Bessel functions to first order in m. As can be seen in fig. 5.2, only the first two orders have significant contributions for $m \ll 1$, and we get

$$J_0(m) \approx 1, \quad J_1(m) \approx \frac{m}{2} \quad \text{and} \quad J_n(m) \approx 0 \quad \forall n > 1\,. \tag{5.6}$$

The complex field amplitude of the modulated laser then reads

$$\mathrm{E}(\tau) \approx E_0\left(e^{i2\pi\Phi_c(\tau)} + i\frac{m}{2}e^{i2\pi(\Phi_c(\tau)+\Phi_m(\tau))} + i\frac{m}{2}e^{i2\pi(\Phi_c(\tau)-\Phi_m(\tau))}\right). \tag{5.7}$$

Let us introduce the upper and lower sideband total phases,

$$\Phi_{\mathrm{sb}^+}(\tau) = \Phi_c(\tau) + \Phi_m(\tau) \quad \text{and} \quad \Phi_{\mathrm{sb}^-}(\tau) = \Phi_c(\tau) - \Phi_m(\tau)\,, \tag{5.8}$$

such that the modulated laser beam is written as the superposition of three *virtual beams*,

$$\mathrm{E}(\tau) \approx E_0\Big(e^{i2\pi\Phi_c(\tau)} + i\frac{m}{2}e^{i2\pi\Phi_{\mathrm{sb}^+}(\tau)} + i\frac{m}{2}e^{i2\pi\Phi_{\mathrm{sb}^-}(\tau)}\Big) \tag{5.9a}$$

$$\equiv \mathrm{E}^c(\tau) + \mathrm{E}^{\mathrm{sb}^+}(\tau) + \mathrm{E}^{\mathrm{sb}^-}(\tau) \tag{5.9b}$$

For the purpose of our simulation, we will model $\mathrm{E}^c(\tau)$, $\mathrm{E}^{\mathrm{sb}^+}(\tau)$ and $\mathrm{E}^{\mathrm{sb}^-}(\tau)$ as independent beams. As before, we are only interested in the phase or frequency of these beams.

We can decompose the phases in eq. (5.8) in terms of large phase drifts and small fluctuations, as described in eq. (4.4), to get

$$\Phi_c(\tau) = \nu_0\tau + \phi_c^o(\tau) + \phi_c^\epsilon(\tau)\,, \tag{5.10a}$$

$$\Phi_m(\tau) = \phi_m^o(\tau) + \phi_m^\epsilon(\tau)\,. \tag{5.10b}$$

Notice that since $\Phi_m(\tau)$ represents the 2.4 GHz electrical signal used for modulation, it contains no term proportional to the central laser frequency ν_0. We define the upper and lower sideband phase drifts and fluctuations,

$$\phi_{\mathrm{sb}^+}^o(\tau) = \phi_c^o(\tau) + \phi_m^o(\tau) \quad \text{and} \quad \phi_{\mathrm{sb}^+}^\epsilon(\tau) = \phi_c^\epsilon(\tau) + \phi_m^\epsilon(\tau)\,, \tag{5.11a}$$

$$\phi_{\mathrm{sb}^-}^o(\tau) = \phi_c^o(\tau) - \phi_m^o(\tau) \quad \text{and} \quad \phi_{\mathrm{sb}^-}^\epsilon(\tau) = \phi_c^\epsilon(\tau) - \phi_m^\epsilon(\tau)\,, \tag{5.11b}$$

such that by plugging eqs. (5.10a) and (5.10b) in eq. (5.8), we recover the usual two-variable decompositions for the upper and lower sideband total phases,

$$\Phi_{\mathrm{sb}^+}(\tau) = \nu_0\tau + \phi_{\mathrm{sb}^+}^o(\tau) + \phi_{\mathrm{sb}^+}^\epsilon(\tau)\,, \tag{5.12a}$$

$$\Phi_{\mathrm{sb}^-}(\tau) = \nu_0\tau + \phi_{\mathrm{sb}^-}^o(\tau) + \phi_{\mathrm{sb}^-}^\epsilon(\tau)\,. \tag{5.12b}$$

Equivalently, we can decompose the carrier and modulating signal phases in terms of frequency offsets and fluctuations,

$$\nu_c(\tau) = \nu_0 + \nu_c^o(\tau) + \nu_c^\epsilon(\tau)\,, \tag{5.13}$$

$$\nu_m(\tau) = \nu_m^o(\tau) + \nu_m^\epsilon(\tau)\,, \tag{5.14}$$

such that the upper and lower sideband frequencies can be written as

$$\nu_{\mathrm{sb}^+}(\tau) = \nu_0 + \nu_{\mathrm{sb}^+}^o(\tau) + \nu_{\mathrm{sb}^+}^\epsilon(\tau)\,, \tag{5.15}$$

$$\nu_{\mathrm{sb}^-}(\tau) = \nu_0 + \nu_{\mathrm{sb}^-}^o(\tau) + \nu_{\mathrm{sb}^-}^\epsilon(\tau)\,, \tag{5.16}$$

with the upper and lower sideband frequency offsets and fluctuations,

$$\nu_{\mathrm{sb}^+}^o(\tau) = \nu_c^o(\tau) + \nu_m^o(\tau) \quad \text{and} \quad \nu_{\mathrm{sb}^+}^\epsilon(\tau) = \nu_c^\epsilon(\tau) + \nu_m^\epsilon(\tau)\,, \tag{5.17}$$

$$\nu_{\mathrm{sb}^-}^o(\tau) = \nu_c^o(\tau) - \nu_m^o(\tau) \quad \text{and} \quad \nu_{\mathrm{sb}^-}^\epsilon(\tau) = \nu_c^\epsilon(\tau) - \nu_m^\epsilon(\tau)\,. \tag{5.18}$$

5.2.3 *Pseudo-random noise modulation*

As discussed in section 3.6.4, the laser beams will carry an additional modulation with a PRN code used for absolute ranging and timing synchronization. This step-wise modulation is performed at a relatively high frequency of around 2 MHz, far outside our simulation bandwidth. We therefore do not model the actual phase modulation. As shown in [34], this modulation also causes a small additional noise in our measurement band, at a level below $1\,\mathrm{pm}/\sqrt{\mathrm{Hz}}$ in units of displacement, which we neglect.

Instead, as described in section 6.3.2, we model the PRN measurement by directly propagating the time deviations of each spacecraft timer with respect to their TPSs alongside the laser beams. The model used for the onboard timers themselves is described in section 6.1.3.

Note that at the moment, we only model the PRN measurement in the ISC interferometers, and completely ignore their presence in the other interferometers.

5.2.4 *Model for a modulated beam*

From sections 5.2.2 and 5.2.3, we model an actual laser beam using three independent virtual beams for the carrier, the upper and the lower sidebands, as well as an independent variable representing the local timer deviations encoded in the PRN modulation.

One difference is that they lie at a different frequencies, and are thus affected differently by Doppler shifts.

In addition, eqs. (5.11a) and (5.11b) show that the information content of the upper and lower sidebands are almost identical. We make the assumption that they can be combined in such a way that we can treat them as one signal, with a readout noise that is reduced by a factor of $\sqrt{2}$. Therefore, we only simulate the upper sideband. For clarity, we drop the sign in all sideband indices and simply use *sb* when we refer to the upper sideband. Ultimately, each laser *ij* is then implemented by propagating at most 5 variables,

$$\nu_{ij}(\tau) \equiv (\nu^o_{ij,c}(\tau), \nu^\epsilon_{ij,c}(\tau), \nu^o_{ij,\mathrm{sb}}(\tau), \nu^\epsilon_{ij,\mathrm{sb}}(\tau), \delta\hat{\tau}_i(\tau))\,, \tag{5.19}$$

where

- $\nu^o_{ij,c}(\tau)$ and $\nu^\epsilon_{ij,c}(\tau)$ are the carrier frequency offsets and fluctuations,
- $\nu^o_{ij,\mathrm{sb}}(\tau)$ and $\nu^\epsilon_{ij,\mathrm{sb}}(\tau)$ are the sideband frequency offsets and fluctuations, and
- $\delta\hat{\tau}_i(\tau)$ describes the local timer deviations of the generating spacecraft as described in section 6.1.3, in relevant laser beams only.

We can express all these quantities in units of phase,

$$\Phi_{ij}(\tau) \equiv (\phi^o_{ij,c}(\tau), \phi^\epsilon_{ij,c}(\tau), \phi^o_{ij,\mathrm{sb}}(\tau), \phi^\epsilon_{ij,\mathrm{sb}}(\tau), \delta\hat{\tau}_i(\tau))\,, \tag{5.20}$$

where

- $\phi^o_{ij,c}(\tau)$ and $\phi^\epsilon_{ij,c}(\tau)$ are the carrier phase drifts and fluctuations,
- $\phi^o_{ij,\mathrm{sb}}(\tau)$ and $\phi^\epsilon_{ij,\mathrm{sb}}(\tau)$ are the sideband phase drifts and fluctuations, and
- $\delta\hat{\tau}_i(\tau)$ still describes the local timer deviations of the generating spacecraft, in relevant laser beams only.

5.3 LASER BEAMS AT THE SOURCE

In this section, we derive the expression of a modulated beam generated by the laser source ij. All signals in this section are functions of the spacecraft proper time (TPS) of spacecraft i, which we call τ_i.

As described above, the modulated beam is modelled by the carrier and sideband virtual beams, as well as the local timer deviations.

5.3.1 *Carrier beam*

The total phase $\phi_{ij,c}(\tau)$ of the carrier at generation is decomposed in terms of drift and fluctuations,

$$\phi^o_{ij,c}(\tau) = \int_{\tau_{i,0}}^{\tau} O_{ij}(\tau)\mathrm{d}\tau \quad \text{and} \quad \phi^\epsilon_{ij,c}(\tau) = p_{ij}(\tau)\,, \tag{5.21}$$

with $O_{ij}(\tau)$ as the carrier frequency offset for this laser source with respect to the central frequency ν_0, and $p_{ij}(\tau)$ as the laser source phase fluctuations expressed in cycles. As explained in section 7.3, $p_{ij}(\tau)$ can either describe the noise $N^p_{ij}(\tau)$ of a cavity-stabilized laser, c.f. appendix D.1, or the fluctuations resulting from an offset frequency lock, c.f. section 7.3. Likewise, $O_{ij}(\tau)$ is either set as an initial offset from the nominal frequency, or computed based on the locking conditions.

In terms of frequency fluctuations, we then simply have

$$\nu^o_{ij,c}(\tau) = O_{ij}(\tau)\,, \tag{5.22a}$$
$$\nu^\epsilon_{ij,c}(\tau) = \dot{p}_{ij}(\tau)\,. \tag{5.22b}$$

5.3.2 *Clock sidebands*

As disussed in section 6.1.1, the frequency offsets and fluctuations for the modulating signal are derived from the pilot tone, which itself is derived from the USO. They therefore inherit any USO timing errors q_i, such that we have

$$\Phi_{ij,m}(\tau) = \nu^m_{ij}(\tau + q_i(\tau) + M_{ij}(\tau)) \tag{5.23}$$

for the total phase of the modulating signal. We define here $\nu^m_{ij} = 2.4\,\mathrm{GHz}$ and $2.401\,\mathrm{GHz}$ as the constant nominal frequency of the left and right MOSAs,

Note that these frequencies are per definition at exactly their nominal values, while the real modulation signals will have a frequency offset due to the terms q_i and M_i in eq. (5.23).

respectively. We added a modulation noise term $M_{ij}(\tau)$ (c.f. appendix D.2 and section 6.1.2), accounting for any imperfections between the sideband signal and the pilot tone. These can arise from either the electrical frequency conversion or the optical modulation. As discussed in detail in section 6.1.1, we decompose q_i into large drifts and small fluctuations:

$$q_i(\tau) = q_i^o(\tau) + q_i^\epsilon(\tau)\,, \tag{5.24}$$

where q_i^o models large deterministic drifts of the *USO* while $q_i^\epsilon(\tau)$ describes stochastic fluctuations.

These are expressed as timing jitter. As such, the total phase of the modulating signal can be decomposed into

$$\phi_{ij,m}^o(\tau) = \nu_{ij}^m(\tau + q_i^o(\tau))\,, \tag{5.25a}$$
$$\phi_{ij,m}^\epsilon(\tau) = \nu_{ij}^m(q_i^\epsilon(\tau) + M_{ij}(\tau))\,. \tag{5.25b}$$

Inserting these terms in eqs. (5.11a) and (5.18), we get

$$\phi_{ij,\mathrm{sb}}^o(\tau) = \int_{\tau_{i,0}}^{\tau} O_{ij}(\tau)\mathrm{d}\tau + \nu_{ij}^m(\tau + q_i^o(\tau))\,, \tag{5.26a}$$
$$\phi_{ij,\mathrm{sb}}^\epsilon(\tau) = p_{ij}(\tau) + \nu_{ij}^m(q_i^\epsilon(\tau) + M_{ij}(\tau))\,, \tag{5.26b}$$

and

$$\nu_{ij,\mathrm{sb}}^o(\tau) = O_{ij}(\tau) + \nu_{ij}^m(1 + \dot{q}_i^o(\tau))\,, \tag{5.27a}$$
$$\nu_{ij,\mathrm{sb}}^\epsilon(\tau) = \dot{p}_{ij}(\tau) + \nu_{ij}^m(\dot{q}_i(\tau) + \dot{M}_{ij}(\tau))\,. \tag{5.27b}$$

Note that there is only one clock per spacecraft, such that we use the same q_i for sideband beams on both optical benches. $M_{ij}(\tau)$, on the other hand, is unique for each sideband.

5.4 LASER BEAM INTERFERENCE

Photoreceivers are used to measure the power of the electromagnetic field of the two interfering laser beams in each interferometer on our optical benches.

We derive here the expressions of this electromagnetic power near the surface of a photodiode for two general modulated beams. Note that we do not consider any noise in the readout of that power yet, such as shot noise.

5.4.1 *Beatnote from simple beams*

Using definitions given in eq. (5.2), let us write the complex amplitude for two simple beams 1 and 2 interfering at a photodiode onboard spacecraft i,

$$\mathrm{E}_1(\tau) = E_{1,0}(\tau)e^{i2\pi\Phi_1(\tau)} \quad \text{and} \quad \mathrm{E}_2(\tau) = E_{2,0}(\tau)e^{i2\pi\Phi_2(\tau)}\,. \tag{5.28}$$

We ignore any effects due to spatial dimensions of the beam or the photodiode, and assume that such effects will be modelled as either an equivalent phase error in the readout signal, or as an independent quantity.

As an example, DWS could be modelled as a direct measurement of beam tilt angles, with all beam angles represented by independent variables.

The power of the total electromagnetic field[3] measured near the photodiode is

$$P(\tau) \propto |\mathrm{E}_1(\tau) + \mathrm{E}_2(\tau)|^2 . \tag{5.29}$$

Substituting the expressions of the two beams yields

$$\begin{aligned} P(\tau) \propto\ & |E_{1,0}(\tau)|^2 + |E_{2,0}(\tau)|^2 \\ & + 2E_{1,0}(\tau)E_{2,0}(\tau)\cos(2\pi(\Phi_1(\tau) - \Phi_2(\tau))) . \end{aligned} \tag{5.30}$$

The power near the photodiode has a periodic component with a total phase of $\Phi_{\mathrm{PD}}(\tau) = \Phi_1(\tau) - \Phi_2(\tau)$. We call this periodic signal the beatnote.

Let us use the two-variable representation described in eq. (4.4),

$$\Phi_1(\tau) = \nu_0\tau + \phi_1^o(\tau) + \phi_1^\epsilon(\tau) \tag{5.31a}$$
$$\Phi_2(\tau) = \nu_0\tau + \phi_2^o(\tau) + \phi_2^\epsilon(\tau) , \tag{5.31b}$$

to express the total phase of the beatnote as the sum of large phase drifts and small phase fluctuations,

$$\Phi_{\mathrm{PD}}(\tau) = \phi_{\mathrm{PD}}^o(\tau) + \phi_{\mathrm{PD}}^\epsilon(\tau) , \tag{5.32}$$

with

$$\phi_{\mathrm{PD}}^o(\tau) = \phi_1^o(\tau) - \phi_2^o(\tau) \tag{5.33a}$$
$$\phi_{\mathrm{PD}}^\epsilon(\tau) = \phi_1^\epsilon(\tau) - \phi_2^\epsilon(\tau) . \tag{5.33b}$$

We simulate the equivalent instantaneous frequency defined as $\nu_{\mathrm{PD}}(\tau) = \dot{\Phi}_{\mathrm{PD}}(\tau)$. It can be written as

$$\nu_{\mathrm{PD}}(\tau) = \nu_{\mathrm{PD}}^o(\tau) + \nu_{\mathrm{PD}}^\epsilon(\tau) , \tag{5.34}$$

where the beatnote frequency offsets $\nu_{\mathrm{PD}}^o(\tau)$ and the beatnote frequency fluctuations $\nu_{\mathrm{PD}}^\epsilon(\tau)$ are defined by

$$\nu_{\mathrm{PD}}^o(\tau) = \nu_1^o(\tau) - \nu_2^o(\tau) \tag{5.35a}$$
$$\nu_{\mathrm{PD}}^\epsilon(\tau) = \nu_1^\epsilon(\tau) - \nu_2^\epsilon(\tau) . \tag{5.35b}$$

5.4.2 *Beatnote polarity*

A closer look at eq. (5.30) shows that we do not have direct access to the total phase $\Phi_{\mathrm{PD}}(\tau)$ of the beatnote, but rather measure its cosine value[4]. Cosine is

3 By using the complex electrical field, this expression already contains an implicit time average, removing oscillating components at the total laser frequency [44].

4 Note that we could have just as well modelled our signal using a sine instead of a cosine function, in which case the arbitrariness of this sign is not as obvious. However, we can always write $\sin(\phi) = \cos(\phi - \pi/2)$, and absorb the additional term $\pi/2$ into the definition of the initial phase to again get a symmetric function. This is valid since the starting time of our measurements and the initial phase of the beams at that time are completely arbitrary in our model.

an even, periodic function, therefore the total phase can only be known up to a sign and a multiple of 2π.

Physically, the ambiguity in the sign θ_{PD} corresponds to the fact that the electrical signal does not contain any information about which of the two interfering laser beams is of higher frequency. In practice, however, θ_{PD} can be determined at all times by inducing a frequency offset of known polarity on the local laser beam and observing the resulting change in the beatnote frequency.

The laser frequency has to be adjustable to enable the frequency locking scheme, cf. section 7.3.

In addition, once all lasers are locked, the beatnote polarities can simply be read from the frequency plan, as described in section 3.6.2.

Therefore, we will not include this additional factor θ_{PD} in the remaining analysis of this thesis, but instead assume it is either removed directly by the phasemeter, or in a first processing step on-ground.

5.4.3 *Beatnotes from modulated beams*

In section 5.2.2, we showed that a modulated laser beam can be written as the superposition of three virtual beams, the carrier, the upper and the lower sideband, each of them in the form of a simple beam.

To study the electromagnetic field of two interfering modulated beams near a photodiode, we write each of the two beams $k = 1, 2$ as the sum of three virtual beams,

$$\mathrm{E}_k(\tau) = \mathrm{E}_k^c(\tau) + \mathrm{E}_k^{\mathrm{sb}^+}(\tau) + \mathrm{E}_k^{\mathrm{sb}^-}(\tau)\,, \tag{5.36}$$

with total phases

$$\Phi_{k,c}(\tau) = 2\pi\nu_0\tau + \Phi_{k,c}^o(\tau) + \Phi_{k,c}^e(\tau)\,, \tag{5.37a}$$
$$\Phi_{k,\mathrm{sb}^+}(\tau) = 2\pi\nu_0\tau + \Phi_{k,\mathrm{sb}^+}^o(\tau) + \Phi_{k,\mathrm{sb}^+}^e(\tau)\,, \tag{5.37b}$$
$$\Phi_{k,\mathrm{sb}^-}(\tau) = 2\pi\nu_0\tau + \Phi_{k,\mathrm{sb}^-}^o(\tau) + \Phi_{k,\mathrm{sb}^-}^e(\tau)\,, \tag{5.37c}$$

or the equivalent instantaneous frequencies

$$\nu_{k,c}(\tau) = \nu_0 + \nu_{k,c}^o(\tau) + \nu_{k,c}^e(\tau)\,, \tag{5.38a}$$
$$\nu_{k,\mathrm{sb}^+}(\tau) = \nu_0 + \nu_{k,\mathrm{sb}^+}^o(\tau) + \nu_{k,\mathrm{sb}^+}^e(\tau)\,, \tag{5.38b}$$
$$\nu_{k,\mathrm{sb}^-}(\tau) = \nu_0 + \nu_{k,\mathrm{sb}^-}^o(\tau) + \nu_{k,\mathrm{sb}^-}^e(\tau)\,. \tag{5.38c}$$

We again need to compute

$$\begin{aligned} P(\tau) &\propto \left|\mathrm{E}_1(\tau) + \mathrm{E}_2(\tau)\right|^2 \\ &= \left|\mathrm{E}_1^c(\tau) + \mathrm{E}_1^{\mathrm{sb}^+}(\tau) + \mathrm{E}_1^{\mathrm{sb}^-}(\tau) + \mathrm{E}_2^c(\tau) + \mathrm{E}_2^{\mathrm{sb}^+}(\tau) + \mathrm{E}_2^{\mathrm{sb}^-}(\tau)\right|^2. \end{aligned} \tag{5.39}$$

Expanding this expression yields cross terms between all 6 virtual beams, which correspond to beatnotes at their difference frequencies.

Since the sidebands are modulated at a relatively high frequency of about 2.4 GHz, most of these beatnote frequencies are far outside of the phasemeters

measurement bandwidth of approximately 5 MHz to 25 MHz [46]. Only three lie inside this region,

- The carrier-carrier beatnote, of total phase and frequency

$$\Phi_{\mathrm{PD},c}(\tau) = \Phi_{1,c}(\tau) - \Phi_{2,c}(\tau)\,, \tag{5.40a}$$
$$\nu_{\mathrm{PD},c}(\tau) = \nu_{1,c}(\tau) - \nu_{2,c}(\tau)\,, \tag{5.40b}$$

- The upper sideband-upper sideband beatnote, of total phase and frequency

$$\Phi_{\mathrm{PD},\mathrm{sb}^+}(\tau) = \Phi_{1,\mathrm{sb}^+}(\tau) - \Phi_{2,\mathrm{sb}^+}(\tau)\,, \tag{5.41a}$$
$$\nu_{\mathrm{PD},\mathrm{sb}^+}(\tau) = \nu_{1,\mathrm{sb}^+}(\tau) - \nu_{2,\mathrm{sb}^+}(\tau)\,, \tag{5.41b}$$

- The lower sideband-lower sideband beatnote, of total phase and frequency

$$\Phi_{\mathrm{PD},\mathrm{sb}^-}(\tau) = \Phi_{1,\mathrm{sb}^-}(\tau) - \Phi_{2,\mathrm{sb}^-}(\tau)\,, \tag{5.42a}$$
$$\nu_{\mathrm{PD},\mathrm{sb}^-}(\tau) = \nu_{1,\mathrm{sb}^-}(\tau) - \nu_{2,\mathrm{sb}^-}(\tau)\,, \tag{5.42b}$$

The frequency offsets $\nu_c^o(\tau)$, $\nu_{\mathrm{sb}^+}^o(\tau)$, and $\nu_{\mathrm{sb}^-}^o(\tau)$ are chosen such that the three aforementioned beatnotes never overlap (c.f. section 7.3) and can be tracked individually. Each of these beatnote frequencies can be decomposed again as a sum of large frequency offsets and small fluctuations, and we recover equations similar to eqs. (5.35a) and (5.35b). Therefore, the virtual beams of a modulated laser beam can be implemented as three distinct beams in the simulation, from which we form three beatnotes.

Because we only consider one sideband virtual beam (c.f. section 5.2.4), we only simulate the carrier-carrier and one of the sideband-sideband beatnotes.

5.5 LASER BEAM PROPAGATION

Before giving the expression for the signals detected on all photodiodes in section 5.6, we need to derive a model for the propagation of the laser beams from the laser source to the different photodiodes.

As described in section 5.2.4, we model modulated beams as the superposition of simple beams, each treated independently. Consequently, the same propagation equations apply to both carrier and sideband beams. We will therefore suppress the labels $()_{\mathrm{c/sb}}$ for all variables, with the understanding that all equations are valid for both carrier and sideband beams.

The result of that propagation will of course be different when applied to the different variables!

The propagation of the timer deviations is modelled independently in section 6.3

5.5.1 *Propagation of a simple beam*

In this section, we study the relationship between the phase and frequency of a simple beam at two different points in space, A and B. Let us call τ_A and τ_B the proper times of observers co-moving with A and B.

We assume that the total phase of the beam before propagation is given as a function of τ_A, which we call $\Phi_A(\tau)$. We use eq. (4.4) to write it as the sum of a nominal frequency, large phase drifts, and small phase fluctuations,

$$\Phi_A(\tau) = \nu_0 \tau + \phi^o_A(\tau) + \phi^\epsilon_A(\tau)\,. \tag{5.43}$$

The total phase after propagation can be written as a function of τ_B, which we write as $\Phi_B(\tau)$. In all generality, it is given by

$$\Phi_B(\tau) = \Phi_A(\tau_{BA}(\tau))\,, \tag{5.44}$$

where $\tau_{BA}(\tau)$ is the time at which a photon is emitted at A, expressed in the time coordinate τ_A, as a function of the time of its reception at B, expressed in the time coordinate τ_B.

In `LISANode` and `LISAInstrument`, fractional delays are implemented using Lagrange interpolating polynomials, see appendix B.

In the simulation, we implement this propagation by applying fractional delay filters on time series generated according to the timescale of τ_A. For this application, it is most useful to introduce the proper pseudo-range (PPR),

$$d_{BA}(\tau) = \tau - \tau_{BA}(\tau)\,, \tag{5.45}$$

such that

$$\Phi_B(\tau) = \Phi_A(\tau - d_{BA}(\tau))\,. \tag{5.46}$$

Note that this PPR includes not only the time of flight of a photon, but also conversions between reference frames associated to τ_A and τ_B.

Since we model small in-band and large out-of-band effects independently (c.f. section 4.3.2), we need to decompose the PPR in a similar manner,

$$d_{BA}(\tau) = d^o_{BA}(\tau) + d^\epsilon_{BA}(\tau)\,, \tag{5.47}$$

with $d^o_{BA}(\tau)$ describing slowly varying PPR offsets (e.g., due to constant pathlengths and variations in orbital motion, relativistic effects, and coordinate transformations) and $d^\epsilon_{BA}(\tau)$ as small in-band PPR fluctuations (e.g., due to gravitational waves and optical path noises).

Applying this decomposition to eqs. (5.43) and (5.44), we have

$$\begin{aligned}\Phi_B(\tau) = \nu_0 \cdot [\tau - d^o_{BA}(\tau) - d^\epsilon_{BA}(\tau)] + \phi^o_A(\tau - d^o_{BA}(\tau) - d^\epsilon_{BA}(\tau)) \\ + \phi^\epsilon_A(\tau - d^o_{BA}(\tau) - d^\epsilon_{BA}(\tau))\,.\end{aligned} \tag{5.48}$$

Since both $d^\epsilon_{BA}(\tau)$ and $\phi^\epsilon_A(\tau)$ represent small fluctuations, we neglect effects to second order in any quantity with the superscript $(\,)^\epsilon$. We expand the previous equation to first oder in $d^\epsilon_{BA}(\tau)$ and $\phi^\epsilon_A(\tau)$ to get

$$\begin{aligned}\Phi_B(\tau) = \nu_0 \cdot [\tau - d^o_{BA}(\tau) - d^\epsilon_{BA}(\tau)] + \phi^o_A(\tau - d^o_{BA}(\tau)) \\ - \nu^o_A(\tau - d^o_{BA}(\tau)) \cdot d^\epsilon_{BA}(\tau) + \phi^\epsilon_A(\tau - d^o_{BA}(\tau))\,.\end{aligned} \tag{5.49}$$

We can express the phase after propagation as the sum of large phase drifts and small phase fluctuations, $\Phi_B(\tau) = \nu_0\tau + \phi^o_B(\tau) + \phi^\epsilon_B(\tau)$, with

$$\phi^o_B(\tau) = \phi^o_A(\tau - d^o_{BA}(\tau)) - \nu_0 d^o_{BA}(\tau)\,, \tag{5.50a}$$
$$\phi^\epsilon_B(\tau) = \phi^\epsilon_A(\tau - d^o_{BA}(\tau)) - (\nu_0 + \nu^o_A(\tau - d^o_{BA}(\tau))) \cdot d^\epsilon_{BA}(\tau)\,. \tag{5.50b}$$

We write the equivalent instantaneous frequency as the sum of a large frequency offsets and small frequency fluctuations,

$$\nu_B(\tau) = \nu_0 + \nu^o_B(\tau) + \nu^\epsilon_B(\tau)\,, \tag{5.51}$$

where we have defined

$$\nu^o_B(\tau) = \dot\phi^o_B(\tau) = \nu^o_A(\tau - d^o_{BA}(\tau))\big(1 - \dot d^o_{BA}(\tau)\big) - \nu_0 \dot d^o_{BA}(\tau)\,, \tag{5.52a}$$
$$\begin{aligned}\nu^\epsilon_B(\tau) = \dot\phi^\epsilon_B(\tau) = {}& \nu^\epsilon_A(\tau - d^o_{BA}(\tau))\big(1 - \dot d^o_{BA}(\tau)\big) \\ & - (\nu_0 + \nu^o_A(\tau - d^o_{BA}(\tau))) \cdot \dot d^\epsilon_{BA}(\tau)\,.\end{aligned} \tag{5.52b}$$

Here, we have neglected first order terms in $\dot\nu^o_A d^\epsilon_{BA}(\tau)$, so these equations are only valid if the laser frequency is evolving slowly.

To estimate the order of magnitude of the term $\dot\nu^o_A d^\epsilon_{BA}(\tau)$ we neglected compared to the term $\nu^o_A \dot d^\epsilon_{BA}(\tau)$ we included, we can observe the rate of change in the example frequency plan presented in fig. 3.9. This is plotted in fig. 5.3. As we can see, we have $\dot\nu^o_A < 4\,\mathrm{Hz\,s^{-1}}$ for the whole 4 year duration. ν^o_A, on the other hand, is of the order of 10 MHz. We consider both ν^o_A and $\dot\nu^o_A$ as constant scaling factors for this estimate.

$d^\epsilon_{BA}(\tau)$ and $\dot d^\epsilon_{BA}(\tau)$ are noise terms, which we can evaluate in the frequency domain. We have

$$\mathcal{F}\left[\dot d^\epsilon_{BA}(\tau)\right] = 2\pi f \mathcal{F}\left[d^\epsilon_{BA}(\tau)\right]\,. \tag{5.53}$$

The usual LISA measurement band is 10^{-4} Hz to 1 Hz, such that even at the lower limit of 10^{-4} Hz, we have

$$\begin{aligned}\nu^o_A \mathcal{F}\left[\dot d^\epsilon_{BA}\right] &\approx 10^4\,\mathrm{Hz\,s^{-1}}\mathcal{F}\left[d^\epsilon_{BA}\right] \\ &\gg \dot\nu^o_A \mathcal{F}\left[d^\epsilon_{BA}\right] \approx 4\,\mathrm{Hz\,s^{-1}}\mathcal{F}\left[d^\epsilon_{BA}\right]\,.\end{aligned} \tag{5.54}$$

Note that the term $\nu^o_A \dot d^\epsilon_{BA}(\tau)$ is already a very small correction to the dominant term $\nu_0 \dot d^\epsilon_{BA}(\tau)$, such that we can savely neglect these additional terms.

At the time of writing, we actually scale all pathlength noise terms with just ν_0 in both `LISANode` and `LISA Instrument`. This is planned to be updated to reflect the equations in this thesis in the near future.

5.5.2 *Propagation inside the spacecraft*

Let us first study the propagation of a simple beam inside a single spacecraft i. We can locally assume a flat spacetime, such that the two time coordinates are one and the same. As such, all functions in this subsection depend on the associated TPS τ_i.

Here, the point B represents the target interferometer, e.g., $B = \mathrm{isc}_{ij}$, while A represents the laser source, e.g., $A = ij$.

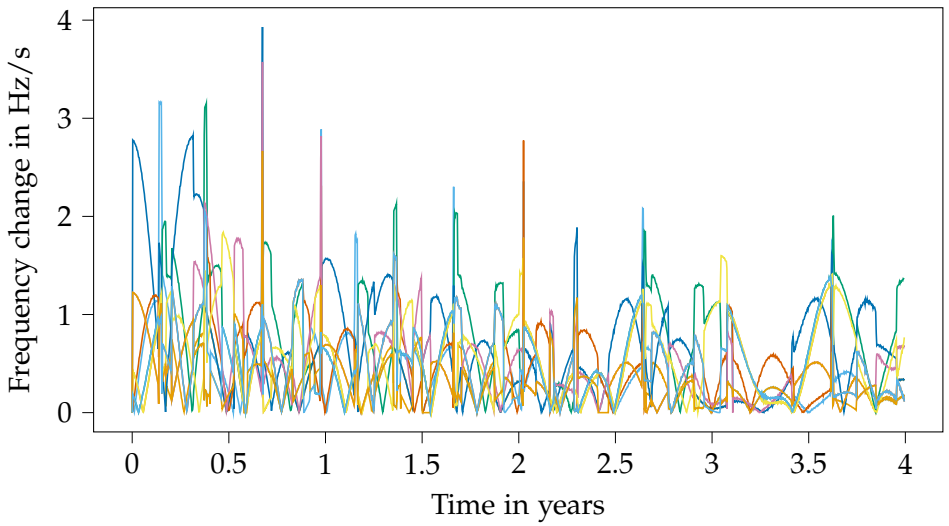

FIGURE 5.3: Magnitude of beatnote frequency derivatives for all 9 beatnotes in example frequency plan, data provided by G. Heinzel.

Using eq. (5.47), we can model the PPR as a the sum of a constant and a noise due to small optical pathlength fluctuations, expressed in seconds, so we define

$$d^o_{BA}(\tau) = C_{B\leftarrow A} \quad \text{and} \quad d^\epsilon_{BA}(\tau) = n_{B\leftarrow A}(\tau)\,. \tag{5.55}$$

Substituting these expressions in eqs. (5.50a) and (5.50b) yields the propagated phase drifts and fluctuations,

$$\phi^o_B(\tau) = \phi^o_A(\tau - C_{B\leftarrow A}) - \nu_0 C_{B\leftarrow A}\,, \tag{5.56a}$$
$$\phi^\epsilon_B(\tau) = \phi^\epsilon_A(\tau - C_{B\leftarrow A}) - (\nu_0 + \nu^o_A(\tau - C_{B\leftarrow A}))n_{B\leftarrow A}(\tau)\,. \tag{5.56b}$$

Expressed as equivalent frequencies, from eqs. (5.52a) and (5.52b), we have

$$\nu^o_B(\tau) = \nu^o_A(\tau - C_{B\leftarrow A})\,, \tag{5.57a}$$
$$\nu^\epsilon_B(\tau) = \nu^\epsilon_A(\tau - C_{B\leftarrow A}) - (\nu_0 + \nu^o_A(\tau - C_{B\leftarrow A}))\dot{n}_{B\leftarrow A}(\tau)\,. \tag{5.57b}$$

Note that our notation for the left-hand side of eqs. (5.56a), (5.56b), (5.57a) and (5.57b) has to capture both the photodiode the beam is interfering at as well as the source laser.

We will therefore include both of these informations in the label of the propagated beam, as introduced in section 5.1. For example, the phase fluctuations of the local beam in the ISC interferometer would be $\phi^\epsilon_{\mathrm{isc}_{ij}\leftarrow ij}(\tau)$.

We describe below the noises currently modelled in the simulation for the different interferometers.

5.5.2.1 *Local beams in inter-spacecraft and reference interferometers*

We add a generic optical pathlength noise term to the propagated beam. Therefore, we apply eqs. (5.56a), (5.56b), (5.57a) and (5.57b) with

$$C_{\mathrm{isc}_{ij}\leftarrow ij} = 0\,, \tag{5.58a}$$

$$n_{\mathrm{isc}_{ij}\leftarrow ij} = N^{\mathrm{ob}}_{\mathrm{isc}_{ij}\leftarrow ij}(\tau)\,. \tag{5.58b}$$

5.5.2.2 *Adjacent beams in test-mass and reference interferometers*

The beams are exchanged between the optical benches using an optical fibre. We model any non-reciprocal noise terms related to the propagation through these fibres by backlink noise term $N^{\mathrm{bl}}_{ij\leftarrow ik}(\tau)$. We model it as an equivalent pathlength change in seconds. In addition, as before, we add an optical pathlength noise term, such that we can apply eqs. (5.56a), (5.56b), (5.57a) and (5.57b) with

$$C_{(\mathrm{ref/tm})_{ij}\leftarrow ik} = 0\,, \tag{5.59a}$$

$$n_{(\mathrm{ref/tm})_{ij}\leftarrow ik} = N^{\mathrm{bl}}_{ij\leftarrow ik}(\tau) + N^{\mathrm{ob}}_{(ref/tm)_{ij}\leftarrow ik}(\tau)\,. \tag{5.59b}$$

5.5.2.3 *Local test-mass interferometers*

As shown in fig. 5.1, the local laser beam is reflected off the test mass before impinging on the photodiode associated with the local test-mass interferometer.

In reality, the motion of the test-mass and spacecraft will be coupled by the DFACS, as described in section 3.4.4. A detailed study for the perfomance analysis of this control loop is outside the scope of this thesis, see [12] for details of the expected performance based on LISA Pathfinder.

For this thesis, we will simply assume that the local laser beam picks up an additional noise term $N^{\delta}_{ij}(\tau)$ due to the movement of the free-falling test mass, which we model in appendix D.3. This noise is assumed to represent the movement of the test-mass *towards* the measuring optical bench, such that a positive value corresponds to an decrease in pathlength, and thus a decrease of the delay received by the beam, which in turn causes a positive phase shift.

In addition, we include a second noise term $N^{\Delta}_{ij}(\tau)$ due to the movement of the spacecraft, which is assumed to represent the movement of the optical bench *away* from the test-mass[5]. A positive value now corresponds to an increase in pathlength. See fig. 5.4 for a sketch of how we define these quantities.

Note that this noise is missing in the actual simulation at the time of writing of the thesis, and should be added in a future version. We include it in the analytical model for completeness.

Notice that both of these terms enter with a factor 2, since the beam travels to the test-mass and back.

5 In other words, both $N^{\delta}_{ij}(\tau)$ and $N^{\Delta}_{ij}(\tau)$ are given by the displacement vector of test-mass and optical bench, projected on the same vector pointing towards the distant spacecraft. Note that at the time of writing, only $N^{\delta}_{ij}(\tau)$ is included in the simulation.

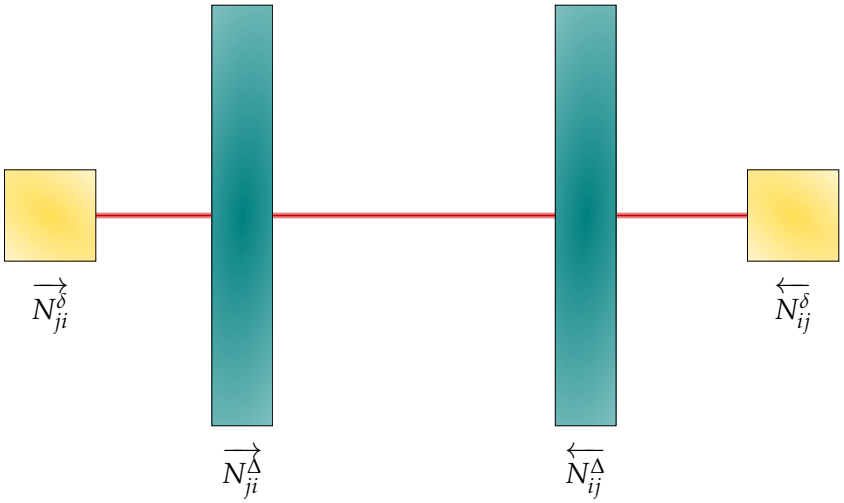

FIGURE 5.4: Definition of line-of-sight displacement of test-masses and optical benches. Positive values of N^{δ}_{ij} and N^{Δ}_{ij} indicate movement *towards* the distant spacecraft.

Therefore, we apply eqs. (5.56a), (5.56b), (5.57a) and (5.57b) with

$$C_{\mathrm{tm}_{ij}\leftarrow ij} = 0\,, \tag{5.60a}$$

$$n_{\mathrm{tm}_{ij}\leftarrow ij} = 2(N^{\Delta}_{ij}(\tau) - N^{\delta}_{ij}(\tau)) + N^{\mathrm{ob}}_{tm_{ij}\leftarrow ij}(\tau)\,, \tag{5.60b}$$

to model the propagation to the local test-mass interferometer, where we again add an additional noise term accounting for optical pathlength noise.

5.5.3 *Inter-spacecraft propagation*

Let us now focus on the inter-spacecraft propagation of a simple laser beam received by the telescope ij.

Following appendix A.1, this laser beam was emitted by spacecraft j and is received by spacecraft i.

The phase and frequency of the beam before propagation is naturally expressed as a function of emitter TPS, τ_j, while those of the received beam, as well as the PPR, are expressed as functions of the receiver TPS, τ_i.

For this subsection, we consider the spacecraft as free-falling point masses, and model effects due to orbital mechanics and GWs. In addition, we include the noise term N^{Δ}_{ij} introduced in section 5.5.2.3, accounting for jitter of the spacecraft position with respect to its nominal position. As before, we only consider the displacement within the sensitive direction, with a positive value indicating movement towards the distant spacecraft, as depicted in fig. 5.4. Therefore, both N^{Δ}_{ij} terms cause a decrease in pathlength between the two optical benches.

Following eq. (5.47), the PPR offsets $d^{o}_{ij}(\tau)$ should contain any large out-of band fluctuations. This includes effects due to post-Minkowskian expansions and conversions between different reference frames. We do not repeat the full calculation of these expression, but instead rely on the results presented in [11] for the simulation results presented in this thesis.

For this term, we don't distinguish between noise added by the sending and receiving spacecraft.

We include the effect of gravitational signals, the spacecraft jitter and a small optical pathlength noise term in the PPR fluctuations,

$$d^{\epsilon}_{ij}(\tau) = H_{ij}(\tau) - N^{\Delta}_{ji}(\tau - d^{o}_{ij}(\tau)) - N^{\Delta}_{ij}(\tau) + N^{\mathrm{ob}}_{isc_{ij}\leftarrow ji}(\tau)\,. \tag{5.61}$$

Note that the distant spacecrafts jitter enters at the time of emission, while the local one enters at the time of reception.

$H_{ij}(\tau)$ is the overall effect of GWs integrated over the photon path, expressed as the variation of the photon time of flight. We do not compute the actual values of the $H_{ij}(\tau)$ in the simulation, but treat them as an external input provided by other consortium WGs[6].

Substituting these expressions in eqs. (5.50a) and (5.50b) yields the phase drifts and fluctuations of the beam received by MOSA ij, which will be measured in isc_{ij},

$$\phi^o_{\mathrm{isc}_{ij}\leftarrow ji}(\tau) = \phi^o_{ji}(\tau - d^o_{ij}(\tau)) - \nu_0 d^o_{ij}(\tau)\,, \tag{5.62a}$$

$$\begin{aligned}\phi^\epsilon_{\mathrm{isc}_{ij}\leftarrow ji}(\tau) = {}& \phi^\epsilon_{ji}(\tau - d^o_{ij}(\tau)) - (\nu_0 + \nu^o_{ji}(\tau - d^o_{ij}(\tau))) \\ & \times \left(H_{ij}(\tau) - N^\Delta_{ji}(\tau - d^o_{ij}(\tau)) - N^\Delta_{ij}(\tau) + N^{\mathrm{ob}}_{isc_{ij}\leftarrow ji}(\tau)\right).\end{aligned} \tag{5.62b}$$

Expressed as equivalent frequencies, from eqs. (5.52a) and (5.52b), we have

$$\nu^o_{\mathrm{isc}_{ij}\leftarrow ji}(\tau) = \nu^o_{ji}(\tau - d^o_{ij}(\tau))(1 - \dot{d}^o_{ij}(\tau)) - \nu_0 \dot{d}^o_{ij}(\tau)\,, \tag{5.63a}$$

$$\begin{aligned}\nu^\epsilon_{\mathrm{isc}_{ij}\leftarrow ji}(\tau) = {}& \nu^\epsilon_{ji}(\tau - d^o_{ij}(\tau))(1 - \dot{d}^o_{ij}(\tau)) - (\nu_0 + \nu^o_{ji}(\tau - d^o_{ij}(\tau))) \\ & \times \Big(\dot{H}_{ij}(\tau) - \dot{N}^\Delta_{ji}(\tau - d^o_{ij}(\tau))(1 - \dot{d}^o_{ij}(\tau)) \\ & \qquad - \dot{N}^\Delta_{ij}(\tau) + \dot{N}^{\mathrm{ob}}_{isc_{ij}\leftarrow ji}(\tau)\Big).\end{aligned} \tag{5.63b}$$

5.6 PHOTODIODE SIGNALS

In this section, we give an overview over the different interferometric signals on optical bench ij. They are computed using the usual two-variable decomposition, as described in section 5.4.

Photoreceivers, which consists of photodiodes and the associated readout electronics, convert optical power at the photodiode surface to a proportional voltage which can be processed further. As discussed in section 5.4.1, the EM-field at the photodiode has a time-varying component, of which we model only the total phase or frequency. The electrical voltage produced by the photoreceiver will therefore also be time-varying, and we again model only its total phase or frequency. It consists of the phase/frequency of the EM field at the photodiode, plus an additional readout noise term $N^{\mathrm{ro}}(\tau)$, whose magnitude for each interferometer is described in appendix D.5. It accounts for both optical effects, like shot noise, as well as electronic noise added by the photoreceiver.

Since we do not really distinguish between different noises related to this readout, we simply call the resulting signal the *photodiode signal*.

6 We refer to section 2.2 for how GWs affect light propagation times in general, and to the literature for a more detailed treatment in the case of LISA, e.g., [94].

In summary, we model the photodiode signals in the ISC interferometer as

$$\phi^{o}_{\mathrm{isc}_{ij},c/\mathrm{sb}}(\tau) = (\phi_{\mathrm{isc}_{ij}\leftarrow ji})^{o}_{c/\mathrm{sb}}(\tau) - (\phi_{\mathrm{isc}_{ij}\leftarrow ij})^{o}_{c/\mathrm{sb}}(\tau)\,, \tag{5.64a}$$

$$\nu^{o}_{\mathrm{isc}_{ij},c/\mathrm{sb}}(\tau) = (\nu_{\mathrm{isc}_{ij}\leftarrow ji})^{o}_{c/\mathrm{sb}}(\tau) - (\nu_{\mathrm{isc}_{ij}\leftarrow ij})^{o}_{c/\mathrm{sb}}(\tau)\,, \tag{5.64b}$$

$$\begin{aligned}\phi^{\epsilon}_{\mathrm{isc}_{ij},c/\mathrm{sb}}(\tau) = {}& (\phi_{\mathrm{isc}_{ij}\leftarrow ji})^{\epsilon}_{c/\mathrm{sb}}(\tau) - (\phi_{\mathrm{isc}_{ij}\leftarrow ij})^{\epsilon}_{c/\mathrm{sb}}(\tau) \\ & + N^{\mathrm{ro}}_{\mathrm{isc}_{ij},c/\mathrm{sb}}(\tau)\,,\end{aligned} \tag{5.64c}$$

$$\begin{aligned}\nu^{\epsilon}_{\mathrm{isc}_{ij},c/\mathrm{sb}}(\tau) = {}& (\nu_{\mathrm{isc}_{ij}\leftarrow ji})^{\epsilon}_{c/\mathrm{sb}}(\tau) - (\nu_{\mathrm{isc}_{ij}\leftarrow ij})^{\epsilon}_{c/\mathrm{sb}}(\tau) \\ & + \dot{N}^{\mathrm{ro}}_{\mathrm{isc}_{ij},c/\mathrm{sb}}(\tau)\,,\end{aligned} \tag{5.64d}$$

while those in the reference and test-mass interferometers are given as

$$\phi^{o}_{\mathrm{ifo}_{ij},c/\mathrm{sb}}(\tau) = (\phi_{\mathrm{ifo}_{ij}\leftarrow ik})^{o}_{c/\mathrm{sb}}(\tau) - (\phi_{\mathrm{ifo}_{ij}\leftarrow ij})^{o}_{c/\mathrm{sb}}(\tau)\,, \tag{5.65a}$$

$$\nu^{o}_{\mathrm{ifo}_{ij},c/\mathrm{sb}}(\tau) = (\nu_{\mathrm{ifo}_{ij}\leftarrow ik})^{o}_{c/\mathrm{sb}}(\tau) - (\nu_{\mathrm{ifo}_{ij}\leftarrow ij})^{o}_{c/\mathrm{sb}}(\tau)\,, \tag{5.65b}$$

$$\begin{aligned}\phi^{\epsilon}_{\mathrm{ifo}_{ij},c/\mathrm{sb}}(\tau) = {}& (\phi_{\mathrm{ifo}_{ij}\leftarrow ik})^{\epsilon}_{c/\mathrm{sb}}(\tau) - (\phi_{\mathrm{ifo}_{ij}\leftarrow ij})^{\epsilon}_{c/\mathrm{sb}}(\tau) \\ & + N^{\mathrm{ro}}_{\mathrm{ifo}_{ij},c/\mathrm{sb}}(\tau)\,,\end{aligned} \tag{5.65c}$$

$$\begin{aligned}\nu^{\epsilon}_{\mathrm{ifo}_{ij},c/\mathrm{sb}}(\tau) = {}& (\nu_{\mathrm{ifo}_{ij}\leftarrow ik})^{\epsilon}_{c/\mathrm{sb}}(\tau) - (\nu_{\mathrm{ifo}_{ij}\leftarrow ij})^{\epsilon}_{c/\mathrm{sb}}(\tau) \\ & + \dot{N}^{\mathrm{ro}}_{\mathrm{ifo}_{ij},c/\mathrm{sb}}(\tau)\,,\end{aligned} \tag{5.65d}$$

where 'ifo' can stand for either 'ref' or 'tm'.

Note that we give here only the signals for optical bench ij, with the index k on the right-hand side chosen such that whole set of indices satisfies $\{i,j,k\} = \{1,2,3\}$.

6

CLOCK AND TIMING DISTRIBUTION MODEL

In this chapter we describe how we model the onboard clocks, and how their timing signals are distributed through the constellation.

As described in section 3.5, the electric photodiode signals from chapter 5 are digitized by an analog-to-digital converter (ADC) before their phase is reconstructed in a digital phase-locked loop (DPLL). Any timing jitter of the ADC itself will be corrected by overlaying each signal with a pilot tone (cf. section 3.6.3), which therefore effectively acts as timing reference for the phasemeter measurements. We will assume this pilot tone correction works perfectly, and directly consider the pilot tone as the reference clock for all phasemeter measurements.

As described in section 3.7, different timing signals are derived from the USO and distributed through the constellation, which we will model in section 6.1. We will then formulate how errors in these timing signal affect the phase and frequency of the digitized signal in section 6.2.

Finally, we give a high-level model of the PRN measurement (cf. section 3.6.4) in section 6.3.

6.1 CLOCK MODEL

We describe here all signals and effects related to the onboard clocks. For most of the clock signals, we give specific frequency values, which are to be seen as placeholders until the design of the frequency distribution system (FDS) for LISA is finalized.

6.1.1 *USO model*

In LISA, each spacecraft uses one dedicated clock from which all timing signals are derived. It is realized by an ultra-stable oscillator (USO), generating a clock signal with a nominal frequency of $\nu_{\mathrm{USO}} = 10\,\mathrm{MHz}$.

Following appendix C.1.2, we model the USO signal as a periodic signal of the form

$$V_{\mathrm{USO}}(\tau) = \cos(2\pi\nu_{\mathrm{USO}}[\tau + q_i(\tau)])\,, \tag{6.1}$$

where we further decompose the clocks timing jitter $q_i(\tau)$ using two time series,

$$q_i(\tau) = q_i^o(\tau) + q_i^\epsilon(\tau)\,. \tag{6.2}$$

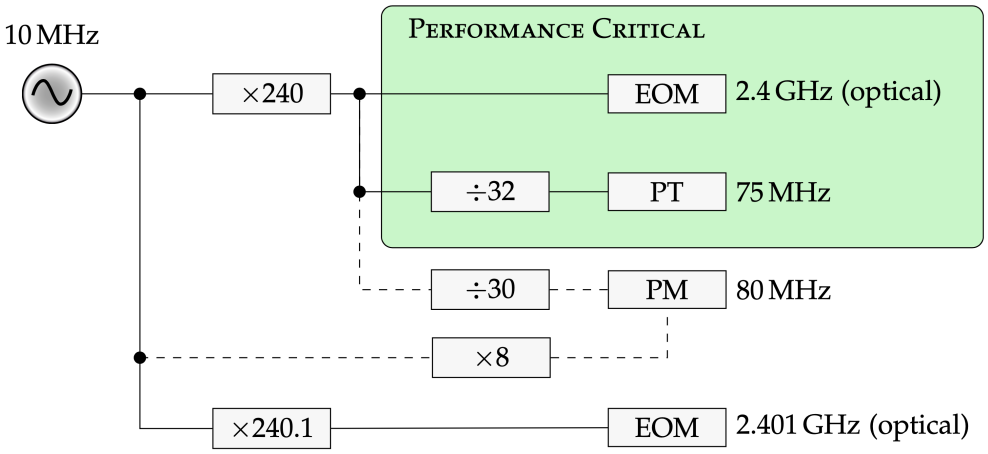

Figure 6.1: Overview over USO frequency distribution on one optical bench, based on [15]. Not depicted is a possible electrical comparison between the 2.4 GHz and 2.401 GHz signal. Note that the PM clock is not performance critical, and could be synthesized from either the 2.4 GHz signal or directly from the USO, indicated by two possible connections in dotted lines.

$q_i^o(\tau)$ models large deterministic effects, such as clock frequency offsets and drifts, while $q_i^\epsilon(\tau)$ models stochastic fluctuations.

$q_i(\tau)$ describes the timing deviations of the local USO hosted by spacecraft i, expressed in the TPS τ_i. We simulate the clock in terms of fractional frequency fluctuations, where the two components are given by

$$\dot{q}_i^o(\tau) = y_{0,i} + y_{1,i}\tau + y_{2,i}\tau^2 \quad \text{and} \quad \dot{q}_i^\epsilon(\tau) = \dot{N}_i^q(\tau)\,, \tag{6.3}$$

with a random jitter $\dot{N}_i^q(\tau)$, a constant deterministic frequency offset $y_{0,i}$, a linear frequency drift scaled by the constant $y_{1,i}$, and a quadratic frequency drift scaled by the constant $y_{2,i}$. Note that constant time offsets of the onboard timers are introduced and discussed in section 6.1.3.

See appendix C for a detailed overview on clock frequency stability. The model we use in the simulation is given in appendix D.8, and is based on an estimate for the LISA USO performance provided by the SYRTE 'Theory and Metrology group' [81].

6.1.2 *Derived clock signals*

As described in section 3.7, the USO signal is converted to different frequencies in the FDS. Figure 6.1 shows a schematic overview of how the most relevant clock signals are generated on each spacecraft.

The USOs 10 MHz signal is upconverted to 2.4 GHz and 2.401 GHz. These signals are used as input for EOMs on the left- and right-handed optical benches to create the optical sidebands discussed in chapter 5.

In addition, the 2.4 GHz signal is used to generate a 75 MHz pilot tone and a 80 MHz phasemeter clock using frequency dividers. Note that the 80 MHz phasemeter clock could also be directly synthesized from the USO, since it is not performance critical.

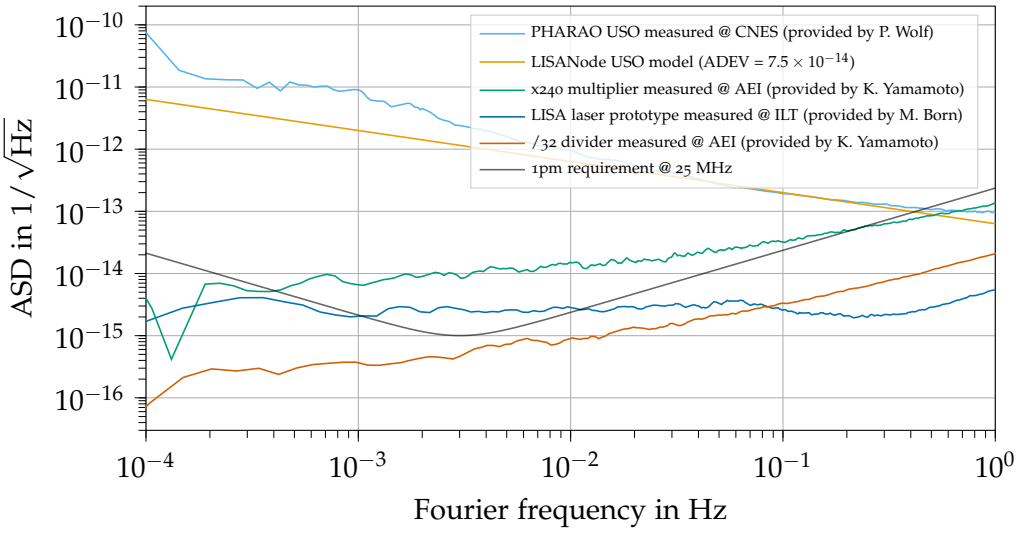

FIGURE 6.2: Noises added by different components in the frequency distribution system, expressed in fractional frequency. USO noise is dominant, and would cause equivalent displacement noise many orders of magnitude above 1 pm assuming a 25 MHz beatnote. Noise added by optical modulation and /32 divider are performance critical.

Figure 6.2 gives the expected noise of the different components[1]. These noise levels are shown converted to fractional frequency fluctuations, such that they can all be compared on the same scale. As a reference, we give the 1 pm requirement curve converted to fractional frequency fluctuations of a 25 MHz beatnote, as derived in appendix C.5.1.

We see that the components in the conversion chain from 10 MHz USO to 75 MHz pilot tone add additional timing at a much lower level than that of the USO itself.

Therefore, we assume that the statistical properties of the pilot tone $V_{\mathrm{PT}}(\tau)$ are identical to those of the generating USO, as described in section 6.1.1. In the following, $q_i(\tau)$ therefore directly stands for the pilot tone timing jitter.

We do not model the 80 MHz signal, as its timing jitter is removed by the pilot tone correction, which we assume works perfectly.

See section 3.6.3 for more information on pilot tone correction.

Imperfections in the frequency conversion between the pilot tone and any other clock derived signal are modelled by an additional noise term on the derived signal. For example, the total phase of the 2.4 GHz signal is modelled as

$$2.4\,\mathrm{GHz} \times (\tau + q_i(\tau) + M_{ij}(\tau))\,, \tag{6.4}$$

with $M_{ij}(\tau)$ as an additional modulation noise term. In principle, $M_{ij}(\tau)$ includes both errors from the ÷32 frequency divider and the optical modulators. However, as we see in fig. 6.2, noise from the optical modulators is dominant, and we give a model in appendix D.2.

In particular the fibre amplifiers behind the EOMs, see e.g. [14] for more information. We show in fig. 6.2 more recent measurement, which are also limited by noise from the fibre amplifier.

The 2.401 GHz signals phase, on the other hand, contains additional noise terms due to the ×240 and ×240.1 frequency converters. This additional noise is expected to surpass the optical modulation noise, and would be limiting the clock correction performance. We show that it can be removed by

1 We thank K. Yamamoto and M. Born from the Albert Einstein Institute (AEI) as well as P. Wolf from SYRTE for providing these measurements!

utilizing the sideband beatnotes in the reference interferometers, as described in section 13.3.3.2.

Therefore, the performance-critical part of the frequency conversion chain is to go from the 75 MHz pilot tone to the 2.4 GHz optical sideband. As we will show in chapter 13, the corresponding modulation noise M_{ij} will ultimately limit the achievable clock correction.

6.1.3 *Timer model*

In order to model timestamping and pseudo-ranging (c.f. section 6.3), we not only need the frequency fluctuations of the local clock, but also the time shown by each spacecraft timer. These times must be tracked down to at least ns-precision while reaching values of around 10^8 s at the end of the 10 years of extended mission [55]. The use of double-precision floating-point numbers is not compatible with such a dynamic range. Therefore, we simulate offsets of that timer relative to the spacecraft proper time (TPS) $\delta\hat{\tau}_i^{\tau_i}(\tau) \equiv \delta\hat{\tau}_i(\tau)$, called timer deviations, which evolve slowly with time. The total on-board clock time (THE)[2] $\hat{\tau}_i^{\tau_i}(\tau)$ as a function of the TPS can then be computed by

$$\hat{\tau}_i^{\tau_i}(\tau) = \tau + \delta\hat{\tau}_i(\tau)\,. \tag{6.5}$$

Timer deviations are closely related to the USO timing jitter,

$$\delta\hat{\tau}_i(\tau) = q_i(\tau) + \delta\hat{\tau}_{i,0}\,. \tag{6.6}$$

In this equation, $\delta\hat{\tau}_{i,0}$ accounts for the fact that we don't know the true time $\tau_{i,0}$ at which we turn on the timer, i.e., we can't relate the initial phase of the clock signal $q_i(\tau_{i,0})$ to any external time frame. Using eq. (6.3), we obtain

$$\delta\hat{\tau}_i(\tau) = \delta\hat{\tau}_{i,0} + \int_{\tau_{i,0}}^{\tau} N_i^q(\tau')\,\mathrm{d}\tau' + y_{0,i}\tau + \frac{1}{2}y_{1,i}\tau^2 + \frac{1}{3}y_{2,i}\tau^3 \tag{6.7}$$

for the timer deviations, which corresponds to

- a constant time offset $\delta\hat{\tau}_{i,0}$,
- a random walk following the frequency fluctuations $N_i^q(\tau)$,
- a linear drift due to the frequency offset $y_{0,i}$,
- a quadratic component due to the linear frequency drift $y_{1,i}$, and
- a cubic component due to the quadratic frequency drift $y_{2,i}$.

Note that the deterministic frequency drift and offset are the most relevant parts for the long term evolution; however, the stochastic part is typically not a white noise, and can reach values larger than our desired ns-timing accuracy. As such, we consider the total $\delta\hat{\tau}_i(\tau)$ for computing timing errors.

2 This timescale will be realized in practice by the so-called spacecraft elapsed time (SCET), which is the only timescale directly available onboard the satellites.

6.2 SIGNAL SAMPLING

6.2.1 *Signal sampling in terms of phase*

The photodiode signals recorded on spacecraft i (cf. chapter 5) are generated according to the spacecraft proper time (TPS) τ_i. The measurements which are eventually telemetered, however, are recorded and timestamped in the on-board clock time (THE). This means that we need to simulate a resampling of the photodiode signals from the TPS to the THE. If an arbitrary signal s is expressed in terms of phase, this can be achieved following eq. (A.5),

As described above, the onboard clock time is for our purposes defined by the pilot tone, which is the timing reference for all phasemeter measurements.

$$s^{\hat{\tau}_i}(\tau) = s^{\tau_i}(\tau_i^{\hat{\tau}_i}(\tau))\,. \tag{6.8}$$

Therefore, we need to compute the TPS $\tau_i^{\hat{\tau}_i}(\tau)$ given a THE time τ. This quantity can be computed by writing eq. (6.5) evaluated at $\tau_i^{\hat{\tau}_i}(\tau)$,

$$\hat{\tau}_i^{\tau_i}(\tau_i^{\hat{\tau}_i}(\tau)) = \tau_i^{\hat{\tau}_i}(\tau) + \delta\hat{\tau}_i(\tau_i^{\hat{\tau}_i}(\tau))\,. \tag{6.9}$$

We apply the identity eq. (A.5) to the left-hand side, which gives after rearranging

$$\tau_i^{\hat{\tau}_i}(\tau) = \tau - \delta\hat{\tau}_i(\tau_i^{\hat{\tau}_i}(\tau))\,. \tag{6.10}$$

We can solve this implicit equation for $\tau_i^{\hat{\tau}_i}(\tau)$ iteratively, by computing

$$\delta\hat{\tau}_i^0(\tau) = \delta\hat{\tau}_i(\tau)\,, \tag{6.11a}$$
$$\delta\hat{\tau}_i^{n+1}(\tau) = \delta\hat{\tau}_i(\tau - \delta\hat{\tau}_i^n(\tau))\,, \tag{6.11b}$$

such that

$$\lim_{n\to\infty} \delta\hat{\tau}_i^n(\tau) = \delta\hat{\tau}_i(\tau_i^{\hat{\tau}_i}(\tau))\,. \tag{6.12}$$

Since the timer deviations are evolving slowly, the iteration converges quickly. In the simulation, we model the timestamping error by iterating the equation twice, to get

$$\tau_i^{\hat{\tau}_i}(\tau) \approx \tau - \delta\hat{\tau}_i^2(\tau)\,. \tag{6.13}$$

We then perform Lagrange interpolation to time shift all measurements to the correct recording times, i.e., for any frame-independent measurement $s^{\tau_i}(\tau)$ expressed in the TPS, we compute

$$s^{\hat{\tau}_i}(\tau) \approx s^{\tau_i}(\tau - \delta\hat{\tau}_i^2(\tau))\,. \tag{6.14}$$

Note that this is only valid for measurements expressed in phase. As we will see in section 6.2.2, Equation (6.8) does not hold when the measurements are expressed in terms of frequency.

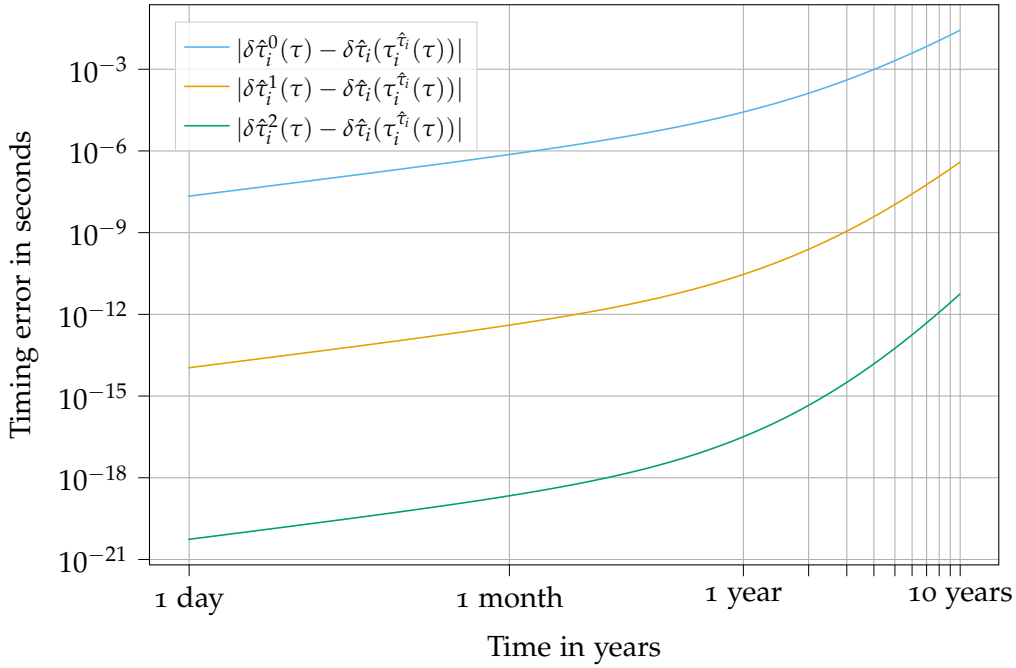

FIGURE 6.3: Error in iterative computation of $\tau_i^{\hat{\tau}_i}(\tau)$ at different iterative orders.

6.2.1.1 *Validity of iterative solution*

We want to evaluate if eq. (6.13) remains valid for the whole mission duration, such that we can use it in our simulations. At very long time scales, the timer deviations are dominated by the deterministic effects in eq. (6.7), i.e., by $q_i^o(\tau)$. As such, we can approximate

$$\hat{\tau}_i^{\tau_i}(\tau) \approx \tau + y_{0,i}\tau + \frac{1}{2}y_{1,i}\tau^2 + \frac{1}{3}y_{2,i}\tau^3 \,. \tag{6.15}$$

In general, the inverse function of a 3rd order polynomial is not guaranteed to exist. Given the very small values for the coefficients $y_{0,i}$, $y_{1,i}$ and $y_{2,i}$, however, eq. (6.15) is a one-to-one function for the mission duration, with a unique inverse.

Assuming the clock parameters are given by eq. (D.12), we can compute an analytical inverse of that function (using the computer algebra system Mathematica), such that we get an exact solution for $\tau_i^{\hat{\tau}_i}(\tau)$. We can then evalute that solution using exact integer arithmetic. This allows us to evalute the errors in our iterative solutions, which are plotted in fig. 6.3. Assuming that we want to compute $\tau_i^{\hat{\tau}_i}(\tau)$ with ns accuracy, we observe that:

- $\delta\hat{\tau}_i^0(\tau)$ is not sufficient even on the time scale of days,
- $\delta\hat{\tau}_i^1(\tau)$ is sufficient at time scales up to 3 years,
- $\delta\hat{\tau}_i^2(\tau)$ is sufficient for the full extended mission duration of 10 years.

6.2.2 *Sampling errors in terms of frequency*

The effect of resampling can also be expressed in terms of total frequency, where it manifests as a Doppler-like frequency shift. Note that we compute the frequency now by taking the derivative with respect to the THE, since this is the time reference which the phasemeter will use to measure the

frequency of the signal. From eq. (6.21), and denoting function composition as $(\Phi_{\mathrm{PD}}^{\tau_i} \circ \tau_i^{\hat{\tau}_i})(\tau) = \Phi_{\mathrm{PD}}^{\tau_i}(\tau_i^{\hat{\tau}_i}(\tau))$, we have

$$\nu_{\mathrm{PD}}^{\hat{\tau}_i}(\tau) = \frac{\mathrm{d}\Phi_{\mathrm{PD}}^{\hat{\tau}_i}}{\mathrm{d}\tau}(\tau) = \frac{\mathrm{d}(\Phi_{\mathrm{PD}}^{\tau_i} \circ \tau_i^{\hat{\tau}_i})}{\mathrm{d}\tau}(\tau)\,. \tag{6.16}$$

Using the chain rule,

$$\nu_{\mathrm{PD}}^{\hat{\tau}_i}(\tau) = \frac{\mathrm{d}\Phi_{\mathrm{PD}}^{\tau_i}}{\mathrm{d}\tau}\left(\tau_i^{\hat{\tau}_i}(\tau)\right) \times \frac{\mathrm{d}\tau_i^{\hat{\tau}_i}}{\mathrm{d}\tau}(\tau) = \nu_{\mathrm{PD}}^{\tau_i}(\tau_i^{\hat{\tau}_i}(\tau)) \times \frac{\mathrm{d}\tau_i^{\hat{\tau}_i}}{\mathrm{d}\tau}(\tau)\,. \tag{6.17}$$

To compute the derivative of $\tau_i^{\hat{\tau}_i}(\tau)$, we differentiate eq. (6.10),

$$\frac{\mathrm{d}\tau_i^{\hat{\tau}_i}}{\mathrm{d}\tau}(\tau) = 1 - \frac{\mathrm{d}(\delta\hat{\tau}_i \circ \tau_i^{\hat{\tau}_i})}{\mathrm{d}\tau}(\tau) = 1 - \frac{\mathrm{d}\delta\hat{\tau}_i}{\mathrm{d}\tau}\left(\tau_i^{\hat{\tau}_i}(\tau)\right) \times \frac{\mathrm{d}\tau_i^{\hat{\tau}_i}}{\mathrm{d}\tau}(\tau)\,. \tag{6.18}$$

Finally, using $\frac{\mathrm{d}\delta\hat{\tau}_i}{\mathrm{d}\tau} = \dot{q}_i(\tau)$, we can rearrange this equation, to get

$$\frac{\mathrm{d}\tau_i^{\hat{\tau}_i}}{\mathrm{d}\tau}(\tau) = \frac{1}{1 + \dot{q}_i(\tau_i^{\hat{\tau}_i}(\tau))}\,, \tag{6.19}$$

which yields

$$\nu_{\mathrm{PD}}^{\hat{\tau}_i}(\tau) = \frac{\nu_{\mathrm{PD}}^{\tau_i}(\tau_i^{\hat{\tau}_i}(\tau))}{1 + \dot{q}_i(\tau_i^{\hat{\tau}_i}(\tau))} \approx \frac{\nu_{\mathrm{PD}}^{\tau_i}(\tau - \delta\hat{\tau}_i^2(\tau))}{1 + \dot{q}_i(\tau - \delta\hat{\tau}_i^2(\tau))} \tag{6.20}$$

for the total frequency.

6.2.3 *Sampling in two-variable decomposition*

We now want to describe the effect of timing errors in the two-variable decomposition. This will allow us to decompose the previously described sampling errors into two seperate effects, large, deterministic offsets in the measurement timestamps and small, stochastic fluctuations which enter as an additional noise term. The latter represent what is often referred to as "clock noise", see, e.g., [64]. However, we want to reinforce that this decomposition is entirely artifical – both of these effects described the same physical process, the instability of the USO, just on different time scales.

6.2.3.1 *Decomposition in terms of phase*

As described above, the resampling to the THE happens when the signals are digitized by the ADC, which is triggered according to the onboard clock. As such, it is applied to the total phase of each photodiode signal, given by eq. (5.32),

$$\Phi_{\mathrm{PD}}^{\hat{\tau}_i}(\tau) = \Phi_{\mathrm{PD}}^{\tau_i}(\tau_i^{\hat{\tau}_i}(\tau)) = \phi_{\mathrm{PD}}^{o}(\tau_i^{\hat{\tau}_i}(\tau)) + \phi_{\mathrm{PD}}^{\epsilon}(\tau_i^{\hat{\tau}_i}(\tau))\,. \tag{6.21}$$

Since $\phi_{\mathrm{PD}}^{o}(\tau)$ is very quickly evolving, small timing fluctuations in $\tau_i^{\hat{\tau}_i}(\tau)$ will couple into the measurement described by $\phi_{\mathrm{PD}}^{\epsilon}(\tau)$. So there is a cross coupling

between $\phi^o_{\mathrm{PD}}(\tau)$ and $\phi^\epsilon_{\mathrm{PD}}(\tau)$, and we cannot just time shift both components individually.

We can insert eq. (6.6) and eq. (6.2) in to eq. (6.10) to get

$$\tau_i^{\hat{\tau}_i}(\tau) = \tau - \delta\hat{\tau}_{i,0} - q_i^o(\tau_i^{\hat{\tau}_i}(\tau)) - q_i^\epsilon(\tau_i^{\hat{\tau}_i}(\tau))\,. \tag{6.22}$$

Because clock-noise fluctuations $\dot{q}_i^\epsilon$ are modelled as band-limited noise (c.f. section 6.1.1), they remain very small and we can expand the ϕ^o term in eq. (6.21) to first order in $\dot{q}_i^\epsilon$,

$$\begin{aligned}\Phi^{\hat{\tau}_i}_{\mathrm{PD}}(\tau) &= \phi^o_{\mathrm{PD}}(\tau - \delta\hat{\tau}_{i,0} - q_i^o(\tau_i^{\hat{\tau}_i}(\tau)) - q_i^\epsilon(\tau_i^{\hat{\tau}_i}(\tau))) + \phi^\epsilon_{\mathrm{PD}}(\tau_i^{\hat{\tau}_i}(\tau)) \\ &\approx \phi^o_{\mathrm{PD}}(\tau - \delta\hat{\tau}_{i,0} - q_i^o(\tau_i^{\hat{\tau}_i}(\tau))) + \phi^\epsilon_{\mathrm{PD}}(\tau_i^{\hat{\tau}_i}(\tau)) \\ &\quad - \nu^o_{\mathrm{PD}}(\tau - \delta\hat{\tau}_{i,0} - q_i^o(\tau_i^{\hat{\tau}_i}(\tau)))q_i^\epsilon(\tau_i^{\hat{\tau}_i}(\tau))\,,\end{aligned} \tag{6.23}$$

to get the two variables

$$\phi^{\hat{\tau}_i,o}_{\mathrm{PD}}(\tau) \approx \phi^o_{\mathrm{PD}}(\tau - \delta\hat{\tau}_{i,0} - q_i^o(\tau - \delta\hat{\tau}_i^2(\tau)))\,, \tag{6.24}$$

$$\begin{aligned}\phi^{\hat{\tau}_i,\epsilon}_{\mathrm{PD}}(\tau) &\approx \phi^\epsilon_{\mathrm{PD}}(\tau - \delta\hat{\tau}_i^2(\tau)) \\ &\quad - \nu^o_{\mathrm{PD}}(\tau - \delta\hat{\tau}_{i,0} - q_i^o(\tau - \delta\hat{\tau}_i^2(\tau)))q_i^\epsilon(\tau - \delta\hat{\tau}_i^2(\tau))\,.\end{aligned} \tag{6.25}$$

6.2.3.2 *Decomposition in terms of frequency*

For frequency, we start with eq. (6.20), and again decompose clock noise $\dot{q}_i$ into two variables as explained in section 6.1.1. We can expand to first order in $\dot{q}_i^\epsilon$ to get

$$\frac{1}{1 + \dot{q}_i^o(\tau_i^{\hat{\tau}_i}(\tau)) + \dot{q}_i^\epsilon(\tau_i^{\hat{\tau}_i}(\tau))} \approx \frac{1}{1 + \dot{q}_i^o(\tau_i^{\hat{\tau}_i}(\tau))} - \frac{\dot{q}_i^\epsilon(\tau_i^{\hat{\tau}_i}(\tau))}{[1 + \dot{q}_i^o(\tau_i^{\hat{\tau}_i}(\tau))]^2}\,. \tag{6.26}$$

So in total, we have

$$\nu^{\hat{\tau}_i}_{\mathrm{PD}}(\tau) \approx \nu^{\tau_i}_{\mathrm{PD}}(\tau_i^{\hat{\tau}_i}(\tau))\left[\frac{1}{1 + \dot{q}_i^o(\tau_i^{\hat{\tau}_i}(\tau))} - \frac{\dot{q}_i^\epsilon(\tau_i^{\hat{\tau}_i}(\tau))}{[1 + \dot{q}_i^o(\tau_i^{\hat{\tau}_i}(\tau))]^2}\right]. \tag{6.27}$$

We now expand $\nu^{\tau_i}_{\mathrm{PD}}(\tau) = \nu^{\tau_i,o}_{\mathrm{PD}}(\tau) + \nu^{\tau_i,\epsilon}_{\mathrm{PD}}(\tau)$, and neglect the small coupling of $q_i^\epsilon(\tau)$ to the already small fluctuations $\nu^{\tau_i,\epsilon}_{\mathrm{PD}}(\tau)$. We collect the terms to express the photodiode signal offsets $\nu^{\hat{\tau}_i,o}_{\mathrm{PD}}(\tau)$ and fluctuations $\nu^{\hat{\tau}_i,\epsilon}_{\mathrm{PD}}(\tau)$ after shifting to the THE, using eq. (6.14),

$$\nu^{\hat{\tau}_i,o}_{\mathrm{PD}}(\tau) \approx \frac{\nu^{\tau_i,o}_{\mathrm{PD}}(\tau - \delta\hat{\tau}_i^2(\tau))}{1 + \dot{q}_i^o(\tau - \delta\hat{\tau}_i^2(\tau))}\,, \tag{6.28}$$

$$\nu^{\hat{\tau}_i,\epsilon}_{\mathrm{PD}}(\tau) \approx \frac{\nu^{\tau_i,\epsilon}_{\mathrm{PD}}(\tau - \delta\hat{\tau}_i^2(\tau))}{1 + \dot{q}_i^o(\tau - \delta\hat{\tau}_i^2(\tau))} - \frac{\nu^{\tau_i,o}_{\mathrm{PD}}(\tau - \delta\hat{\tau}_i^2(\tau))\dot{q}_i^\epsilon(\tau - \delta\hat{\tau}_i^2(\tau))}{[1 + \dot{q}_i^o(\tau - \delta\hat{\tau}_i^2(\tau))]^2}\,. \tag{6.29}$$

In the simulation, we model this effect by first rescaling frequency offsets of the photodiode signals, so we would obtain

$$\frac{\nu^{\tau_i,o}_{\mathrm{PD}}(\tau)}{1 + \dot{q}_i^o(\tau)}\,. \tag{6.30}$$

We then add this quantity to the frequency fluctuations of the photodiode signals, correctly rescaled, to obtain

$$\frac{\nu_{\mathrm{PD}}^{\tau_i,\epsilon}(\tau)}{1+\dot{q}_i^o(\tau)} - \frac{\nu_{\mathrm{PD}}^{\tau_i,o}(\tau)\dot{q}_i^\epsilon(\tau)}{[1+\dot{q}_i^o(\tau)]^2}\,. \tag{6.31}$$

Note that all quantities are still evaluated at τ.

Lastly, these quantities are resampled at $\tau - \delta\hat{\tau}_i^2(\tau)$ using Lagrange interpolation to retrieve eqs. (6.28) and (6.29).

For clarity's sake, we drop the time arguments in our signals, such that they are inherently given in the corresponding spacecraft THE. We introduce the first-order timestamping operator $\mathbf{T}_i$, which shifts a signal $s(\tau)$ from the TPS to the THE of spacecraft i. Formally, its action is given by

$$\mathbf{T}_i s(\tau) = s(\tau - \delta\hat{\tau}_i^2(\tau))\,. \tag{6.32}$$

Its pendant for frequency includes the rescaling by $1+q_i^o$, and is defined as

$$\dot{\mathbf{T}}_i s(\tau) = \mathbf{T}_i\left[\frac{s(\tau)}{1+\dot{q}_i^o(\tau)}\right]. \tag{6.33}$$

The photodiode signals read, in the THE,

$$\nu_{\mathrm{PD}}^{\hat{\tau}_i,o} \approx \dot{\mathbf{T}}_i \nu_{\mathrm{PD}}^{\tau_i,o} \quad \text{and} \quad \nu_{\mathrm{PD}}^{\hat{\tau}_i,\epsilon}(\tau) \approx \dot{\mathbf{T}}_i\left[\nu_{\mathrm{PD}}^{\tau_i,\epsilon} - \frac{\nu_{\mathrm{PD}}^{\tau_i,o}\dot{q}_i^\epsilon}{1+\dot{q}_i^o}\right], \tag{6.34}$$

where we suppressed the explicit time argument.

6.3 PSEUDO-RANGING

As sketched in section 3.2, LISA noise reduction algorithms, such as TDI, require knowledge of the propagation time of the laser beams between the spacecraft, or *ranging*. Technically, this is realized in LISA by generating a PRN code representing the time shown by the local clock on the sending spacecraft, which is modulated and transmitted via the outgoing laser beam. This code is then recovered from the phase measurement of that beam, and correlated with a local copy of the code generated according to the receiving spacecrafts clock. We call the result the measured pseudo-range (MPR). See section 3.6.4 (and references there) for more details on the technical implementation.

In this section, we first derive the equations for the MPRs in terms of clock time differences, c.f. section 6.3.1. Since we only simulate timer deviations, we reformulate these equations in section 6.3.2 so they are directly applicable to our simulation.

Pseudo-ranging simulation is performed at f_s^{phy}, while the MPRs are ultimately downsampled to a lower rate f_s^{meas}, alongside the other measurements.

6.3.1 *Pseudo-ranging as clock time difference*

Since the PRN code is modulated onto the laser beam, it suffers the same delays when propagating between the spacecraft[3].

As described in section 5.2.3, we do not model the actual phase modulation of the PRN. Instead, we directly compute the difference R_{ij} between times shown by local clocks (i.e. THE times).

Following the conventions used in section 5.5, we consider in the following paragraphs a beam received by optical bench ij at the receiver TPS τ, which was emitted from optical bench ji at emitter TPS $\tau_{ji}(\tau) = \tau - d_{ij}(\tau)$. Here, the PPR $d_{ij}(\tau)$ contains the photon time of flight, as well as the conversion between time coordinates.

Conceptually, the MPR measures the difference between the THE $\hat{\tau}_i^{\tau_i}(\tau)$ shown by the local clock of the receiving spacecraft at the event of reception of the beam, and the THE $\hat{\tau}_j^{\tau_j}(\tau - d_{ij}(\tau))$ shown by the local clock of the sending spacecraft at the event of emission of the beam. Thus, we can model the MPR as the difference

$$R_{ij}(\tau) = \hat{\tau}_i(\tau) - \hat{\tau}_j(\tau - d_{ij}(\tau)) + N_{ij}^R(\tau)\,, \tag{6.35}$$

where $N_{ij}^R(\tau)$ is a ranging noise term modelling imperfections in the overall correlation scheme. See appendix D.7 for its model in the simulation.

6.3.2 *Pseudo-ranging in terms of timer deviations*

As explained in section 6.1.3, we do not simulate the total THE $\hat{\tau}_i(\tau)$ for each spacecraft, but only deviations $\delta\hat{\tau}_i(\tau)$ from the TPS,

$$\hat{\tau}_i(\tau) = \tau + \delta\hat{\tau}_i(\tau) \quad \text{and} \quad \hat{\tau}_j(\tau) = \tau + \delta\hat{\tau}_j(\tau)\,. \tag{6.36}$$

Inserting these definitions into eq. (6.35) yields

$$R_{ij}(\tau) = \delta\hat{\tau}_i(\tau) - \left[\delta\hat{\tau}_j\big(\tau - d_{ij}(\tau)\big) - d_{ij}(\tau)\right] + N_{ij}^R(\tau)\,. \tag{6.37}$$

Let us define $\delta\hat{\tau}_{\mathrm{isc}_i \leftarrow j}(\tau)$,

$$\delta\hat{\tau}_{\mathrm{isc}_i \leftarrow j}(\tau) \approx \delta\hat{\tau}_j(\tau - d_{ij}(\tau)) - d_{ij}(\tau)\,, \tag{6.38}$$

the clock time of the sending spacecraft propagated to the photodiode of the distant inter-spacecraft interferometer.

We can then express the MPR as the simple difference

$$R_{ij}(\tau) \approx \delta\hat{\tau}_i(\tau) - \delta\hat{\tau}_{\mathrm{isc}_{ij} \leftarrow j}(\tau) + N_{ij}^R(\tau)\,. \tag{6.39}$$

This is the measurement we generate in the simulation, where we make the additional assumption that $d_{ij} \equiv d_{ij}^o$ for this measurement. This is valid,

3 We assume here that the vacuum between the satellites is sufficiently good that we can neglect (or compensate) any dispersion effects.

since the terms contained in d_{ij}^{ϵ} only create timing jitters much less than a nanosecond (cf. section 5.5).

Notice that in eq. (6.39), we compute the MPR as a function of the receiving TPSs, so that formally $R_{ij} = R_{ij}^{\tau_i}$. In reality, the MPR is measured according to the THE of the receiving spacecraft, $R_{ij}^{\hat{\tau}_i}$. Similarly to all other measurement, we simulate this by first generating $R_{ij}^{\tau_i}$ and then resampling the resulting time series to get $R_{ij}^{\hat{\tau}_i}$, as described in section 6.2.

7

ONBOARD PROCESSING

The onboard phasemeters track the phase evolution (or, almost equivalently, the instantaneous frequencies) of sampled and digitized versions of the MHz beatnotes described in section 5.6, using a digital phase-locked loop (DPLL) which runs at 80 MHz. The resultant phase is downsampled in multiple steps (cf. [36]) to the final measurement rate.

As described above, we do not simulate the phasemeter at this high sampling rate, but instead rely on high-level models to capture the most significant effects.

During the sampling process, clock imperfections couple into the measurements. We described this effect in chapter 6, and modelled its impact on the phase of the digitized signal by shifting all measurements from the TPS to the THE. We will now assume that the DPLL is able to perfectly reconstruct the phase of this digitized signal.

Following [47], we assume that one of the last downsampling steps inside the phasemeter creates a timeseries at $f_s^{\text{phy}} = 16\,\text{Hz}$, which then gets further filtered and decimated to $f_s^{\text{meas}} = 4\,\text{Hz}$.

We model this last step in the processing chain by including a digital finite impulse response (FIR) filter in our simulation, which we model in section 7.1. The resulting phasemeter signals are given in section 7.2.

These phasemeter equations still contain unevaluated terms for the laser offsets and frequency fluctuations, which are determined by the laser locking schemes. We describe these locking conditions and the different locking schemes in section 7.3.

Finally, we conclude by describing additional data streams available from contact to ground stations in section 7.4.

7.1 FILTERING AND DOWNSAMPLING

High-order digital low-pass FIR filters are expected to be used to prevent noise aliasing in the frequency band relevant for LISA data analysis, between $10^{-4}\,\text{Hz}$ and 1 Hz [56]. Therefore, they must strongly attenuate the signals above the Nyquist frequency, while maintaining a high gain and low phase distortion below 1 Hz. In reality, this will be performed by cascading filters to go all the way from 80 MHz to $f_s^{\text{meas}} = 4\,\text{Hz}$ [36], and their precise implementation is under development.

As explained below, the transition band can actually extend slightly above the Nyquist frequency, up to $f_s^{\text{meas}} - 1\,\text{Hz}$.

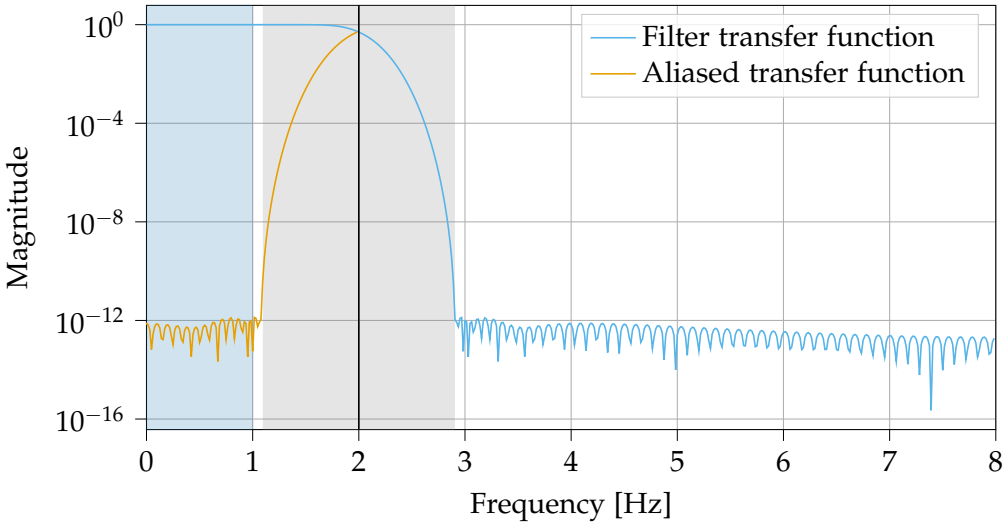

FIGURE 7.1: Antialiasing filter transfer function magnitude. The transition band (grey) is chosen to avoid aliasing into the measurement band (blue).

In the simulation, we only use a single filtering and downsampling step to go from f_s^{phy} to the final measurement sampling rate of $f_s^{\text{meas}} = 4\,\text{Hz}$.

We build a digital symmetrical FIR filter from a Kaiser windowing function, using the following parameters:

- the transition band extends from 1.1 Hz to 2.9 Hz,
- the minimum attenuation above 2.9 Hz is 240 dB.

Note that the filter transition band extends above the Nyquist frequency, such that there will be a significant amount of aliasing during downsampling, as depicted in fig. 7.1. However, since aliasing happens by reflection across the Nyquist frequency, any noise in the band $[f_s/2, f_s - 1\,\text{Hz}]$ will be aliased into the band $[1\,\text{Hz}, f_s/2]$, such that it stays outside our measurement band of $[10^{-4}\,\text{Hz}, 1\,\text{Hz}]$. We will revisit how the aliased noise appears in our final signals in section 12.3.3.

The filter coefficients c_k are computed based on these parameters using the `kaiserord` method of the scipy library [95]. The filter is then applied by computing the $n'th$ sample of the output series y from the input series x via

$$y[n] = \sum_{k=0}^{N} c_k x[n-k]\,, \tag{7.1}$$

with N as the order of the filter.

Analytically, we model the filter by applying a filter operator $\mathbf{F}$ to the photodiode signals. I.e., we simply write

$$y(t) = \mathbf{F}x(t)\,, \tag{7.2}$$

where we extend the definition in eq. (7.1) to also be applicable to a continous time function. Inspecting eq. (7.1), $\mathbf{F}$ is a linear operator.

In the frequency domain, the effect of the filter is described by multiplying the signals by its transfer function,

$$\mathcal{H}_{\mathbf{F}}(\omega) = \sum_{k=0}^{N} c_k e^{-i\omega k / f_s^{\mathrm{phy}}} , \tag{7.3}$$

whose magnitude is plotted in fig. 7.1.

Once the signals are filtered, we use a four-fold decimation, i.e. we select only 1 sample out of 4.

7.2 PHASEMETER SIGNALS

We call phasemeter signals the downsampled, filtered signals output by the phasemeter, i.e. the inter-spacecraft, test-mass, reference carrier and sideband beatnotes, as well as the MPRs. These are the signals ultimately telemetered down to Earth.

As mentioned before, there are other data streams - such as the angular readouts provided by DWS - which we do not model here.

For these phasemeter signals, we introduce a clear notation that uses the name of the associated interferometer and its index, completed by the type of beam (carrier or sideband). The real phasemeter will only produce the total frequency or the total phase of the signal. For our studies, however, it is often useful to also have access to the underlying offsets and fluctuations in two seperate variables, which is why we give here the signals in this form. The simulation will provide an additional output for the total frequency, as discussed in section 7.2.1.

As usual, we will denote the decomposition used by $(...)^{\epsilon}$ or $(...)^{o}$. E.g., $\mathrm{ref}^{\epsilon}_{ij,c}(\tau)$ is the phasemeter output for the reference carrier frequency fluctuations of optical bench ij.

These expressions are derived from the photodiode signals given in section 5.6, accounting for clock noise as described in section 6.2.3. As before, the time shift due to the on-board clocks is expressed by applying the time stamping operators $\mathbf{T}_i$ and $\dot{\mathbf{T}}_i$, see eqs. (6.32) and (6.33). Finally, we apply the filter operator, as discussed in section 7.1. The final expressions are then given as functions of the THEs.

For readabilities sake, we drop all time arguments in these expressions. We use delay operators to account for time shifts which appear when propagating signals. We denote $\mathbf{D}_{ij}$ the delay operator associated with the PPR $d^o_{ij}(\tau)$ defined in section 5.5.3, such that for any signal $s(\tau)$,

$$\mathbf{D}_{ij} s(\tau) = s(\tau - d^o_{ij}(\tau)) . \tag{7.4}$$

Furthermore, we introduce the Doppler-delay operator, which is defined as

$$\dot{\mathbf{D}}_{ij} s(\tau) = (1 - \dot{d}^o_{ij}(\tau)) s(\tau - d^o_{ij}(\tau)) . \tag{7.5}$$

We summarize below the different signals we simulate. Again, we give expressions only for optical bench ij, with the index k on the right-hand

side chosen such that whole set of indices satisfies $\{i,j,k\} = \{1,2,3\}$. All other optical benches can be derived by the usual index permutations, see appendix A.1.

We will also use a shorthand notation for the beatnote frequency offsets in the TPS, which we define by

$$a^c_{ij} \equiv \nu^o_{\mathrm{isc}_{ij},c} = \dot{\mathbf{D}}_{ij} O_{ji} - \nu_0 \dot{d}^o_{ij} - O_{ij}\,, \tag{7.6a}$$
$$a^{\mathrm{sb}}_{ij} \equiv \nu^o_{\mathrm{isc}_{ij},\mathrm{sb}} = a_{ij} + \dot{\mathbf{D}}_{ij}(\nu^m_{ji}(1+\dot{q}^o_j)) - \nu^m_{ij}(1+\dot{q}^o_i)\,, \tag{7.6b}$$
$$b^c_{ij} \equiv \nu^o_{\mathrm{ref}_{ij},c} = O_{ik} - O_{ij}\,, \tag{7.6c}$$
$$b^{\mathrm{sb}}_{ij} \equiv \nu^o_{\mathrm{ref}_{ij},\mathrm{sb}} = b_{ij} + (\nu^m_{ik} - \nu^m_{ij})(1+\dot{q}^o_i)\,. \tag{7.6d}$$

In addition, most of the laser related terms p_{ij}, O_{ij} will be determined by the laser locking scheme, as described in section 7.3.

Our phasemeter signals are then given as:

6 carrier-carrier beatnotes in the inter-spacecraft interferometers,

$$\mathrm{isc}^o_{ij,c} = \mathbf{F}\dot{\mathbf{T}}_i a^c_{ij}\,, \tag{7.7a}$$
$$\begin{aligned}\mathrm{isc}^\epsilon_{ij,c} = \mathbf{F}\dot{\mathbf{T}}_i \Big[&\dot{\mathbf{D}}_{ij}\dot{p}_{ji} - (\nu_0 + \mathbf{D}_{ij}\nu^o_{ji,c})\Big(\dot{H}_{ij} - \dot{\mathbf{D}}_{ij}\dot{N}^\Delta_{ji} - \dot{N}^\Delta_{ij} + \dot{N}^{\mathrm{ob}}_{\mathrm{isc}_{ij}\leftarrow ji}\Big) \\ &- \Big(\dot{p}_{ij} - (\nu_0 + \nu^o_{ij,c})\dot{N}^{\mathrm{ob}}_{\mathrm{isc}_{ij}\leftarrow ij}\Big) + \dot{N}^{\mathrm{ro}}_{\mathrm{isc}_{ij},c} - \frac{a^c_{ij}\dot{q}^\epsilon_i}{1+q^o_i}\Big]\,.\end{aligned} \tag{7.7b}$$

6 sideband-sideband beatnotes in the inter-spacecraft interferometers,

$$\mathrm{isc}^o_{ij,\mathrm{sb}} = \mathbf{F}\dot{\mathbf{T}}_i a^{\mathrm{sb}}_{ij}\,, \tag{7.8a}$$
$$\begin{aligned}\mathrm{isc}^\epsilon_{ij,\mathrm{sb}} = \mathbf{F}\dot{\mathbf{T}}_i \Big[&\dot{\mathbf{D}}_{ij}\big(\dot{p}_{ji} + \nu^m_{ji}[\dot{q}^\epsilon_j + \dot{M}_{ji}]\big) - \big(\dot{p}_{ij} + \nu^m_{ij}[\dot{q}^\epsilon_i + \dot{M}_{ij}]\big) \\ &- (\nu_0 + \mathbf{D}_{ij}\nu^o_{ji,\mathrm{sb}})\Big(\dot{H}_{ij} - \dot{\mathbf{D}}_{ij}\dot{N}^\Delta_{ji} - \dot{N}^\Delta_{ij} + \dot{N}^{\mathrm{ob}}_{\mathrm{isc}_{ij}\leftarrow ji}\Big) \\ &+ (\nu_0 + \nu^o_{ij,\mathrm{sb}})\dot{N}^{\mathrm{ob}}_{\mathrm{isc}_{ij}\leftarrow ji} + \dot{N}^{\mathrm{ro}}_{\mathrm{isc}_{ij},\mathrm{sb}} - \frac{a^{\mathrm{sb}}_{ij}\dot{q}^\epsilon_i}{1+q^o_i}\Big]\,.\end{aligned} \tag{7.8b}$$

6 carrier-carrier beatnotes in the reference interferometers,

$$\mathrm{ref}^o_{ij,c} = \mathbf{F}\dot{\mathbf{T}}_i b^c_{ij}\,, \tag{7.9a}$$
$$\begin{aligned}\mathrm{ref}^\epsilon_{ij,c} = \mathbf{F}\dot{\mathbf{T}}_i \Big[&(\dot{p}_{ik} - (\nu_0 + \nu^o_{ik,c})(\dot{N}^{\mathrm{bl}}_{ij} + \dot{N}^{\mathrm{ob}}_{\mathrm{ref}_{ij}\leftarrow ik})) \\ &- (\dot{p}_{ij} - (\nu_0 + \nu^o_{ij,c})\dot{N}^{\mathrm{ob}}_{\mathrm{ref}_{ij}\leftarrow ij}) + \dot{N}^{\mathrm{ro}}_{\mathrm{ref}_{ij},c} - \frac{b^c_{ij}\dot{q}^\epsilon_i}{1+q^o_i}\Big]\,.\end{aligned} \tag{7.9b}$$

6 sideband-sideband beatnotes in the reference interferometers,

$$\mathrm{ref}^o_{ij,\mathrm{sb}} = \mathbf{F}\dot{\mathbf{T}}_i b^{\mathrm{sb}}_{ij}\,, \tag{7.10a}$$
$$\begin{aligned}\mathrm{ref}^\epsilon_{ij,\mathrm{sb}} = \mathbf{F}\dot{\mathbf{T}}_i \Big[&(\dot{p}_{ik} + \nu^m_{ik}[\dot{q}_i + \dot{M}_{ik}] - (\nu_0 + \nu^o_{ik,\mathrm{sb}})(\dot{N}^{\mathrm{bl}}_{ij} + \dot{N}^{\mathrm{ob}}_{\mathrm{ref}_{ij}\leftarrow ik})) \\ &- (\dot{p}_{ij} + \nu^m_{ij}[\dot{q}_i + \dot{M}_{ij}] - (\nu_0 + \nu^o_{ij,\mathrm{sb}})\dot{N}^{\mathrm{ob}}_{\mathrm{ref}_{ij}\leftarrow ij}) \\ &+ \dot{N}^{\mathrm{ro}}_{\mathrm{ref}_{ij},\mathrm{sb}} - \frac{b^{\mathrm{sb}}_{ij}\dot{q}^\epsilon_i}{1+q^o_i}\Big]\,.\end{aligned} \tag{7.10b}$$

6 carrier-carrier beatnotes in the test-mass interferometers,

$$\mathrm{tm}^{o}_{ij,c} = \mathbf{F}\dot{\mathbf{T}}_i b^{c}_{ij}\,, \tag{7.11a}$$

$$\begin{aligned}\mathrm{tm}^{\epsilon}_{ij,c} = \mathbf{F}\dot{\mathbf{T}}_i \Big[&(\dot{p}_{ik} - (\nu_0 + \nu^{o}_{ik,c})(\dot{N}^{\mathrm{bl}}_{ij} + \dot{N}^{\mathrm{ob}}_{\mathrm{tm}_{ij}\leftarrow ik})) \\ &- (\dot{p}_{ij} - (\nu_0 + \nu^{o}_{ij,c})(2(N^{\Delta}_{ij} - N^{\delta}_{ij}) + N^{\mathrm{ob}}_{tm_{ij}\leftarrow ij}(\tau))) \\ &+ \dot{N}^{\mathrm{ro}}_{\mathrm{tm}_{ij},c} - \frac{b^{c}_{ij}\dot{q}^{\epsilon}_{i}}{1+q^{o}_{i}}\Big]\,.\end{aligned} \tag{7.11b}$$

6 MPRs,

$$R_{ij} = \mathbf{FT}_i\left[d^{o}_{ij} - (\mathbf{D}_{ij}\delta\hat{\tau}_j - \delta\hat{\tau}_i) + N^{R}_{ij}\right]. \tag{7.12}$$

7.2.1 *Output in total frequency*

In reality, we will not have access to the two beatnote components, but only the total phase or the total frequency. The simulation accounts for that by providing an additional output variable for each interferometer.

It is generated by first computing the photodiode signals in the usual two-variable decomposition, $\nu^{o}_{\mathrm{PD,ij}}, \nu^{\epsilon}_{\mathrm{PD,ij}}$, as described in chapter 5. These are then added to compute the total frequency of the photodiode signal,

$$\nu_{\mathrm{PD,ij}} = \nu^{o}_{\mathrm{PD,ij}} + \nu^{\epsilon}_{\mathrm{PD,ij}}\,. \tag{7.13}$$

We then apply eq. (6.20) to directly resample this total frequency, using the total clock error q_i. This means we perform no first-order expansion of the clock errors for this case.

The resulting variable is then filtered and downsampled as described in section 7.1. This is done to include any numerical artifacts the FIR filter might introduce into the frequency variable.

7.3 FREQUENCY MANAGEMENT

As discussed in section 3.6.2, all beatnote frequencies in LISA are controlled to fall in a range between 5 MHz and 25 MHz[1].

The problem of finding such frequency plans has recently been studied in [46], and exact solutions have been found. We will use these solutions as an input to the simulation.

In this section, we describe how we simulate the laser locking control loop in section 7.3.1. We then list the frequency locking schemes available for LISA in its baseline configuration in section 7.3.2.

1 The exact frequency range remains to be defined. In addition, some margins are required for both the upper and lower bounds to account for the sideband beatnotes, which are offset by 1 MHz from the carrier beatnotes.

7.3.1 *Laser locking*

Laser locking is achieved by controlling the frequency of a laser such that a given beatnote frequency $\nu_{\mathrm{PD}}(\tau)$ remains equal to a pre-programmed reference value $\nu_{\mathrm{PD},r}(\tau)$. We do not simulate the actual control loop here, but instead directly compute the correct offsets and fluctuations of the locked laser for the locking condition to be satisfied. We perform this simulation in the TPS.

We consider the frequency lock to be perfect[2]. This means that the locking beatnote offset is exactly equal to the desired value, and the locked lasers fluctuations are chosen in such a way that they exactly cancel the fluctuations in the beatnote signal.

This is true with respect to the local clock in the THE, the frequency in the TPS will be different from the desired value!

In terms of phase, the result of this control is that the measured beatnote phase $\Phi_{\mathrm{PD}}(\tau)$ is controlled to be exactly equal to a pre-programmed reference value $\Phi_{\mathrm{PD},r}(\tau)$. The locked lasers phase drifts and fluctuations are given as

$$\phi_l^o(\tau) \quad \text{and} \quad \phi_l^\epsilon(\tau)\,, \tag{7.14}$$

while those of the reference laser are

$$\phi_r^o(\tau) \quad \text{and} \quad \phi_r^\epsilon(\tau)\,. \tag{7.15}$$

The locking condition is derived by solving

$$\phi_{\mathrm{PD}}^{\tau_i,o}(\tau) = \phi_{\mathrm{PD},r}^{\tau_i,o}(\tau) \quad \text{and} \quad \phi_{\mathrm{PD}}^{\tau_i,\epsilon}(\tau) = \phi_{\mathrm{PD},r}^{\tau_i,\epsilon}(\tau)\,. \tag{7.16}$$

The laser control loop operates on data delivered by the phasemeter at a high frequency of 80 MHz[3]. As such, we simulate the locking before applying any filtering or downsampling.

As explained in section 5.4.2, the phasemeter treats all frequencies as positive. The sign of the beatnote contains the information about which of the two lasers has the higher frequency, such that it is an essential information for the control loop to work properly. Fortunately, it is possible to determine the beatnote polarity by actuating the locked laser with a known frequency offset and observing the change in the beatnote.

We can there assume that the beatnote polarity is known at all times, and model the photodiode signals total phase without it, as

$$\Phi_{\mathrm{PD}}(\tau) = \Phi_r(\tau) - \Phi_l(\tau)\,. \tag{7.17}$$

We end up with photodiode signals as given in section 5.6, including readout noise terms,

$$\phi_{\mathrm{PD}}^o(\tau) = \phi_r^o(\tau) - \phi_l^o(\tau)\,, \tag{7.18}$$
$$\phi_{\mathrm{PD}}^\epsilon(\tau) = \phi_r^\epsilon(\tau) - \phi_l^\epsilon(\tau) + N_{\mathrm{PD}}^{\mathrm{ro}}(\tau)\,, \tag{7.19}$$

2 In reality, the locking control loops will have finite gain and bandwidth, such that the locking beatnotes can still contain out-of-band glitches and noise residuals.

3 K. Yamamoto, AEI phasemeter team, personal communication May 2021.

The reference signal $\phi^{\tau_i}_{\mathrm{PD},r}(\tau)$ is determined by the phasemeter clock, which is derived from the onboard USO (see section 6.1.1), such that it is a perfect phase ramp at the desired beatnote frequency $\nu_{\mathrm{PD},r}$ when expressed in the THE. Our control loop is simulated in the TPS, and using eqs. (6.5) and (A.5), we obtain

$$\phi^{\tau_i}_{\mathrm{PD},r}(\tau) = \phi^{\hat{\tau}_i}_{\mathrm{PD},r}(\hat{\tau}_i(\tau)) = \nu_{\mathrm{PD},r}(\tau + q_i(\tau))\,. \tag{7.20}$$

We decompose this into large phase drifts and small fluctuations,

$$\phi^{\tau_i,o}_{\mathrm{PD},r}(\tau) = \nu_{\mathrm{PD},r}(\tau + q^o_i(\tau)) \quad \text{and} \quad \phi^{\tau_i,\epsilon}_{\mathrm{PD},r}(\tau) = \nu_{\mathrm{PD},r} q^\epsilon_i(\tau)\,. \tag{7.21}$$

Substituting eq. (7.21) in eqs. (7.18) and (7.19), we find the locked laser phase drifts and fluctuations

$$\phi^o_l(\tau) = \phi^o_r(\tau) - \nu_{\mathrm{PD},r}(\tau + q^o_i(\tau))\,, \tag{7.22}$$
$$\phi^\epsilon_l(\tau) = \phi^\epsilon_r(\tau) - \nu_{\mathrm{PD},r} q^\epsilon_i(\tau) + N^{\mathrm{ro}}_{\mathrm{PD}}(\tau)\,. \tag{7.23}$$

Taking the derivative of these equations yields equivalent expressions in frequency,

$$\nu^o_l(\tau) = \nu^o_r(\tau) - \nu_{\mathrm{PD},r}(1 + \dot{q}^o_i(\tau))\,, \tag{7.24}$$
$$\nu^\epsilon_l(\tau) = \nu^\epsilon_r(\tau) - \nu_{\mathrm{PD},r}\dot{q}^\epsilon_i(\tau) + \dot{N}^{\mathrm{ro}}_{\mathrm{PD}}(\tau)\,. \tag{7.25}$$

Note that these equations describe the locked laser *at the photodiode*. To properly simulate this effect, we need the locked lasers frequency *at the source*, which we denote here as $\bar{\nu}_l(\tau)$. We recall from eq. (5.57b) that we subtract a noise term $n_{B\leftarrow A}(\tau)$ from the fluctuations during propagation, such that we have

$$\begin{aligned}\bar{\nu}^\epsilon_l(\tau) &= \nu^\epsilon_l(\tau) + (\nu_0 + \nu^o_l(\tau))n_{B\leftarrow A}(\tau) \\ &= \nu^\epsilon_r(\tau) - \nu_{\mathrm{PD},r}\dot{q}^\epsilon_i(\tau) + \dot{N}^{\mathrm{ro}}_{\mathrm{PD}}(\tau) \\ &\quad + (\nu_0 + \nu^o_l(\tau))n_{B\leftarrow A}(\tau)\end{aligned} \tag{7.26}$$

for the locked lasers fluctuations at the source.

Note that in the current version of the code, we do not use the desired beatnote frequencies as input, but use the desired offset with respect to the primary laser instead. Inspecting eq. (7.24), we see that the two are simply related by a sign. This will be changed in a future version in order to allow an easier interface to the frequency plans provided in [46], which are formulated in terms of desired beatnote frequency.

7.3.2 *Locking configurations*

In total, 5 of the 6 lasers in the constellation will be locked (directly or indirectly) to one primary laser. Each of the locked lasers is locked to either

Configuration	LA 12	LA 23	LA 31	LA 13	LA 32	LA 21
N1-LA12	Primary	Local	Distant	Local	Local	Distant
N2-LA12	Primary	Local	Distant	Local	Distant	Distant
N3-LA12	Primary	Local	Local	Local	Distant	Distant
N4-LA12	Primary	Distant	Distant	Local	Local	Distant
N5-LA12	Primary	Distant	Distant	Local	Local	Local
N6-LA12	Primary	Local	Local	Distant	Distant	Distant

TABLE 7.1: Definition of 6 fundamental locking configurations, with laser 12 as primary laser

- the adjacent laser, using the reference interferometer, so that eqs. (7.24) and (7.26) read

$$O_{ij}(\tau) = \nu^{o}_{\mathrm{ref}_{ij}\leftarrow ik}(\tau) - \nu_{\mathrm{ref}_{ij},r}(1+\dot{q}^{o}_{i}(\tau))\,, \tag{7.27a}$$

$$\begin{aligned} p_{ij}(\tau) = {} & \nu^{\epsilon}_{\mathrm{ref}_{ij}\leftarrow ik}(\tau) - \nu_{\mathrm{ref}_{ij},r}\dot{q}^{\epsilon}_{i}(\tau) + \dot{N}^{\mathrm{ro}}_{\mathrm{ref}_{ij}}(\tau) \\ & + (\nu_0 + O_{ij}(\tau))\dot{N}^{\mathrm{ob}}_{\mathrm{ref}_{ij}\leftarrow ij}\,, \end{aligned} \tag{7.27b}$$

- or to the distant laser, using the inter-spacecraft interferometer, such that we get

$$O_{ij}(\tau) = \nu^{o}_{\mathrm{isc}_{ij}\leftarrow ji}(\tau) - \nu_{\mathrm{isc}_{ij},r}(1+\dot{q}^{o}_{i}(\tau))\,, \tag{7.28a}$$

$$\begin{aligned} p_{ij}(\tau) = {} & \nu^{\epsilon}_{\mathrm{isc}_{ij}\leftarrow ji}(\tau) - \nu_{\mathrm{isc}_{ij},r}\dot{q}^{\epsilon}_{i}(\tau) + \dot{N}^{\mathrm{ro}}_{\mathrm{isc}_{ij}}(\tau) \\ & + (\nu_0 + O_{ij}(\tau))\dot{N}^{\mathrm{ob}}_{\mathrm{isc}_{ij}\leftarrow ij}\,, \end{aligned} \tag{7.28b}$$

where the index k is again chosen such that the whole set fullfils $\{i,j,k\} = 1,2,3$.

These expressions can be substituted into the phasemeter equations in section 7.2 to derive the phasemeter signals with locked lasers.

As discussed in [46], there are 6 distinct non-swapping locking topologies. For each of them, we have the freedom to choose the primary laser, such that, in total, we have 36 possible locking configurations. We give the locking conditions for the 6 configurations with laser 12 as the primary laser in table 7.1. The other 30 combinations can be deduced by applying permutations of the indices, as described in appendix A.1.

Notice that we use a different notation for the locking configuration than what is proposed in [46]. We ordered the different configurations first by considering the length of consecutive laser locks, and second by favoring those for which the adjacent lasers on the same spacecraft are locked together.

The two notations are related in table 7.2.

Conf.	In [46]
N1	N1c
N2	N2b
N3	N1a
N4	N2c
N5	N1b
N6	N2a

TABLE 7.2: Notation in this thesis converted to the one used in [46].

7.4 TELEMETRY

The data produced by the phasemeters will be packaged and telemetered to the European Space Tracking (ESTRACK) ground stations. We currently do

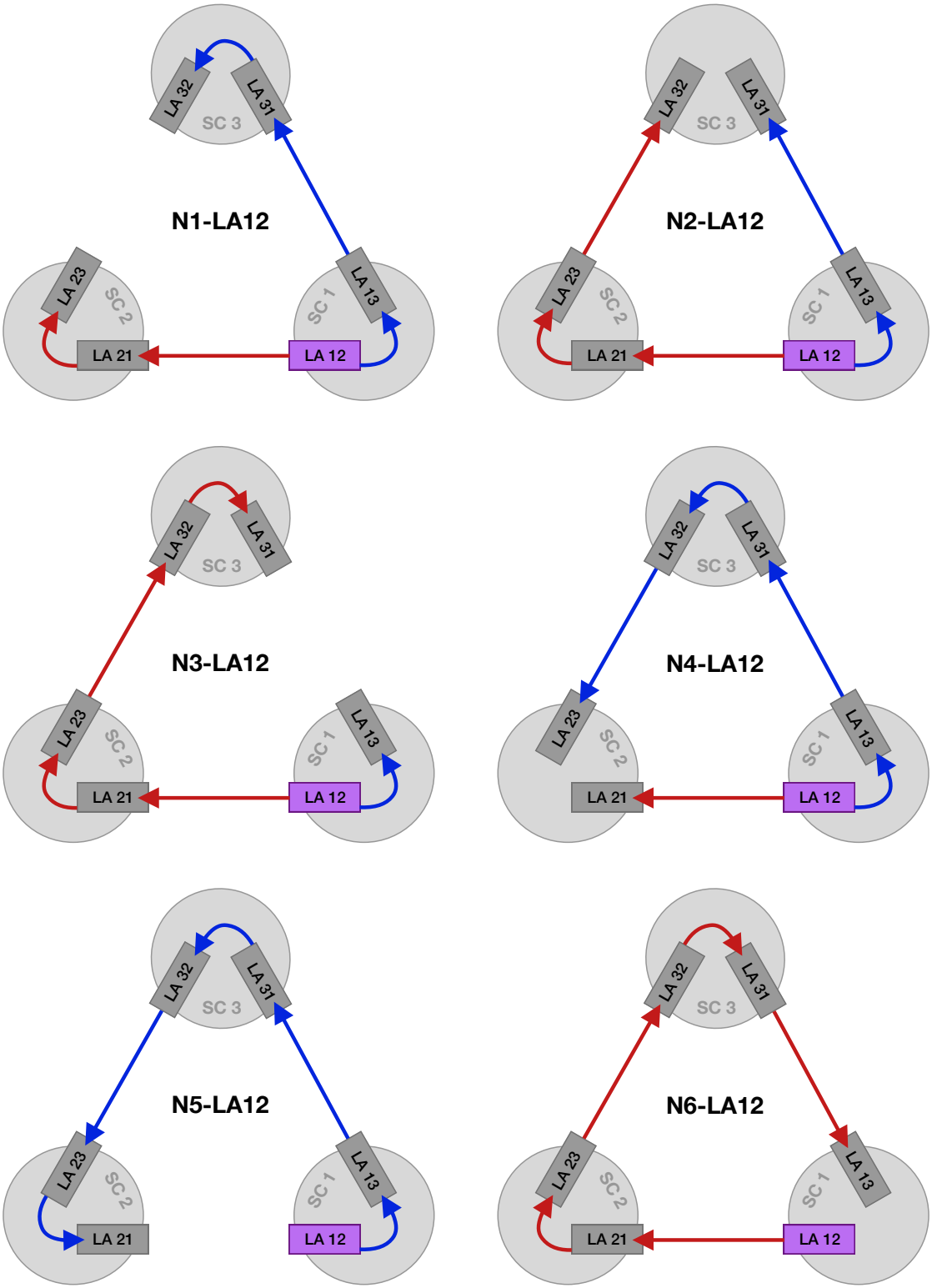

FIGURE 7.2: Laser locking configurations for LA 12 as the primary laser, from [16].

not simulate any artefacts due to this process. Instead, our simulation products match exactly to the phasemeter signals described in section 7.2.

In addition to facilitating the data downlink, contact to ground stations will also allow estimation of the offsets of the THEs to the respective TPS. This could be achieved using a similar scheme to that used in Global Astrometric Interferometer for Astrophysics (GAIA) [53], although the details for how this will be done for LISA are not finalized at the time of writing of this thesis.

We do not simulate this procedure in detail, but give a high-level model by providing the deviations of the THEs to the respective TPS as an additional output. This estimate carries a noise term accounting for the expected uncertainty achievable from such a ground-based time comparison, tentatively set to a standard deviation of 1 ms. Note that we do not include the synchronization to TCB in the data processing described in part iii, and thus do not further consider this measurement.

8

SIMULATION RESULTS

We present here first results of our simulations, performed using `LISANode`.

We first discuss our simulation parameters in section 8.1, and show time-domain plots of the simulated data streams. We then discuss the residual noise levels observed in the different interferometers in section 8.2, and finally conclude in section 8.3 by summarizing the available measurements.

As mentioned in section 4.2, `LISANode` is a rapidly evolving project with multiple contributors. At the time of writing of this thesis, not all effects described above are fully implemented in the simulation.

And many more are under development which are not described above!

The main differences at the time of writing are:

- The additional coupling of pathlength noises to laser frequency offsets (cf. eq. (5.52b)) are not included. Instead, all pathlength noises are scaled by only the central laser frequency ν_0.
- Frequency fluctuations are output renormalized by the the central laser frequency ν_0 and multiplied by the beatnote polarity described in section 5.4.2. Frequency offsets are output in units of MHz.
- Spacecraft jitter $N_{ij}^{\Delta}(\tau)$ described in sections 5.5.2.3 and 5.5.3 is not simulated.
- Modulation noise terms described in section 6.1.2 have the same level for right- and lefthanded optical benches, neglecting the effect of the frequency conversion chain from the pilot tone to the 2.401 GHz sideband.
- Laser locking is implemented as described in section 7.3, but there is no interface for a time-varying frequency plan for the full mission duration as those shown in section 3.6.2. Instead, all relative offset frequencies are set to fixed linear ramps at the beginning of the simulation.
- The simulation includes some additional minor optical pathlength noise terms we neglected in section 5.5 for clarity.

8.1 SIMULATION PARAMETERS

We give here results for the simulation. We enable all noises described above, but include no gravitational wave signal. We simulate 10^6 s, using delays computed from the ESA provided orbits shown in fig. 3.3. Lasers are locked in the laser locking scheme `N1-LA12` (cf. section 7.3) with frequency offsets set to the starting values of the frequency plan shown in fig. 3.9. The simulation

With the exception of spacecraft jitter N_{ij}^{Δ}, which is not yet included in the simulation.

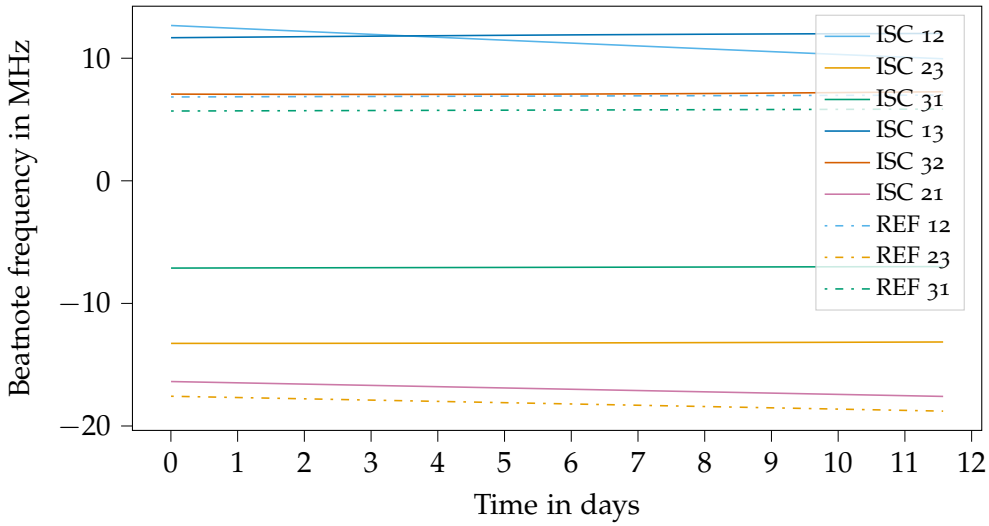

FIGURE 8.1: Simulated total beatnote frequencies.

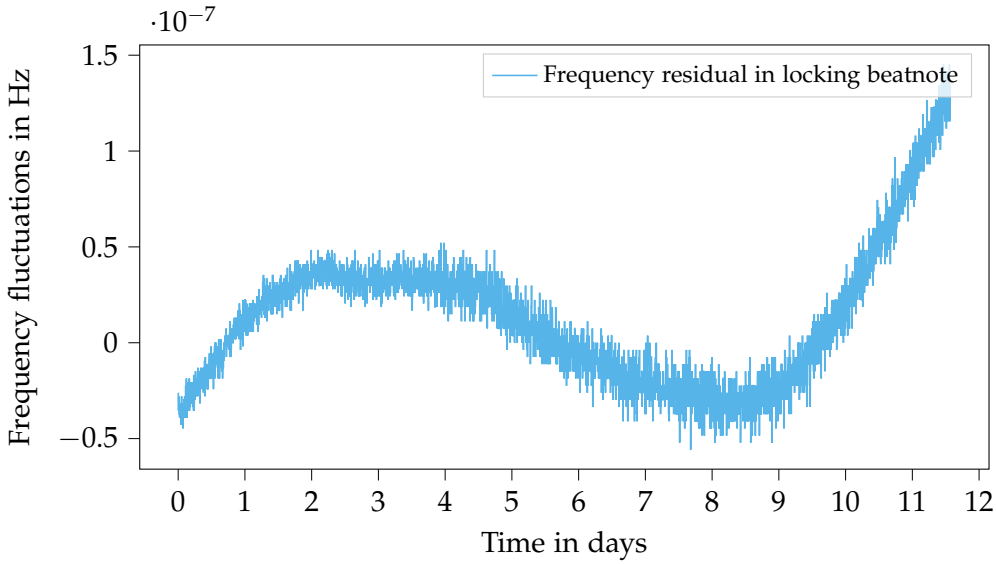

FIGURE 8.2: Residual noise in a locking beatnote after detrending. We are limited by numerical artifacts.

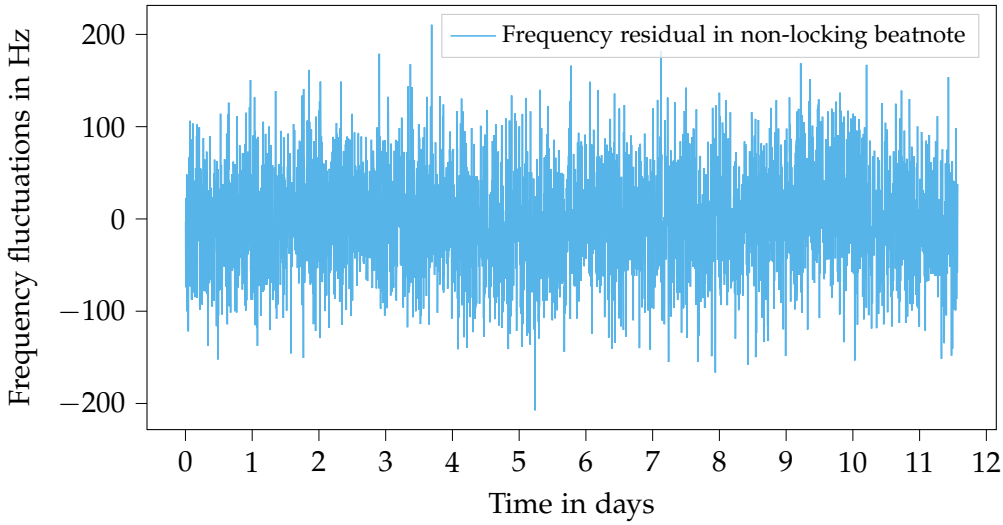

FIGURE 8.3: Residual noise in a non-locking ISC beatnote after detrending. We are limited by laser frequency noise.

took 24 min on a single desktop CPU core[1], which is ≈ 700 times faster than real-time.

We analyze the output in total frequency, to which we apply a third order polynomial least-square fit to remove large trends. Figure 8.1 shows the total frequency before the fit, while Figure 8.2 and Figure 8.3 show the post-fit residuals for a locking and a non-locking ISC beatnote, respectively.

As expected, the non-locking beatnotes carry large frequency fluctuations due to unsuppressed laser frequency noise. The locking beatnotes residuals, on the other hand, appear to be dominated by numerical noise and a residual trend after the polynomial fit.

8.2 NOISE LEVELS

We estimate PSDs using the log-scale power spectral density (LPSD) method described in [89][2].

We overlay all plots with a 10 pm noise allocation curve, which is a typical target noise level for a single link in LISA [10]. It is given in units of frequency as

$$\sqrt{S_{\mathrm{IFO}}}(f) = \frac{2\pi f}{1064\,\mathrm{nm}} \cdot \frac{10\,\mathrm{pm}}{\sqrt{\mathrm{Hz}}} \cdot \sqrt{1 + \left(\frac{2\,\mathrm{mHz}}{f}\right)^4} \tag{8.1}$$

8.2.1 *Non-locking ISC interferometer*

We show in fig. 8.4 the noise level in a non-locking ISC interferometer, isc_{12}. We observe that it is dominated by laser noise.

We can derive a simple model for the residual noise level by considering only laser noise in eqs. (7.7b) and (7.28b), which yields

$$\mathrm{isc}^{\epsilon}_{12} \approx \mathbf{D}_{12}\mathbf{D}_{21}\dot{p}_{12} - \dot{p}_{12}\,, \tag{8.2}$$

where $\dot{p}_{12}$ is the laser noise of the primary laser, whose noise level is shown in grey in fig. 8.4. The PSD can be estimated to be proportional to the squared magnitude of the fourier transform (cf. appendix C for more information PSD estimation), which gives

$$\begin{aligned} \left|\mathcal{F}\left[\mathrm{isc}^{\epsilon}_{12}\right]\right|^2(f) &\approx \left|(e^{i2\pi(d^o_{12}+d^o_{21})f} - 1)\mathcal{F}\left[\dot{p}_{12}\right](f)\right|^2 \\ &\approx 4\sin^2(2\pi f d)\left|\mathcal{F}\left[\dot{p}_{12}\right](f)\right|^2\,, \end{aligned} \tag{8.3}$$

where d is the average arm length in seconds. We overlay this model with our simulated data in fig. 8.4, which shows perfect agreement.

1 This is with the highest level of C++ compiler optimizations (`-O3`), on a Linux workstation equipped with an AMD Ryzen 3700x. Compilation took an additional 2 min 5 s.

2 We use a python implementation of this method developed by C. Vorndamme at AEI, with the following parameters: `olap="default", bmin=1, Lmin=0, Jdes=2000, Kdes=1000, order=-1, win=np.kaiser, psll=300`.

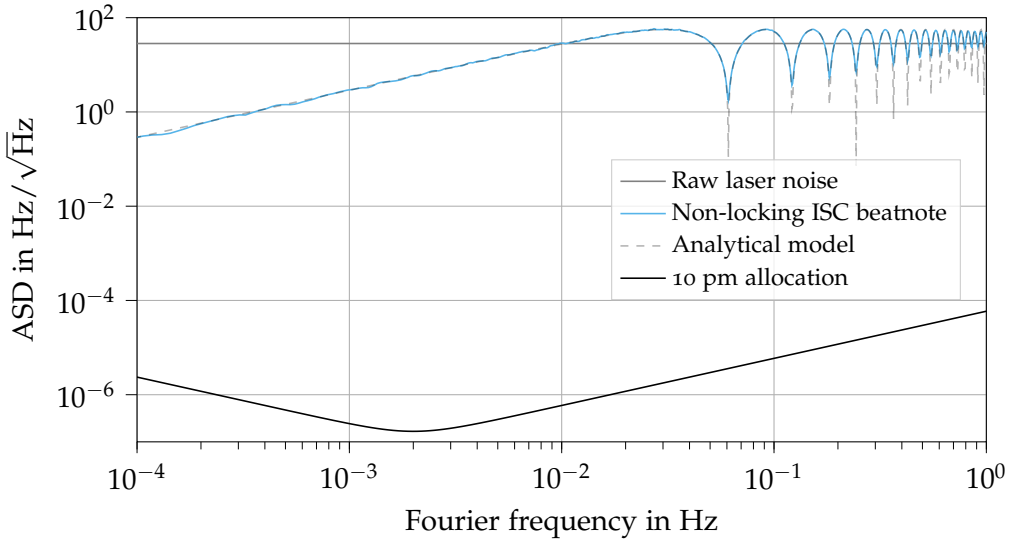

FIGURE 8.4: Residual noise in a non-locking ISC beatnote. Laser frequency noise is modulated by the roundtrip light travel time.

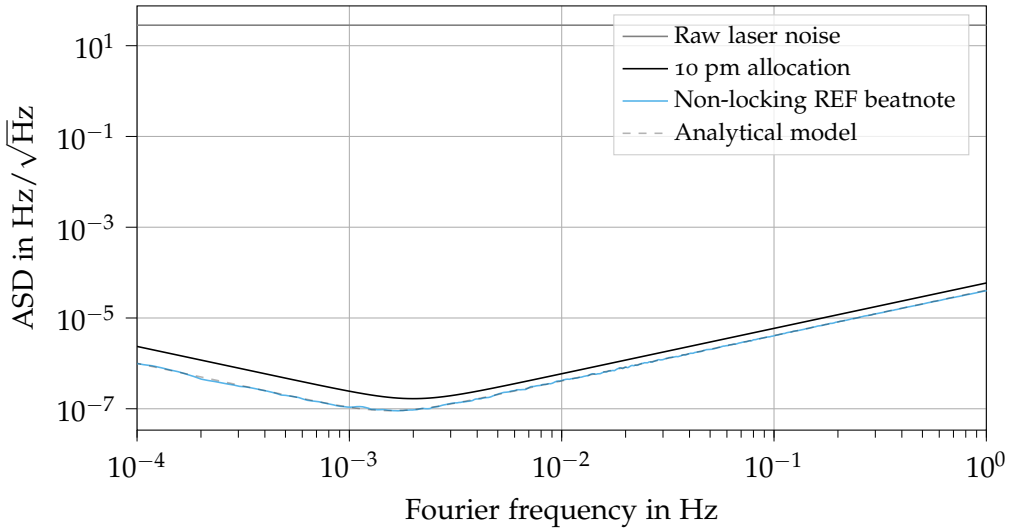

FIGURE 8.5: Residual noise in a non-locking reference beatnote. Non-common noises with the locking adjacent reference interferometer are visible.

8.2.2 *Non-locking REF interferometer*

We show in fig. 8.5 the noise level in a non-locking reference interferometer, ref_{12}.

In our locking scheme N1, one of the two reference interferometers on each spacecraft is always used for locking, such that all noise is cancelled in the adjacent ref_{13}. Since both reference interferometers on the same spacecraft interfere the same lasers, any common noise between ref_{13} and ref_{12} will be cancelled in both interferometers. This applies for example to laser frequency noise, but not to noise sources unique to the two reference interferometers.

Inspecting fig. 8.5, we observe a colored noise which can be explained by these non-common noise sources, which in our model are optical pathlength noise (cf. appendix D.6), backlink noise (cf. appendix D.4), and readout noise (cf. appendix D.5). We can add up the PSDs for these noise terms in both

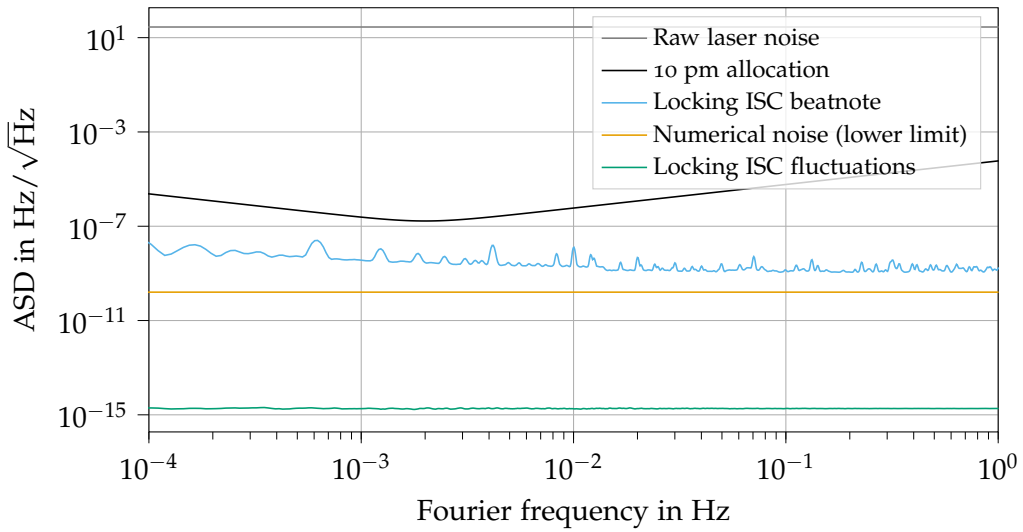

FIGURE 8.6: Residual noise in locking beatnote. We are limited by numerical effects. Simulating just fluctuations allows for a significantly lower numerical noise floor.

interferometers to explain the observed noise floor. Note that this includes a factor $\sqrt{2}$ to account for non-common noise terms in *both* interferometers, which due to the laser locking condition are both transferred to ref_{12}.

This estimate is only valid for locking configurations N1, N3 and N5, which use one reference interferometer per spacecraft for locking. In configurations N2, N4 and N6, on the other hand, we expect a laser noise dominated residual for one of the reference beatnotes, similar to that described in section 8.2.1.

8.2.3 *Locking interferometer*

Since we model a perfect frequency lock in section 7.3, we would expect no noise in the locking beatnotes. In practice, the noise level will be limited by numerical effects, such as the limited dynamic range of our variables. We can give a rough estimate for a lower limit of the expected numerical quantization noise by estimating the least significant bit of a double precision variable as

$$\mathrm{LSB} = 1.1 \times 10^{-16} \times \mathrm{Mag}\,, \tag{8.4}$$

where Mag is the magnitude of the variable. Mag is given in our case as the value of the respective beatnote frequency before detrending, so around 10 MHz. Following [50], numerical quantization noise causes a white noise at the level

$$\sqrt{S_{\mathrm{LSB}}}(f) = \frac{\mathrm{LSB}}{\sqrt{6 f_s}}\,. \tag{8.5}$$

We show in fig. 8.4 the noise level in a locking interferometer, isc_{31}. We observe that our noise floor is not perfectly white, and is about one order of magnitude above the lower limit derived above.

Since the shift to THE, all onboard filtering as well as the polynomial detrending was performed on this variable in total frequency, we would expect some

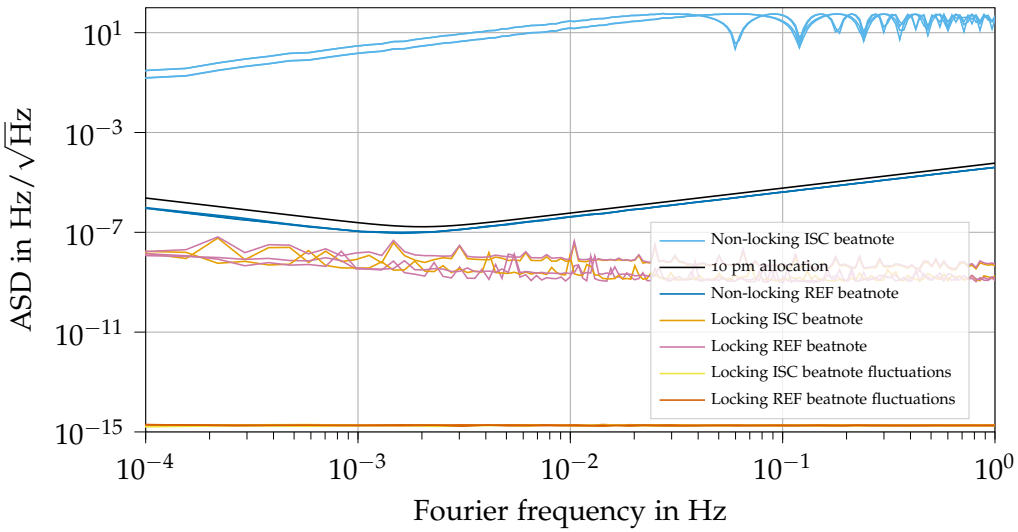

FIGURE 8.7: Residual noise in all beatnotes. Non-locking ISC beatnotes contain modulated laser noise, while non-locking reference beatnotes contain only secondary noises. All locking beatnotes are plotted using both the total frequency and the fluctuations, which shows that the residual noise level is due to numerical effects.

accumulation of numerical errors, which can explain this increased noise level.

Overall, the noise is more than a factor ten below the 10 pm allocation, such that we are confident the simulated variables can be used for data analysis studies.

To verify that our locking conditions are implemented correctly, we also overlay the PSD computed from the variable containing just the frequency fluctuations, as described in section 4.3.2. We see that we get a white noise floor at $2 \times 10^{-15}\,\mathrm{Hz}/\sqrt{\mathrm{Hz}}$, many orders of magnitude below the required levels.

8.3 SUMMARY

We plot in fig. 8.7 an overview of the noise level in all ISC and reference beatnotes. We show the locking beatnotes using both the total frequency and just the frequency fluctuations, allowing a significantly reduced noise floor.

We see that all beatnotes can be grouped into the three classes described above:

- Non-locking ISC beatnotes, dominated by laser noise,
- Non-locking reference beatnotes, dominated by secondary noises, and
- Locking beatnotes, dominated by numerical noise, which is significantly reduced when using just the frequency fluctuations.

With locking schemes N2, N4 and N6, some of the GW signal will also be visible in the non-locking reference beatnotes, but again buried by un-suppressed laser noise.

The non-locking beatnotes would contain our gravitational wave signal. It is buried below roughly 8 order of magnitudes of laser frequency noise, such that these raw data streams are not usable for extracting GW signals.

We will study how to suppress this overwhelmingly large LFN - as well as other noise sources - in part iii.

Part III

INITIAL NOISE REDUCTION PIPELINE FOR LISA

9

THE INITIAL NOISE REDUCTION PIPELINE

As was shown at the end of part ii, the raw measurements are not directly usable for GW detection. The primary reason for this is the presence of overwhelming amounts of laser frequency noise in the non-locking beatnotes, which exceeds the level expected from GWs by several orders of magnitude.

Although laser noise is certainly the most dominant noise source in LISA, it is not the only one. Several other effects need to be subtracted using ancillary measurements, most notably longitudinal spacecraft jitter along the sensitive axis, tilt-to-length (TTL) couplings due to angular jitters, and clock noise. And the main laser noise suppression step of TDI itself requires as input time series of delays, which need to be recovered from the noisy onboard ranging measurements described in section 6.3.

In addition, the treated data has to be transformed to a global time scale such as the Barycentric Coordinate Time (TCB) to allow for multi-messenger observation and accurate modelling of the source parameters.

Multi-messenger astronomy refers to the simultaneous observation of astrophysical events using different effects, such as GWs, EM radiation, neutrinos or cosmic rays.

These processing steps are summarized under the name initial noise-reduction pipeline (INREP). Its input are the raw measurements as they are produced and telemetered by the three satellites, called level 0 (L0) data, and the output are variables allowing direct extraction of gravitational wave signals in the astrophysical data analysis, called level 1 (L1) data[1].

9.1 THE INREP PROCESSING ELEMENTS

Many of the processing steps of the full INREP are currently still being developed inside LDPG, and some of them allow multiple alternatives which need to be carefully studied and evaluated against each other.

We give below an overview over *one* possible version of the INREP, which we will show can sufficiently suppress the two limiting noise sources included in the simulated data presented in chapter 8, laser frequency noise and clock noise. These simulation results are shown in section 9.2. We include a processing step to remove longitudinal spacecraft jitter for completeness, even though this noise source it is not included in the simulated data.

1 The full LISA data processing chain is still being developed, and might include additional processing elements operating in-between L0, INREP and L1. For the scope of this thesis, we will use L0 synonymous with the simulated data presented at the end of chapter 8, and do not consider any additional processing steps except those described below.

Finally, we mention TTL subtraction and synchronization to TCB as final processing steps. Their detailed development is beyond the scope of this thesis.

9.1.1 *Initial data treatment*

As outlined in chapter 8, the raw data of the interferometric measurements received from the spacecraft will be given either as total phase or alternatively as total frequency. See appendix C.1.2 for the definition of these quantities.

At the time of writing this thesis, the actual raw data format is not yet decided. The data will be expressed in a format optimized for transmitting it to earth, and needs to be converted to physical units in a first processing step[2].

For the purpose of this thesis, we will assume that this conversion has already happend, and that we get data in physical units. Matching the output of our simulation, we will assume all data to be given as total frequency, in Hz. We will further assume that all variables are given as double precision floating point variables, which is in line with the options currently being evaluated as part of the phasemeter prototyping performed at the AEI[2].

As we already saw in chapter 8, it can be beneficial (or even necessary) to remove large trends from the data even for simple data analysis steps such as spectral estimation.

In addition, as we will see in chapter 13, some of the main noise suppression steps need adjustment depending on if one uses the total frequency or just the residual after large trends have been removed.

For these reasons, we will include a processing element to perform this kind of decomposition, similar to what we already described in chapter 8. The result will be two variables for each measurement, whose information content is modelled by the phasemeter equations given in section 7.2, plus a significant numerical noise in the fluctuations. As we saw in chapter 8, this additional noise is at a level which should not affect our final results.

9.1.2 *Ranging noise reduction*

As we will see in chapter 13, one option to perform the TDI processing is to directly combine the data streams provided by the different spacecraft with delays containing both the physical light travel time as well as the offsets between the spacecraft clocks.

Such measurements are directly given by the measured pseudo-range (MPR) described in section 6.3, with the caveat that these carry an unacceptably high level of measurement noise. This ranging noise can be significantly reduced by combining the PRN measurement with the sideband measurements, as we will describe in section 13.4.

2 G. Heinzel, personal communication, 2021.

A simpler alternative is to just apply a polynomial fit to the measured ranging data, removing any in-band random fluctuations. This has the disadvantage of also removing in-band clock fluctuations, which should be included in the MPR. We chose this option for the data shown below, since it is sufficient to suppress laser noise below the requirements.

Another problem which can arise is that the measured ranges can suffer from a constant systematic bias, for example due to processing- or cable transmission delays. Ideally, such delays would be modelled and measured on-ground, such that they can be compensated for in a simple calibration step. Any remaining biases can be found and removed by estimating the optimal delays to be applied in TDI using TDI-ranging [87].

This procedure is beyond the scope of the thesis, and we will not include any constant bias in our ranging data. Nevertheless, we will give a model for how a constant bias couples into TDI in section 12.3.2.1.

9.1.3 *Removal of spacecraft jitter and reduction to three lasers*

As described in section 12.1, the first major noise removal step is to combine the ISC measurements with the reference and test-mass interferometer measurements to construct a virtual test-mass to test-mass measurement for each of the six laser links, with one laser per spacecraft.

We remark that this step is not strictly required for the simulated data set described in chapter 8: we do not simulate spacecraft jitter, and we used a locking scheme which already removes the frequency fluctuations of one of the two lasers on each spacecraft. However, it will be required in the final mission, so we will include this processing step for completeness.

9.1.4 *Time delay interferometry*

TDI is the main laser noise reduction step, and the main topic discussed in part iii of this thesis. Its goal is to combine the raw measurements described in chapter 7 to construct virtual equal arm interferometers in which laser noise is suppressed by many orders of magnitude.

We will introduce the basic principles of TDI in chapter 10. The result of TDI are timeseries of synthesized interferometer measurements, which suppresses laser noise below the requirements.

As we will discuss in chapter 11, there is a large space of possible TDI variables, all reducing laser noise to the same level given realistic orbits. We show results of a numerical search for variables of so-called second generation TDI, similar to those previously presented in the literature [92, 63], where we identify additional variables of 14 links missing in those references. We will also discuss the relationship between these different variables, as well as their information content, in section 11.5.1.

Following this work on the fundamentals of TDI, we move to more practical considerations in chapter 12. In particular, we discuss how the intermediary variables free of longitudinal spacecraft motion are constructed, and how to estimate the residual noise levels observed in the final TDI variables.

9.1.5 *Clock noise correction*

Cf. section 13.4.1 for the alternative using the total frequency

Assuming that the main TDI processing is performed using just frequency fluctuations, in-band clock noise will not be suppressed in the resulting variable, and needs to be removed in an additional processing step.

We will describe a generic algorithm for how to apply this clock correcion to almost any TDI variable in section 13.3, and discuss the limiting effects and residual clock noise levels.

9.1.6 *TTL subtraction*

E.g., due to misaligned optical components or movements of the test-masses or spacecraft.

Another noise source potentially being reduced in the INREP is tilt-to-length (TTL) coupling. TTL describes any coupling of the angular tilt of the laser beams into the longitudinal pathlength readout. TTL coupling has been observed in both LISA Pathfinder [97] and GRACE-FO [77], and it is expected to also be major noise source for LISA.

Optimal strategies for mitigating the impact of TTL coupling are currently being studied inside the LISA consortium, and their details are beyond the scope of this thesis. These can include pre-flight and in-flight hardware calibrations, as well as subtraction of residual TTL noise in post-processing using a readout of the beam angles via DWS. This offline correction could be performed as an additional processing after the main TDI variable is constructed, similar in principle to the clock noise correction described above.

A major challenge in subtracting TTL noise in post processing in LISA is determining the coupling coefficient for how a given beam tilt couples into the phase readout. Contrary to LISA Pathfinder, the raw measurements of LISA will be covered by laser frequency noise, which has to be reduced by TDI before the errors due to TTL coupling become apparent. Any calibration procedures to determine the coupling coefficients therefore have to operate on the TDI output, which contains a linear combination of many delayed measurements in which multiple coupling coefficients enter.

For more details, see [35, 52].

9.1.7 *Reference frame conversion*

Using the processing steps described above, the TDI variables produced are given in the time frame of the three independent spacecraft clocks.

The final TDI variables are needed in a global reference frame, like TCB, to facilitate the astrophysical data analysis. We briefly discuss how this could be achieved using a combination of the on-board measurements with on-ground observations in a Kalman-like optimal filter in section 13.5, but the detailed development of this algorithm is ongoing and outside the scope of this thesis.

9.2 SIMULATION RESULTS

We show here that the pipeline described above is able to remove all dominant noise sources included in our simulation. In summary, we perform the following processing steps on the simulated data presented in chapter 8:

We perform the polynomial detrending of the interferometric beatnotes as described in section 8.1. We then apply a fourth order polynomial fit to the MPRs, to recover a time series of delays free of in-band noise.

We then construct the intermediary variables η_{ij} as described in section 12.1, using the fit-residual of the beatnotes as input. These are used to compute the second generation Michelson variables X_2, Y_2 and Z_2, given in section 10.2. They are still dominated by clock noise, which we remove in the additional processing step derived in section 13.3.

We show in fig. 9.1 only the result for X_2. The other two variables arrive at the same final noise level, given by the secondary noises.

The residual is then well explained by the dominant secondary noise sources included in our simulation, which are test-mass acceleration noise at low frequency, and readout noise at high frequencies. We overlay the expected noise level as described in section 12.2.2, which agrees well with our simulation result.

It is important to point out we still neglect some processing steps, as described above:

- We do not simulate any constant biases in the ranging data, and thus don't include a processing step to determine and correct them.
- We do not simulate any angular jitters, and consequently do not include any TTL correction.
- We do not perform the final transformation to TCB, but remark that we do not expect this step to significantly affect the noise reduction.

In addition, we want to point out that the simulation model presented in part ii includes some simplifying assumptions. Relaxing these might reveal additional processing requirements in the future.

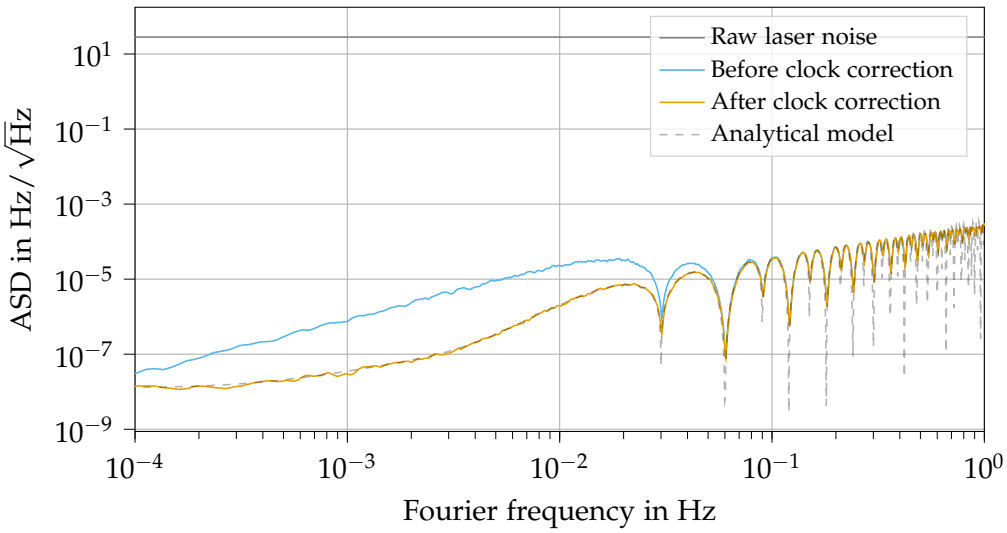

FIGURE 9.1: INREP result, residual noise in 2nd generation Michelson X_2. Clock noise is dominant at low frequencies, and removed in an extra processing step. Final result is well explained by levels of test-mass and readout noise given in section 8.2, modulated by the TDI transfer function derived in section 12.2.2. The secondary noises will ultimately limit the instrument performance, and replace the 10 pm requirement in this plot.

10

INTRODUCTION TO TIME-DELAY INTERFEROMETRY (TDI)

As described in section 3.2, the easiest way to attempt to suppress laser noise in LISA would be to combine two round-trip measurements starting from a single spacecraft. Using the configuration described in chapter 8, we can construct such a variable by taking the difference between the two ISC beatnotes recorded on spacecraft 1. The result is an un-equal arm Michelson interferometer.

As explained in section 2.3.1, we expect laser noise in an unequal arm interferometer to be suppressed by a factor $2\pi f \Delta\tau$, where $\Delta\tau$ is the armlength mismatch in seconds. In our case, we have $\Delta\tau \approx 0.2\,\mathrm{s}$, so we expect a laser noise residual still many orders of magnitude above the 10 pm allocation. This is verified in fig. 10.1, where we constructed such a variable out of the simulated data presented in chapter 8.

The proposed solution to this problem is to construct virtual equal arm interferometers on ground using a post-processing technique known as time-delay interferometry. This method was first proposed in [82], and has been continously developed over the last 20 years, with many authors contributing results. For more information on the history and fundamental working principles of TDI, we recommend the excellent review article by M. Tinto and S.V. Dhurandar, and references therein [83].

We derive the basic steps needed to construct laser noise reducing variables, following a similar approach to that described in [92, 63], in section 10.1. The key ideas presented in this section will form the basis for the arguments presented in chapters 11 to 13.

We then review the achievable level of laser noise suppression in the different TDI *generations* in section 10.2, and finally sketch the ideas of studying TDI from an algebraic perspective in section 10.3.

As before, we will use the notation conventions outlined in appendix A.

10.1 CONSTRUCTION OF TDI COMBINATIONS

10.1.1 *Interferometric measurements*

Cf. section 12.1 for how this assumption can be realized in reality.

To understand the basic principles of TDI, it is instructive to consider a simplified LISA model. We consider in this chapter only laser noise, with phasemeter measurements expressed in total phase. Furthermore, we assume only a single unique laser per spacecraft.

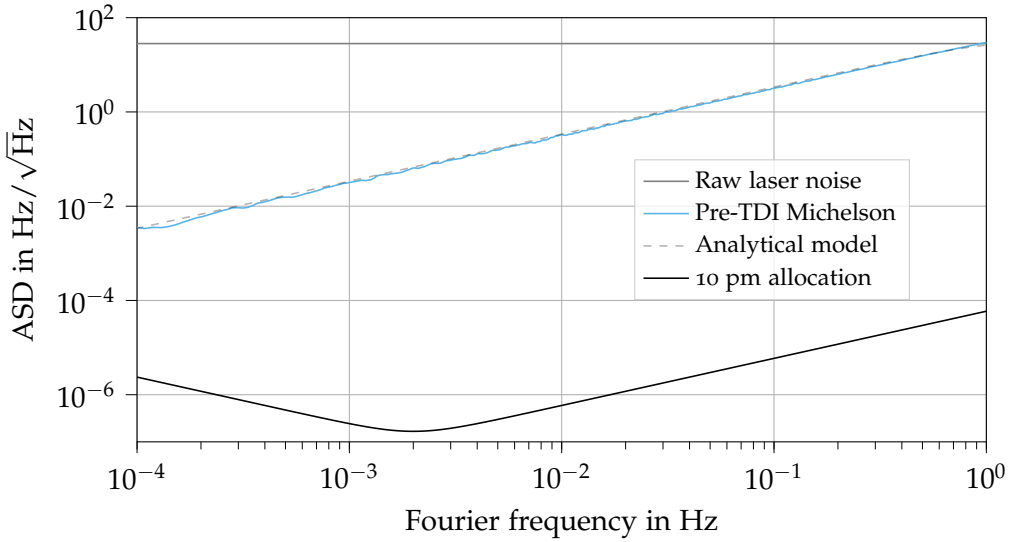

FIGURE 10.1: Noise in a simple Michelson configuration. Arm-length mismatches of $\Delta\tau \approx 0.2\,\text{s}$ cause large laser noise residual.

We model only the two ISC interferometers on each spacecraft, which measure the beatnote between the local laser with the two incoming lasers from the remote spacecraft. In total, we get 6 beatnotes, which we call η_{ij}. Here, i, j take the values from 1 to 3, with the first index indicating the receiving spacecraft, as usual.

Following the derivation in chapter 5, the interspacecraft measurements are then given as

$$\eta_{ij} = \mathbf{D}_{ij}\Phi_j - \Phi_i\,, \tag{10.1}$$

with Φ_i as the total phase of the unique laser on spacecraft i. We omit any time arguments in this equation. The delay operator $\mathbf{D}_{ij}$ indicates that Φ_j should be evaluated at the time associated to the event of emission from the distance spacecraft, while η_{ij} and Φ_i are evaluated at the event of reception.

We assume in this chapter that all variables are given according to a global time frame, such as TCB, and that all spacetime events are identified by a coordinate time t and an associated spacecraft. The above equation then becomes

$$\eta_{ij}(t) = \Phi_j(t - d_{ij}(t)) - \Phi_i(t)\,, \tag{10.2}$$

with $d_{ij}(t)$ as the light travel time in the TCB, computed at time of reception t. Since the spacecraft are not static, the delays are in general time varying functions.

Our goal in TDI is to combine multiple of the one-way measurements η_{ij} to construct virtual equal arm interferometers on ground, which suppress laser noise. We will perform this construction step-by-step, always combining two measurement in such a way that one common laser noise term in them cancels.

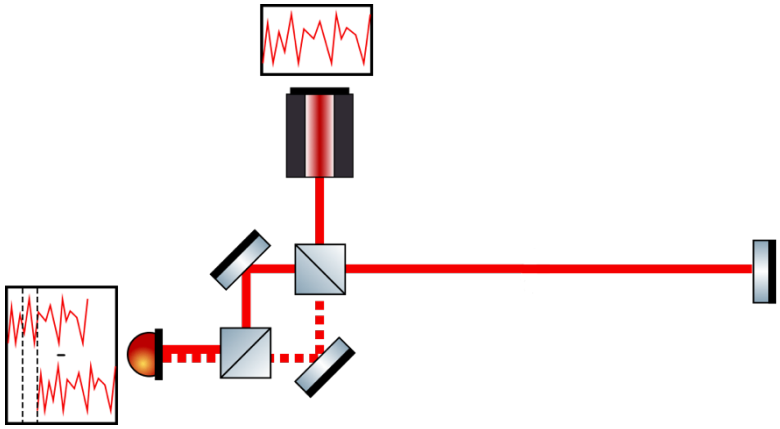

FIGURE 10.2: Idealized transponder signal, where the distant satellites acts as a mirror. The sending spacecraft measures a differential signal between the phase at emission and that at reception, which is delayed by a full round-trip. Adapted from [22].

10.1.2 *Virtual laser locking*

Consider a TDI toy model: we want to create a 'virtual' transponder signal, where a laser beam is being emitted from spacecraft 1 towards spacecraft 2, reflected, and send back to spacecraft 1, where it interferes with a non-delayed version of the same beam. We can label the final time of reception as t_r, the time of reflection at spacecraft 2 as t_t, and the original time of emission as t_e. This is sketched in fig. 10.2.

This is equivalent to locking the laser on spacecraft 2 to the incoming laser from spacecraft 1, but in post-processing.

As described above, $d_{ij}(t)$ is defined as the propagation time for a single link, so we have

$$t_t = t_r - d_{12}(t_r)\,, \tag{10.3a}$$
$$t_e = t_t - d_{21}(t_t)\,. \tag{10.3b}$$

We can combine these two equations to get t_e as a function of t_r,

$$t_e = t_r - d_{12}(t_r) - d_{21}(t_r - d_{12}(t_r))\,. \tag{10.4}$$

We can now write the phase received after a full roundtrip as

$$\begin{aligned}\mathbf{D}_{121}\Phi_1(t) &\equiv \mathbf{D}_{12}(\mathbf{D}_{21}\Phi_1(t)) \\ &= \mathbf{D}_{12}\Phi_1(t - d_{21}(t)) \\ &= \Phi_1(t - d_{21}(t - d_{12}(t)) - d_{12}(t))\,,\end{aligned} \tag{10.5}$$

where we defined the nested delay operator $\mathbf{D}_{121} = \mathbf{D}_{12}\mathbf{D}_{21}$.

In general, delay operators are not commutative, so e.g. $\mathbf{D}_{12}\mathbf{D}_{21} \neq \mathbf{D}_{21}\mathbf{D}_{12}$.

Our full transponder signal is then given as

$$T = \mathbf{D}_{121}\Phi_1 - \Phi_1\,. \tag{10.6}$$

In order to construct this signal, we can use the two one-way measurements η_{12} and η_{21}, which are given by

$$\eta_{12} = \mathbf{D}_{12}\Phi_2 - \Phi_1\,, \qquad \eta_{21} = \mathbf{D}_{21}\Phi_1 - \Phi_2\,. \tag{10.7}$$

These contain the same laser phases, just evaluated at different times. If the delays are known perfectly, we can construct

$$\begin{aligned}\eta_{12} + \mathbf{D}_{12}\eta_{21} &= \mathbf{D}_{12}\Phi_2 - \Phi_1 + \mathbf{D}_{121}\Phi_1 - \mathbf{D}_{12}\Phi_2 \\ &= \mathbf{D}_{121}\Phi_1 - \Phi_1\,.\end{aligned} \tag{10.8}$$

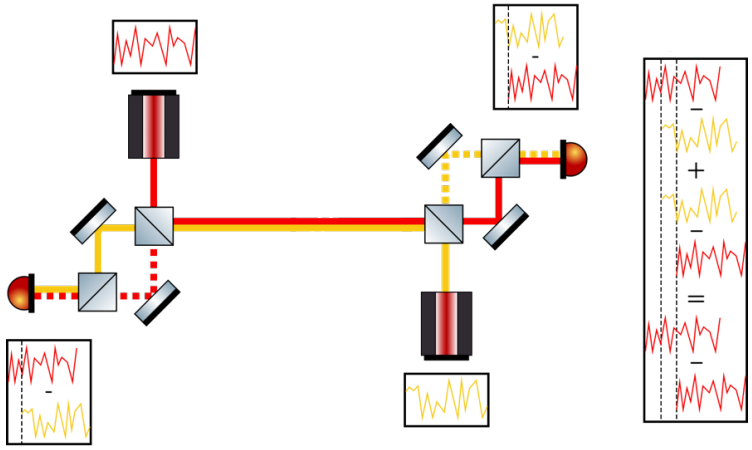

FIGURE 10.3: Synthesized transponder signal. Both spacecraft measure the phase difference between their local laser at emission and the distant laser at reception, which is delayed by a single link. Adding the signals of both spacecraft with the correct delays yields the full round-trip measurement shown in fig. 10.2. Adapted from [22].

Here, η_{12} is evaluated at t_r, while η_{21} is evaluated t_t. Both η contain a laser noise term $\Phi_2(t_t)$, which cancel exactly, and we perfectly reconstruct our desired transponder signal. This is sketched in fig. 10.3.

We can now keep adding new terms using the same principle, always cancelling one laser noise term from an event of emission with another one from an event of reception. This allows us to construct any signal of the form

$$\begin{aligned} T_1 &= \eta_{i_1 i_2} + \mathbf{D}_{i_1 i_2}\eta_{i_2 i_3} + \mathbf{D}_{i_1 i_2 i_3}\eta_{i_3 i_4} + \cdots + \mathbf{D}_{i_1 \ldots i_{n-1}}\eta_{i_{n-1} i_n} \\ &= \mathbf{D}_{i_1 i_2 \ldots i_n}\Phi_{i_n} - \Phi_{i_1}\,, \end{aligned} \tag{10.9}$$

where we generalize the nested delay to

$$\mathbf{D}_{i_1 i_2 \ldots i_n} = \mathbf{D}_{i_1 i_2}\mathbf{D}_{i_2 i_3}\ldots\mathbf{D}_{i_{n-1} i_n}\,. \tag{10.10}$$

T_1 now corresponds to an interferometer where one beam was emitted from spacecraft i_n, relayed by spacecrafts $i_{n-1}\ldots i_2$, and finally received and interfered on spacecraft i_1.

10.1.3 *Laser noise cancellation in two beam interferometers*

To achieve laser noise cancellation, we can introduce a second term of the same kind, with a different set of delays,

$$T_2 = \mathbf{D}_{j_1 j_2 \ldots j_n}\Phi_{j_m} - \Phi_{j_1}\,, \tag{10.11}$$

and look at their difference:

$$\mathrm{TDI} = T_1 - T_2 = \mathbf{D}_{i_1 i_2 \ldots i_n}\Phi_{i_n} - \Phi_{i_1} - \mathbf{D}_{j_1 j_2 \ldots j_m}\Phi_{j_m} + \Phi_{j_1}\,. \tag{10.12}$$

We see that if $i_1 = j_1$ and $i_n = j_m$, we get

$$\mathrm{TDI} = (\mathbf{D}_{i_1 i_2 \ldots i_n} - \mathbf{D}_{j_1 j_2 \ldots j_m})\Phi_{i_n}\,. \tag{10.13}$$

This means we are left with only one unique laser noise term, which is suppressed by the difference of nested delay operators representing different photon paths.

Physically, this signal represents an interferometer: two beams are emitted from spacecraft i_n, received at spacecraft i_1, and travel among the spacecraft as indicated by the list of spacecraft indices appearing in the nested delays, from right to left. The problem of laser noise suppression is now translated into the problem of finding the correct photon paths, which itself depends on the orbital dynamics governing the light travel times for each inter-satellite link.

There is of course a trivial solution to laser noise cancellation, which is $i_1 \dots i_n = j_1 \dots j_m$, such that the two beams travel exactly the same path. This amounts to directly subtracting our measurement from itself, yielding exact cancellation of all noises, but also all signals. We are therefore only searching for non-trivial solutions, such that $i_1 \dots i_n \neq j_1 \dots j_m$

10.2 TDI GENERATIONS

Traditionally, the solutions of the problem of finding laser noise reducing TDI combinations have been categorized into different simplified scenarios:

- 0th generation TDI, considering all delays to be constant and equal,
- 1st generation TDI, considering all delays to be constant, equal along two direction of the same link (e.g., $\mathbf{D}_{12} = \mathbf{D}_{21}$), but unequal for different links (e.g., $\mathbf{D}_{12} \neq \mathbf{D}_{13}$),
- 1.5th generation TDI, considering all delays to be constant and unequal, and
- 2nd generation TDI, considering all delays to be linearly evolving functions of time.

As we already saw in section 3.2, second generation TDI is sufficient for the laser noise suppression requirements in LISA. We will still give an example of a third generation combination in section 10.2.5.

Note that since higher generations impose increasingly strict conditions, any TDI solution at a given generation N is also a solution of lower generation $M < N$.

As an example, we give for each generation the Michelson X combination. None of them are perfect equal arm-length interferometers, and their arm-length mismatch $\Delta\tau$ is dominated by the next-to-leading order contributions to the arm length neglected in their derivation. We can model this up to 2nd generation by considering a third order expansion for the light travel times,

The three Michelson combinations centered on spacecraft 1, 2 and 3 are traditionally called X, Y and Z.

$$\mathbf{D}_A x(t) = x(t - d_A - \dot{d}_A t - \frac{1}{2}\ddot{d}_A t^2)\,, \tag{10.14}$$

with d_A, $\dot{d}_A$ and $\ddot{d}_A$ constant. We will then give a model for the leading order arm length mismatch terms up to 2nd generation. Following section 2.3.1, we

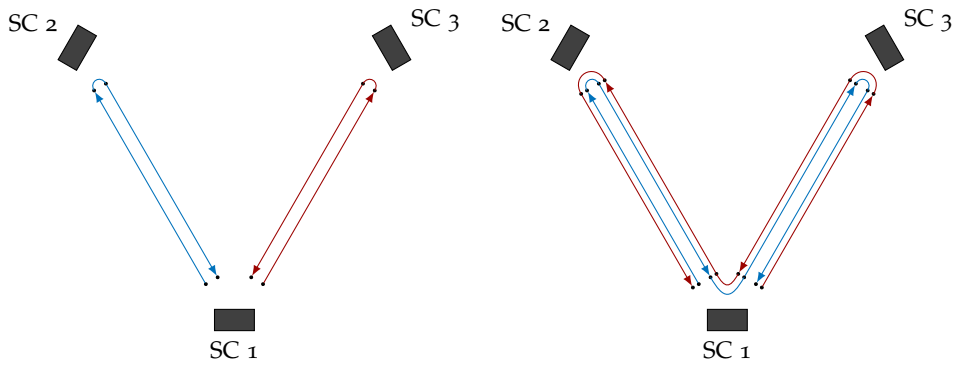

FIGURE 10.4: Schematic overview of the 0th and first generation Michelson combinations. Two beams are emitted from spacecraft 1. For the 0th generation, they are recombined after a single round-trip, while for 1st generation, they each travel to both spacecraft 2 and 3 before being recombined, cancelling constant armlength mismatches.

expect a laser noise residual in the TDI variable (expressed in frequency) of

$$S_{X_i^\nu}(\omega) = \Delta\tau_i^2 \omega^2 S_\nu(\omega)\,, \tag{10.15}$$

where ω is the angular Fourier frequency, i an index denoting the generation, and S_ν as the raw laser frequency noise PSD.

We show a simplified numerical simulation in section 10.2.6 to verify that these models are accurate.

10.2.1 *0th generation TDI*

If all delays are constant and equal, the condition for laser noise cancellation is simply that we need the same number of delays for each beam. This corresponds to $n = m$ in eq. (10.13). An example of a 0th generation TDI combination is the simple Michelson (sketched in fig. 10.4 (left)),

$$\begin{aligned} X_0 &= \eta_{12} + \mathbf{D}_{12}\eta_{21} - \eta_{13} - \mathbf{D}_{13}\eta_{31} \\ &= (\mathbf{D}_{121} - \mathbf{D}_{131})\Phi_1\,. \end{aligned} \tag{10.16}$$

This is equivalent to the simple Michelson combination we considered in the beginning of this chapter, with the only difference being that we can construct such a signal regardless of the laser locking configuration, for each of the three spacecraft.

See section 12.2 for more information how the different locking schemes impact TDI.

The leading order contributions to the armlength mismatch is simply

$$\Delta\tau_0 \approx 2(d_{12} - d_{13})\,, \tag{10.17}$$

which as we saw before leads to laser noise residuals far above the requirements.

10.2.2 *1st generation TDI*

First generation combinations were first proposed in [82].

Since all delays are constant, their order does not matter, and we have

$$[\mathbf{D}_A, \mathbf{D}_B] = \mathbf{D}_A\mathbf{D}_B - \mathbf{D}_B\mathbf{D}_A = 0 \tag{10.18}$$

for the commutator of any two delays. This means we can freely exchange the order in which the spacecraft indicies appear in the two nested delays in eq. (10.13). This yields the simple condition that the visited spacecraft have to be identical for both paths. Formally, we have

As described in appendix A, we sometimes use upper latin letters as placeholder for any index pair ij.

$$\{i_k | k = 1 \dots n\} = \{j_k | k = 1 \dots n\} \tag{10.19}$$

for the sets of all indices i_k and j_k in eq. (10.13).

An example of a 1st generation TDI combination is a variant of the Michelson, where each of the two beam visits both spacecraft, but in opposite order (sketched in fig. 10.4 (right)):

$$\begin{aligned} X_1 &= \eta_{12} + \mathbf{D}_{12}\eta_{21} + \mathbf{D}_{121}\eta_{13} + \mathbf{D}_{1213}\eta_{31} \\ &\quad - [\eta_{13} + \mathbf{D}_{13}\eta_{31} + \mathbf{D}_{131}\eta_{12} + \mathbf{D}_{1312}\eta_{21}] \\ &= (\mathbf{D}_{12131} - \mathbf{D}_{13121})\Phi_1 \,. \end{aligned} \tag{10.20}$$

As argued below, X_1 is actually also automatically TDI generation 1.5. Therefore, the leading order contributions to the armlength mismatch are proportional to $\dot{d}_A$, and we can compute them via a first order expansion in $\dot{d}$ as

$$\Delta\tau_1 \approx 4d(\dot{d}_{31} - \dot{d}_{12}) \,, \tag{10.21}$$

where d is the average arm length in seconds, and we assumed $\dot{d}_{ij} \approx \dot{d}_{ji}$.

10.2.3 *1.5th generation TDI*

In 1.5th generation TDI (also called 'modified' 1st generation TDI), all the conditions of 1st generation apply, but we further distinguish the direction in which the delays are computed. This gives the more restrictive condition that the individual delays appearing in the expanded nested delays of both paths must be identical.

Expanding the nested delays in X_1, we observe that it also satisfies this stricter condition, so it is automatically 1.5th generation.

Generalized 1.5th generation combinations were first proposed in [84].

An example of a 1st generation TDI combination which is not 1.5th generation is the Sagnac combination, where the two beams travel in a circle around the constellation, in opposite directions:

$$\begin{aligned} \alpha_1 &= \eta_{12} + \mathbf{D}_{12}\eta_{23} + \mathbf{D}_{123}\eta_{31} - [\eta_{13} + \mathbf{D}_{13}\eta_{32} + \mathbf{D}_{132}\eta_{21}] \\ &= (\mathbf{D}_{12}\mathbf{D}_{23}\mathbf{D}_{31} - \mathbf{D}_{13}\mathbf{D}_{32}\mathbf{D}_{21})\Phi_1 \,. \end{aligned} \tag{10.22}$$

Indeed, the leading-order contribution to the arm-length mismatch for α_1 is simply

$$\Delta\tau_{\alpha_1} \approx (d_{12} + d_{23} + d_{31}) - (d_{13} + d_{32} + d_{21}) \,, \tag{10.23}$$

which only vanishes under the condition $d_{ij} = d_{ji}$.

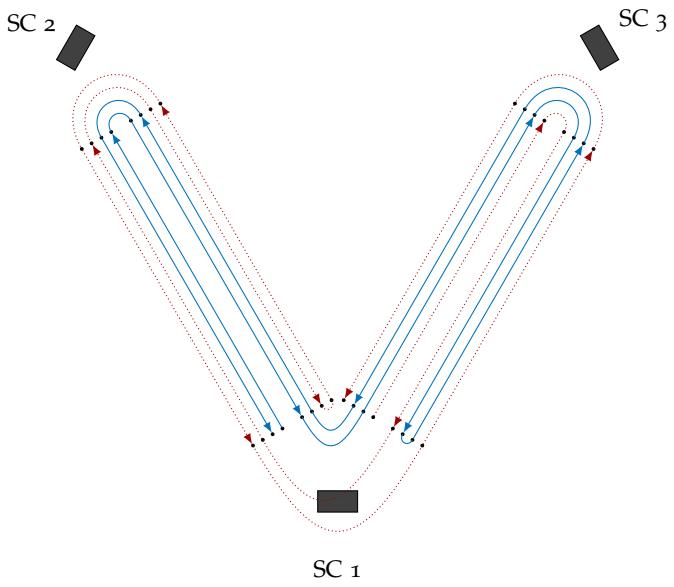

FIGURE 10.5: Schematic overview of the 2nd generation Michelson combination. Here, both beams travel to both spacecraft 2 and 3 twice before being recombined, cancelling spacecraft movement to first order.

10.2.4 *2nd generation TDI*

In second generation TDI, the delays are no longer modelled as constants, but instead as linear functions of time,

$$\mathbf{D}_A x(t) = x(t - d_A - \dot{d}_A t)\,, \tag{10.24}$$

with d_A and $\dot{d}_A$ constant. Therefore, we can no longer freely commute two delays, since nested delays yield non-symmetric terms (we neglect any terms of the form $\dot{d}_A \dot{d}_B$):

$$\mathbf{D}_A \mathbf{D}_B x(t) \approx x((1 - \dot{d}_A - \dot{d}_B)t - d_A - d_B + d_A \dot{d}_B) \tag{10.25}$$

This is easily generalized to an arbitrary number of delays, where each delay couples to all the linear terms in the delays to it's right:

$$\mathbf{D}_{A_1 \ldots A_n} x(t) \approx x\left(\left(1 - \sum_{k=1}^{n} \dot{d}_{A_k}\right) t - \sum_{k=1}^{n} d_{A_k} + \sum_{k=1}^{n} d_{A_k} \sum_{m=k+1}^{n} \dot{d}_{A_m}\right) \tag{10.26}$$

Note that only the last summand,

$$\sum_{k=1}^{n} d_{A_k} \sum_{m=k+1}^{n} \dot{d}_{A_m}\,, \tag{10.27}$$

depends on the order of the delays. Therefore, in order to achieve laser noise cancellation to first order in $\dot{d}$, the two beams must be chosen in such a way that

- Both beams contain the same overall delays, and
- they are ordered in such a way that eq. (10.27) yields the same result for both.

An example of a 2nd generation TDI combination is yet another variant of the Michelson, where each of the two beam visits both distant spacecraft twice (sketched in fig. 10.5):

$$\begin{aligned} X_2 = {} & \eta_{12} + \mathbf{D}_{12}\eta_{21} + \mathbf{D}_{121}\eta_{13} + \mathbf{D}_{1213}\eta_{31} + \mathbf{D}_{12131}\eta_{13} \\ & + \mathbf{D}_{121313}\eta_{31} + \mathbf{D}_{1213131}\eta_{12} + \mathbf{D}_{12131312}\eta_{21} \\ & - \big[\eta_{13} + \mathbf{D}_{13}\eta_{31} + \mathbf{D}_{131}\eta_{12} + \mathbf{D}_{1312}\eta_{21} + \mathbf{D}_{13121}\eta_{12} \\ & \quad + \mathbf{D}_{131212}\eta_{21} + \mathbf{D}_{1312121}\eta_{13} + \mathbf{D}_{13121213}\eta_{31}\big] \\ = {} & (\mathbf{D}_{121313121} - \mathbf{D}_{131212131})\Phi_1 \,. \end{aligned} \tag{10.28}$$

These combinations were first described in [85].

For its armlength mismatch, we consider terms to first order in $\ddot{d}_{ij} \approx \ddot{d}_{ji}$ and second order in $\dot{d}_{ij} \approx \dot{d}_{ji}$ and again use the average armlength d, to get

$$\Delta\tau_2 = 8d\big[\big(\dot{d}_{12}^2 - \dot{d}_{31}^2\big) - 2d\big(\ddot{d}_{12} - \ddot{d}_{31}\big)\big] \,. \tag{10.29}$$

Here, the first term matches the previous result from the literature [24]. The second term is proportional to $\ddot{d}_{12} - \ddot{d}_{31}$, which we will estimate to be dominant for the ESA provided orbits (cf. section 10.2.5).

10.2.5 *3rd and higher generation TDI*

In principle, the above reasoning could be continued to include higher and higher polynomial orders. Third generation TDI would mean that the arms are equal to first order in all contributions given in eq. (10.14).

However, as we saw in fig. 3.4, 2nd generation TDI is sufficient to reach the required laser noise suppression in LISA.

Indeed, we can compute numerically from the orbits shown in fig. 3.3 that the orders of magnitude for the arm length derivatives can be approximated as $d_A \approx 8.3\,\mathrm{s}$, $\dot{d}_A \approx 10^{-9}$ and $\ddot{d}_A \approx 10^{-15}\,\mathrm{s}^{-1}$. Since laser noise 'only' needs to be suppressed by roughly 8 orders of magnitude, we see that the armlength mismatch $\Delta\tau_2$ given in eq. (10.29) should be sufficient. In addition, we can confirm that the contribution of $\ddot{d}_A$ should be the dominant contribution to $\Delta\tau_2$.

In addition to not being required, the analytical problem of finding third generation TDI combinations also seems rather challenging. Due to the quadratic time dependence, the number of terms in a nested delay goes with the square of the number of delays, which means we would have to solve analytical formulas with a very large number of terms.

As a an example for a third generation combination, we can take an educated guess based on an argument from [92]. They conjecture that each TDI combinations of 2nd generation can be constructed from 1st generation combinations by 'splicing'. For example, each of the two beams in the 2nd generation Michelson combination contains exactly the same delays as

both beams combined in the first generation version, such that each arm is transversed twice, with a reversed direction for the second pass.

Extending that idea, we can guess the third generation Michelson combination to be the interferometer evaluating to

$$X_3 = (\mathbf{D}_{12131312131212131} - \mathbf{D}_{13121213121313121})\Phi_1\,, \tag{10.30}$$

which is a splicing of the 2nd generation combination, where each arm is now traversed four times by each beam.

This is by no means a conclusive study, but merely a quick test to check the general feasability of this combination.

To test this hypothesis, we can numerically evaluate the difference in light travel time for the first and second beam, assuming a 2nd order fit of realistic orbits given in fig. 3.3. The computations where performed using Mathematica, with the working precision of all numerical values set to 50 digits precision.

For reference, using this method, the X_2 combinations time difference between the two paths evaluates to 9.7×10^{-12} s, which exactly what we would expect from inserting the values of d, $\dot{d}$ and $\ddot{d}$ determined by our orbital fit into eq. (10.29). Our 'third generation' Michelson X_3, on the other hand, evaluates to just 8.6×10^{-20} s, an improvement of 8 orders of magnitude, and indeed below the level we would expect from terms proportional to either $\dot{d}_A^2$ or $\ddot{d}_A$.

10.2.6 *Simulation comparison across generations*

To verify the laser noise suppressing capabilities of the different TDI generations, we present results using a simplified simulation using `LISA Instrument`, where we disable all noises except laser noises. We simulate 10^5 samples, and do not simulate laser locking. The same realistic ESA orbits and the same sampling rates are used as in chapter 8. In addition, we use the same transition band for the anti-aliasing filter, but increase the attenuation to 320 dB in order to not be limited by aliasing[1].

Cf. appendix B for more information on the practical implementation of delays.

We then compute the 0th, 1st, 2nd and 3rd generation Michelson variables described above, using `PyTDI`, where we chose an interpolation order of 65.

The results are shown in fig. 10.6. We observe that our model matches the achieved laser noise level well for 0th, 1st and 2nd generation, although the 2nd generation variable is limited by a white numerical noise floor below 2×10^{-3} Hz. This is even more pronounced for the 3rd generation variant, which is completely limited by numerical noise, with an estimated theoretical

1 The attenuation of the filter given in chapter 7 was intentionally chosen to limit the level of aliased noise to just below the 1 pm allocation (with some margin). A stronger filter would be computationally more expensive, which might impose additional requirements on the instrument hardware. In this chapter, we are more interested in the fundamental limits of TDI than being true to the instrument design, such that we can use a higher attenuation in order to highlight the maximum achievable laser noise suppression.

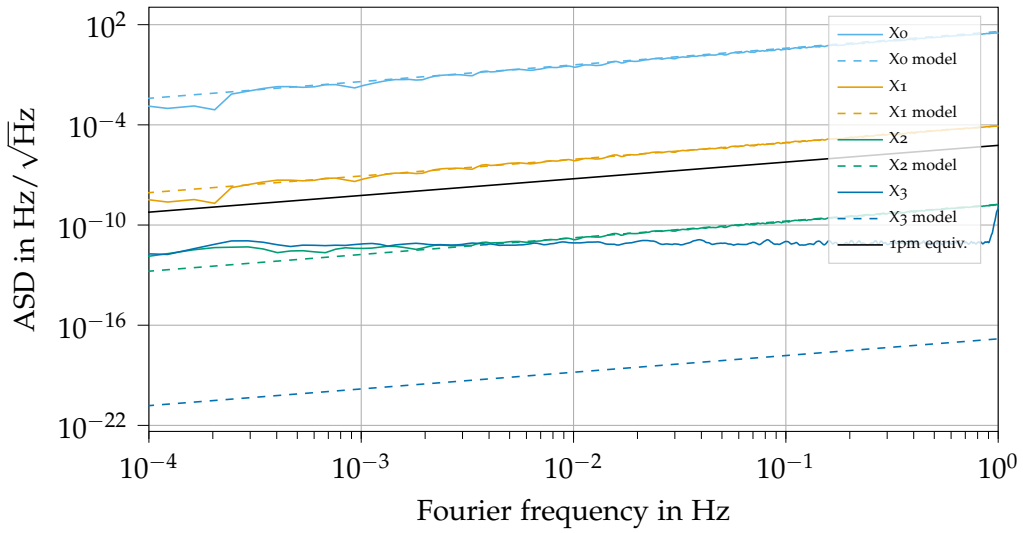

FIGURE 10.6: Laser noise residual in different Michelson X generations.

laser noise residual[2] far below the other variables. The sharp increase of X_3 close to 1 Hz can be explained by the interpolation errors discussed in section 12.3.2.2.

10.3 THE ALGEBRA OF COMMUTATIVE AND NON-COMMUTATIVE DELAY OPERATORS

It can be useful in practice to study and describe TDI combinations from an algebraic perspective. In fact, the problem of up to 1.5th generation TDI can be exactly solved using algebraic methods, see [83]. It turns out that the entire space of 1.5th generation variables can be generated from just 6 fundamental combinations [69], while for 1st generation, even 4 combinations are sufficient [32].

To the knowledge of the author, the algebraic problem of second generation TDI is to date still unsolved [83], and no finite set of generators is known. This opens up the question which, and how many, second generation TDI combinations one should compute to extract all available information. We will briefly explore this question at the end of chapter 11.

Regardless, it is useful to realize that once 2nd generation TDI combinations are found, they can be manipulated algebraically.

Cf. chapter 11 for a review of possible second generation combinations.

Formally, we observe the following properties of the delay operators of first and second generation TDI:

- Each delay operator $\mathbf{D}_{ij}$ has a left and right inverse $\mathbf{D}_{\overline{ji}}$, which exactly cancels the applied time shift (see chapter 11 for more information, in particular eq. (11.2)).

2 Note that we neglected terms proportional to $\ddot{d}_A$ in the computation of $\Delta\tau$ in section 10.2.5, which might cause a residual laser noise at a higher level than estimated here.

- Delay operators are linear operators, in the sense that

$$\begin{aligned} \mathbf{D}_{ij}(x(t)+y(t)) &= \mathbf{D}_{ij}x(t)+\mathbf{D}_{ij}y(t)\,, \\ \mathbf{D}_{ij}(ax(t)) &= a\mathbf{D}_{ij}x(t)\,, \end{aligned} \tag{10.31}$$

  for any constant $a \in \mathbb{R}$ and any time dependent functions $x(t), y(t)$.

- Delay operators of first generation are commutative, while those of second generation are non-commutative.

Using that delay operators are linear, we can factorize any given TDI combination as

$$\text{TDI} = \sum_{ij\in\mathcal{I}_2} P_{ij}\eta_{ij}\,, \tag{10.32}$$

where the set of index touples $\mathcal{I}_2 = \{ij \mid i,j \in \{1,2,3\}, i \neq j\}$ has six elements and each P_{ij} is a polynomial[3] of delay operators.

For example, the first generation Michelson combination can be factorized as

$$\begin{aligned} X_1 &= \eta_{12} + \mathbf{D}_{12}\eta_{21} + \mathbf{D}_{121}\eta_{13} + \mathbf{D}_{1213}\eta_{31} \\ &\quad - [\eta_{13} + \mathbf{D}_{13}\eta_{31} + \mathbf{D}_{131}\eta_{12} + \mathbf{D}_{1312}\eta_{21}] \\ &= (1-\mathbf{D}_{131})(\eta_{12}+\mathbf{D}_{12}\eta_{21}) - (1-\mathbf{D}_{121})(\eta_{13}+\mathbf{D}_{13}\eta_{31})\,, \end{aligned} \tag{10.33}$$

which means its defining polynomials P_{ij} are

$$\begin{aligned} P_{12} &= (1-\mathbf{D}_{131})\,, & P_{23} &= 0\,, & P_{31} &= -(1-\mathbf{D}_{121})\mathbf{D}_{13}\,, \\ P_{21} &= (1-\mathbf{D}_{131})\mathbf{D}_{12}\,, & P_{32} &= 0\,, & P_{13} &= -(1-\mathbf{D}_{121})\,. \end{aligned}$$

We know from the previous sections that the laser noise appearing in each η_{ij} is strongly suppressed in the full TDI combination. However, this is not the case for most other noises. For the purpose of estimating the coupling of non-suppressed effects, like gravitational waves and most noise sources, it is therefore often sufficient to analyze eq. (10.32) under the assumption that all delays appearing in the P_{ij} are constant, or even equal to one average delay. Therefore, any result valid for 0th, 1st or 1.5th generation variables are applicable to the non-suppressed quantities in the second generation variables as well, with increasing level of accuracy.

For example, assuming that all delays are equal, we can write X_1 in terms of the simple Michelson X_0,

$$\begin{aligned} X_1 &= (1-\mathbf{D}_{131})(\eta_{12}+\mathbf{D}_{12}\eta_{21}) + (1-\mathbf{D}_{121})(\eta_{13}+\mathbf{D}_{13}\eta_{31}) \\ &\approx (1-\mathbf{D}^2)\underbrace{(\eta_{12}+\mathbf{D}\eta_{21}-\eta_{13}-\mathbf{D}\eta_{31})}_{X_0}\,, \end{aligned} \tag{10.34}$$

3 Note that these operator-valued polynomials don't obey the same rules valid for real-valued polynomials. In particular, a polynomial of delay operators has in general no multiplicative inverse. In addition, the delay operators of 2nd generation TDI are non-commutative, such that the order of operators must be preserved when factorizing these polynomials.

where we used $\mathbf{D}$ as the unique equal delay operator of oth generation TDI. Likewise, we can write X_2 in terms of X_1 assuming that delays commute, or even in terms of X_0 if they are all assumed equal:

$$\begin{aligned} X_2 =& (1 - \mathbf{D}_{131} - \mathbf{D}_{13121} + \mathbf{D}_{1213131})(\eta_{12} + \mathbf{D}_{12}\eta_{21}) \\ & - (1 - \mathbf{D}_{121} - \mathbf{D}_{12131} + \mathbf{D}_{1312121})(\eta_{13} + \mathbf{D}_{13}\eta_{31}) \\ \approx& (1 - \mathbf{D}_{12131})X_1 \,. \\ \approx& (1 - \mathbf{D}^4)(1 - \mathbf{D}^2)X_0 \,. \end{aligned} \tag{10.35}$$

These properties are very useful in practice. For example, the relationship between X_2 and X_1 was used in [86] to generalize an already known clock correction algorithm from first to second generation, and it is also regularly used in the LISA performance model group to relate noise residuals for second generation TDI to those of first generation TDI.

We will also use a similar reasoning to relate all second generation combinations found in chapter 11 and presented in table 11.3 to the four generators of first generation TDI, cf. section 11.5.1.

11

TDI COMBINATIONS

We presented in chapter 10 how TDI combinations can be built out of the one-way measurements to construct arbitrary two-beam interferometers.

We will extend this approach to construct more general multi-beam interferometers, following the ideas described by [92, 63], in section 11.1. Here, we also introduce a concise notation for identifying TDI combinations.

We then generalize the conditions for laser noise cancellation in the different TDI generations in section 11.2, and discuss different symmetries the combinations can obey in section 11.3.

Finally, we use these formulations in section 11.4 to perform an independent replication of the search method outlined in [92, 63], finding additional 14 link combinations which were previously missed. A full summary of the found combinations is given in table 11.3. We then relate these combinations to the generators of first generation TDI in section 11.5, and show simulation results indicating that just four combinations are sufficient to recover all information encoded in the 2nd generation TDI combinations in section 11.5.1. Finally, we show how these decompositions can be applied to actual simulated data in section 11.5.2

The results reported in this chapter where produced independently by the author, but with regular exchange and comparison of results with the LISA group in Trento, in particular M. Muratore, D. Vetrugno and S. Vitale.

11.1 LASER NOISE CANCELLATION IN MULTI-BEAM INTERFEROMETERS

We have discussed how to construct two-beam interferometers allowing laser noise cancellation in chapter 10. This approach can be generalized to construct TDI combinations utilizing an arbitrary (even) number of beams, by combining multiple two-beam interferometers.

To understand this, it is useful to consider the spacetime events involved in each measurement η_{ij}. Each η_{ij} represents a one-way measurement, where incoming light from the distant spacecraft is interfered with the local laser beam. The resulting measurement is the difference of the phase of the local laser at the event of reception of the distant beam and that of the distant laser at the event of its emission. We used this property in section 10.1.2 to combine multiple η_{ij}'s such that the laser entering at the event of reception in one of the η_{ij} exactly cancels with the same laser entering at the event of emission of another η_{ij}.

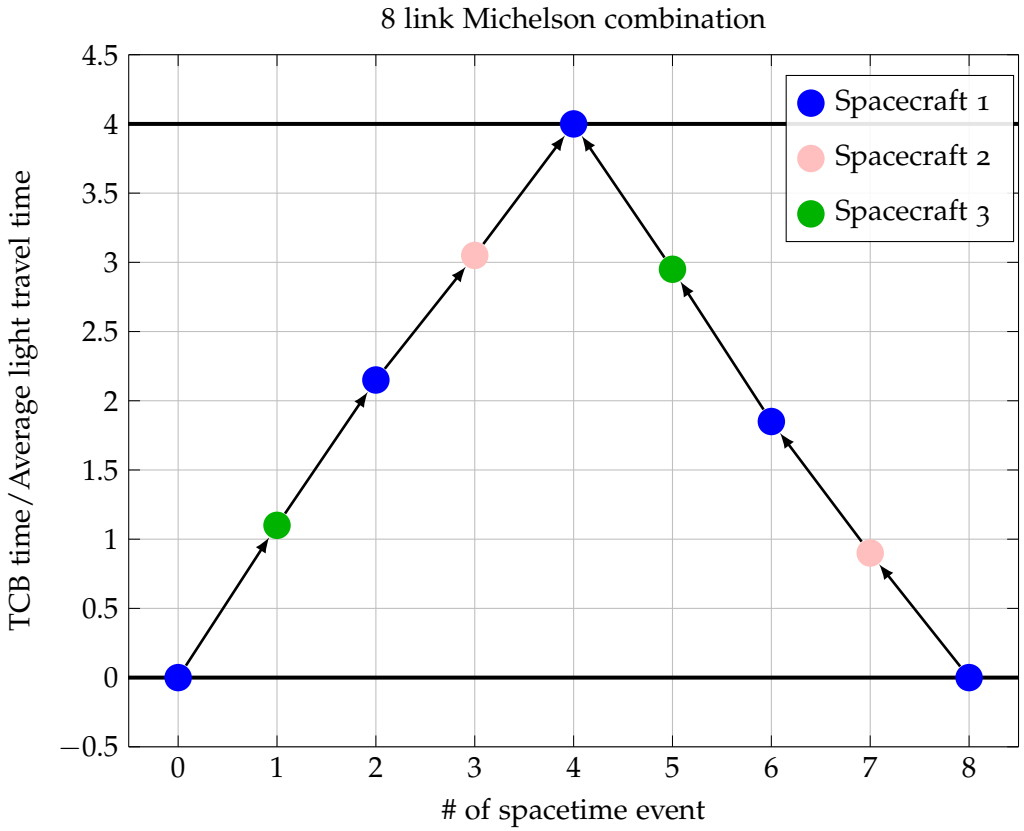

FIGURE 11.1: A schematic overview of 1.5th generation Michelson combination. The x-axis denotes the number of events in the TDI combination, starting at one of the emission events. The colors indicate which spacecraft is visited in each link. The y-axis denotes the coordinate time at each event, normalized by the average light travel time. Even though the arms are unequal, the overall path is closed, meaning that the first and last event in the chain happen simultaneously on the same spacecraft, and laser noise cancels. Light-travel times chosen only for visualization.

This allowed construction of single-beam interferometers, where one of the beams is emitted at an emission event, relayed in an arbitrary path along the constellation, and then recombined with a non-delayed version at a reception event. Furthermore, in section 10.1.3, we combined two such beams which share a common reception event to construct a virtual interferometer, cancelling laser noise if the two respective emission events are simultaneous.

This means so far, we used two different laser noise cancellation mechanisms when combining measurements:

- Cancellation at a simultaneous reception and emission event, and
- Cancellation at two simultaneous reception events.

Obviously, there is a third option to combine the η_{ij}'s which we didn't use so far, which is cancellation at two simultaneous *emission* events.

As an example, fig. 11.1 shows a schematic overview of the emission and reception events involved in the first generation Michelson combination. The x-axis is a simple counter indexing these events, while the y-axis shows the coordinate time at which the beam arrives at a certain spacecraft.

In the classical TDI description outlined in section 10.1.3, the two beams are combined at a reception event. Therefore, the figure is to be read starting from the event labelled #4, where two beams are received simultaneously. Each of the two beams can then be tracked back to their inital event of

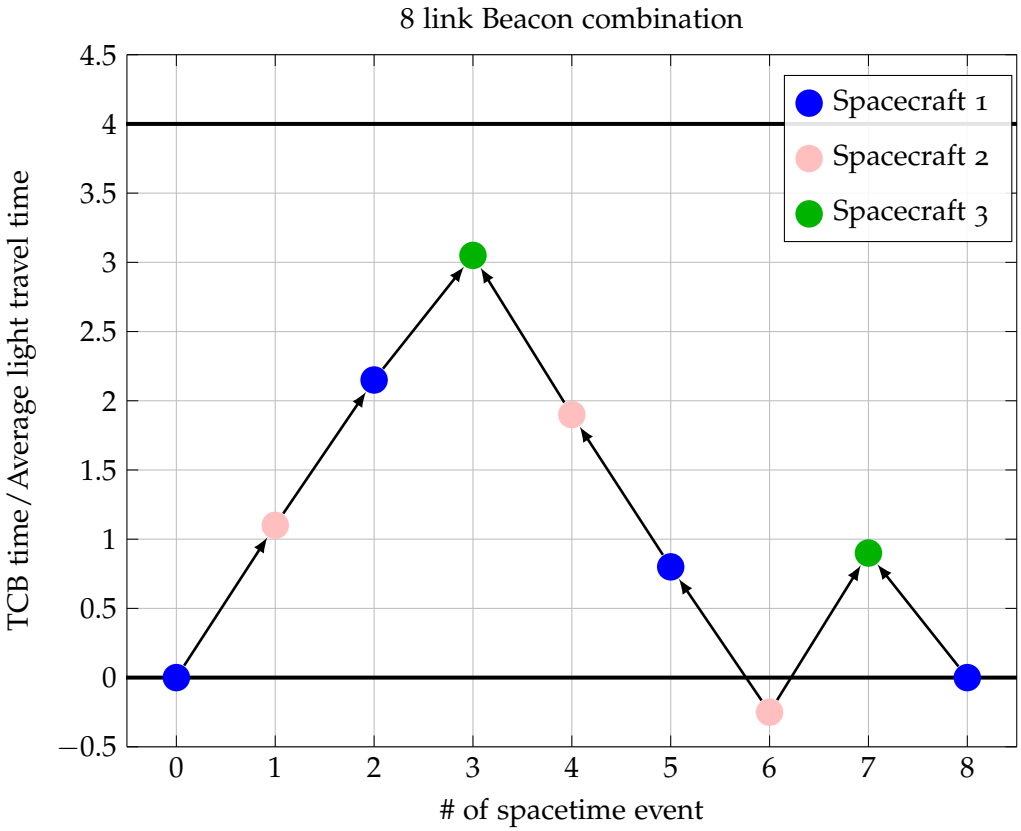

FIGURE 11.2: 1.5th generation 'beacon'-type TDI combination utilizing 4 beams/two interferometers. The only simultaneous events are the very beginning and end of the chain. Combination given in [92]. This combination has a smaller temporal foot-print than the Michelson combination. Light-travel times chosen only for visualization.

emission by going through the sequence either descending (from #4 to #0) or ascending (from #4 to #8). Laser noise is cancelled if the two emission events are simultaneous[1].

However, we can just as well time shift our whole combination to start at the emission time from the first spacecraft, labelled #0 in the figure. We then track a beam which is emitted at time $t = 0$ forwards through time, computing it's reception times going through events #1 to #4. At event #4, it is combined with the second beam, and we change direction. We then compute the emission times of the second beam while going through the rest of the sequence, from events #4 to #8. The condition for laser noise cancellation has not changed, the first and last event have to be simultaneous. The advantage of going through the sequence in this order is that it is easy to generalize it to include more than two beams, or equivalently more than one measurement event. Figure 11.2 shows an example of such a combination, which uses two measurement events/interferometers. In this example, the two measurement events on spacecraft 3 have to be aligned in time in such a way that the shared emission event on spacecraft 2 (# 6 in the figure) is simultaneous for both interferometers. We still have the same condition for laser noise cancellation, i.e., the *whole* photon path has to be closed, which means the first and last event in the chain have to be in the same spacecraft and simultaneous.

1 'Simultaneous' meaning here that the time difference between the two events is sufficient small that the residual laser noise is below the required level, as discussed in chapter 10.

In practice, constructing TDI variables starting not from a reception event but from an emission event requires knowledge of not only the delays $\mathbf{D}_{ij}$, which give the emission time of a beam on spacecraft j given a reception time i, but also the advancements $\mathbf{D}_{\overline{ij}}$, which give the reception time of a beam on spacecraft j given an emission time on spacecraft i.

Formally, if the coordinate times of the events of emission and reception of a beam emitted from spacecraft i and received by spacecraft j are denoted t_i^e and t_j^r, respectively, we have

$$\mathbf{D}_{ji}x(t_j^r) = x(t_i^e)\,, \quad \mathbf{D}_{\overline{ij}}x(t_i^e) = x(t_j^r)\,, \tag{11.1}$$

which immediately yields the identity

$$\mathbf{D}_{ij}\mathbf{D}_{\overline{ji}}x(t) = \mathbf{D}_{\overline{ji}}\mathbf{D}_{ij}x(t) = x(t)\,. \tag{11.2}$$

In LISA, we only directly measure $\mathbf{D}_{ij}$, cf. section 6.3. The advancements can be calculated out of these using an iterative procedure on eq. (11.2), see appendix B.4.

We will use the same notation for nested advancements which we used for nested delays. I.e., we have

$$\mathbf{D}_{\overline{i_1 i_2 \ldots i_n}} = \mathbf{D}_{\overline{i_1 i_2}}\mathbf{D}_{\overline{i_2 i_3}}\ldots\mathbf{D}_{\overline{i_{n-1} i_n}}\,, \tag{11.3}$$

which gives the time of reception of a beam on spacecraft i_n which was emitted from spacecraft i_1, being relayed by all the spacecraft corresponding to the indices inbetween, from left to right. Note that eq. (11.2) generalizes to

$$\mathbf{D}_{\overline{i_1 i_2 \ldots i_n}}\mathbf{D}_{i_n i_{n-1}\ldots i_1} = \mathbf{D}_{i_n i_{n-1}\ldots i_1}\mathbf{D}_{\overline{i_1 i_2 \ldots i_n}} = 1\,. \tag{11.4}$$

As an example of how to construct a TDI variable starting at an emission event, let us consider again the 1st generation Michelson combination,

$$\begin{aligned} X_1 &= \eta_{12} + \mathbf{D}_{12}\eta_{21} + \mathbf{D}_{121}\eta_{13} + \mathbf{D}_{1213}\eta_{31} \\ &\quad - [\eta_{13} + \mathbf{D}_{13}\eta_{31} + \mathbf{D}_{131}\eta_{12} + \mathbf{D}_{1312}\eta_{21}] \\ &= (\mathbf{D}_{12131} - \mathbf{D}_{13121})\Phi_1\,. \end{aligned} \tag{11.5}$$

This equation is to be evaluated at a reception time on spacecraft 1. As argued above, we can simply time-shift the whole combination by applying $\mathbf{D}_{\overline{13121}}$, such that it is evaluated at an emission event at one of the beams, which yields

As described in appendix A, we seperate nested delays and advancements in $\mathbf{D}$ by a semicolon, i.e., $\mathbf{D}_{\overline{13121};13121} \equiv \mathbf{D}_{\overline{13121}}\mathbf{D}_{13121}$

$$\begin{aligned} \mathbf{D}_{\overline{13121}}X_1 =& \mathbf{D}_{\overline{13121}}\eta_{12} + \mathbf{D}_{\overline{13121}}\mathbf{D}_{12}\eta_{21} + \mathbf{D}_{\overline{13121}}\mathbf{D}_{121}\eta_{13} + \mathbf{D}_{\overline{13121}}\mathbf{D}_{1213}\eta_{31} \\ &- \mathbf{D}_{\overline{13121}}[\eta_{13} + \mathbf{D}_{13}\eta_{31} + \mathbf{D}_{131}\eta_{12} + \mathbf{D}_{1312}\eta_{21}] \\ =& \mathbf{D}_{\overline{13}}\eta_{31} + \mathbf{D}_{\overline{131}}\eta_{13} + \mathbf{D}_{\overline{1312}}\eta_{21} + \mathbf{D}_{\overline{13121}}\eta_{12} \\ &- \mathbf{D}_{\overline{13121}}[\eta_{13} + \mathbf{D}_{13}\eta_{31} + \mathbf{D}_{131}\eta_{12} + \mathbf{D}_{1312}\eta_{21}] \\ =& (1 - \mathbf{D}_{\overline{13121};13121})\Phi_1\,. \end{aligned} \tag{11.6}$$

We can make the following observations:

- All delays and advancements in the final result are shifted to the second term, while the first term enters without any timeshift. This leads to the interpretation of this signal in [92] that we have constructed an interferometer where one of the beams travels forwards and backwards in time, and interferes with itself at it's event of emission.
- The nested delays and advancements in that second term enter exactly in the same order as the visited spacecraft in our visualization, cf. fig. 11.1.
- Each η_{ij} is evaluated at such times that the two laser noise contributions in them correspond to the emission and reception events in our visualization. For example:
  - The first term $\mathbf{D}_{\overline{13}}\eta_{31}$ contains laser noise from spacecraft 1 at the event of emission at the time origin of the combination (#0), and laser noise of spacecraft 3 at the event of reception (#1),
  - the 'middle' term $\mathbf{D}_{\overline{13121}}\eta_{12} - \mathbf{D}_{\overline{13121}}\eta_{13}$ is the recombination event (#4), at which both beams interfere; here, both η's are evaluated at the same time, such that the common noise of spacecraft 1 cancels,
  - and the final term $\mathbf{D}_{\overline{13121};1312}\eta_{21}$ is evaluated at the second to last event (#7). This η_{21} contains a laser noise term which is then emitted at the last event in our figure (#8).

11.1.1 *Algorithm for TDI variable construction*

The above observations lead us to a general algorithm of how to construct any multi-beam interferometer. We assume that the combination we want to construct is given as a string of visited spacecraft, directly corresponding to the nested delays in eq. (11.6). Paths in forward time direction are indicated with a positive sign, while those with a backward time direction receive a negative sign. For example, the 1st generation Michelson combination described in eq. (11.6) would be encoded as `"13121 -13121"`, but this notation is not restricted to two-beam interferometers.

This algorithm was first described in [92], and updated here to our notation.

The full algorithm[2] to build a TDI combination given by a photon path is then:

- Expand the nested photon path into a list of single links. E.g.,

$$\texttt{"13121 -13121"} \to [13, 31, 12, 21, -13, -31, -12, -21]\,. \tag{11.7}$$

- Create an empty list of delays/advancements $\mathcal{T} = [\,]$, and initialize an expression $\mathcal{C} = 0$.

2 The last step is optional. Without it, the resulting TDI combinations usually contain a large number of nested timeshifts, which can become computationally expensive when actually computing the TDI response. It is therefore often advisable to multiply the final combination by the inverse of the first half of $\mathcal{T}$, such that half of the timeshifts in the combination are cancelled. Physically, this timeshift corresponds to building the combination starting from the central event instead of the first event.

- Iterate through the expanded photon path, doing the following operations, assuming the indices are ij:
  - If the entry is positive (an advancement), add
    $$\mathcal{C} \mathrel{+}= \mathcal{T}\mathbf{D}_{\overline{ij}}\eta_{ji}\,. \tag{11.8}$$
  - If the entry is negative (a delay), instead subtract
    $$\mathcal{C} \mathrel{-}= \mathcal{T}\eta_{ij} \tag{11.9}$$
  - Then, append either $\mathbf{D}_{\overline{ij}}$ or $\mathbf{D}_{ij}$ to $\mathcal{T}$.
- Apply am overall timeshift to the combination undoing the first half of $\mathcal{T}$ to reduce the total number of time shifts (Optional).

We will denote the application of this algorithm by TDI["string"]. For example, we would write for the first generation Michelson

$$\begin{aligned}\text{TDI}[\texttt{"13121 -13121"}] = (1-\mathbf{D}_{131})\eta_{12} + (\mathbf{D}_{12}-\mathbf{D}_{1312})\eta_{21} \\ -(1-\mathbf{D}_{121})\eta_{13} - (\mathbf{D}_{13}-\mathbf{D}_{1213})\eta_{31}\,.\end{aligned} \tag{11.10}$$

This algorithm is functionally identical to that presented in [92] and simply updated to agree with our notation. We can convert our photon paths to the notation used there (and the other way around) using the following steps:

- Expand nested delays:
  $$\texttt{"13121 -13121"} \to [13, 31, 12, 21, -13, -31, -12, -21]$$
- Replace the two spacecraft indices with corresponding link, so exchange
  $$\begin{array}{ccc} 12 \leftrightarrow 3', & 23 \leftrightarrow 1', & 31 \leftrightarrow 2', \\ 21 \leftrightarrow 3, & 32 \leftrightarrow 1, & 13 \leftrightarrow 2, \\ -12 \leftrightarrow -3, & -23 \leftrightarrow -1, & -23 \leftrightarrow -2, \\ -21 \leftrightarrow -3', & -32 \leftrightarrow -1', & -13 \leftrightarrow -2'. \end{array}$$
- Collapse the resulting list back into a string, e.g.,
  $$\texttt{"2 2' 3' 3 -2' -2 -3 -3'"}.$$

11.2 CONDITIONS FOR LASER NOISE CANCELLATION

We can evaluate if a string corresponds to a combination which is TDI generation 1, 1.5 or 2 using modified versions of the rules presented in section 10.2.

Combinations satisfying these conditions can then be found numerically, by simply generating and testing all possible TDI strings up to a given length.

11.2.1 *1st Generation*

If all armlengths are constant and symmetric, it is sufficient if the same spacecraft are visited on the forward and backwards paths of the combination. Formally, we have to count the total number of occurences of each spacecraft in all positive substrings, which has to be equal to the number of occurences of each spacecraft in all negative substrings.

For example, the Sagnac combination is given by the string `"1321 -1321"`, which fulfills this condition.

11.2.2 *1.5th Generation*

As before, we now have to consider the direction of links. This requires to expand the photon path into a list of delays, and then count that the same links are used in forward and backwards direction.

Since all delays are still constant, we can freely commute them in this list. Using eq. (11.2), we see that each advancement $\mathbf{D}_{\overline{ij}}$ cancels with a corresponding delay $\mathbf{D}_{ji}$.

In summary, the algorithm to check if a string is TDI 1.5 is:

- Expand the TDI string into list of advancements and delays. For example:

$$\texttt{"13121 -13121"} \rightarrow [13, 31, 12, 21, -13, -31, -12, -21] \tag{11.11}$$

- Count the number of each advancement ij, which has to be equal to the number of each corresponding delay $-ji$.

11.2.3 *2nd Generation*

The algorithm described in section 11.1.1 always yields an expression of the form

$$\text{TDI} = (1 - \mathbf{D}_{i_1 \ldots i_n})\Phi_{i_n}\,, \tag{11.12}$$

with the chain of delays in the second term corresponding exactly to the indices of the TDI string. We have to check if the overall nested time shift in that term evaluates to zero when performing a first order approximation in the arm lengths.

For this study, it is more useful to not apply the optional last step of the algorithm, such that all timeshifts are shifted to the second laser noise term.

11.2.3.1 *Forward time shifts for linear delays*

We first need to determine how the forward timeshifts $\mathbf{D}_{\overline{A}}$ are related to the delays $\mathbf{D}_A$ in the linear approximation. We have again

$$\mathbf{D}_A x(t) = x(t - d_A - \dot{d}_A t)\,, \tag{11.13}$$

with d_A and $\dot{d}_A$ assumed constant for the delays.

We want to model our advancements in exactly the same form, which will allow us to reuse eq. (10.26). So we use[3]

$$\mathbf{D}_{\overline{A}} x(t) = x(t - a_{\overline{A}} - \dot{a}_{\overline{A}} t)\,. \tag{11.14}$$

Utilizing eq. (11.2), we then see that

$$\begin{aligned} x(t) &= \mathbf{D}_{\overline{A}} \mathbf{D}_A x(t) \\ &= \mathbf{D}_{\overline{A}} x(t - d_A - \dot{d}_A t) \\ &= x(t - a_{\overline{A}} - \dot{a}_{\overline{A}} t - d_A - \dot{d}_A (t - a_{\overline{A}} - \dot{a}_{\overline{A}} t)) \\ &= x(t - a_{\overline{A}} - d_A + \dot{d}_A a_{\overline{A}} + (\dot{a}_{\overline{A}} \dot{d}_A - \dot{a}_{\overline{A}} - \dot{d}_A) t) \end{aligned} \tag{11.15}$$

For the equation to hold, the terms with and without a time-dependence both need to cancel independently, yielding the two solutions

$$a_{\overline{A}} = -\frac{d_A}{1 - \dot{d}_A}\,, \tag{11.16}$$

$$\dot{a}_{\overline{A}} = -\frac{\dot{d}_A}{1 - \dot{d}_A}\,. \tag{11.17}$$

We can expand both expressions to first order in $\dot{d}_A$ to get

$$a_{\overline{A}} \approx -d_A (1 + \dot{d}_A)\,, \tag{11.18}$$

$$\dot{a}_{\overline{A}} \approx -\dot{d}_A\,. \tag{11.19}$$

11.2.3.2 *Laser noise cancellation to first order in $\dot{L}$*

We can reuse the result and reasoning we had in section 10.2 to show that the overall nested time shift is structurally identical to eq. (10.26),

$$\mathbf{D}_{\tilde{A}_1 \ldots \tilde{A}_n} x(t) = x\left(\left(1 - \sum_{k=1}^{n} \dot{T}_{\tilde{A}_k}\right) t - \sum_{k=1}^{n} T_{\tilde{A}_k} + \sum_{k=1}^{n} T_{\tilde{A}_k} \sum_{m=k+1}^{n} \dot{T}_{\tilde{A}_m}\right). \tag{11.20}$$

The difference is that we now allow each $\tilde{A}_i$ to be either an advancement or a delay, replacing $T_{\tilde{A}_i} \to d_{A_i}$, $\dot{T}_{\tilde{A}_i} \to \dot{d}_{A_i}$ for a delay, and $T_{\tilde{A}_i} \to -d_{\overline{A}_i}(1 + \dot{d}_{\overline{A}_i})$, $\dot{T}_{\tilde{A}_i} \to -\dot{d}_{\overline{A}_i}$ for an advancement. The bar on $\overline{A}_i$ acts as a reminder that when we use this formula in the two index convention, we need to reverse the order of indices for the advancements to get the correct inverse operator.

Using these replacement rules, we see immediately that the sum $\sum_{k=1}^{n} \dot{T}_{\tilde{A}_k}$ cancels as long as the same arms are transversed an equal number of times in forward and backwards direction, which is exactly the condition for TDI generation 1.5.

3 Note that in the two index convention, we have $\mathbf{D}_{\overline{ij}}$ as the inverse of the delay $\mathbf{D}_{ji}$, with the indices switched. In our one-index notation for delays, we will use $\mathbf{D}_{\overline{A}}$ as the inverse of $\mathbf{D}_A$.

In addition, we need to check if all delays and advancements in the last two sums cancel, i.e., that

$$\sum_{k=1}^{n} T_{\tilde{A}_k} \sum_{m=k+1}^{n} \dot{T}_{\tilde{A}_m} = \sum_{k=1}^{n} T_{\tilde{A}_k} \,, \tag{11.21}$$

at least to first order in $\dot{L}$. The first order approximation means here that we can use the simplified substitution $T_{\tilde{A}_i} \to -L_{\overline{A}_i}$ for the advancements in the left side of the equation, while we need to use the full expression for the right side of the equation.

Equation (11.21) can be checked by either evaluating it symbolically, or by implementing an appropriate counting algorithm on the links appearing in the nested delay, as described in [92]. We chose the former option for convenience, using the computer algebra software `Mathematica`.

11.2.3.3 *Laser noise cancellation expressed in the Fermi frame*

It was argued in [63] that the search for TDI combinations can in principle be performed in any reference frame, since the simultaneity of two events (here the emission and reception events of the beams) remains true in any reference frame[4].

Furthermore, it was shown that there exists a reference frame in which the terms for L and $\dot{L}$ have certain symmetries, and can be expressed in terms of the relative coordinate velocity[5] of the spacecraft:

$$L_{ij} = L_{0,ij}\left(1 - \frac{v_{ij}}{c}\right) \tag{11.22}$$

$$L_{ji} = L_{0,ij}\left(1 - \frac{v_{ji}}{c}\right) \tag{11.23}$$

$$\dot{L}_{ij} = \dot{L}_{ji} = v_{ij} + v_{ji} \,. \tag{11.24}$$

Using these conditions and neglecting effects second order in v_{ij} in expressions equivalent to eq. (11.21) led to the discovery of some new 2nd generation TDI combinations in [63] which were previously discarded by the search algorithm described in [92]. Notably, it was shown that several new 12 link combinations suppress laser noise to the same level as the previously known 16 link combinations.

4 In reality, the recombination events are not exactly simultaneous, but occur with a small time offset on the order of ps when expressed in the TCB [63]. It might be possible to construct a coordinate system with a coordinate singularity which blows up this ps time interval to an arbitrarily large number, which conversely would mean that finding a 'small' overall light travel time in such a coordinate system would not translate to an equally small time interval in the TCB. This is not the case for the systems considered here, for which the relative scaling of these time intervals due to coordinate transformations is small enough to not affect the result.

5 Note that in these equations (taken directly from [63], see there for more information), the armlength are expressed in meters, not seconds, explaining the occurence of the speed of light c, which is absent in all our equations.

11.3 SYMMETRIES OF TDI STRINGS AND STRING NORMAL FORM

In the previous sections, we introduced a concise notation for defining TDI combinations, and reviewed an algorithm based on [92] for how to construct the corresponding interferometers out of the six one-way measurements. However, there are multiple symmetry operations we can apply to a TDI string without changing the resultant combination in a meaningful way. Therefore, each TDI string should be seen as a representative of an equivalence class of distinct TDI combinations.

Furthermore, some combinations are related by simple permutations of the spacecraft indices used in them. Thus, each string can also be seen as representative of another equivalence class of core TDI combinations, from which all distinct combinations can be generated by index permutations.

We will use a sorting criterion to pick one unique representative for each of these equivalence classes.

Note that such symmetries are also discussed in [92, 63]. We list them here for completeness, and to discuss how they are applied in our notation.

11.3.1 *String reversal*

We constructed our algorithm to use the first event in the string as starting point for the combination. However, we could have just as well started from the opposite end. Practically, this means that the order of visited spacecraft is reversed, while links which previously where interpreted as delays are now advancements, and vice versa. This has two minor impacts which should not lead us to consider these as different combinations.

For one, the sign will be flipped, since we assigned a positive sign to advancements and a negative sign to delays in our algorithm. This sign assignment was in itself arbitrary, such that this has no physical meaning. Secondly, the reversed combination will have a small time shift, since the starting time is now defined at the last spacecraft, not the first. As before, an overall timeshift does not distinguish a combination. In addition, the first and last event of the chain can be seen as almost simultaneous within the assumptions of a given TDI generation, such that this timeshift is indeed irrelevant in most situations.

Thus, two strings can be seen as equivalent if one can be produced from the other by reversing the order and changing all signs.

11.3.2 *Cyclic string shifts*

Applying a cyclic shift of all string indices, e.g.,

`"12 21 13 31 -12 -21 -13 -31"` $\rightarrow$ `"21 13 31 -12 -21 -13 -31 12"`

(11.25)

only has a very subtle impact on the resultant combination. If the photon path described by the combination is perfectly closed, the first and last event are simultaneous. This means that the cyclically shifted combination contains exactly the same events, with exactly the same laser noise cancellations at simultaneous events, and the only change is an overall shift in the starting time.

In reality, the photon path is not perfectly closed, such that the first and last event are not simultaneous. We therefore have the additional effect that the 'open' end of the path is at a different spacecraft. Non-closedness of the path represents an armlength mismatch of the synthesized interferometer, which will cause a small residual laser noise, as discussed in section 12.3.1.

This means we can in principle control which laser noise remains unsuppressed via cyclic string shifts. This might be exploitable if the lasers have different noise characteristics, such as is the case if they are all locked to one master laser in the constellation, and this noise appears in them with different delays.

Regardless of this minor technical detail, we will consider two combinations equivalent if one can be produced by the other via a cyclic string shift.

11.3.3 *Equivalent strings and normal representative*

Two strings are seen as equivalent if either of them can be produced from the other one by any combination of string reversals or cyclic shifts.

Since the cyclic permutation group of a list of N elements has itself N elements, and there are two versions of each string due to string reversal, we have a total of $2N$ members of the equivalence class for each string of length N.

We will choose a unique representative for each equivalence class via the following criteria:

- Favor strings which start with the longest list of consecutive advancements.
- Out of those, favor strings for which the starting indices are ascending (`"12"`, `"23"`, `"31"`).
- Out of those, prefer the lowest numerical ordering of the spacecraft appearing in the sequence (e.g., `"121..."` is favored over `"231..."` or `"123..."`).

11.3.4 *Permutation of spacecraft indices*

LISA obeys the symmetries of an equilateral triangle. In total, there are six possible permutations of the set of spacecraft indices. These can all be written

as multiple applications of the cyclic permutations, $1 \to 2, 2 \to 3, 3 \to 1$, and the mirror symmetry along the separating axis between spacecraft 2 and 3, i.e., by exchanging indices $2 \leftrightarrow 3$, as described in appendix A.

This implies that for any TDI string of a given TDI generation there exist 6 versions which are all of the same generation. They differ by the starting spacecraft and by exchanging the order in which the other two spacecraft appear.

Contrary to the previous two kinds of symmetries, some of these 6 versions can be seen as distinct combinations. We previously discarded combinations as equivalent if the same signals enter in them, up to an overall time-shift or a timing mismatch to be neglected at given TDI generation. This is not the case when changing the starting spacecraft or the order in which spacecraft are visited. For example, the Michelson combination X does not use any measurements between spacecraft 2 and 3, while its equivalents Y and Z constructed by cyclically shifting all spacecraft indices do use these measurements. They therefore contain different signals, and are seen as distinct combinations.

Some combinations are mirror symmetric. For example, exchanging the role of spacecraft 2 and 3 in the Michelson X combination is equivalent to a reversal of the string, which we previously identified to be equivalent to just a sign flip.

11.3.5 *Time reversal symmetry*

Reversing just the time direction of all links in a TDI string yields another TDI string of the same generation as the original[6]. In many cases, this time-reversed string is truly equivalent to the original, in the sense of section 11.3.3, or it is equivalent to one of the permutations described in section 11.3.4.

However, there are a few cases in which it is not equivalant to either. As an example, we show in fig. 11.3 the time-reversed version of the Beacon combination we originally discussed in fig. 11.2. In the original version of the variable, both spacecraft 1 and 2 emit two beams each, while all measurements are performed on spacecraft 3.

In the time-reversed version, on the other hand, all beams are emitted from spacecraft 3, while they are interfered and measured on spacecraft 1 and 2. This change in topology of the combination cannot be produced by a simple exchange of spacecraft labels, such that both the original and the time reversed version should be seen as distinct combinations.

6 We thank S. Vitale for pointing out this additional symmetry!

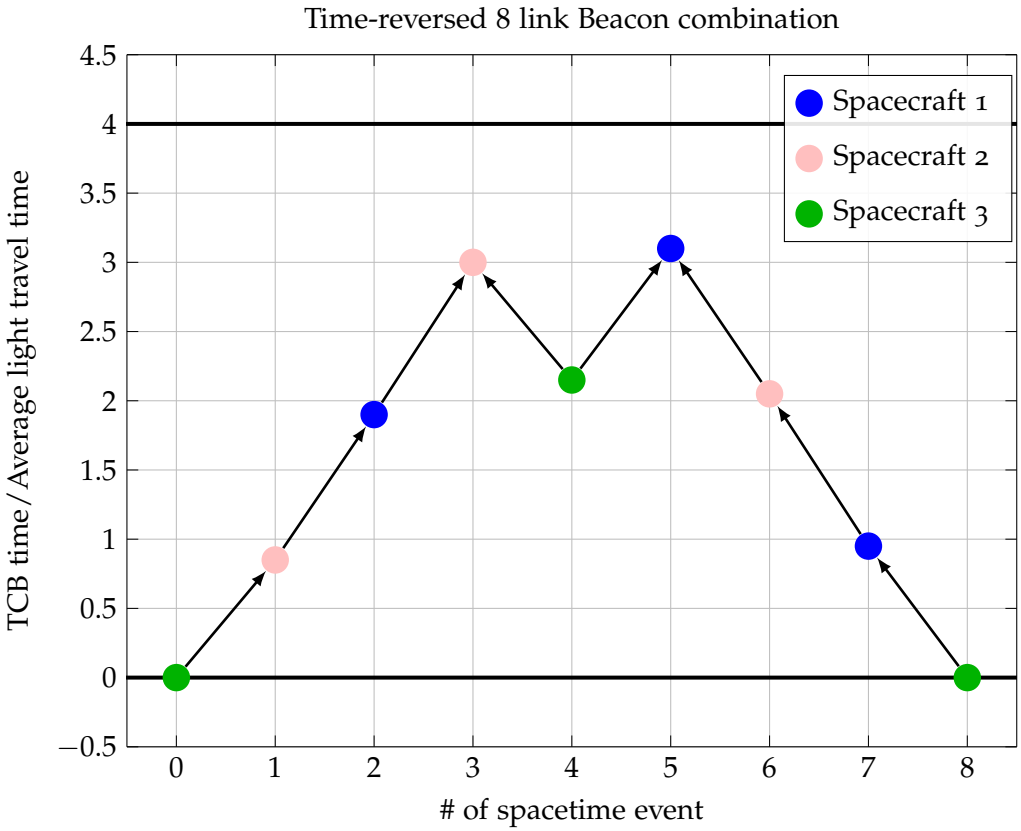

FIGURE 11.3: 1.5th generation 'beacon'-type TDI combination utilizing 4 beams/two interferometers after a time reversal. The combination is not time symmetric. Contrary to fig. 11.2, all beams are now emitted from S/C 3, and measured on S/C 1 and 2. Light-travel times chosen only for visualization.

11.3.6 *Core combinations and equivalence*

We call a *distinct combination* the equivalence class of strings which can be produced from each other just by string reversal or cyclic string shifts. Therefore, the three Michelson combinations X_1, Y_1 and Z_1 are distinct combinations.

We call a *core combination* the set of strings which can be produced from each other by either string reversal, cyclic string shifts, permutations of the spacecraft indices or time reversal. For example, X_1, Y_1 and Z_1 are distinct combinations, but represent the same core combination.

Note that for time-symmetric combinations, each core combination represents 3 or 6 distinct combinations, depending on if the combination is mirror symmetric or not. Likewise, for non time-symmetric combinations, there are 6 or 12 versions, again depending on the mirror symmetry.

To summarize, depending on its symmetries, each core TDI combination represents 3, 6 or 12 distinct combination.

Since each distinct combination of length N itself represents $2N$ possible strings (cf. section 11.3.3), the equivalence class of one core TDI combination of length N has either $6N$, $12N$ or $24N$ members.

11.4 SEARCH ALGORITHM RESULTS

We reproduced the search algorithm outlined in [92], including the generalization utilizing the Fermi coordinate frame proposed in [63].

Our version of the search algorithm operates in multiple steps:

1. Generate all possible non-trivial paths of a given length N starting from `"12"`, and keep those which are 1.5th generation TDI.
2. Reduce the resulting set to the set of core combinations using the definitions in section 11.3.
3. Check each core combination for being second generation TDI using the definitions in section 11.2.3. Here, we construct two datasets, one using the stricter criterium in [92], and one using the relaxed criterium from [63].

The resulting lists of core combinations can then be expanded to the list of distinct combinations by generating all possible index permutations and time reversals and then removing those which are equivalent in the sense of section 11.3.3.

Non-trivial means here that we neglect paths which contain structures like `"ij -ji"`, which, following the description in section 11.1, would just cancel immediately when computing the combination. We also restrict ourselves to paths which start with the link `"12"`. Furthermore, we reject paths which end at `"-21"`, since that last step would cancel with the first step under a cyclic shift of the sequence.

To be more precise, a sequence of length N must contain $N/2$ forward time links.

Fixing the start of the paths is just an optimization. It is valid since each laser noise cancelling sequence contains at least one forward time link, and at this stage we are not looking for all possible permutations of the combinations. So any valid TDI combination can be brought to start with `"12"` by a permutation of the spacecraft labels and a cyclic shift in the sequence.

We decide which paths are TDI first generation by keeping those which use each link an equal number of times in forward and backward direction. The result still contains many duplicates due to different symmetries, which are resolved as described in section 11.3.

11.4.1 *List of core combinations and their properties*

The results of our search are summarized in table 11.1 and table 11.2.

The numbers of distinct first generation combinations are in perfect agreement with those reported on the website[7] accompanying [92].

7 `http://www.vallis.org/research/tdi.html`

# of links	Core combinations	Distinct combinations
8	3	15
10	2	12
12	22	168
14	85	924
16	579	6090

TABLE 11.1: Number of first generation TDI combinations found in our search. The number of distinct combinations are in agreement with those reported in [92].

For each second generation combination, we state if it is classified as TDI second generation following according to [63], which we will call Fermi[8]-closed, or only according to [92], called $\dot{L}$-closed.

The set of 48 sixteen-link combinations which are $\dot{L}$-closed is equivalent to that reported on `vallis.org/tdi`, modulo string reversals + shifts.

For the Fermi-closed combinations, we found results at slight variance with those reported in [63].

For 12 links, we find the same 3 core combinations reported in [63]. They are all time symmetric, while two of them are also mirror symmetric, such that they represent a total of 12 distinct combinations.

In addition, we find 3 core combinations of length 14, which were not reported in [63]. None of them are mirror symmetric, and one is not time symmetric, such that they represent 24 distinct combinations.

Reaching out to the authors, they confirmed to have accidentally put a preliminary list of combinations in the paper. After review, they could confirm the existence of the twenty-four 14 link combinations. During this exchange, they also realized the additional time symmetry discussed in section 11.3.5, which reduces their list of 35 sixteen-link core combinations to just 28. This should be reflected in an upcoming joint publication with the authors of [63], which will contain the full table of combinations.

After including the time-symmetry to reduce the results of our own search algorithm, we arrived at the same set of 28 sixteen-link core combinations, which represent a total of 174 distinct combinations. This set includes all 48 distinct sixteen-link combinations found in [92].

We give a complete list of all core combinations up to 16 links in table 11.3. The notation was chosen in agreement with the authors of [63], and a similar table is included in [62].

We state for each combination if it is also $\dot{L}$-closed. In addition, we mark if it is mirror or time symmetric, thus if its equivalence class represents 3, 6 or 12 distinct combinations.

Some of the second generation combinations have the particularity to cancel exactly under the assumption that all delays are equal. This means they not only suppress laser noise, but all other noises and signals as well. This is

8 As discussed above, laser noise suppression of a TDI variable does not depend on the reference frame. However, this property becomes obvious only in the Fermi-normal frame, as discussed in [63].

# of links	Core ($\dot{L}$/Fermi-closed)	Distinct ($\dot{L}$/Fermi-closed)
12	0/3	0/12
14	0/3	0/24
16	8/28	48/174

TABLE 11.2: Number of second generation TDI combinations found in our search. The number of $\dot{L}$-closed combinations are in agreement with [92]. We find additional 14 link combinations which are Fermi-closed that were not reported in [63].

indicated in table 11.3 as being "Trivial". We will discuss the reason for this cancellation in section 11.5.1.

11.5 TDI GENERATORS FOR SECONDARY NOISES

Having seen in section 11.4 that the problem of second generation TDI variables offers a rich set of solutions, it is interesting to discuss how many of these contain redundant information.

As we will see in section 12.2, the assumptions of 0th generation – equal and constant arms – are sufficient to describe the level of unsuppressed noises in the standard Michelson combinations. In some cases, in particular at low frequencies and when constructing combinations of combinations, it turns out this assumption is no longer good enough, and we have to go first generation TDI - meaning three unequal, but constant arms.

One important result for 1st generation TDI is that *all* TDI variables can be generated from just 4 basic generators. As shown in [83], one possible set of generators are the 3 Sagnac variables α, β and γ, together with the fully symmetric Sagnac ζ. In our notation, these can be defined as

Note that ζ is defined in [83] only using three distinct delays of first generation TDI, such that we could have chosen either $\mathbf{D}_{ij}$ or $\mathbf{D}_{ji}$ for each delay to represent it. Contrary to [64], we chose the set $\mathbf{D}_{12}$, $\mathbf{D}_{23}$, $\mathbf{D}_{31}$.

$$\alpha = \eta_{12} + \mathbf{D}_{12}\eta_{23} + \mathbf{D}_{123}\eta_{31} - \eta_{13} - \mathbf{D}_{13}\eta_{32} - \mathbf{D}_{132}\eta_{21} \tag{11.26a}$$
$$\beta = \eta_{23} + \mathbf{D}_{23}\eta_{31} + \mathbf{D}_{231}\eta_{12} - \eta_{21} - \mathbf{D}_{21}\eta_{13} - \mathbf{D}_{213}\eta_{32} \tag{11.26b}$$
$$\gamma = \eta_{31} + \mathbf{D}_{31}\eta_{12} + \mathbf{D}_{312}\eta_{23} - \eta_{32} - \mathbf{D}_{32}\eta_{21} - \mathbf{D}_{321}\eta_{13} \tag{11.26c}$$
$$\zeta = \mathbf{D}_{23}\eta_{12} + \mathbf{D}_{31}\eta_{23} + \mathbf{D}_{12}\eta_{31} - \mathbf{D}_{23}\eta_{13} - \mathbf{D}_{12}\eta_{32} - \mathbf{D}_{31}\eta_{21} \tag{11.26d}$$

In terms of TDI strings, the generators are given as

$$\alpha = \mathrm{TDI}[\texttt{"1321 -1321"}] \tag{11.27a}$$
$$\beta = \mathrm{TDI}[\texttt{"2132 -2132"}] \tag{11.27b}$$
$$\gamma = \mathrm{TDI}[\texttt{"3213 -3213"}] \tag{11.27c}$$
$$\zeta \approx \mathbf{D}_{23}\mathrm{TDI}[\texttt{"13 -32 21 -13 32 -21"}] \tag{11.27d}$$

α, β, γ are simple two-beam interferometers, while ζ is a 6 beam interferometer with 3 measurement events, one on each spacecraft. Note that eq. (11.27d) is only valid with $\mathbf{D}_{ij} = \mathbf{D}_{ji}$, while the equations for α, β and γ are exact.

As mentioned above, following [83], we should be able to write

$$\mathrm{TDI} = A'\alpha + B'\beta + C'\gamma + D'\zeta \tag{11.28}$$

for any first generation TDI combination, with A', B', C', D' polynomials of the delay operators. Since second generation combinations are also automatically

first generation combinations[9], the same should hold approximately for all solutions found in section 11.4 when simplifying them assuming only three constant but unequal arms.

This means that under the assumptions of first generation, all information we can extract from any of the combinations given in table 11.3 is in principle already contained in these four generators.

α, β, γ and ζ are of course not suppressing the laser noise to a sufficient level, such that they are not usable for actual data analysis. Still, exploring how each second generation variable is related to their first generation counterparts is useful for categorizing their properties and assessing their information content.

In addition, we will demonstrate in section 11.5.2.2 that there are multiple variables which can be used as second generation versions of all 4 generators, which can be used in the same decompositions, even in the presence of realistic laser noise. This suggests that such 4 variables already contain most information we can hope to extract from our signals.

Other combinations might of course have practical advantages. For example, some combinations do not use all 6 laser links, such that they remain available in the event of a complete loss of the laser link between two of the spacecraft. In addition, as can be seen in fig. 11.5, the typical singularities present in the transfer function of all second generation TDI variables appear at different frequencies for the different combinations. This might allow some combinations to be more favorable for detecting signals close to these singular frequencies. Last but not least, combinations with multiple measurements require shorter segments of data to compute a single data point of the TDI combination. For example, C_1^{16} requires summation of the light travel for 8 links, or about $8 \times 8.33\,\mathrm{s} \approx 67\,\mathrm{s}$ for each of the two beams, while the beams of C_4^{16} only use 4 links at a time, corresponding to just $4 \times 8.33\,\mathrm{s} \approx 33\,\mathrm{s}$.

11.5.1 *Decomposition of geometric combinations*

We show explicitly that each of the combinations given in table 11.3 can be approximated as a linear combination of the first generation generators α, β, γ and ζ.

To simplify the expressions, we apply an overall time shift E to the variable constructed using the algorithm given in section 11.1.1, such that we solve the equation

$$E\ \mathrm{TDI} = A\alpha + B\beta + C\gamma + D\zeta\,. \tag{11.29}$$

9 In the sense that if we replace the 6 non-commutative delay operators $\mathbf{D}_{ij}$ in any 2nd generation variable with only three commutative delay operators (using the symmetry $\mathbf{D}_{ij} = \mathbf{D}_{ji}$), the resulting variable will be first generation TDI. Note that this map is not necessarily bijective; multiple second generation variables could be mapped to the same first generation variable.

Name	Normal string	$\dot{L}$ closed	M.S.	T.S.	Trivial
C_1^{12}	"1231321 -1321231"		✓	✓	
C_2^{12}	"12321 -1321 131 -1231"			✓	
C_3^{12}	"121 -13 32 -21 13 -323 31 -12 23 -31"		✓	✓	
C_1^{14}	"121321 -13212 231 -1231"				
C_2^{14}	"1213 -3213 32 -2123 3123 -31"			✓	
C_3^{14}	"1213 -32 21 -13 32 -2123 31 -12 23 -31"			✓	
C_1^{16}	"121313121 -131212131"	✓	✓	✓	
C_2^{16}	"121323121 -132121231"			✓	
C_3^{16}	"123121321 -132121231"			✓	
C_4^{16}	"12121 -13121 13131 -12131"	✓	✓	✓	✓
C_5^{16}	"1213121 -13121 131 -12131"	✓		✓	
C_6^{16}	"1213212 -23121 132 -21231"	✓		✓	
C_7^{16}	"123123 -31321 1313 -32131"	✓		✓	
C_8^{16}	"12313123 -31321 13 -32131"	✓		✓	
C_9^{16}	"12121 -13212 23132 -21231"			✓	
C_{10}^{16}	"1213121 -13212 232 -21231"			✓	
C_{11}^{16}	"12312321 -1321 13 -321231"				
C_{12}^{16}	"1231321 -13123 313 -32131"			✓	
C_{13}^{16}	"12121 -1321 132 -212 231 -1231"			✓	
C_{14}^{16}	"1213121 -13 32 -2123212 23 -31"		✓	✓	
C_{15}^{16}	"12132 -2123 3121 -13212 23 -31"		✓		
C_{16}^{16}	"1213 -3212 232 -2123 3121 -131"		✓	✓	
C_{17}^{16}	"12132 -21321 1312 -2312 23 -31"				
C_{18}^{16}	"1213 -321 1321 -1312 231 -1231"			✓	
C_{19}^{16}	"1232321 -1321 13 -323 31 -1231"			✓	
C_{20}^{16}	"1232321 -1323 31 -121 13 -3231"			✓	
C_{21}^{16}	"12123 -3121 13 -32 213 -3212 23 -31"	✓			
C_{22}^{16}	"1213 -3212 23 -3121 13 -32 2123 -31"	✓	✓		
C_{23}^{16}	"12121 -13 32 -2123 313 -3212 23 -31"			✓	
C_{24}^{16}	"1231 -121 13 -321 1321 -131 12 -231"		✓		✓
C_{25}^{16}	"12321 -1323 31 -12 232 -21 13 -3231"			✓	
C_{26}^{16}	"12121 -13 32 -21 13 -32123 31 -12 23 -31"			✓	
C_{27}^{16}	"12132 -21 13 -32 21 -13123 31 -12 23 -31"			✓	
C_{28}^{16}	"121 -132 21 -13 32 -21 131 -123 31 -12 23 -31"		✓		✓

TABLE 11.3: Overview of 2nd generation TDI core combinations up to 16 links. The combinations are labelled by C_B^A, with A as the number of links and B as a running index. C_1^{16} is the familiar Michelson X_2 combination. 'M.S.' indicates whether the combination is mirror symmetric, while 'T.S.' indicates whether it is time symmetric. 'Trivial' indicates if the combination is vanishing in the assumption of equal arms.

Name	Timeshift	Expression
C_1^{12}	1	$(1-xyz)\alpha$
C_2^{12}	xy^2	$(y-xz)\alpha$
C_3^{12}	yz	$(y-xz)\zeta$
C_1^{14}	xy	$\left(1-z^2\right)\alpha$
C_2^{14}	yz	$\left(1-z^2\right)\gamma$
C_3^{14}	y	$\left(1-z^2\right)\zeta$
C_1^{16}	1	$\left(1-y^2z^2\right)(\alpha-z\beta-y\gamma+yz\zeta)$
C_2^{16}	1	$\left(1-xyz^3\right)\alpha-z(1-xyz)\beta$
C_3^{16}	1	$\left(1-xyz^3\right)\alpha$
C_4^{16}	y^4z^2	$(y-z)(y+z)(\alpha-z\beta-y\gamma+yz\zeta)$
C_5^{16}	y^2	$\left(1-z^2\right)(\alpha-z\beta-y\gamma+yz\zeta)$
C_6^{16}	xy	$\left(1-z^2\right)(z\alpha-\beta)$
C_7^{16}	xy^3	$(y-xz)(y\alpha-\gamma)$
C_8^{16}	y	$(1-xyz)(y\alpha-\gamma)$
C_9^{16}	$x^2y^2z^2$	$\left(xy-z^3\right)\alpha+\left(z^2-xyz\right)\beta$
C_{10}^{16}	x^2y	$\left(x-yz^3\right)\alpha+\left(yz^2-xz\right)\beta$
C_{11}^{16}	y	$\left(1-x^2z^2\right)\alpha$
C_{12}^{16}	y^2	$(1-xyz)\alpha+(xz-y)\gamma$
C_{13}^{16}	x^2yz	$\left(xy-z^3\right)\alpha$
C_{14}^{16}	y	$\left(xyz^2-z\right)\gamma+\left(1-xyz^3\right)\zeta$
C_{15}^{16}	xz^2	$(xy-z)\gamma+(1-xyz)\zeta$
C_{16}^{16}	yz^2	$\left(xy-z^3\right)\gamma+\left(-xyz+z^2\right)\zeta$
C_{17}^{16}	xy^2z^2	$(y-xz)\beta$
C_{18}^{16}	x	$(x-yz)\alpha$
C_{19}^{16}	xy^2	$\left(y-x^3z\right)\alpha$
C_{20}^{16}	xy^2	$\left(y-x^3z\right)\alpha+\left(x^2z-xy\right)\zeta$
C_{21}^{16}	yz^2	$(xz-y)(\gamma-z\zeta)$
C_{22}^{16}	yz^2	$\left(1-z^2\right)(\gamma-z\zeta)$
C_{23}^{16}	y^2z^2	$\left(xz^2-yz\right)\gamma+\left(y-xz^3\right)\zeta$
C_{24}^{16}	xyz^3	$\left(z^2-y^2\right)\alpha$
C_{25}^{16}	x^2y	$(y-xz)\alpha+(z-xy)\zeta$
C_{26}^{16}	yz	$\left(y-xz^3\right)\zeta$
C_{27}^{16}	x	$(1-xyz)\zeta$
C_{28}^{16}	y^3z	$(y-z)(y+z)\zeta$

TABLE 11.4: Decomposition of variables from table 11.3 into generators α, β, γ and ζ of first generation TDI. Only valid in the approximation of three unequal constant arms, where we donate the three delay operators by x, y and z. 'Timeshift' denotes the delay to be applied to the combination constructed from the algorithm given in section 11.1.1, i.e., the factor E in eq. (11.29).

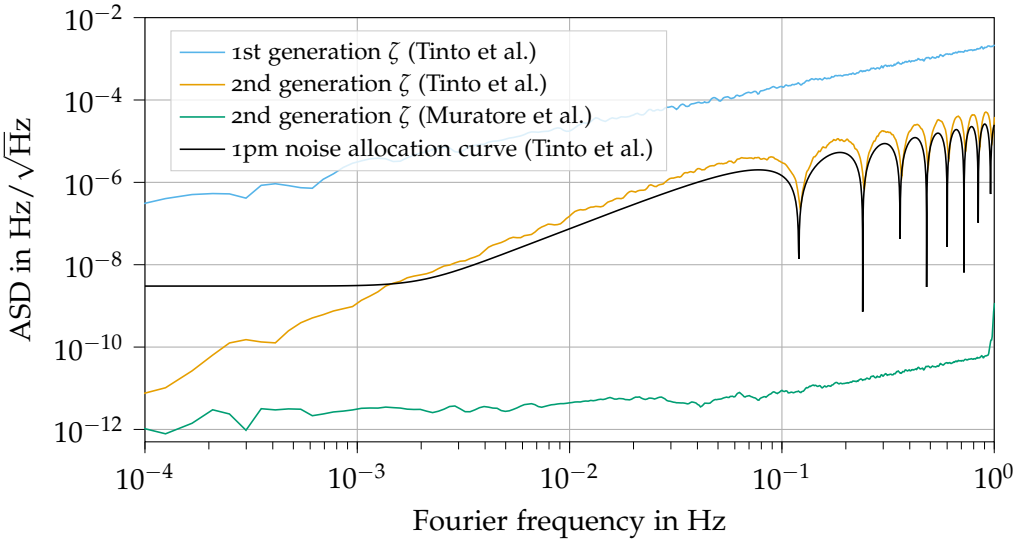

FIGURE 11.4: Laser noise suppression in first generation ζ compared to the second generation version ζ_1 presented in the literature [83] as well as C_{27}^{16}. 1 pm curve multiplied by transfer function of ζ_1.

To avoid confusion (and mimic the notations used in the literature, e.g. [83]), we will replace the usual delay operators appearing in our expressions with three variables x, y, z, according to

$$\mathbf{D}_{12} = \mathbf{D}_{21} = z, \quad \mathbf{D}_{23} = \mathbf{D}_{32} = x, \quad \mathbf{D}_{31} = \mathbf{D}_{13} = y\,. \tag{11.30}$$

We summarize the results in table 11.4. Many of the variables are simple differences of the generators α, β, γ and ζ. This implies that we have multiple options to choose second generation versions of the first generation generators in eqs. (11.27a) to (11.27d). For example, both C_1^{12} and C_2^{12} can be approximated to be proportional to $\dot{\alpha}$. In fact, C_1^{12} and its cyclic permutations are identical to the second generation Sagnac variables previously suggested in the literature (cf. [83]).

In addition, we observe that C_4^{16}, C_{24}^{16} and C_{28}^{16} contain an overall difference term $(y - z)$ or $(y^2 - z^2)$. These terms are vanishing if all delays are assumed equal, which explains why we identified these variables as 'trivial' in table 11.3. We point out, however, that these only vanish if all arms are indeed equal, and are just strongly suppressed in the realistic case of time-varying, unequal arms.

Furthermore, it is argued in [83] that ζ has the special properties of being relatively insensitive to GWs at low frequencies, while α, β and γ are not. We would therefore expect this property to extend to C_3^{12}, C_3^{14}, C_{26}^{16}, C_{27}^{16} and C_{28}^{16}, which approximate a derivative[10] of ζ. This could make these variables interesting for distinguishing a gravitational wave background from instrumental noise.

10 At low frequencies, a difference of delays can be approximated as derivative.

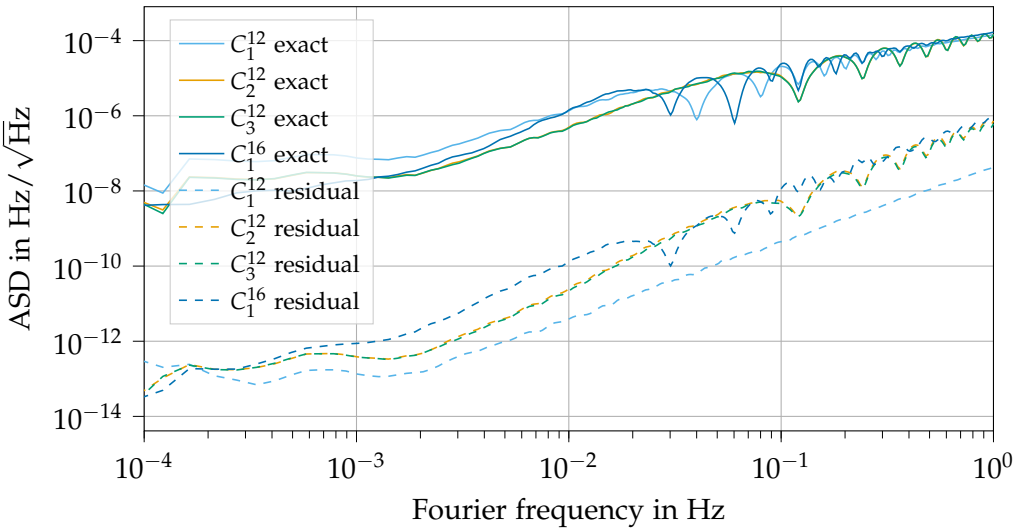

FIGURE 11.5: Secondary noises in exact expression for C_1^{12}, C_2^{12}, C_3^{12} and C_1^{16} compared to residual wrt. approximation given in table 11.4.

Note that all variables given in table 11.3 suppress laser noise to the same level, contrary to the second generation variables ζ_1, ζ_2 and ζ_3 proposed in [83]. In our notation, these are given as

$$\begin{aligned}\zeta_1 =&(\mathbf{D}_{232} - \mathbf{D}_{13}\mathbf{D}_{21}\mathbf{D}_{32})\eta_{12} - (\mathbf{D}_{323} - \mathbf{D}_{12}\mathbf{D}_{31}\mathbf{D}_{23})\eta_{13}\\ &+ (\mathbf{D}_{32}\mathbf{D}_{13} - \mathbf{D}_{12}\mathbf{D}_{313})(\eta_{23} - \eta_{21})\\ &+ (\mathbf{D}_{23}\mathbf{D}_{12} - \mathbf{D}_{13}\mathbf{D}_{212})(\eta_{31} - \eta_{32})\,,\end{aligned} \tag{11.31}$$

and cyclic permutations for ζ_2 and ζ_3.

To verify the different levels of laser noise suppression, we simulate 10^5 samples of data containing only laser noise using `LISA Instrument`, and computed ζ, ζ_1 and C_{27}^{16}, using a high interpolation order 65 such that interpolation artifacts appear mostly off-band. We used travel times computed from the usual ESA provided orbits, as shown in fig. 3.3. The result is plotted in fig. 11.4, where we see that while ζ_1 does perform significantly better than ζ, it does not meet the 1 pm requirement, and is many orders of magnitude above C_{27}^{16}.

11.5.2 *Verification by simulation*

11.5.2.1 *Decomposition in first generation*

To verify that the decompositions shown in table 11.4 are good approximations for the secondary noises, we run a simplified simulation using `LISA Instrument`. We simulate 10^5 samples with only readout noise and test-mass acceleration noise enabled, and do not simulate laser locking. We use the same realistic ESA orbits as in chapter 8, and the same sampling rates and anti-aliasing filter.

As an example, we compute the combinations C_1^{12}, C_2^{12}, C_3^{12} and C_1^{16} exactly, using the algorithm given in section 11.1.1. We do the same for the first generation generators α, β, γ and ζ, as given in eqs. (11.27a) to (11.27d).

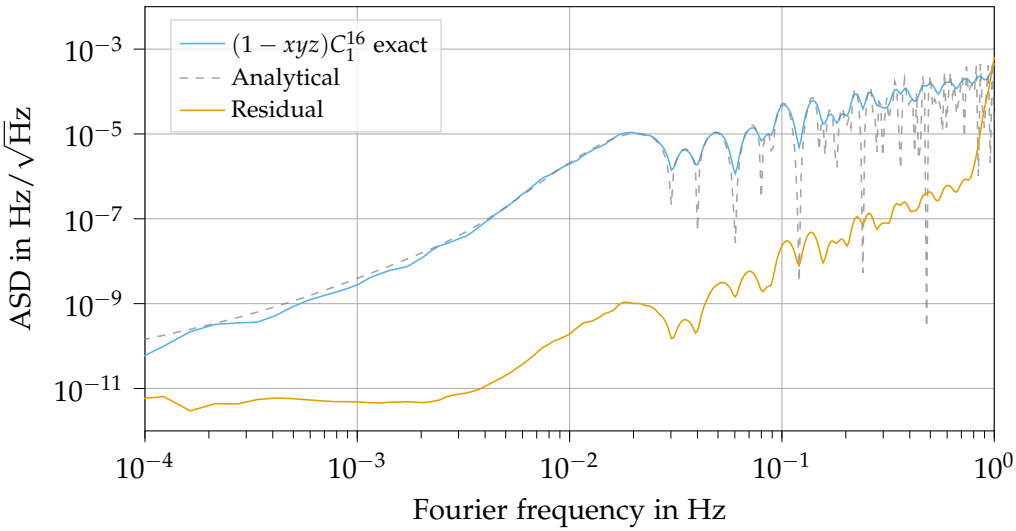

FIGURE 11.6: Exact expression for $(1 - xyz)C_1^{16}$ compared to analytical estimate of secondary noise levels and residual wrt. approximation given in eq. (11.36).

We then estimate the delays x^d, y^d, z^d applied by x, y, z via

Meaning that $xf(t) = f(t - x^d)$, and similar for y, z.

$$x^d = \text{mean}\left[\frac{d_{23}(t) + d_{32}(t)}{2}\right] \tag{11.32}$$

$$y^d = \text{mean}\left[\frac{d_{31}(t) + d_{13}(t)}{2}\right] \tag{11.33}$$

$$z^d = \text{mean}\left[\frac{d_{12}(t) + d_{21}(t)}{2}\right], \tag{11.34}$$

with $d_{ij}(t)$ as the time series of MPRs output by the simulation. We use these delays to compute the expressions given in table 11.4, and compare the results to the exact versions[11] of C_1^{12}, C_2^{12}, C_3^{12} and C_1^{16}.

The result is plotted in fig. 11.5, where we give the amplitude spectral density (ASD) of the exact version compared to the time-domain residual between the exact version and the approximation. We see that the residual is several orders of magnitude below the actual secondary noise levels, such that the expressions given in table 11.4 should indeed give good approximations of the secondary noises in the 2nd generation variables.

11.5.2.2 *Decomposition in second generation*

As a proof of concept that these decompositions are also applicable for the second generation variables, we re-run the same simulation with laser noise enabled.

There are other options we could have used instead, for example the cyclic permutations of C_2^{12} together with C_3^{12}.

Inspecting table 11.4, we observe that C_1^{12} and its cyclic permutations together with C_{27}^{16} give expressions for α, β, γ and ζ with the same pre-factor $(1 - xyz)$.

11 Here, we also have to apply the additional time-shift given in table 11.4.

We can therefore define

$$\tilde{\alpha} = \mathrm{TDI}[\texttt{"1231321 -1321231"}], \tag{11.35a}$$
$$\tilde{\beta} = \mathrm{TDI}[\texttt{"2312132 -2132312"}], \tag{11.35b}$$
$$\tilde{\gamma} = \mathrm{TDI}[\texttt{"3123213 -3213123"}], \tag{11.35c}$$
$$\tilde{\zeta} = \mathbf{D}_{23}\mathrm{TDI}[\texttt{"12132 -21 13 -32 21 -13123 31 -12 23 -31"}]. \tag{11.35d}$$

Since we are allowed to commute delays in our approximation, we can use these generators in our expressions given in table 11.4 to construct versions of the TDI variables which are modulated[12] by $(1 - xyz)$.

For example, we get

$$\begin{aligned} \tilde{C}_1^{16} &= \left(1 - y^2z^2\right)\left(\tilde{\alpha} - z\tilde{\beta} - y\tilde{\gamma} + yz\tilde{\zeta}\right) \\ &\approx (1 - xyz)\left(1 - y^2z^2\right)(\alpha - z\beta - y\gamma + yz\zeta) \\ &\approx (1 - xyz)C_1^{16}\,. \end{aligned} \tag{11.36}$$

To determine if this decomposition is accurate, we can construct the exact expression for any of these variables, and then apply the same factor $(1 - xyz)$ to it. We demonstrate this in fig. 11.6 for C_1^{16}. Laser noise is fully suppressed, and the noise level of the simulated data (in orange) is perfectly explained by the enabled secondary noises (in dotted grey). We show that the residual noise between the exact variable $(1 - xyz)C_1^{16}$ and our approximate solution $\tilde{C}_1^{16}$, computed as $(1 - xyz)C_1^{16} - \tilde{C}_1^{16}$, is several orders of magnitude below the secondary noises.

These results indicate that a set of second generation versions of the generators of first generation TDI such as those given in eqs. (11.35a) to (11.35d) might be sufficient for most data analysis needs.

12 This modulation can probably be removed using a suitable integrating filter, or at least compensated by dropping one delay difference already present in all second generation variables (for example, removing the factor $\left(1 - y^2z^2\right)$ from $\tilde{C}_1^{16}$) to get a variable with similar response, without additional suppression at low frequencies. We go here the other way around by including the factor $(1 - xyz)$ in the constructed variable to show a proof-of-principle that the decomposition works.

12

TDI IN PRACTICE

So far, we have described the basic principles behind TDI using a simplifed model of the LISA measurements expressed in total phase. In this chapter, we will discuss how these measurements can be constructed out of the raw data streams, what the technical limitations of TDI are and how TDI has to be adapted if the input data is given in frequency instead of phase.

We first briefly revisit the first INREP processing steps of constructing the virtual test-mass to test-mass measurement out of the three interferometers on each optical bench in section 12.1.

We then discuss the impact laser locking has on the secondary noise levels in TDI in section 12.2, and study different limiting factors for the achievable laser noise reduction in section 12.3.

Finally, we discuss how TDI has to be adapted when using phasemeter measurements given in units of frequency instead of phase in section 12.4.

12.1 SPLIT INTERFEROMETRY AND INTERMEDIARY VARIABLES

As outlined in sections 3.4.3 and 9.1.3, one of the first processing steps in the INREP is to combine data produced by the three interferometers on each optical bench to synthesize a total of 6 virtual test-mass to test-mass measurements. This can be described in two steps, as we outline below. Similar expressions for the intermediary variables can be found in the literature (cf. for example [64]). We give them here updated to our notation, and respecting the sign conventions introduced in chapter 5.

12.1.1 *Removal of optical bench displacement noise*

As described in section 3.4.4, the spacecraft will try to follow a free-falling test-mass along each sensitive axis by means of the DFACS.

However, as shown in LISA Pathfinder [12], this control system is not perfect, and the inter-spacecraft interferometer will contain residual jitter on the order of nm, which is 3 orders of magnitude above the desired level of pm.

The solution to this problem is to construct the so-called ξ variable,

$$\xi_{12} = \mathrm{isc}_{12} + \frac{\mathrm{ref}_{12} - \mathrm{tm}_{12}}{2} + \frac{\mathbf{D}_{12}(\mathrm{ref}_{21} - \mathrm{tm}_{21})}{2}\,, \tag{12.1}$$

In reality, the delays $\mathbf{D}_{12}$ will not be known perfectly, and need to be implemented using an interpolation scheme, cf. section 9.1.3. In addition, the individual spacecraft clocks need to be taken into account when combining data from different spacecraft, cf. chapter 13. We neglect these technical issues for now.

which combines the inter-spacecraft interferometer with the difference of reference and test-mass interferometer to construct a virtual test-mass to test-mass measurement[1].

This construction is symmetric among all 6 optical benches, which is why it is sufficient to give here only the expression for ξ_{12}. The expressions for all other 6 optical benches can be deduced by applying the usual 6 index permutations, cf. appendix A.

Note that *if* the DFACS was perfect, and there was no additional sensing noise entering the control loop, the test-mass interferometer would only measure a constant phase offset, yielding the simplification $\xi_{ij} \approx \mathrm{isc}_{ij}$.

12.1.2 *Reduction to three lasers*

This is the case for locking schemes N1, N3 and N5.

The second goal of constructing the intermediary variable is to remove the frequency fluctuations of half the lasers in the constellation. This could be realized in hardware by choosing a locking scheme in which the two lasers on each spacecraft are locked to each other, cf. section 7.3. However, we cannot assume that the laser locking is perfect; in addition, we do not want to exclude the remaining locking schemes. Regardless of the locking scheme, we always have the option to remove half of the laser contributions in a post-processing step, by constructing the intermediary variables η_{ij}. They are given as

$$\eta_{12} = \xi_{12} + \frac{\mathbf{D}_{12}(\mathrm{ref}_{21} - \mathrm{ref}_{23})}{2} \tag{12.2a}$$

$$\eta_{13} = \xi_{13} + \frac{(\mathrm{ref}_{12} - \mathrm{ref}_{13})}{2} \tag{12.2b}$$

Contrary to ξ, the η variables are not symmetric across all 6 optical benches, but differ between the left and right handed one aboard each spacecraft. This loss of symmetry is due to our choice which of the two lasers of the spacecraft to remove. Therefore, we have to give expressions for η_{12} and η_{13}, and those of the other spacecraft can be deduced form cyclic index permutation, cf. appendix A.

Note that both reference beatnotes on the spacecraft measure the interference of the same lasers, so they nominally measure the same signal, just with opposite signs (up to secondary noises). If one of them is used to lock the local lasers, this signal is just equal to a pre-programmed frequency offset. In the limit of assuming a perfect frequency lock (with no residual in-band fluctuations), we could neglect it, and get $\eta \approx \xi$.

1 We assume here that the beatnote signs (cf. section 5.4.2) have been fixed in the phasemeter or in a first processing step. In addition, we neglect that the optical bench motion terms N_{ij}^{Δ} enter eq. (7.7b) and eq. (7.11b) scaled by different laser frequency offsets. Since the laser frequency offsets are known from the frequency plan, we could include these scaling factors. But we remark that neglecting them will only create a residual noise scaled by roughly $20\,\mathrm{MHz}/282\,\mathrm{THz} \approx 7 \times 10^{-8}$, which is far below the needed level of suppression. We therefore omit them for clarity.

12.2 SECONDARY NOISE LEVELS IN TDI

We have so far described TDI in terms of a generic laser phase Φ or phase and frequency fluctuations p_i and $\dot{p}_i$, respectively.

As described in section 7.3, all but one laser in LISA will be locked to one primary laser. The locked lasers frequency will be controlled to drive the phasemeter signal used for locking to a pre-programmed reference value. In that process, it will inherit any noise of the primary laser, optical pathlength fluctuations during propagation as well as readout noises in the phasemeter channel used for locking. This effect is compounded when multiple lasers are locked in a chain, which is required to reach all lasers in the constellation.

Therefore, each term p_i in the phasemeter equations given in section 7.2 is actually a complicated combination of multiple noise terms with potentially several delays. At first sight, this seems to imply a complicated coupling of these noise terms into the final TDI observable.

However, it turns out that all of these additional noise terms are suppressed alongside the laser noise, such that the choice of the locking configuration does not significantly impact the secondary noise levels in the final variable.

12.2.1 *Secondary noises in TDI with locked lasers*

As described in section 5.3, p_{ij} denotes the phase fluctuations of the laser associated to MOSA ij. These can be either the inherent frequency fluctuations due to the cavity used for frequency stabilizations, or fluctuations imprinted on the laser due to laser locking.

If we neglect the onboard filter, the timestamping errors and any technical imperfections in TDI for now, the intermediary variables (cf. section 12.1) can be written as

We use here expressions in phase fluctuations, but the same reasoning can be extended to frequency fluctuations by using the Doppler-delays introduced in section 12.4.

$$\eta_{ij} = \mathbf{D}_{ij} p_j - p_i + N_{\eta_{ij}} \,, \tag{12.3}$$

where we dropped the second index of the respective p_{ij} still present after construction of η_{ij}, and $N_{\eta_{ij}}$ accounts for all secondary noise terms in η_{ij} which enter with different correlations than the laser noise terms.

If we were to replace the p_i terms with the expressions derived from the locking rules given in section 7.3, some of the η_{ij} would cancel at this point, and others would become a complicated combination of noise terms; however, it is useful to keep p_i unevaluated for now.

We know from section 10.3 that we can factorize any TDI combination as given in eq. (10.32),

$$\mathrm{TDI} = \sum_{ij \in \mathcal{I}_2} \mathbf{P}_{ij} \eta_{ij} \,. \tag{12.4}$$

This is neglecting any technical imperfection in constructing the TDI variable, as discussed in section 12.3, which add terms proportional to all 6 lasers. These additional terms are also highly suppressed, and therefore also not relevant for the un-suppressed secondary noises.

Furthermore, we know from chapter 10 that the TDI variable is constructed in such a way that only the laser phase fluctuations p_i of a single laser appear in them, scaled by a difference term corresponding to photon paths with almost equal time delays. As we saw in section 10.2, this difference of delays corresponds to a suppression of more than 10 orders of magnitude across the whole LISA frequency band[2]. On the other hand, any noise sources entering η_{ij} with different correlations than the laser noise terms will not be meaningfully suppressed, but simply have their spectrum modulated by the delay polynomials $\mathbf{P}_{ij}$.

Overall, we get

$$\text{TDI} = [\mathbf{D}_{A_1 \dots A_n} - \mathbf{D}_{B_1 \dots B_n}] p_i + \sum_{ij \in \mathcal{I}_2} \mathbf{P}_{ij} N_{\eta_{ij}} \,, \tag{12.5}$$

where we used $A_1 \dots A_n$ and $B_1 \dots B_n$ as placeholder for the photon paths defining the combination. Which p_i appears in our combination is determined by the starting spacecraft of the TDI string used to define the combination.

It is argued in section 11.3 that we can apply cyclic string shifts to a combination without meaningfully changing its output. This allows us to change which laser noise p_i appears in eq. (12.5).

Following section 7.3, each p_i can be written as a potentially delayed version of the primary lasers phase fluctuations, plus any secondary noises entering either in the propagation to or the readout at the interferometer used for locking.

We use a simplified notation to describe this relationship, by writing

$$p_i = \mathbf{D}_{\text{lock}} p_0 + N_{p_i} \tag{12.6}$$

for a locked laser, with p_0 as the laser noise of the primary laser, $\mathbf{D}_{\text{lock}}$ a series of delays depending on the locking scheme and N_{p_i} a term summarizing all secondary noise terms entering due to the locking.

Inserting this expression into eq. (12.5), we get

$$\text{TDI} = [\mathbf{D}_{A_1 \dots A_n} - \mathbf{D}_{B_1 \dots B_n}](\mathbf{D}_{\text{lock}} p_0 + N_{p_i}) + \sum_{ij \in \mathcal{I}_2} \mathbf{P}_{ij} N_{\eta_{ij}} \,. \tag{12.7}$$

We see that the secondary noise terms for each η_{ij} (without considering the laser locking) appear scaled by $\mathbf{P}_{ij}$, while all the additional secondary noise term imprinted on the laser beam are suppressed by the same delay term as the laser noise.

Since laser noise needs to be suppressed by roughly 8 order of magnitudes, we conclude that the additional secondary noise terms entering with the same suppression are completely negligible compared to the terms entering scaled by the delay polynomials $\mathbf{P}_{ij}$.

For example, if we assume each noise term $N_{\eta_{ij}}$ to be uncorrelated to the others, we can estimate the residual noise level in any TDI variable by computing

$$S_{\text{TDI}_{N_\eta}} \approx \sum_{ij \in \mathcal{I}_2} \left| \widetilde{\mathbf{P}}_{ij} \widetilde{N}_{\eta_{ij}} \right|^2 . \tag{12.8}$$

2 The fundamental arm length mismatch of the photon paths making up a second generation TDI combination is $\Delta\tau \approx 10\,\text{ps}$, such that the residual laser noise is scaled by $2\pi f \Delta\tau < 10^{-10}$.

As argued in section 10.3, it is here often sufficient to compute the Fourier transform of the delay polynomials $\widetilde{\mathbf{P}}_{ij}$ under the assumption that all delays are equal.

This is usually the case as long as the combination in question does not meaningfully suppress the noise being considered.

12.2.2 *Examples*

As examples of transfer functions for secondary noises, we want to compute how the two limiting secondary noises included in our simulation, readout noise and test-mass acceleration noise, couple into the second generation Michelson variable X_2.

Under the assumption of three equal arms, the $\mathbf{P}_{ij}$ of X_2 are simply given as

$$\mathbf{P}_{12} = -\mathbf{P}_{13} = (1-\mathbf{D}^4)(1-\mathbf{D}^2)\,, \tag{12.9}$$

$$\mathbf{P}_{21} = -\mathbf{P}_{31} = (1-\mathbf{D}^4)(1-\mathbf{D}^2)\mathbf{D}\,, \tag{12.10}$$

with the Fourier transform

$$\widetilde{\mathbf{P}}_{12} = -\widetilde{\mathbf{P}}_{13} = (1-e^{-i\omega 4d})(1-e^{-i\omega 2d})\,, \tag{12.11}$$

$$\widetilde{\mathbf{P}}_{21} = -\widetilde{\mathbf{P}}_{31} = (1-e^{-i\omega 4d})(1-e^{-i\omega 2d})e^{-i\omega d}\,. \tag{12.12}$$

Here, following [39], it is useful to define

$$C_{XX} = \left|(1-e^{-i\omega 4d})(1-e^{-i\omega 2d})\right|^2 = 64\cos^2(d\omega)\sin^4(d\omega)\,. \tag{12.13}$$

For readout noise, we need to distinguish between readout noise in the ISC, reference and test-mass interferometers. We assume all of these to be uncorrelated, with noise levels given in appendix D.5.

Inserting the phasemeter equations given in chapter 7 into the intermediary variables given in section 12.1, and ignoring all terms except for the readout noise, we get

$$\eta_{12} = \dot{N}^{\mathrm{ro}}_{\mathrm{isc}_{12,c}} + \frac{\dot{N}^{\mathrm{ro}}_{\mathrm{ref}_{12,c}} - \dot{N}^{\mathrm{ro}}_{\mathrm{tm}_{12,c}}}{2} + \mathbf{D}_{12}\left(\dot{N}^{\mathrm{ro}}_{\mathrm{ref}_{21,c}} - \frac{\dot{N}^{\mathrm{ro}}_{\mathrm{ref}_{23,c}} + \dot{N}^{\mathrm{ro}}_{\mathrm{tm}_{21,c}}}{2}\right), \tag{12.14}$$

$$\eta_{13} = \dot{N}^{\mathrm{ro}}_{\mathrm{isc}_{13,c}} + \frac{\dot{N}^{\mathrm{ro}}_{\mathrm{ref}_{12,c}} - \dot{N}^{\mathrm{ro}}_{\mathrm{tm}_{13,c}}}{2} + \mathbf{D}_{13}\left(\frac{\dot{N}^{\mathrm{ro}}_{\mathrm{ref}_{31,c}} - \dot{N}^{\mathrm{ro}}_{\mathrm{tm}_{31,c}}}{2}\right), \tag{12.15}$$

and cyclic for the other η_{ij}.

All readout noise terms are assumed to be uncorrelated, but some of them appear in multiple η_{ij}. For these, we cannot directly use eq. (12.8), but need to instead collect the correct factors and delays of all terms appearing in the TDI combinations before computing the squared magnitude.

Overall, this gives

$$S_{X_2^{\mathrm{ro}}} = \left[4(S_{\dot{N}^{\mathrm{ro}}_{\mathrm{isc}}} + S_{\dot{N}^{\mathrm{ro}}_{\mathrm{ref}}}) + (3+\cos(2\omega d))S_{\dot{N}^{\mathrm{ro}}_{\mathrm{tm}}}\right] C_{XX}\,. \tag{12.16}$$

For the test-mass acceleration noise, we instead simply have

$$\eta_{ij} = -\nu_0(\dot{N}^{\delta}_{ij} - \mathbf{D}_{ij}\dot{N}^{\delta}_{ji}), \quad \forall ij \in \mathcal{I}_2\,. \tag{12.17}$$

We can assume all 6 test-masses to be uncorrelated and collect the respective terms, to get the PSD

$$S_{X_2^{\mathrm{tm}}} = 4\nu_0^2(3+\cos(2\omega d))C_{XX}S_{\dot{N}^{\delta}}\,, \tag{12.18}$$

where $S_{\dot{N}^{\delta}}$ is the jitter of a single test-mass expressed as a dimensionless fractional frequency shift.

These formulas are verified by the simulation results presented in fig. 9.1, where the secondary noise level in X, Y and Z could be perfectly explained by the sum of eqs. (12.16) and (12.18).

12.3 LASER NOISE RESIDUALS

As discussed in section 10.2, TDI has a fundamental limit to the achievable level of noise suppression determined by the armlength mismatch of the corresponding interferometer.

However, there are additional technical noise couplings which can limit the achievable overall noise suppression.

Contrary to the secondary noises described in section 12.2.1, the residual laser noise will depend on the locking scheme. We will derive all couplings below for the special case of locking scheme N1-L12, but remark that the same principle is applicable to all other locking schemes. In addition, it should be noted that the locking schemes break the usual triangle symmetry, such that the cyclic permutations of the same variable (e.g., the three Michelson variables X, Y and Z) will have different laser noise residuals.

We consider only the primary lasers phase fluctuations p_0. Following section 7.3, this laser noise term is distributed throughout the whole constellation, such that we get in our locking scheme

$$p_{12} = p_{13} = p_0\,, \tag{12.19a}$$
$$p_{21} = p_{23} = \mathbf{D}_{21}p_0\,, \tag{12.19b}$$
$$p_{31} = p_{32} = \mathbf{D}_{31}p_0\,, \tag{12.19c}$$

for the different laser fluctuations.

12.3.1 *Fundamental armlength mismatch*

In the absence of technical imperfections, we know from chapters 10 and 11 that the TDI combinations are designed to give a laser noise residual of the form

$$\mathrm{TDI} = [\mathbf{D}_{A_1\ldots A_n} - \mathbf{D}_{B_1\ldots B_n}]p_i \tag{12.20}$$
$$= [\mathbf{D}_{A_1\ldots A_n} - \mathbf{D}_{B_1\ldots B_n}]\mathbf{D}_{\mathrm{lock}}p_0 \tag{12.21}$$

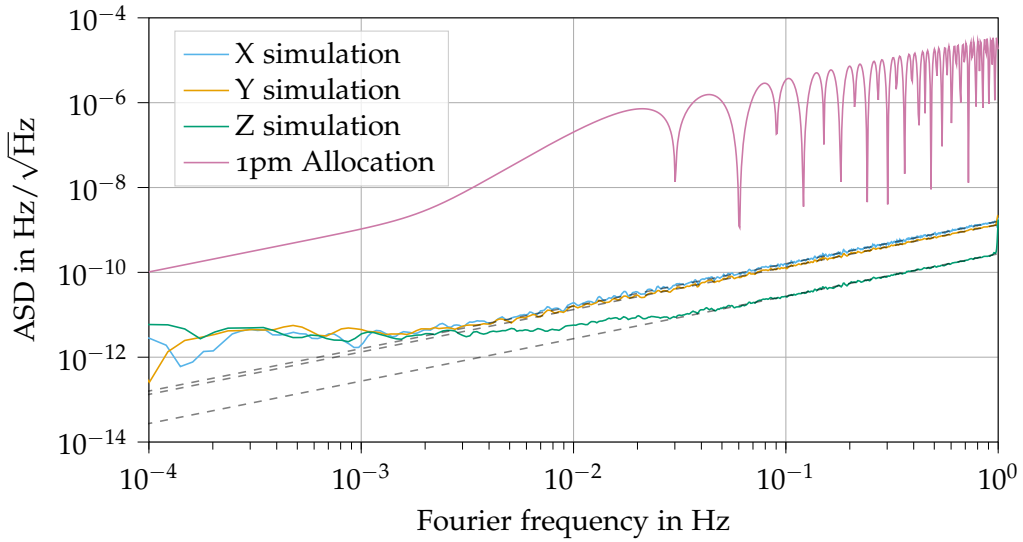

FIGURE 12.1: Fundamental laser locking limit for TDI X, Y and Z with laser locking enabled. The same analytical model we derived without laser locking (in dotted grey) still applies.

where p_i is the laser noise for the starting spacecraft of any combination, and all other laser noise terms cancel. Here, $[\mathbf{D}_{A_1 \ldots A_n} - \mathbf{D}_{B_1 \ldots B_n}]$ is a placeholder for the actual delay commutator defined by the photon path of the particular combination under study.

Inserting eqs. (12.19a) to (12.19c) into this equation shows that we get the same fundamental laser noise suppression limit we had before, with the only difference that the primary lasers noise appears with up to one additional delay $\mathbf{D}_{\text{lock}}$, which does not affect the noise level.

Thus, the Fourier transform of this term can be approximated as

$$\mathcal{F}\left[[\mathbf{D}_{A_1 \ldots A_n} - \mathbf{D}_{B_1 \ldots B_n}]\mathbf{D}_{\text{lock}} p_0\right] \approx \omega \Delta\tau e^{-i\omega Q d} \widetilde{p_0}(\omega)\,, \tag{12.22}$$

with $Q = n$ if the photon path starts at spacecraft 1 and $Q = n + 1$ otherwise. $\Delta\tau$ is the armlength mismatch of the TDI combination.

To verify this, we run a simulation of 10^5 s using `LISANode`, with only laser noise enabled and no bias in the ranging. The light-travel time between the spacecraft are computed based on the ESA orbits, as shown in fig. 3.3. We use the locking scheme N1-LA12, and a stronger anti-aliasing filter with 320 dB attenuation in order to not be limited by aliasing. We then compute the second generation TDI X, Y and Z using a high interpolation order of 65, such that interpolation errors appear off-band. The result is plotted in fig. 12.1, and agrees well with the analytical model given in section 10.2, overlayed in grey. At low frequencies, we are limited by numerical errors.

12.3.2 *Technical imperfections*

The algorithm outlined in chapters 10 and 11 works under the assumption that the delay operators applied in post-processing are identical to those modelling the actual propagation between the spacecraft. In addition, they

did not account for the filter operator present in the phasemeter equations given in section 7.2.

We can model these effects in multiple steps. First, we can insert eqs. (12.19a) to (12.19c) into the phasemeter equations given in chapter 7 and those for the intermediary variables given in section 12.1 to get[3]

$$\eta_{12} = \mathbf{F}(\mathbf{D}_{121} - 1)p_0\,, \tag{12.23a}$$
$$\eta_{13} = \mathbf{F}(\mathbf{D}_{131} - 1)p_0\,, \tag{12.23b}$$
$$\eta_{23} = \mathbf{F}(\mathbf{D}_{231} - \mathbf{D}_{21})p_0\,, \tag{12.23c}$$
$$\eta_{32} = \mathbf{F}(\mathbf{D}_{321} - \mathbf{D}_{31})p_0\,, \tag{12.23d}$$
$$\eta_{21} = 0\,, \tag{12.23e}$$
$$\eta_{31} = 0\,. \tag{12.23f}$$

Here, we neglected the impact of the timestamping operator, which we will discuss in detail in chapter 13.

As described above, we can write any TDI combination as

$$\mathrm{TDI} = \sum_{ij \in \mathcal{I}_2} \mathbf{P}_{ij}\eta_{ij}\,, \tag{12.24}$$

which now simplifies to

$$\begin{aligned}\mathrm{TDI} = \big[&\mathbf{P}_{12}\mathbf{F}(\mathbf{D}_{121} - 1) + \mathbf{P}_{13}\mathbf{F}(\mathbf{D}_{131} - 1) \\ &+ \mathbf{P}_{23}\mathbf{F}(\mathbf{D}_{231} - \mathbf{D}_{21}) + \mathbf{P}_{32}\mathbf{F}(\mathbf{D}_{321} - \mathbf{D}_{31})\big]\,p_0\,.\end{aligned} \tag{12.25}$$

The delay polynomials $\mathbf{P}_{ij}$ contain the delays we apply in post-processing, for which we use the different symbol $\mathcal{D}_{ij}$. They will be affected by any ranging errors in our MPR (cf. section 12.3.2.1) as well as errors due to the interpolation (cf. section 12.3.2.2).

Instead of modelling these errors in each delay appearing in each $\mathbf{P}_{ij}$, we will go the other way around, and replace all propagation delays $\mathbf{D}_{ij}$ appearing in eq. (12.25) with offline delays $\mathcal{D}_{ij}$. Each of these replacement will introduce an additive error term, as described below. In addition, we can commute the filter operator $\mathbf{F}$ with all delays to its right, such that it appears right next to the laser noise p_0.

Overall, this will yield a laser noise residual as in eq. (12.21), where the delay commutator now consists of only offline delays and is applied to the filtered laser noise, in addition to a number of additional noise terms as described below.

For each of these effects, we will run a simulation to highlight it by choosing appropriate parameters. Not that these parameters are usually not realistic, and lead to higher residual laser noise levels than we will have in the actual mission. In all cases, we simulate 10^5 s using `LISANode`, with laser noise enabled using the locking scheme N1-LA12 and a strong anti-aliasing filter

3 Note that with this locking scheme, and considering only laser noise, we have simply $\eta_{ij} \equiv \mathrm{isc}_{ij}$, as described in section 12.1.

with an attenuation of 320 dB. We will overlay in each case the analytical model given in section 12.3.2.4, but considering only the single effect under study.

12.3.2.1 *Ranging errors*

We call ranging errors any mismatch between the delays we apply in post-processing and the real propagation delays. This is not to be confused with the fundamental armlength mismatch presented in section 12.3.1, which only depends on the orbital mechanics.

Depending on in which reference frame the data is given, the real delays we should apply can be either light travel times computed in the TCB or they could be MPRs including the clock desynchronizations, cf. chapter 13.

In our case, we will consider as a first step offline delays $\mathcal{D}^{\mu}_{ij}$ which carry a constant bias[4] μ with respect to the true delays, but are still considered free of interpolation errors, such that we have

$$\mathbf{D}_{ij} f(t) = f(t - d_{ij}) \quad \text{and} \quad \mathcal{D}^{\mu}_{ij} f(t) = f(t - d_{ij} - \mu_{ij}) \,. \tag{12.26}$$

Assuming that μ_{ij} is small, we can introduce the operator Δ^{μ}_{ij}, defined by

$$\Delta^{\mu}_{ij} f(t) = (\mathbf{D}_{ij} - \mathcal{D}^{\mu}_{ij}) f(t) \approx \mu_{ij} \dot{f}\big(t - d_{ij}\big) \,. \tag{12.27}$$

In the Fourier domain, we simply get

$$\mathcal{F}\left[\Delta^{\mu}_{ij}\right](\omega) \approx \mu_{ij} \omega e^{-i\omega d_{ij}} . \tag{12.28}$$

To test this in the simulation, we use a large ranging bias of 10 m in each arm and again use a high interpolation order of 65. The result is shown in fig. 12.2, where the overlayed analytical model in dotted grey agrees perfectly with the simulated result, except at very low frequencies where we are again limited by numerical effects. Interestingly, TDI X appears to be significantly less sensitive to ranging noise in this locking scheme, presumably due to the special role spacecraft 1 has in both the locking scheme and the TDI combination.

12.3.2.2 *Interpolation errors*

As described in detail in appendix B, the interpolation with Lagrange polynomials causes an error depending on the fractional delay. We will track this error term by introducing the operator Δ^{I}_{ij}, given as

$$\Delta^{I}_{ij} = (\mathcal{D}^{\mu}_{ij} - \mathcal{D}_{ij}) \,. \tag{12.29}$$

It is derived in appendix B.2, with its Fourier transform given in eq. (B.26). It can be written as

$$\mathcal{F}\left[\Delta^{I}_{ij}\right](\omega) = e^{-i\omega d_{ij}} \widetilde{\epsilon}_{ij}(\omega) \,, \tag{12.30}$$

4 As described in section 13.5, the ranging data can be filtered to remove most in-band fluctuations. A detailed analysis of the coupling of in-band ranging noise is under development inside the LDPG with contributions from the author of this thesis, but was not finalized at the time of writing. It should be available in the future in an upcoming publication.

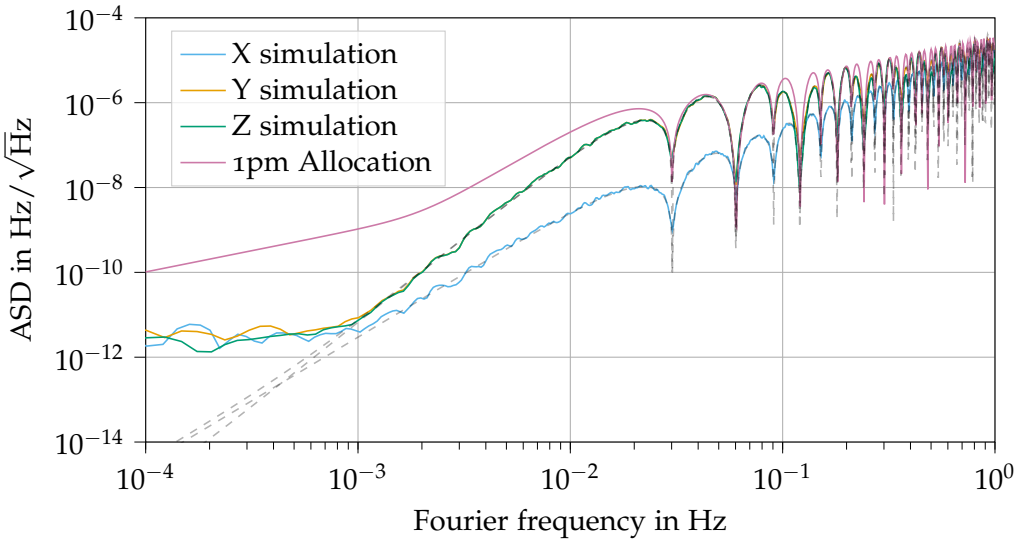

FIGURE 12.2: Laser noise residual due to a constant ranging bias for TDI X, Y and Z with laser locking enabled. To highlight the effect, we use a large bias of 10 m in each arm. The coupling into X is strongly suppressed compared to Y and Z. Model overlayed in dotted grey.

where $\widetilde{\epsilon}_{ij}$ is a term depending on the Lagrange interpolation coefficients c_k^ϵ,

$$\widetilde{\epsilon}_{ij}(\omega) = \left[\left(\sum_{k=-p+1}^{p} c_k^\epsilon e^{i\omega(k/f_s + d_{ij}^\epsilon)} \right) - 1 \right] . \tag{12.31}$$

See appendix B.2 for more details.

Together with eq. (12.27), we then get

$$\mathbf{D}_{ij} = \mathcal{D}_{ij} + \Delta_{ij}^I + \Delta_{ij}^\mu . \tag{12.32}$$

For a nested delay, we instead get

$$\begin{aligned} \mathbf{D}_{ijk} &= (\mathcal{D}_{ij} + \Delta_{ij}^I + \Delta_{ij}^\mu)(\mathcal{D}_{jk} + \Delta_{jk}^I + \Delta_{jk}^\mu) && \text{(12.33a)} \\ &\approx \mathcal{D}_{ijk} + \underbrace{\Delta_{ij}^I \mathcal{D}_{jk} + \mathcal{D}_{ij}\Delta_{jk}^I}_{\equiv \Delta_{ijk}^I} + \underbrace{\Delta_{ij}^\mu \mathcal{D}_{jk} + \mathcal{D}_{ij}\Delta_{jk}^\mu}_{\equiv \Delta_{ijk}^\mu} , && \text{(12.33b)} \end{aligned}$$

where we neglect terms second order in Δ_{ij}^I or Δ_{ij}^μ.

To test this in the simulation, we use the same input data as in section 12.3.1, but this time we compute the TDI variables with a very low interpolation order of just 5. The result is shown in fig. 12.3, again overlaying the analytical model with the simulation results. We see that our model in dotted grey reproduces the general trend and noise level, but is unable to capture the finer structure.

12.3.2.3 *Flexing-filtering coupling*

We need to move all filter operators next to the laser noise term p_0. It was argued in [24] that the filter operator does not commute with a time-varying

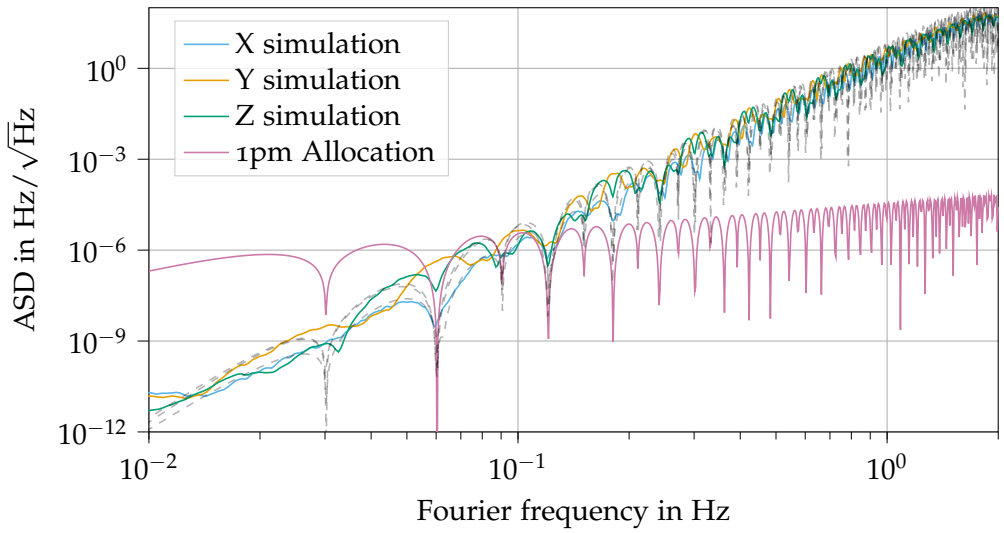

FIGURE 12.3: Laser noise residual due to interpolation errors in TDI X, Y and Z with laser locking enabled. To highlight the effect, we use a very small interpolation order of just 5. The model overlayed in dotted grey captures the general trend and noise level, but is not able to explain the fine structure of the noise.

delay, giving rise to the so-called flexing-filtering coupling. We can keep track of each commutation by introducing a filter-delay commutator:

$$\left[\mathbf{F}, \mathcal{D}_{ij}\right] = \mathbf{F}\mathcal{D}_{ij} - \mathcal{D}_{ij}\mathbf{F}\,. \tag{12.34}$$

This definition is straightforwardly applied to nested delay operators by commuting $\mathbf{F}$ with each individual delay. For example,

$$\begin{aligned}\mathbf{F}\mathcal{D}_{ij}\mathcal{D}_{jk} &= \mathcal{D}_{ij}\mathbf{F}\mathcal{D}_{jk} + \left[\mathbf{F}, \mathcal{D}_{ij}\right]\mathcal{D}_{jk} &(12.35)\\ &= \mathcal{D}_{ij}\mathcal{D}_{jk}\mathbf{F} + \underbrace{\left[\mathbf{F}, \mathcal{D}_{ij}\right]\mathcal{D}_{jk} + \mathcal{D}_{ij}\left[\mathbf{F}, \mathcal{D}_{jk}\right]}_{=\left[\mathbf{F}, \mathcal{D}_{ij}\mathcal{D}_{jk}\right]}\,, &(12.36)\end{aligned}$$

The Fourier transform of $\left[\mathbf{F}, \mathcal{D}_{ij}\right]$ is given in [24, 20], and can be approximated as

$$\mathcal{F}\left[\left[\mathbf{F}, D_{ij}\right]\right] \approx -\omega e^{-i\omega d_{ij}}\dot{d}_{ij}\mathcal{K}_{\mathbf{F}}(\omega)\,, \tag{12.37}$$

where $\mathcal{K}_{\mathbf{F}}$ is the frequency domain derivative of the filter transfer function $\mathcal{H}_{\mathbf{F}}$ (cf. eq. (7.3)),

$$\mathcal{K}_{\mathbf{F}}(\omega) = \frac{\mathrm{d}\mathcal{H}_{\mathbf{F}}}{\mathrm{d}\omega}(\omega) = \frac{i}{f_s^{\mathrm{phy}}}\sum_{k=-M}^{M} k c_k e^{i\omega k/f_s^{\mathrm{phy}}}\,. \tag{12.38}$$

Here, we have $M = \frac{N-1}{2}$, where N is the filter order as used in eq. (7.3). Following [24], we assumed that the group delay of the filter $\mathcal{H}_{\mathbf{F}}$ has been compensated in a first processing step, by shifting all filtered time series by $N-1$ samples, such that the sum does not start at $k = 0$. This significantly reduces the impact of this effect.

To check the validity of this model for the flexing-filtering coupling, we run a simulation with the filter design parameters set to a transition band spanning from 1 mHz to 1 Hz, while keeping the attenuation at 320 dB. We observe that the analytical model can explain the extra noise present at high frequencies between 0.1 Hz and 1 Hz, while we are limited by noise due to the

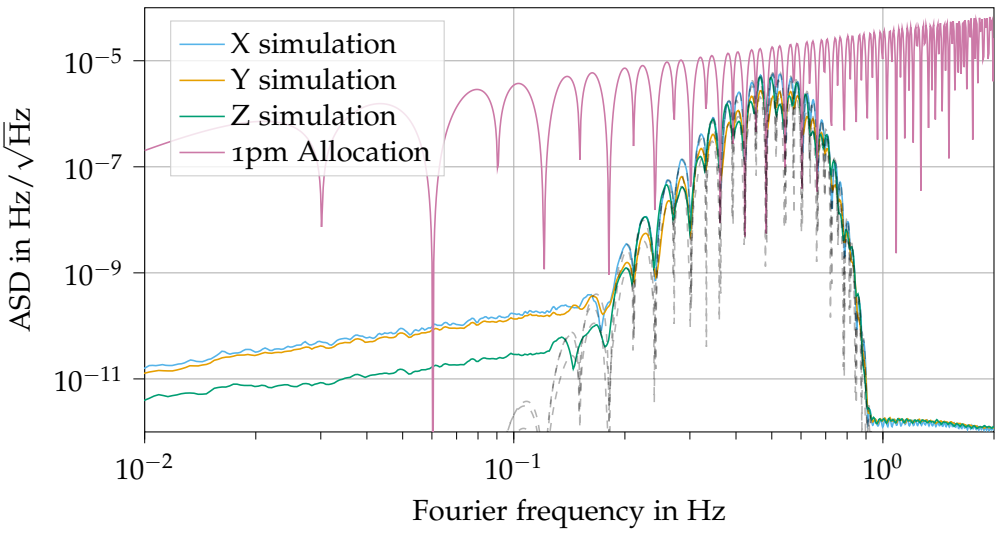

FIGURE 12.4: Laser noise residual due to flexing-filtering coupling in TDI X, Y and Z with laser locking enabled. To highlight the effect, we used a very wide transition band spanning from 1 mHz to 1 Hz together with a strong attenuation of 320 dB. The model overlayed in dotted grey captures the general trend and noise level, but is not able to fully explain the fine structure of the noise.

fundamental armlength mismatch at lower frequencies. However, similar to the interpolation errors, the model fails to fully reproduce the fine structure of the observed noise.

12.3.2.4 *Summary of technical imperfections*

We observe that each propagation delay in eq. (12.25) yields a delay-filter commutator in addition to the terms given in eq. (12.32). It is therefore useful to define

$$\mathcal{R}_{ij} = \mathbf{F}\Delta^I_{ij} + \mathbf{F}\Delta^\mu_{ij} + \left[\mathbf{F}, \mathcal{D}_{ij}\right], \tag{12.39}$$

with the Fourier transform

$$\widetilde{\mathcal{R}}_{ij}(\omega) \approx \left[(\widetilde{\epsilon}_{ij}(\omega) + \omega\mu_{ij})\mathcal{H}_{\mathbf{F}}(\omega) - \dot{d}_{ij}\mathcal{K}_{\mathbf{F}}(\omega)\right] e^{-i\omega d_{ij}}, \tag{12.40}$$

and its nested variant

$$\mathcal{R}_{ijk} = \mathbf{F}\Delta^I_{ijk} + \mathbf{F}\Delta^\mu_{ijk} + \left[\mathbf{F}, \mathcal{D}_{ijk}\right], \tag{12.41}$$

with the Fourier transform

$$\begin{aligned}\widetilde{\mathcal{R}}_{ijk}(\omega) \approx \big[&(\widetilde{\epsilon}_{ij}(\omega) + \widetilde{\epsilon}_{jk}(\omega) + (\mu_{ij} + \mu_{jk})\omega)\mathcal{H}_{\mathbf{F}}(\omega) \\ &- (\dot{d}_{ij} + \dot{d}_{jk})\mathcal{K}_{\mathbf{F}}(\omega)\big] e^{-i\omega(d_{ij}+d_{jk})}.\end{aligned} \tag{12.42}$$

We can now insert these expressions into eq. (12.25) to get

$$\begin{aligned}\mathrm{TDI} = &\Big[\mathbf{P}_{12}(\mathcal{D}_{121} - 1) + \mathbf{P}_{13}(\mathcal{D}_{131} - 1) + \mathbf{P}_{23}(\mathcal{D}_{231} - \mathcal{D}_{21}) \\ &+ \mathbf{P}_{32}(\mathcal{D}_{321} - \mathcal{D}_{31})\Big]\mathbf{F}p_0 \qquad (12.43a)\\ &+ \Big[\mathbf{P}_{12}\mathcal{R}_{121} + \mathbf{P}_{13}\mathcal{R}_{131} + \mathbf{P}_{23}[\mathcal{R}_{231} - \mathcal{R}_{21}] \\ &+ \mathbf{P}_{32}[\mathcal{R}_{321} - \mathcal{R}_{31}]\Big]p_0\,. \qquad (12.43b)\end{aligned}$$

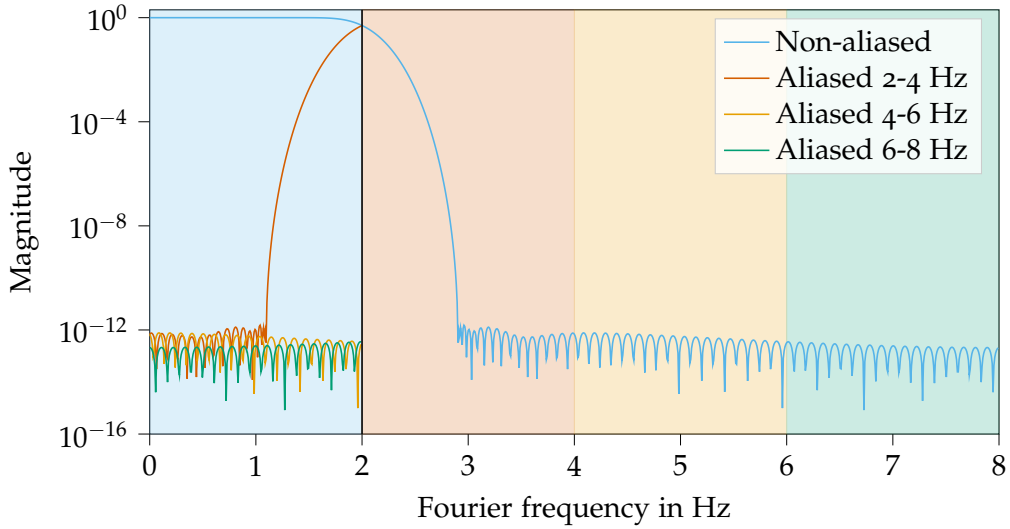

FIGURE 12.5: Aliasing during downsampling from 16 Hz to 4 Hz. Signals in the red, yellow and green areas are aliased into the main band in blue. Shown for filter transfer function without laser locking modulation for clarity.

We want to analyze the residual noise in the frequency domain, for which we will assume all delays appearing in the $\mathbf{P}_{ij}$ to be constant. The term labelled eq. (12.43a) has the Fourier transform as given in eq. (12.22), such that we get

$$\begin{aligned}\mathcal{F}\left[\mathrm{TDI}\right](\omega) \approx \Big[&\omega\Delta\tau e^{-i\omega Qd}\mathcal{H}_{\mathbf{F}}(\omega) + \widetilde{\mathbf{P}}_{12}\widetilde{\mathcal{R}}_{121} + \widetilde{\mathbf{P}}_{13}\widetilde{\mathcal{R}}_{131} \\ &+ \widetilde{\mathbf{P}}_{23}\left[\widetilde{\mathcal{R}}_{231} - \widetilde{\mathcal{R}}_{21}\right] + \widetilde{\mathbf{P}}_{32}\left[\widetilde{\mathcal{R}}_{321} - \widetilde{\mathcal{R}}_{31}\right]\Big]\widetilde{p}_0\,.\end{aligned} \tag{12.44}$$

Since we replaced all delays appearing in the TDI combination by those applied in post-processing, $\Delta\tau$ is now the armlength mismatch computed using these offline delays[5].

In terms of PSD, since we only have a single laser noise term, we can compute

$$\begin{aligned}S_{\mathrm{TDI}_{p_0}} \approx \Big|&\omega\Delta\tau e^{-i\omega Qd}\mathcal{H}_{\mathbf{F}}(\omega) + \widetilde{\mathbf{P}}_{12}\widetilde{\mathcal{R}}_{121} + \widetilde{\mathbf{P}}_{13}\widetilde{\mathcal{R}}_{131} \\ &+ \widetilde{\mathbf{P}}_{23}\left[\widetilde{\mathcal{R}}_{231} - \widetilde{\mathcal{R}}_{21}\right] + \widetilde{\mathbf{P}}_{32}\left[\widetilde{\mathcal{R}}_{321} - \widetilde{\mathcal{R}}_{31}\right]\Big|^2 S_{p_0}\,.\end{aligned} \tag{12.45}$$

12.3.3 *Aliasing*

As described in chapter 7, the phasemeter signals will be filtered and downsampled before being transmitted down to earth. The anti-aliasing filter used in this step has a strong, but finite attenuation at high frequencies, such that there will be a small residual noise level left after filtering, which gets aliased into our measurement band when downsampling. In the real mission, this will happen in multiple steps going all the way from the high phasemeter sampling rate of 80 MHz down to the same rate used for transmission. We

5 This includes the potentially large ranging bias. However, since TDI combinations are by construction insensitive to constant armlength mismatches, we expect no big change in the resulting values.

work under the assumption that the last filtering step in the real phasemeter will be the dominant effect, and that it is comparable to that used in the simulation[6].

We can model how this effect enters our simulation in the following steps:

- Compute the Fourier transform of the laser noise in each η_{ij} up to the physical sampling rate. This depends on the locking scheme.
- Apply the filter transfer function as given in eq. (7.3).
- Compute the aliased noise in each η_{ij} by reflecting the spectrum across the Nyquist frequency. Since we downsample by a factor 4, we get a total of three aliased noise terms, $N_{ij}^{A_1}$, $N_{ij}^{A_2}$ and $N_{ij}^{A_3}$, for each η_{ij}. Here, $N_{ij}^{A_k}$ is the noise in the band $[k\pi f_s^{\text{meas}}, (k+1)\pi f_s^{\text{meas}}]$, expressed in angular frequency.
- Apply the usual delay polynomials $\mathbf{P}_{ij}$ to each term, treating the $N_{ij}^{A_k}$ as uncorrelated for different k but fully correlated for the same k.

We get for the Fourier transform of each η_{ij}

$$\tilde{\eta}_{12}(\omega) = \mathcal{H}_{\mathbf{F}}(\omega)(e^{-i\omega(d_{12}+d_{21})} - 1)\tilde{p}_0\,, \tag{12.46a}$$
$$\tilde{\eta}_{13}(\omega) = \mathcal{H}_{\mathbf{F}}(\omega)(e^{-i\omega(d_{13}+d_{31})} - 1)\tilde{p}_0\,, \tag{12.46b}$$
$$\tilde{\eta}_{23}(\omega) = \mathcal{H}_{\mathbf{F}}(\omega)(e^{-i\omega(d_{23}+d_{31})} - e^{-i\omega d_{21}})\tilde{p}_0\,, \tag{12.46c}$$
$$\tilde{\eta}_{32}(\omega) = \mathcal{H}_{\mathbf{F}}(\omega)(e^{-i\omega(d_{32}+d_{21})} - e^{-i\omega d_{31}})\tilde{p}_0\,, \tag{12.46d}$$
$$\tilde{\eta}_{21}(\omega) = 0\,, \tag{12.46e}$$
$$\tilde{\eta}_{31}(\omega) = 0\,, \tag{12.46f}$$

from which we can compute the aliased terms as

$$\tilde{N}_{ij}^{A_1}(\omega) = \tilde{\eta}_{ij}(2\pi f_s^{\text{meas}} - \omega)\,, \tag{12.47a}$$
$$\tilde{N}_{ij}^{A_2}(\omega) = \tilde{\eta}_{ij}(2\pi f_s^{\text{meas}} + \omega)\,, \tag{12.47b}$$
$$\tilde{N}_{ij}^{A_3}(\omega) = \tilde{\eta}_{ij}(4\pi f_s^{\text{meas}} - \omega)\,, \tag{12.47c}$$

which is to be evaluated for values of ω up to the Nyquist rate, πf_s^{meas}.

The Nyquist frequency is here given in angular frequency, diving it by 2π gives the more familiar $\frac{f_s^{\text{meas}}}{2}$.

Note that noise in the bands $[\pi f_s^{\text{meas}}, 2\pi f_s^{\text{meas}}]$ and $[3\pi f_s^{\text{meas}}, 4\pi f_s^{\text{meas}}]$ appears reflected in our measurement band. The noise in the band $[2\pi f_s^{\text{meas}}, 3\pi f_s^{\text{meas}}]$ is reflected twice, such that the two effects cancel and it is simply shifted without reflection, see fig. 12.5.

For each k, the aliased terms represent signals which are physically at different frequencies. This is why we assume that they are fully un-correlated to each other and to the in-band laser noise described above.

6 The phasemeter design is not finalized yet, but the sampling rates used in our simulation (16 Hz and 4 Hz) are under consideration for the final two downsampling steps of the phasemeter [47]

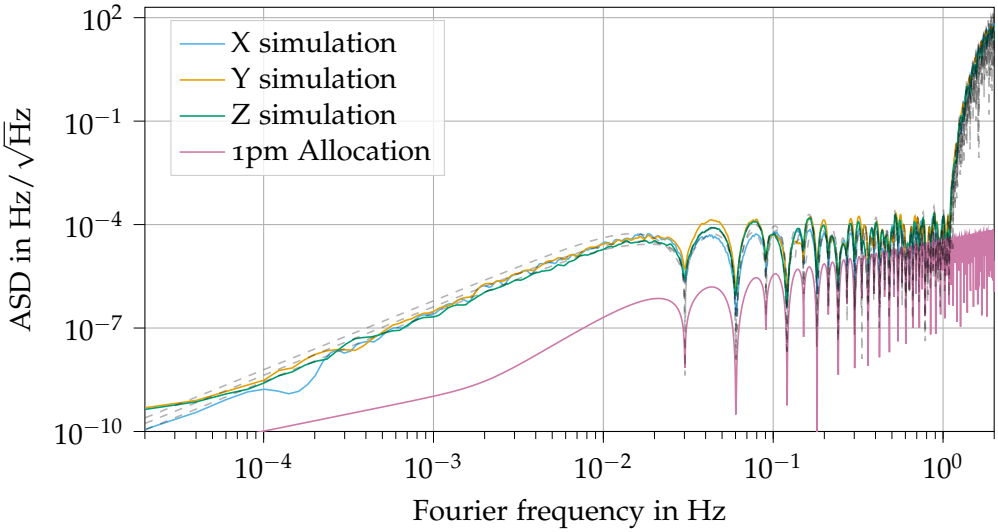

FIGURE 12.6: Laser noise residual due to aliasing in TDI X, Y and Z with laser locking enabled. To highlight the effect, we used a weak anti-aliasing filter with an attenuation of 120 dB. The model overlayed in dotted grey generally explains the noise well, but sometimes fails to fully explain the fine structure of the noise.

We then compute for each set of aliased noise terms how they couple into TDI,

$$S_{\mathrm{TDI}^{A_k}} = \left| \sum_{i,j \in \mathcal{I}_2} \widetilde{\mathbf{P}}_{ij}(\omega) \widetilde{N}_{ij}^{A_k}(\omega) \right|^2 . \tag{12.48}$$

which we evaluate numerically. The overall PSD of the aliased noise is then computed as

$$S_{\mathrm{TDI}^{A}} = \sum_{k=1}^{3} S_{\mathrm{TDI}^{A_k}} . \tag{12.49}$$

To test this model, we run a simulation with the same parameters as those in section 12.3.1, but with the filter attenuation set to just 120 dB. The result is shown in fig. 12.6, where we see that our model can mostly explain the observed aliased noise well. However, as we also observed for the interpolation errors and the flexing filtering coupling, the model is not perfect, and some parts of the spectrum are not fully reproduced[7].

12.3.4 *Overall laser noise level*

To estimate the final residual laser noise level, we run a simulation with the default parameters as described in part ii, but disabling all noises except laser noise, plus an additional bias of 1 m in each ranging measurement. We simulate again 10^5 s, using the locking scheme N1-LA12. For TDI, we use

7 The error is within an order of magnitude, such that all models presented here should still be useful to estimate the residual noise levels. It would be interesting to further explore the source of the discrepancy between the simulation and our models as a follow-up work. Such studies are ongoing inside the LISA consortium, with contributions from the author of this thesis, and might be published in the future.

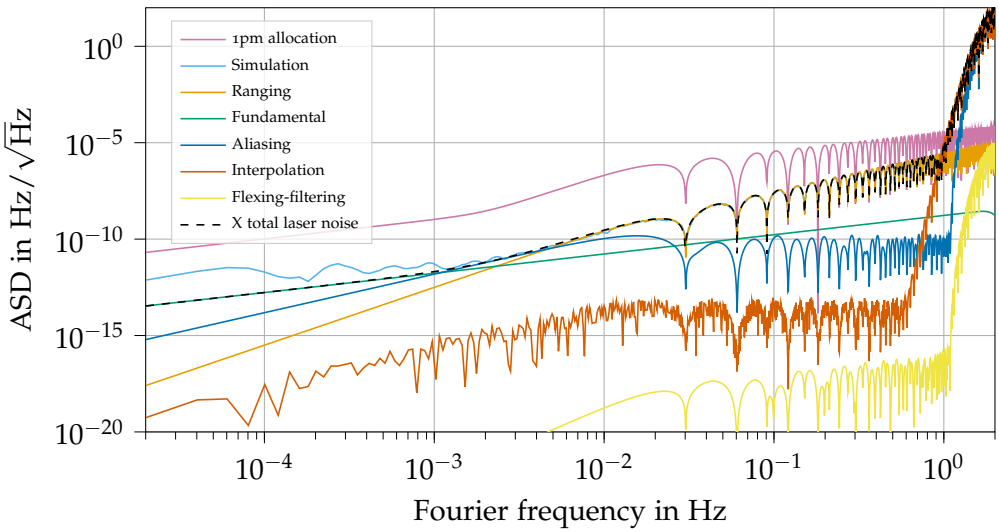

FIGURE 12.7: Overall laser noise residual in TDI X with laser locking enabled, using realistic simulation parameters. The simulation result is well explained by our analytical models, except for the numerical noise floor at low frequencies.

interpolation order 41[8], and compute just TDI X for clarity. We overlay the different contributions of the analytical models.

The residual laser noise is well explained by our models, down to around 1 mHz where we hit the usual noise floor of our simulations. If not for this numerical deviation, the fundamental armlength mismatch would limit at frequencies below 1 mHz, while aliasing is limiting in the band between 1 mHz and 4 mHz. Above 4 mHz, the most significant residual is caused by the 1 m ranging bias, until the interpolation errors take over close to the Nyquist frequency. The strong increase around 1 Hz is a combination of interpolation errors and aliasing. Flexing-filtering coupling is sub-dominant throughout the whole measurement band, and the overall laser noise residual is comfortably below the 1 pm allocation curve for the whole measurement band up to 1 Hz.

12.4 TDI IN UNITS OF FREQUENCY

This section is based on a publication developed in close collaboration with J.-B. Bayle and M. Staab, available as [23].

It is structured as follows: in section 12.4.1, we review the context of this section, and give the expression of the interferometric measurements in terms of frequency and show how Doppler shifts couple. Then, in section 12.4.2, we evaluate the additional noise due to these Doppler shifts in the TDI variables and show that it does not meet the requirements. A procedure to mitigate this effect is presented in section 12.4.3. We show that the Doppler couplings can be reduced to levels below the requirements, and confirm the analytical study by numerical simulations in section 12.4.4.

8 This value has been shown to be sufficient for our sampling rate of 4 Hz to not get significant interpolation artefacts below Fourier frequencies of 1 Hz.

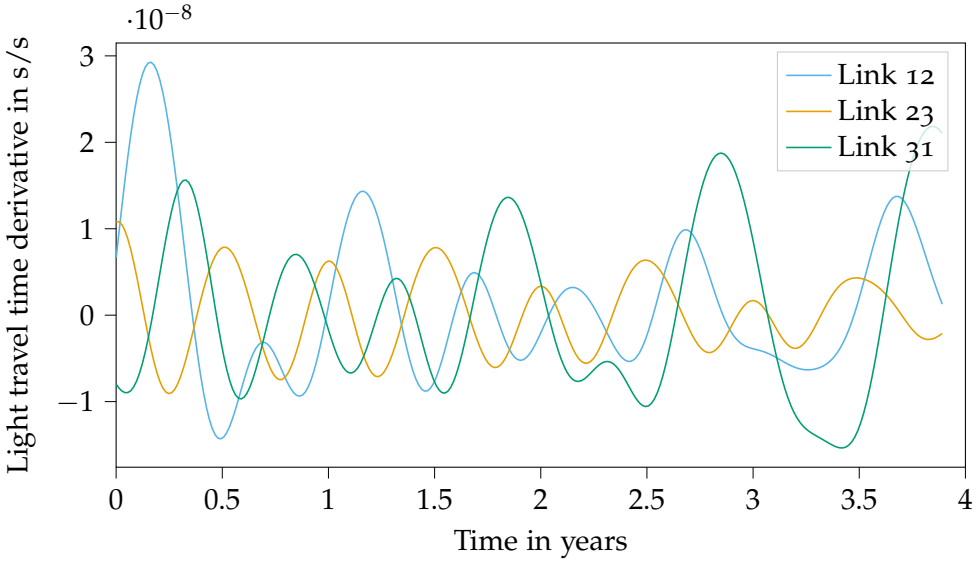

FIGURE 12.8: Light travel time derivatives $\dot{d}_{ij}$ for ESA provided orbits. Only plotted for clockwise direction, since $\dot{d}_{ij}$ deviates from $\dot{d}_{ji}$ only on the percent level.

12.4.1 *Introduction*

Most TDI studies indifferently assume that the measurements are expressed in terms of interferometric beatnote phases or frequencies [83], but many of these studies disregard the Doppler shifts which arise when using units of frequency [83, 93, 66, 24]. The introduction to TDI presented in chapter 12 of this thesis was also performed in phase, while our simulations are performed in frequency. To properly process the simulated data, we therefore need to adapt the TDI algorithm to correctly account for Doppler shifts.

Indeed, the relative motion of the spacecraft induces time-varying frequency shifts in the beatnote frequencies that reduce the performance of standard TDI algorithms. In fact, as we show below, in the presence of the Doppler effect, the standard formulation of TDI applied to data in units of frequency no longer suppresses laser-noise to the level required. We however demonstrate that TDI algorithms can be easily modified to account for Doppler shifts when using units of frequency. Ultimately, we recover the same laser noise-reduction performance as one obtains when using units of phase.

We stay in the simplified LISA model used in chapter 10, in that we consider each spacecraft as a point mass on a free-fall trajectory. We assume these trajectories to be again given by the same ESA provided orbits for which we show the computed light travel times $d_{ij}(t)$ in fig. 3.3. As described in section 5.5.3, the time derivatives of these light travel times affect the laser frequency observed after propagation, which is known as a Doppler shift. The light travel time derivatives for the orbits considered in this thesis are shown in fig. 12.8

The reasoning in this chapter holds regardless of in which reference frame the variables are expressed, such that we do not distinguish between PPRs, MPRs and LTTs. In addition, we do not distinguish between d_{ij} and d^o_{ij}.

Moreover, we will again assume here that each spacecraft i contains only one laser with laser noise p_i, which is used in both optical benches. We will also neglect all optical pathlength and clock noise, the onboard filters, laser locking, as well as the timestamping operator in the equations presented in

section 7.2, such that the relevant measurement equations given in eq. (7.7b) simplify to

$$\dot{\eta}_{ij} \equiv \mathrm{isc}^{e}_{ij,c} = (1 - \dot{d}_{ij})\mathbf{D}_{ij}\dot{p}_j - \dot{p}_i \,, \tag{12.50}$$

where we explicitly expanded the Doppler-delay operator $\dot{\mathbf{D}}_{ij}$ used in eq. (7.7b).

We observe that compared to the η expressed in phase which we presented in chapter 10, we get additional laser noise terms scaled by $\dot{d}_{ij}$.

12.4.2 *Residual noise due to Doppler shifts in TDI*

As an example for how these new laser noise terms propagate through TDI, we consider again the second-generation Michelson variable X_2 introduced in chapter 10, which reads

$$\begin{aligned} X_2 = {} & (1 - \mathbf{D}_{121} - \mathbf{D}_{12131} + \mathbf{D}_{1312121})(\eta_{13} + \mathbf{D}_{13}\eta_{31}) \\ & - (1 - \mathbf{D}_{131} - \mathbf{D}_{13121} + \mathbf{D}_{1213131})(\eta_{12} + \mathbf{D}_{12}\eta_{21}) \,. \end{aligned} \tag{12.51}$$

In the following, we shall ignore any technical reasons for imperfect laser noise reduction discussed in section 12.3 and only consider the maximum theoretical laser noise reduction achievable.

Following section 10.2, we know that the TDI combination evaluates to

$$X_2 = [\mathbf{D}_{13121}, \mathbf{D}_{12131}]p_1 \,, \tag{12.52}$$

which gives

$$S_{X_2^{\Phi}}(\omega) = \omega^2 \Delta\tau^2 S_{\Phi}(\omega) \,, \tag{12.53}$$

in terms of PSD, where $S_{\Phi}(\omega)$ is dominated by the PSD of the laser noise expressed in cycles and $\Delta\tau^2$ is the usual armlength mismatch of the combination.

Now, let us assess the impact of Doppler shifts if one uses naively the traditional second generation TDI algorithm using measurements in units of frequency. For this, we can insert eq. (12.50) in eq. (12.51). The only structural difference between eq. (12.50) and eq. (10.1) is the additional Doppler term $\dot{d}_{ij}\mathbf{D}_{ij}p_j$. Because TDI is a linear operation, we can immediately give the residual laser noise in terms of frequency when applying the same algorithm,

$$X_2^{\nu} = [\mathbf{D}_{13121}, \mathbf{D}_{12131}]p_1 + \delta X_2^{\nu} \,, \tag{12.54}$$

where δX_2^{ν} is a function of the Doppler shifts,

$$\begin{aligned} \delta X_2^{\nu} = {} & (1 - \mathbf{D}_{131} - \mathbf{D}_{13121} + \mathbf{D}_{1213131}) \\ & \times (\dot{d}_{12}\mathbf{D}_{12}\dot{p}_2 + \dot{d}_{21}\mathbf{D}_{121}\dot{p}_1) \\ & - (1 - \mathbf{D}_{121} - \mathbf{D}_{12131} + \mathbf{D}_{1312121}) \\ & \times (\dot{d}_{13}\mathbf{D}_{13}\dot{p}_3 + \dot{d}_{31}\mathbf{D}_{131}\dot{p}_1) \,. \end{aligned} \tag{12.55}$$

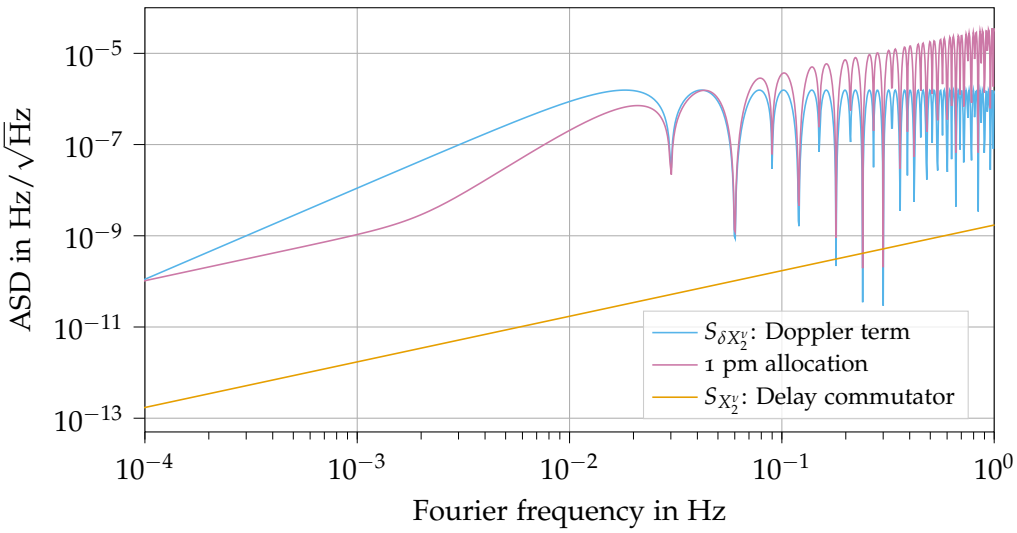

FIGURE 12.9: Amplitude spectral density of the second generation TDI combination when using measurements expressed in units of frequency. The blue curve shows the amplitude of Doppler-related terms, c.f. eq. (12.57), the orange curve shows the amplitude of the delay commutators, c.f. eq. (12.58), while the red curve presents the usual LISA 1 pm-noise allocation.

A rough estimation of this Doppler coupling can be computed from $\delta X_2^v \approx \bar{\dot{d}} p_i$, where $\bar{\dot{d}}$ is the average light travel time derivative. Plugging orders of magnitudes for the TTs derivatives and laser noise yields a Doppler coupling at 10^{-6} Hz, above the expected level for our GW signals (10^{-7} Hz). It is also above the level of the traditional residuals of TDI, given by the first term of eq. (12.54) and shown in fig. 12.9. As a consequence, the PSD of the residual noise for the X_2^v TDI variable is dominated by the Doppler coupling,

$$S_{X_2^v}(\omega) \approx S_{\delta X_2^v}(\omega)\,. \tag{12.56}$$

Assuming that all laser frequencies are uncorrelated, a more precise computation yields the PSD of this extra residual noise,

$$\begin{aligned} S_{\delta X_2^v}(\omega) \approx 16 S_\nu \sin^2(\omega \bar{d}) \sin^2(2\omega \bar{d}) \\ \times \left(\bar{\dot{d}}_{12}^2 + \bar{\dot{d}}_{31}^2 + (\bar{\dot{d}}_{12} - \bar{\dot{d}}_{31})^2\right). \end{aligned} \tag{12.57}$$

This is to be compared with the residual laser noise in terms of frequency when one disregards Doppler effects. It is given by replacing S_Φ with S_ν in eq. (12.53),

$$S_{[X_2^v]}(\omega) = \omega^2 \Delta d^2 S_\nu(\omega)\,. \tag{12.58}$$

In fig. 12.9, we show those analytical curves alongside the usual 1 pm-noise allocation curve, given by dividing eq. (8.1) by a factor 10.

The extra residual laser noise due to Doppler terms is above or at the same level as the GW signal, and far above the usual laser noise residual when one disregards the Doppler effect. Therefore, a procedure to mitigate this effect is required if one wishes to use frequency measurements.

12.4.3 *Adapting time-delay interferometry for Doppler shifts*

We included Doppler shifts in our equations in section 7.2 by utilizing the Doppler-delay operator, defined as

$$\dot{\mathbf{D}}_{ij} = (1 - \dot{d}_{ij})\mathbf{D}_{ij}\,, \tag{12.59}$$

such that laser noise entering eq. (12.50) takes the same algebraic form as its phase counterpart eq. (10.1),

$$\dot{\eta}_{ij} = \dot{\mathbf{D}}_{ij}\dot{p}_j - \dot{p}_i\,. \tag{12.60}$$

We now introduce a new type of second generation TDI combination by considering the standard expression from eq. (12.51) but using the Doppler-delay operators introduced in eq. (12.59). The new TDI variable reads

$$\begin{aligned}\dot{X}_2 = {} & (1 - \dot{\mathbf{D}}_{121} - \dot{\mathbf{D}}_{12131} + \dot{\mathbf{D}}_{1312121})(\dot{\eta}_{13} + \dot{\mathbf{D}}_{13}\dot{\eta}_{31}) \\ & - (1 - \dot{\mathbf{D}}_{131} - \dot{\mathbf{D}}_{13121} + \dot{\mathbf{D}}_{1213131})(\dot{\eta}_{12} + \dot{\mathbf{D}}_{12}\dot{\eta}_{21})\,.\end{aligned} \tag{12.61}$$

The algebraic form of this expression is now identical in phase and frequency, and we immediately recover the residual noise given in eq. (12.53),

$$\dot{X}_2^{\nu} = \left[\dot{\mathbf{D}}_{13121}, \dot{\mathbf{D}}_{12131}\right]\dot{p}_1\,. \tag{12.62}$$

A direct comparison with eq. (12.54) demonstrates that the new TDI variable introduced in eq. (12.61) is not impacted by the Doppler noise $\delta\dot{X}_2^{\nu}$.

To compute the PSD of the $\dot{X}_2^{\nu}$ residual laser noise, we study the commutator of Doppler-delay operators

$$y = \left[\dot{\mathbf{D}}_{A_1\ldots A_n}, \dot{\mathbf{D}}_{B_1\ldots B_n}\right]. \tag{12.63}$$

As one can observe in fig. 12.8, the light travel time derivatives evolve slowly with time, with $\ddot{d}\Delta t \sim 10^{-14} \ll \dot{d} \sim 10^{-8}$ if $\Delta t \sim 10\,\mathrm{s}$ is the timescale of the TTs considered here. Therefore, we can assume that $\dot{d}$'s are constant when computing y. Equation (12.63) can then be factored as

$$y \approx \left(\prod_{m=1}^{n}(1 - \dot{d}_{A_m})\right)\left(\prod_{m=1}^{n}(1 - \dot{d}_{B_m})\right) \times \left[\mathbf{D}_{A_1\ldots A_n}, \mathbf{D}_{B_1\ldots B_n}\right]. \tag{12.64}$$

The factor that contains the light travel time derivatives is a constant, which, to first order, deviates from 1 by $2\bar{\dot{d}}n \approx 10^{-7}$. We can therefore neglect it when estimating the PSD. For this reason, the PSD of the laser noise residual for the new TDI variable introduced in eq. (12.61) is then given by

$$S_{\dot{X}_2^{\nu}}(\omega) \approx S_{[X_2^{\nu}]}(\omega)\,, \tag{12.65}$$

whose expression is explicitly given in eq. (12.58). A direct comparison with eq. (12.56) shows that the PSD of the new $\dot{X}_2^{\nu}$ TDI variable is not impacted by the unacceptably large contribution from $\delta\dot{X}_2^{\nu}$.

Note that although we demonstrated this method of replacing $\mathbf{D}_{ij}$ by $\dot{\mathbf{D}}_{ij}$ using the variable X_2, it is completely general, and can be applied to any TDI combination.

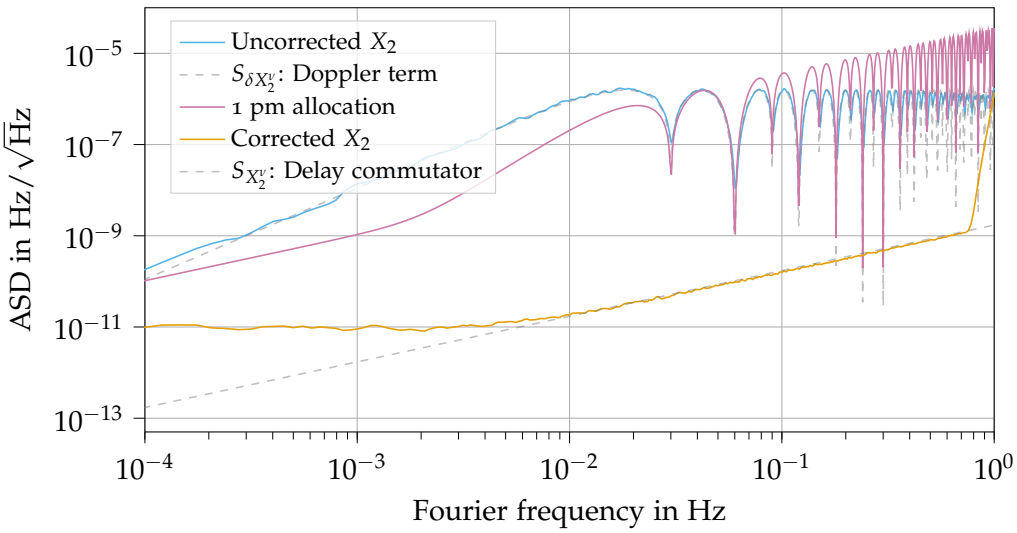

FIGURE 12.10: Amplitude spectral density of the residual laser noise in X_2^v obtained using data in units of frequency, with the traditional algorithms (in blue) and Doppler correction (in orange). The theoretical models from Eqs. (12.57) and (12.58) are superimposed as black dashed lines. These curves need to be compared with the 1 pm-noise allocation (in red).

12.4.4 *Simulation results*

Using `LISA Instrument`, we simulated the interferometric measurements as frequency deviations from the average beatnote frequencies. These frequency deviations include only laser noise, which is Doppler-shifted during propagation. We assumed 3 free-running lasers for this study, and used a high sampling rate, such that effects of onboard filtering appear off band. We used the same realistic orbits and light travel times as presented in figs. 3.3 and 12.8, and simulated 10^6 samples, i.e., a bit less than 12 days.

The TDI processing was performed using PyTDI. In fig. 12.10, we compare 2 different scenarios using the same input data. The blue curve shows the ASD of the residual laser noise when the standard second-generation Michelson X_2^v variable is used. We superimpose the model for the expected excess of noise δX_2^v due to Doppler effect given in eq. (12.57), and check that it matches our simulated results. Alternatively, the orange curve shows the ASD of the residual laser noise when the Doppler-corrected second-generation Michelson $\dot{X}_2^v$ variable is used. It is superimposed with the analytical expectation given in eq. (12.65) in a large part of the band, until we reach a noise floor in agreement with the numerical accuracy typically achieved in our simulations. The increase at very high frequency is an interpolation artifact, which we modelled in section 12.3.2.2.

These simulations confirm the analytical results developed in the previous section. In particular, it shows that the residual noise of the new TDI variable introduced in eq. (12.61) is similar to the one obtained with the standard TDI combinations when the Doppler effect is neglected. In other words, the TDI variable corrects efficiently for the Doppler contribution which otherwise induces an unacceptably large noise.

13

TIME SYNCHRONIZATION AND TDI

So far, we have neglected in part iii of this thesis that the measurements are recorded with three independent spacecraft clocks.

We will discuss in section 13.1 that this does not significantly impact the construction of TDI variables *in principle*, and that laser noise can still be reduced by taking the clock imperfections into account while constructing the variable. We remark in section 13.2 how this would effectively correct both laser and clock noise in the same step. However, this is only true when one uses the total phase or frequency, which implies very stringent requirements on the precision of the applied time shifts.

An alternative is to first detrend all variables, and then operate just on the remaining fluctuations. This eases the requirements on the delays applied in TDI, but requires an additional processing step to remove in-band clock fluctuations, which we outline in section 13.3.

We test these analytical results in section 13.4, by performing simulations with laser- and clock-noise enabled, showing that both of these noise sources can be reduced below the level of other secondary noises, even if we additionally enable ranging noise. This is possible with either schemes, using the total frequency or a detrended variable, but the latter seems to cause smaller numerical errors. These results should be seen as preliminary, since more detailed studies to evaluate the achievable noise suppression and to model the residuals are on-going.

We conclude with an outlook in section 13.4.2, where we briefly discuss the remaining processing steps still missing in section 13.4. In particular, we discuss how the final variables could be synchronized to each other and a global timescale, like TCB, and how one could correct for constant ranging biases.

13.1 TIME SYNCHRONIZATION AS PART OF TDI

The topic of this section is under development as a joint publication[1] with J.-B. Bayle, A. Hees, M. Lilley, M. Staab and P. Wolf.

1 The idea that one could perform TDI directly using the measurements given in their respective clock frames was first formulated in detail by A. Hees at SYRTE. Independently, the authors of [63] also already remarked in their manuscript that "[the] implementation [of TDI] will be based on data timestamping and pseudo-ranging measurements that all happen on board individual satellites, and will not require to pick any global frame to achieve noise cancellation", but it is not further explored there how this can be realized in practice.

We derived TDI in chapter 10 making extensive use of delay operators, by defining the measurements as

$$\eta_{ij} = \mathbf{D}_{ij}\Phi_j - \Phi_i \,. \tag{13.1}$$

Here, the left-hand side η_{ij} as well as the right-hand side Φ_i are evaluated at the same time, corresponding to the event a photon is received and interefered on spacecraft i, while $\mathbf{D}_{ij}\Phi_j$ is evaluated at the corresponding event of emission on spacecraft j.

We assumed in that chapter that all measurements are given in a global time frame, such as TCB, which allows us to write

$$\eta^t_{ij}(t) = \Phi^t_j(t - d^t_{ij}(t)) - \Phi^t_i(t) \,, \tag{13.2}$$

where d^t_{ij} is the light travel time computed in the TCB. This assumption implies the requirement that all measurements need to be shifted from their respective THE in which they are provided by the spacecraft to a common global reference frame.

However, we could have just as well expressed the same equation in any other reference frame, or even using different reference frames for the different quantities without changing any of the physics.

For example, we could express each of the lasers in their associated proper times τ_i, to get

$$\eta^{\tau_i}_{ij}(\tau) = \Phi^{\tau_j}_j(\tau - d^\tau_{ij}(\tau)) - \Phi^{\tau_i}_i(\tau) \,. \tag{13.3}$$

In fact, this is exactly what we did in section 5.5.3 to derive the propagation equations of the simulation model, with $d^\tau_{ij}(\tau)$ as the PPR.

We can even express the measurements as they are given according to the local spacecraft clocks,

$$\eta^{\hat\tau_i}_{ij}(\tau) = \Phi^{\hat\tau_j}_j(\tau - d^{\hat\tau}_{ij}(\tau)) - \Phi^{\hat\tau_i}_i(\tau) \,. \tag{13.4}$$

Here, $\eta^{\hat\tau_i}_{ij}$ and $\Phi^{\hat\tau_i}_i$ are defined as functions of the THE of spacecraft i, while the distant $\Phi^{\hat\tau_j}_j$ is defined as a function of the THE of spacecraft j. Overall, this equation still has to represent the same measurement. This means τ in this equation represents a time a photon is received according to $\hat\tau_i$, while $\tau - d^{\hat\tau}_{ij}(\tau)$ has to represent the time the photon was emitted according to $\hat\tau_j$. Or in other words: $d^{\hat\tau}_{ij}$ is the difference between $\hat\tau_i$ at the event of reception and $\hat\tau_j$ at event of emission, which is exactly the pseudo-ranging measurement described in section 6.3, except for ranging noise.

This means we can simply re-interpret eq. (13.1) to represent eq. (13.4) instead of eq. (13.2). All measurements are then implicitly given in their respective THE, and the delays to be applied by $\mathbf{D}_{ij}$ have to represent the MPRs, including de-synchronizations of the different spacecraft clocks. Since the algebraic form of the equation does not change, all result presented in chapters 10 and 11 are directly applicable to the re-defined variables, and TDI variables

can be constructed in exactly the same way. The same can be extended to the variables expressed in frequency as discussed in section 12.4, since again, the algebraic form of the equation does not change.

The residual laser noise levels presented in chapter 12 are also applicable in principle, with the change that the MPRs should be used in all models instead of the TCB light travel times. This can, for example, lead to increased values of the armlength derivative $\dot{d}$ used in our models, since the clock drifts presented in chapter 6 are potentially higher than the armlength rate of change due to Doppler shifts.

Any TDI variable constructed in this fashion will then be given in the time-frame of the 'starting' spacecraft of that variable. For example, the three Michelson variables X, Y and Z will be given according to the spacecraft clocks of spacecraft 1, 2 and 3, respectively, such that they still need to be synchronized to a common reference frame for astrophysical data analysis. The advantage of this approach is that this synchronization can be performed after laser noise has been suppressed, potentially relaxing the pre-processing requirements by a significant margin.

An alternative to the approach presented here is to time-shift all measurements to a common reference frame, either one of the THEs or a global frame like TCB, before computing the TDI combination. In fact, such a prior synchronization has often been thought to be a required processing step (see, e.g., [64, 96]), and is at the time of writing still considered the baseline approach for LISA data processing. However, we suspect that this will require increased complexity of the pre-processing algorithms compared to directly using the data given in the respective THE.

We will discuss in section 13.2 the required accuracy for the time-shifts applied to our data. This applies both to TDI and to the synchronization to a common time scale, like TCB.

13.2 TIME SYNCHRONIZATION IN DIFFERENT UNITS

To analyze the required accuracy of the time shifts applied to our measurements, we will consider the raw data to be given as total phase[2] measured with respect to the clock time. This could represent any of the interferometric measurements presented in part ii. Following chapter 7, we can write

$$\begin{aligned}\Phi^{\hat{\tau}_i}(\tau) &= \Phi^{\tau_i}(\tau_i^{\hat{\tau}_i}(\tau)) \\ &\approx \Phi^{\tau_i}(\tau - \delta\hat{\tau}_i^2(\tau))\,.\end{aligned} \tag{13.5}$$

2 The reasoning presented here also applies to variables given in total frequency. The only difference is that the timeshifts have to take Doppler-like rescaling factors into account, cf. section 6.2.2. Applying a first order expansion to those then yields a similar equation to eq. (13.6).

where Φ^{τ_i} is the total phase given in the TPS. $\delta\hat{\tau}_i^2(\tau)$ accounts for both large clock offsets and small, zero-mean fluctuations clock jitter. In this section, we will only consider the latter, such that we can expand to first order:

Here, we use that $\dot{\Phi}^{\tau_i}(\tau) \equiv \nu^{\tau_i}(\tau)$.

$$\Phi^{\tau_i}(\tau - \delta\hat{\tau}_i^2(\tau)) \approx \Phi^{\tau_i}(\tau) - \nu^{\tau_i}(\tau)\delta\hat{\tau}_i^2(\tau)\,, \tag{13.6}$$

The clock noise term couples scaled by $\nu^{\tau_i}(\tau) \leq 25\,\mathrm{MHz}$. Therefore, to achieve $\mu\mathrm{cycle}/\sqrt{\mathrm{Hz}}$ phase resolution, $\delta\hat{\tau}_i^2(\tau)$ must have an ASD of $\leq 40\,\mathrm{fs}/\sqrt{\mathrm{Hz}}$.

We ignore here the usual relaxation towards low frequencies for clarity.

As discussed before, the clocks on LISA will not meet this timing requirement. Instead, clock errors must be corrected in post processing.

Since the clock errors enter as a time shift, the most straightforward way of correcting them would be to simply time shift $\Phi^{\hat{\tau}_i}(\tau)$ to the desired reference frame, compensating for the clock errors. This could (in principle) be a global time frame, like TCB, or the time frame of another spacecraft as part of constructing the TDI variable, as discussed in section 13.1.

The challenge with that approach is that any errors in the applied time shifts will affect the measurement with the coupling factor $\nu^{\tau_i}(\tau) \leq 25\,\mathrm{MHz}$, which means that all time shifts applied to the total phase inherit the stringent clock timing stability requirement of $40\,\mathrm{fs}/\sqrt{\mathrm{Hz}}$. This is challenging from two perspectives. For one, any numerical error in the applied time shifts will also strongly couple into the measurement. The total time shifts usually appearing in a TDI variable are of the order 10 s, which is 14 orders of magnitude above the required precision of 40 fs, and therefore not far from the limit of a double precision variable. In addition, reaching this $40\,\mathrm{fs}/\sqrt{\mathrm{Hz}}$ precision is only feasible for synchronization between the three spacecraft clocks, where we can utilize the dedicated clock sideband measurement. There is no measurement available which is expected to allow this level of synchronization between the 3 spacecraft clocks and a global frame, like TCB.

Another numerical challenge when constructing TDI variables out of data given in total phase or frequency is quantization noise present in each interpolated term. Recalling section 10.1, we build TDI combinations by summing multiple delayed measurements η_{ij}. Each individual η_{ij} is not suppressed by its own, and carries a white quantization noise proportional to its magnitude, which can be as high as $\approx 10^{-16} \times 25\,\mathrm{MHz}$ when considering data in total frequency. This means we would get a numerical noise floor around 0.01 nHz accross the whole frequency band, which can be limiting at low frequencies. We show in section 13.4 that this can be somewhat mitigated by computing the TDI variables in a certain factorization, but numerical noise remains limiting in some cases.

An alternative to directly time-shifting the total phase or frequency would be to first remove any linear drifts from them. To illustrate that, we use a simple model for $\Phi^{\tau_i}(\tau)$,

$$\Phi^{\tau_i}(\tau) = \nu\tau + \varphi(\tau)\,, \tag{13.7}$$

where ν is constant and $\varphi(\tau)$ a zero-mean noise term, mostly laser frequency noise, with $\dot{\varphi}(\tau) \ll \nu$. Inserting this into eq. (13.6), we then have

$$\Phi^{\hat{\tau}_i}(\tau) \approx \nu\tau + \varphi(\tau) - \nu \cdot \delta\hat{\tau}_i^2(\tau)\,, \tag{13.8}$$

where we neglected a second order term in $\dot{\varphi}(\tau)\delta\hat{\tau}_i^2(\tau)$. Using that both $\varphi(\tau)$ and $\delta\hat{\tau}_i^2(\tau)$ are assumed to be zero-mean noise processes, we can now apply a linear fit to our raw data to remove the term $\nu\tau$, and get the de-trended phase variable,

$$\phi^{\hat{\tau}_i}(\tau) \approx \varphi(\tau) - \nu \cdot \delta\hat{\tau}_i^2(\tau)\,. \tag{13.9}$$

Any errors in a time shift applied to $\phi^{\hat{\tau}_i}$ will now couple scaled[3] by $\dot{\phi}^{\hat{\tau}_i} \approx 50\,\mathrm{Hz}$, such that the precision requirement on these time shifts is relaxed by 5-6 orders of magnitude.

In addition, each individual delayed term used in the construction of the TDI variable will be much smaller, and therefore introduce significantly less numerical noise. The quantization noise present in the original variable before detrending is still there, but it will be suppressed towards low frequencies by the TDI transfer function.

The downside of detrending is that the clock noise term $\nu\delta\hat{\tau}_i^2(\tau)$ can no longer be compensated by time shifting the data. Instead, it remains as a new noise term, scaled[4] by the beatnote frequency ν.

The final TDI combination will contain many of these noise terms from all measurements entering into it. They will appear with different time shifts applied to them, and scaled by different beatnote frequencies.

As we will show in section 13.3, these noise terms can be compensated by subtracting a combination of the clock noise measured in the sideband interferometers in an additional processing step after the TDI variable is constructed.

13.3 CLOCK NOISE CORRECTION IN TDI

This section is based on a publication developed in close collaboration with J.-B. Bayle [43]. A previous version of this article was also included in [20]. It is a continuation of the work published with M. Tinto in [86].

We described in section 13.2 that one way of doing the INREP processing is to subtract any large trends from the phase or frequency data before constructing the TDI variables. As mentioned there, this approach requires an additional clock noise correction step.

As described in chapter 6, the GHz clock sideband modulations allow an independent measurement of the differential clock jitter, which can be used for clock-noise reduction algorithms. A first version of such an algorithm was presented in [51], which perfectly cancels clock noise assuming constant armlengths. In [86], it was shown that this algorithm can be extended to

3 This is a rough estimate from integrating the laser frequency noise of $30\,\mathrm{Hz}/\sqrt{\mathrm{Hz}}$ up to the Nyquist frequency of 2 Hz.

4 Any large deterministic offset in $\delta\hat{\tau}_i^2(\tau)$ would be absorbed into the fit, such that the measured average beatnote frequency will be different from the actual frequency.

linearly time-varying armlengths and still reduces clock noise below requirements. The correction algorithms given in these references are specific to be applied to either the Michelson or Sagnac combinations. We present here a general clock-noise reduction algorithm which can be directly applied to all second-generation TDI combinations presented in section 11.4.

We study in section 13.3.1 how clock noise enters in the standard TDI combinations, and propose a general algorithm to remove it. In section 13.3.2, we present numerical simulations, and discuss the main results in section 13.3.3. In particular, we give models for the limiting effects and compare the performance of our algorithm against existing clock-noise reduction schemes.

13.3.1 *Clock-noise reduction*

As a starting point, we use a simplified version of the phasemeter equations presented in chapter 7. We disregard all noises expect clock noise q_i^ϵ and modulation noise M_{ij}, and consider neither the filter, the timestamping operator nor laser locking[5]. In addition, we assume that large trends have been removed from the data, such that we can directly use the equations describing the fluctuations. For legibility, we will drop the explicit $(\,)^\epsilon$ for all quantities, e.g., we write $q_i \equiv q_i^\epsilon$ in this section.

These simplifications give

$$\mathrm{isc}_{ij,\mathrm{c}} = -\dot{q}_i a_{ij}\,, \tag{13.10a}$$

$$\begin{aligned}\mathrm{isc}_{ij,\mathrm{sb}} = {} & \nu_{ji}^m \dot{\mathbf{D}}_{ij}(\dot{q}_j + \dot{M}_{ji}) - \nu_{ij}^m(\dot{q}_i + \dot{M}_{ij}) \\ & - \dot{q}_i(a_{ij} + \dot{\mathbf{D}}_{ij}\nu_{ji}^m - \nu_{ij}^m)\,,\end{aligned} \tag{13.10b}$$

for the ISC beatnote fluctuations, and

$$\mathrm{ref}_{ij,\mathrm{c}} = -\dot{q}_i b_{ij}\,, \tag{13.11a}$$

$$\begin{aligned}\mathrm{ref}_{ij,\mathrm{sb}} = {} & \nu_{ik}^m(\dot{q}_i + \dot{M}_{ik}) - \nu_{ij}^m(\dot{q}_i + \dot{M}_{ij}) \\ & - \dot{q}_i(b_{ij} + \nu_{ik}^m - \nu_{ij}^m)\,,\end{aligned} \tag{13.11b}$$

for the reference interferometers.

Under these assumptions, the test-mass (TM) beatnote frequency fluctuations are identical to the reference (REF) ones.

13.3.1.1 *Intermediary variables*

Inserting eqs. (13.10a) and (13.11a) in the expressions given for the intermediary variables in section 12.1, we find how clock noise enter into η_{ij},

$$\eta_{ij} = \dot{\mathbf{D}}_{ij} b_{jk}\dot{q}_j - a_{ij}\dot{q}_i\,, \tag{13.12}$$

$$\eta_{ik} = -(b_{ij} + a_{ik})\dot{q}_i\,. \tag{13.13}$$

5 We included all of these effects in the INREP pipeline results shown in chapter 9, showing that the reduction is effective in any case. We also include them in the dedicated numerical simulations shown in section 13.4.

Note that $b_{ij} = -b_{ik}$, since the two reference interferometers on one spacecraft use the same lasers. In the following, we choose to only use reference beatnote frequencies b_{ij} from left MOSAs.

13.3.1.2 *Clock-noise residuals*

From these intermediary variables, we can build laser noise-free TDI combinations. They can be expressed as polynomials of delay operators $\mathbf{P}_{ij}$, in the form

$$\mathrm{TDI} = \sum_{i,j \in \mathcal{I}_2} \mathbf{P}_{ij} \eta_{ij} \,. \tag{13.14}$$

where $\mathcal{I}_2 = \{(1,2),(2,3),(3,1),(1,3),(3,2),(2,1)\}$ is the set of the 6 MOSA index pairs.

Inserting eqs. (13.12) and (13.13), we find that clock noise enters in the TDI combination as

$$\mathrm{TDI}^q = \sum_{i,j,k \in \mathcal{I}_3^+} [\mathbf{P}_{ki}\dot{\mathbf{D}}_{ki} - \mathbf{P}_{ik}] b_{ij} \dot{q}_i - \sum_{i,j \in \mathcal{I}_2} \mathbf{P}_{ij} a_{ij} \dot{q}_i \,, \tag{13.15}$$

with $\mathcal{I}_3^+ = \{(1,2,3),(2,3,1),(3,1,2)\}$ as the set of triplets of spacecraft indices in ascending order.

To estimate the contribution of clock noise before any correction, we assume that all light travel times are constant and equal to L, such that we can commute delay operators. As shown in [24], these commutators only yield multiplicative terms $\ll 1$. Also, we suppose that all clock noises are uncorrelated but have the same PSD $S_{\dot{q}}(\omega)$. Lastly, we assume that beatnote frequency offsets are constant. The clock noise residual PSD then reads

$$\begin{aligned} S_{\mathrm{TDI}^q}(\omega) \approx \sum_{i,j,k \in \mathcal{I}_3^+} \Big| & a_{ij} \widetilde{\mathbf{P}}_{ij}(\omega) + a_{ji} \widetilde{\mathbf{P}}_{ji}(\omega) \\ & - b_{ij} [\widetilde{\mathbf{P}}_{ik}(\omega) - \widetilde{\mathbf{P}}_{ki}(\omega) \widetilde{\dot{\mathbf{D}}}_{ki}(\omega)] \Big|^2 S_{\dot{q}}(\omega) \,, \end{aligned} \tag{13.16}$$

Here, $\widetilde{\dot{\mathbf{D}}}_{ij}$ and $\widetilde{\mathbf{P}}_{ij}$ are the Fourier transforms of delay operators and polynomials thereof, see [24] for further information.

As an example, we can use eq. (13.16) to work out clock noise residuals in the second-generation Michelson combination X_2,

$$\begin{aligned} X_2 = {} & (1 - \dot{\mathbf{D}}_{121} - \dot{\mathbf{D}}_{12131} + \dot{\mathbf{D}}_{1312121})(\eta_{13} + \dot{\mathbf{D}}_{13}\eta_{31}) \\ & - (1 - \dot{\mathbf{D}}_{131} - \dot{\mathbf{D}}_{13121} + \dot{\mathbf{D}}_{1213131})(\eta_{12} + \dot{\mathbf{D}}_{12}\eta_{21}) \,. \end{aligned} \tag{13.17}$$

We find that

$$S_{X_2^q}(\omega) \approx 16 \sin^2(2\omega L) \sin^2(\omega L) A_{X_2}(\omega) S_{\dot{q}}(\omega) \,, \tag{13.18}$$

with $A_{X_2}(\omega)$ is a scaling factor that depends only on the beatnote frequencies,

$$\begin{aligned} A_{X_2}(\omega) = {} & (a_{12} - a_{13})^2 + a_{21}^2 + a_{31}^2 \\ & - 4 b_{12} (a_{12} - a_{13} - b_{12}) \sin^2(\omega L) \,. \end{aligned} \tag{13.19}$$

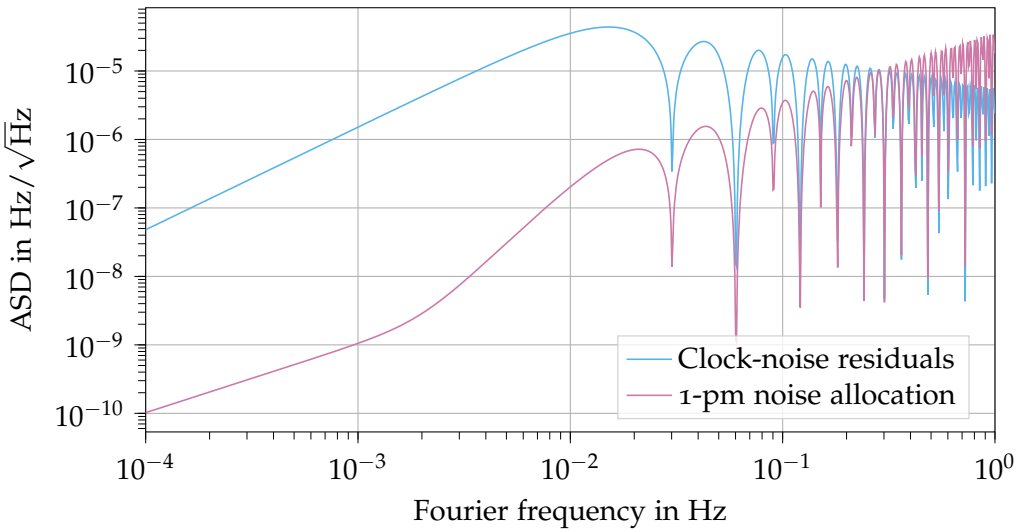

FIGURE 13.1: Comparison of the residual clock noise in second-generation Michelson X_2 combination, and the usual LISA 1 pm noise allocation curve. We assumed here a state-of-the-art space-qualified USO and a realistic set of beatnote frequency offsets.

Figure 13.1 shows this clock noise residual assuming the same USO model presented in chapter 6, with $S_{\dot{q}}(f) = 4 \times 10^{-27} f^{-1}$ in fractional frequency fluctuations, and a realistic set of beatnote frequency offsets. We compared it to a typical 1 pm LISA noise allocation for a single noise source, given by dividing eq. (8.1) by a factor 10.

We see that below 0.2 Hz, clock noise significantly violates this requirement and must be suppressed.

13.3.1.3 *Building correcting expression*

Inspecting eq. (13.15), we observe that clock noise enters in our TDI combination coupled with delay polynomials. We can rearrange it to get

$$\begin{aligned}\text{TDI}^{q} = \sum_{i,j,k\in\mathcal{I}_3^+} \Big[&\mathbf{P}_{ij}(b_{jk} - a_{ij})\dot{q}_i - \mathbf{P}_{ik}(b_{ij} + a_{ik})\dot{q}_i \\ &+ \mathbf{P}_{ij}(\dot{\mathbf{D}}_{ij} b_{jk}\dot{q}_j - b_{jk}\dot{q}_i)\Big] .\end{aligned} \tag{13.20}$$

Following chapter 7, the beatnote frequency offsets a_{ij}, b_{ij} are time-dependent. As such, commuting them with a delay operator yields an error term. This effect will be studied in section 13.3.3.1. We neglect it for now, and write the previous equation as

$$\begin{aligned}\text{TDI}^{q} \approx \sum_{i,j,k\in\mathcal{I}_3^+} \Big[&(b_{jk} - a_{ij})\mathbf{P}_{ij}\dot{q}_i - (b_{ij} + a_{ik})\mathbf{P}_{ik}\dot{q}_i \\ &+ b_{jk}\mathbf{P}_{ij}(\dot{\mathbf{D}}_{ij}\dot{q}_j - \dot{q}_i)\Big] .\end{aligned} \tag{13.21}$$

We observe that clock noise appears on the right side of the $\mathbf{P}_{ij}$, either *directly* as $\dot{q}_i$, or as a *differential term* $\dot{\mathbf{D}}_{ij}\dot{q}_j - \dot{q}_i$.

We will now see that the sideband-sideband beatnotes given in section 7.2 can provide a direct measurement of the differential clock noise. We form the dimensionless quantity

$$r_{ij} = \frac{\mathrm{isc}_{ij,\mathrm{sb}} - \mathrm{isc}_{ij,\mathrm{c}}}{\nu^m_{ji}} \,. \tag{13.22}$$

By inserting eqs. (13.10a) and (13.10b) into the previous expression, we see that r_{ij} directly measures the differential clock noise appearing in eq. (13.20),

$$r_{ij} = \dot{\mathbf{D}}_{ij}\dot{q}_j - \dot{q}_i \,, \tag{13.23}$$

where we neglect the modulation noise for now. The effect of modulation noise and an additional processing step for its partial mitigation are discussed in section 13.3.3.2.

Because the beatnote frequency offsets are measured and the delay polynomials are known, we can subtract $\sum_{i,j,k\in\mathcal{I}_3^+} b_{jk}\mathbf{P}_{ij}r_{ij}$ from our TDI combination to remove the last term of eq. (13.20).

We are left with the first two terms in the sum in eq. (13.20). We discussed in chapter 11 how any arbitrary interferometer can be synthesized out of a set of 6 one-way interferometric measurements η_{ij} between the LISA spacecraft. We observe that the r_{ij} are of exactly the same form as the η_{ij}, just expressed in terms of clock noise instead of laser noise. Therefore, we can apply the usual algorithm given in section 11.1.1 to construct any expression of the form $(\dot{\mathbf{D}}_{i_1,i_2,\ldots,i_n}q_{i_n} - q_{i_1})$ from the r_{ij}.

Each delay polynomial $\mathbf{P}_{ij}$ in eq. (13.14) is the sum of n_{ij} chained delay operators with signs σ^k_{ij}. It can be written as

$$\mathbf{P}_{ij} = \sum_{k=1}^{n_{ij}} \sigma^k_{ij}\dot{\mathbf{D}}_{A^k_{ij},\ldots,B^k_{ij}} \,, \tag{13.24}$$

where we denote the first and last indices of the chained delay operators in the k-th summand with A^k_{ij} and B^k_{ij}, respectively. By design of the TDI algorithm, we always have $B^k_{ij} = i$.

We can then construct a TDI variable for each summand of eq. (13.24), giving

$$R_{ij} = \sum_{k=1}^{n_{ij}} \sigma^k_{ij}\left(\dot{\mathbf{D}}_{A^k_{ij},\ldots,i}\dot{q}_i - \dot{q}_{A^k_{ij}}\right) . \tag{13.25}$$

We have

$$\mathbf{P}_{ij}\dot{q}_i - R_{ij} = \sum_{k=1}^{n_{ij}} \sigma^k_{ij}\dot{q}_{A^k_{ij}} \,. \tag{13.26}$$

In most second generation TDI combinations[6], this last term is vanishing, such that we have $R_{ij} = P_{ij}q_i$. Therefore, we can subtract them from eq. (13.20) to remove the last clock-noise terms.

6 We explicitly tested it for all second generation TDI combinations up to 16 links presented in section 11.4. We conjecture that it is valid for any second generation variable derived from geometric principles.

In the special case where one summand in $\mathbf{P}_{ij}$, say the n-th term, does not contain any delay, we skip it in the construction of R_{ij} (eq. (13.25)). An extra term $\sigma_{ij}^{n}\dot{q}_i$ is to be accounted for in eq. (13.26), which has to cancel with one of the $\sigma_{ij}^{k}\dot{q}_{A_{ij}^k}$.

The full corrected TDI combination therefore reads

$$\mathrm{TDI}^c = \mathrm{TDI} - \sum_{i,j,k\in\mathcal{I}_3^+} \Big[(b_{jk} - a_{ij})R_{ij} - (b_{ij} + a_{ik})R_{ik} + b_{jk}\mathbf{P}_{ij}r_{ij}\Big]\,. \tag{13.27}$$

Note that this algorithm can be applied without modification to TDI variables containing not only delays, but also advancements, as those presented in chapter 11.

13.3.1.4 *Example: correcting clock noise for X_2*

As an example, we apply our algorithm to the second-generation Michelson combination X_2 given in eq. (13.17). Following the decomposition of eq. (13.14),

$$\mathbf{P}_{12} = -(1 - \dot{\mathbf{D}}_{131} - \dot{\mathbf{D}}_{13121} + \dot{\mathbf{D}}_{1213131})\,, \tag{13.28a}$$
$$\mathbf{P}_{23} = 0\,, \tag{13.28b}$$
$$\mathbf{P}_{31} = (1 - \dot{\mathbf{D}}_{121} - \dot{\mathbf{D}}_{12131} + \dot{\mathbf{D}}_{1312121})\dot{\mathbf{D}}_{13}\,, \tag{13.28c}$$
$$\mathbf{P}_{21} = -(1 - \dot{\mathbf{D}}_{131} - \dot{\mathbf{D}}_{13121} + \dot{\mathbf{D}}_{1213131})\dot{\mathbf{D}}_{12}\,, \tag{13.28d}$$
$$\mathbf{P}_{32} = 0\,, \tag{13.28e}$$
$$\mathbf{P}_{13} = (1 - \dot{\mathbf{D}}_{121} - \dot{\mathbf{D}}_{12131} + \dot{\mathbf{D}}_{1312121})\,. \tag{13.28f}$$

Applying the TDI algorithm, we construct the R_{ij} variables satisfying eq. (13.25). They read

$$\begin{aligned} R_{12} = {} & -(1 - \dot{\mathbf{D}}_{131})(r_{12} + \dot{\mathbf{D}}_{12}r_{21}) \\ & + (2 - \dot{\mathbf{D}}_{121} - \dot{\mathbf{D}}_{12131})(r_{13} + \dot{\mathbf{D}}_{13}r_{31})\,, \end{aligned} \tag{13.29a}$$
$$R_{23} = 0\,, \tag{13.29b}$$
$$\begin{aligned} R_{31} = {} & -(2 - \dot{\mathbf{D}}_{131} - \dot{\mathbf{D}}_{13121})(r_{12} + \dot{\mathbf{D}}_{12}r_{21}) \\ & + (1 - \dot{\mathbf{D}}_{121})(r_{13} + \dot{\mathbf{D}}_{13}r_{31}) \\ & + (1 - \dot{\mathbf{D}}_{121} - \dot{\mathbf{D}}_{12131} + \dot{\mathbf{D}}_{1312121})r_{13}\,, \end{aligned} \tag{13.29c}$$
$$\begin{aligned} R_{21} = {} & -(1 - \dot{\mathbf{D}}_{131})(r_{12} + \dot{\mathbf{D}}_{12}r_{21}) \\ & - (1 - \dot{\mathbf{D}}_{131} - \dot{\mathbf{D}}_{13121} + \dot{\mathbf{D}}_{1213131})r_{12} \\ & + (2 - \dot{\mathbf{D}}_{121} - \dot{\mathbf{D}}_{12131})(r_{13} + \dot{\mathbf{D}}_{13}r_{31})\,, \end{aligned} \tag{13.29d}$$
$$R_{32} = 0\,, \tag{13.29e}$$
$$\begin{aligned} R_{13} = {} & -(2 - \dot{\mathbf{D}}_{131} - \dot{\mathbf{D}}_{13121})(r_{12} + \dot{\mathbf{D}}_{12}r_{21}) \\ & + (1 - \dot{\mathbf{D}}_{121})(r_{13} + \dot{\mathbf{D}}_{13}r_{31})\,. \end{aligned} \tag{13.29f}$$

These can be directly inserted into eq. (13.27) to get the corrected variable X_2^c.

13.3.2 *Numerical simulations*

To complement the theoretical studies presented above, we conducted numerical experiments to verify the clock-noise suppression capabilities of this algorithm. We simulate data using `LISA Instrument`, and then use `PyTDI` to generate the second-generation Michelson TDI data streams X_2, as well as the corresponding clock correction, all described in section 13.3.1.

As usual, laser beams and interferometric measurements are simulated in frequency, and we use the usual two-variable decomposition as described in part ii. In order to study the small clock noise residual and not be limited by numerical noise, we directly use the small $(\ )^\epsilon$ variable as input for the TDI construction.

In order not to be limited by other numerical effects, such as interpolation errors or flexing-filtering couplings, we use an unrealistically high sampling rate of 10 Hz for the full simulation chain. By doing so, we omit any simulation of on-board filters. The duration of our simulation is set to 10^5 s, i.e., 10^6 samples.

The propagation of laser beams between spacecraft is stil implemented using Lagrange fractional delay filters of order 31. Given our high sampling rate, they do not cause any observable artefact in our frequency band of interest and remain computationally tractable. Light travel times and their derivatives are computed from realistic orbits provided by ESA, as shown in fig. 3.3. These light travel times include relativistic corrections up to terms in $1/c$, including the Sagnac effect and the Shapiro delay, as described in [11].

We use the following programmed offsets for lasers, see section 7.2,

$$O_{12} = 8.1\,\mathrm{MHz}, \quad O_{21} = -9.5\,\mathrm{MHz}\,, \tag{13.30}$$
$$O_{13} = 1.4\,\mathrm{MHz}, \quad O_{31} = 10.3\,\mathrm{MHz}\,, \tag{13.31}$$
$$O_{23} = 9.2\,\mathrm{MHz}, \quad O_{32} = -11.6\,\mathrm{MHz}\,, \tag{13.32}$$

and do not simulate laser locking.

Our simulated clock noise matches that of a state-of-the-art space-qualified USO with

$$S_{\dot{q}}(f) = 4 \times 10^{-27} f^{-1} \tag{13.33}$$

in fractional frequency deviations, generated using a variant of the infinite RC model [67]. We do not simulate any deterministic clock errors, such as constant timing and frequency offsets or higher order frequency drifts due to aging of the oscillators.

Modulation errors are based on a fit of the 2 W-fiber amplifier (red) curve from figure 5.13 in [14]. In fractional frequency deviations with respect to the modulation frequency, they are given by

$$S_{\dot{N}^m}(f) = 5.2 \times 10^{-14} f^{1/3}\,. \tag{13.34}$$

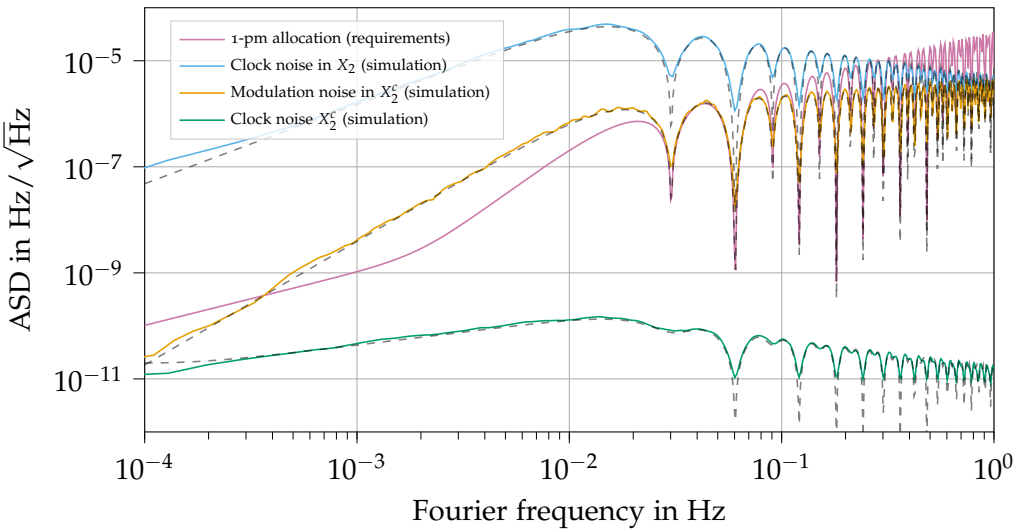

FIGURE 13.2: Simulation results. Blue and green curves represent the uncorrected X_2 and corrected X_2^c combinations in the sole presence of clock noise. The yellow curve shows the level of modulation noise in the corrected variable. Overlaid dashed black lines show our analytical expectations for these quantities. The usual 1 pm-noise allocation curve is shown in red as a reference.

Note that this noise level did not meet the requirements for LISA in [14], and we consequently also expect this noise to violate our 1 pm-noise allocation curve. Laser development is ongoing to achieve the required noise levels in line with the stringent timing requirements[7].

As we saw in chapter 6, only the 2.4 GHz modulation signals on a spacecraft have a direct low-noise relationship to the pilot tone used as timing reference, while the 2.401 GHz signals suffer additional noise due to the $\times 240$ and $\times 240.1$ multiplies in the chain (cf. figs. 6.1 and 6.2). We use a simple model for this effect, by making the working assumption that the right hand-side modulation noises (indexed 13, 32, 21) are 10 times higher than the left hand ones, i.e., with a spectrum

$$S_{\dot{N}^m}(f) = 5.2 \times 10^{-13} f^{1/3}. \tag{13.35}$$

To compute our TDI combinations, we also use order-31 Lagrange fractional delay filters.

Figure 13.2 presents the results of our numerical experiments. We used the LPSD method to estimate the spectra[8]. As a reference, we also plot in red the usual LISA Performance Model's 1 pm-noise allocation curve, given by dividing eq. (8.1) by a factor 10.

The blue and green curves represent the ASDs of the uncorrected X_2 and corrected X_2^c second-generation Michelson TDI combinations, in the sole presence of clock noise (we disabled modulation errors). The black dashed line overlaying the former curve represents the theoretical clock-noise content in X_2 from eq. (13.18). The black dashed line overlaying the green curve, representing our model of the residual clock noise after correction, is discussed in details in section 13.3.3.1 and given by eq. (13.43).

7 M. Hewitson, personal communication, (April 9, 2021).

8 With the following paramters: `olap="default", bmin=1, Lmin=0, Jdes=4000, Kdes=5000, order=-1, win=np.kaiser, psll=240`.

The orange curve represents the modulation errors in the corrected X_2^c combination. We obtain it by enabling modulation errors in addition to clock noise in the previous simulation. In addition, we perform an additional processing step to remove the higher right hand-side modulation noise terms, see section 13.3.3.2. The overlaid black dashed line shows our analytical expectations, also described in the same section.

13.3.3 *Discussion*

We see in fig. 13.2 that our clock-noise reduction algorithm works as expected and that clock noise is reduced to below the noise allocation curve. In addition, our analytical models match perfectly with simulated results.

We discuss in the following paragraphs the models for the residual clock noise after correction, the imperfections in the sideband measurements used for the correction, and other limiting effects that may appear with different simulation parameters but were not visible in our setup. Finally, we compare our algorithm with the previously proposed solution [86].

13.3.3.1 *Time-varying beatnote frequencies*

The residual clock noise after correction is dominated by the effect of time-varying beatnote frequencies, which we neglected when deriving the correction. To evaluate this clock-noise residuals, we take the difference between eq. (13.20) and eq. (13.21). One gets

$$\mathrm{TDI}^{\nu} = \sum_{i,j,k \in \mathcal{I}_3^+} \left(\left[a_{ij}, \mathbf{P}_{ij} \right] + \left[a_{ik}, \mathbf{P}_{ik} \right] \right) q_i \,, \tag{13.36}$$

where we used that the reference beatnote offsets are constants in our setup, and hence can be freely commuted with delays. Here, $[A, B] = AB - BA$ stands for the commutator of A and B.

This is only the case if laser locking is neglected. We will present a more general model including all beatnote frequency derivatives in section 13.3.3.5

We can now assume that all delays are equal and constant, such that a delay operator of N delays can be written as $\mathbf{D}^N$. We can write the delay polynomial $\mathbf{P}_{ij}$ as

$$\mathbf{P}_{ij} = \sum_{\alpha} \lambda_\alpha \mathbf{D}^{N_\alpha} \,, \tag{13.37}$$

with λ_α the factor in front of the term α, and N_α the number of delays associated with the same term. We now have

$$\left[a_{ij}, \mathbf{P}_{ij} \right] = \sum_{\alpha} \lambda_\alpha \left[a_{ij}, \mathbf{D}^{N_\alpha} \right] \,, \tag{13.38}$$

and similarly for $\mathbf{P}_{ik}$.

Let us study one commutator $\left[a_{ij}, \mathbf{D}^N\right]$. This is an operator, which will be applied on q_i. Assuming that a_{ij} is a linear function of time, we can write

$$\begin{aligned}\left[a_{ij}, \mathbf{D}^N\right] &= a_{ij}(t)\mathbf{D}^N - (\mathbf{D}^N a_{ij})\mathbf{D}^N \\ &= (a_{ij} - \mathbf{D}^N a_{ij})\mathbf{D}^N \\ &= Nd\,\dot{a}_{ij}\mathbf{D}^N\,,\end{aligned} \tag{13.39}$$

where $Nd\,\dot{a}_{ij}$ is a constant. We can then go to the frequency domain to write

$$\mathcal{F}\left[\left[a_{ij}, \mathbf{D}^N\right]\right] \approx Nd\,\dot{a}_{ij}e^{-j\omega Nd}\,. \tag{13.40}$$

We can therefore define

$$Q_{ij}(\omega) = \sum_\alpha \lambda_\alpha N_\alpha d\, e^{-j\omega dN}\,, \tag{13.41}$$

such that, still in the frequency domain,

$$\mathcal{F}\left[\left[a_{ij}, \mathbf{P}_{ij}\right]\right] = Q_{ij}\dot{a}_{ij}\,. \tag{13.42}$$

Finally, using that clocks are independent but share the same statistical properties, we obtain the following residual from the time-varying beatnote offsets,

$$S_{\mathrm{TDI}^\nu}(\omega) = S_q(\omega) \sum_{i,j,k\in\mathcal{I}_3^+} \left|Q_{ij}(\omega)\dot{a}_{ij} + Q_{ik}(\omega)\dot{a}_{ik}\right|^2. \tag{13.43}$$

In our simulation, the average value of the beatnote derivatives evaluate to

$$\dot{a}_{12} \approx \dot{a}_{21} \approx -2.0\,\mathrm{Hz\,s^{-1}}\,, \tag{13.44}$$

$$\dot{a}_{13} \approx \dot{a}_{31} \approx 320\,\mathrm{mHz\,s^{-1}}\,, \tag{13.45}$$

$$\dot{a}_{23} \approx \dot{a}_{32} \approx -58\,\mathrm{mHz\,s^{-1}}\,, \tag{13.46}$$

while their average second derivatives are of the order of, or below, $10^{-7}\,\mathrm{Hz\,s^{-2}}$, which is small enough to neglect it in our model. This is also verified by the perfect agreement between model and simulation in fig. 13.2.

13.3.3.2 *Modulation errors*

In section 13.3.1, we introduce modulation errors to model imperfections of the sideband modulation. By inserting eqs. (13.10a) and (13.10b) into eq. (13.22), we see that they appear in r_{ij} as

$$r_{ij} = \frac{\nu^m_{ji}\dot{\mathbf{D}}_{ij}\dot{M}_{ji} - \nu^m_{ij}\dot{M}_{ij}}{\nu^m_{ji}}\,. \tag{13.47}$$

Therefore, our clock noise reduction performance will ultimately be limited by this modulation noise. To achieve the required performance, we must

remove the higher modulation noise contributions from the right hand-sided modulation signals.

To remove these higher modulation noise terms, we need to measure the difference ΔM_i of the two modulation signals on each spacecraft i. It can be measured electrically before the optical modulations are performed, or optically, using the sideband-sideband beatnotes in the reference interferometers.

We study here the second option, and define

$$\Delta M_i = \frac{\mathrm{ref}_{ik,\mathrm{sb}} - \mathrm{ref}_{ik}}{2} - \frac{\mathrm{ref}_{ij,\mathrm{sb}} - \mathrm{ref}_{ij}}{2}\,, \tag{13.48}$$

where the indices $i, j, k \in \mathcal{I}_3^+$. Note that both terms in eq. (13.48) contain the same information. We use here interferometric measurements from both adjacent MOSAs ij and ik to reduce the overall readout noise in ΔM_i, which is uncorrelated in both measurements.

These expressions strongly suppress any other noise sources which affect both carrier and sideband equally, such as laser frequency noise. Inserting eqs. (13.11a) and (13.11b), we see that they contain the modulation noise terms

$$\Delta M_i \approx \nu_{ij}^m \dot{M}_{ij} - \nu_{ik}^m \dot{M}_{ik}\,. \tag{13.49}$$

We now define

$$r_{ij}^c = r_{ij} + \frac{\dot{\mathbf{D}}_{ij}\Delta M_j}{\nu_{ji}^m}\,, \tag{13.50a}$$

$$r_{ik}^c = r_{ik} - \frac{\Delta M_i}{\nu_{ki}^m}\,, \tag{13.50b}$$

which contain the same differential clock noise as r_{ij} and r_{ik}, so that we can use them in place of the latter in the clock-noise reduction procedure described in section 13.3.1. However, substituting previous expressions, it becomes clear that these terms do not contain modulation noise from right-handed MOSAs, as we have

$$r_{ij}^c = \frac{\dot{\mathbf{D}}_{ij}\nu_{jk}^m \dot{M}_{jk} - \nu_{ij}^m \dot{M}_{ij}}{\nu_{ji}^m}\,, \tag{13.51a}$$

$$r_{ik}^c = \frac{\dot{\mathbf{D}}_{ik}\nu_{ki}^m \dot{M}_{ki} - \nu_{ij}^m \dot{M}_{ij}}{\nu_{ki}^m}\,. \tag{13.51b}$$

Since we choose ν_{ij}^m identical on all left-handed MOSAs, this simplifies to

$$r_{ij}^c = \dot{\mathbf{D}}_{ij}\dot{M}_{jk} - \dot{M}_{ij}\,, \tag{13.52a}$$

$$r_{ik}^c = \dot{\mathbf{D}}_{ik}\dot{M}_{ki} - \dot{M}_{ij}\,, \tag{13.52b}$$

The remaining left-sided modulation error terms enter eqs. (13.52a) and (13.52b) with the same pattern as clock noise in eq. (13.23). This extends to the clock

noise correction term we subtract in eq. (13.27), such that the overall modulation noise exactly replaces the clock noise in the original TDI expression. As such, following eq. (13.16), their PSDs are given by

$$\sum_{i,j,k\in\mathcal{I}_3^+} \Big| a_{ij}\widetilde{\mathbf{P}}_{ij}(\omega) + a_{ji}\widetilde{\mathbf{P}}_{ji}(\omega) - b_{ij}[\widetilde{\mathbf{P}}_{ik}(\omega) - \widetilde{\mathbf{P}}_{ki}(\omega)\widetilde{\mathbf{D}}_{ki}(\omega)]\Big|^2 S_M(\omega)\,, \tag{13.53}$$

where we assume that modulation noise is uncorrelated but of equal PSD $S_{\dot{M}}(\omega)$ for all 2.4 GHz sidebands.

In the particular case of X_2, we get

$$16\sin^2(2\omega L)\sin^2(\omega L)A_{X_2}(\omega)S_{\dot{M}}(\omega)\,, \tag{13.54}$$

with A_{X_2} as the same scaling factor as given in eq. (13.19),

$$A_{X_2}(\omega) = (a_{12}-a_{13})^2 + a_{21}^2 + a_{31}^2 - 4b_{12}(a_{12}-a_{13}-b_{12})\sin^2(\omega L)\,. \tag{13.55}$$

We see in fig. 13.2 that this model fits perfectly our numerical results.

13.3.3.3 *Calibration errors*

The clock correction algorithm relies on accurate measurements of the large beatnote frequency offsets a_{ij}, b_{ij}. Therefore, the achievable clock correction will be limited to a level proportional to the fractional error in these coefficients. A simple model for the residual noise from this effect can be derived by replacing the coefficients a_{ij}, b_{ij} in eq. (13.18) with terms representing the calibration error in the respective variables.

In reality, a_{ij}, b_{ij} will be determined with respect to the frequency of the USO, such that large deterministic offsets in its frequency will affect their measured value. We neglected such offsets in our analytical study and simulation, but remark that they are typically at a level below 10^{-6} for a space-qualified USO, as discussed in chapter 6. Therefore, the residual noise due to this effect is smaller than the one presented in section 13.3.3.1.

13.3.3.4 *Other effects*

The clock-noise reduction algorithm presented here relies on the same principles as the laser-noise reduction by the traditional TDI combinations. As such, any effect which limits the latter will also impact the former in a similar fashion. This applies - in principle - to all effects described in section 12.3, except the residual laser noise due to a fundamental armlength mismatch.

However, as seen in fig. 13.2, clock noise only needs to be reduced by around 4 orders of magnitude, whereas laser noise needs to be reduced by around 8 orders of magnitude[9]. Therefore, if these effects are sufficiently small to

9 For a laser noise of $30\,\mathrm{Hz}/\sqrt{\mathrm{Hz}}$ compared to the usual LISA 1 pm noise allocation curve.

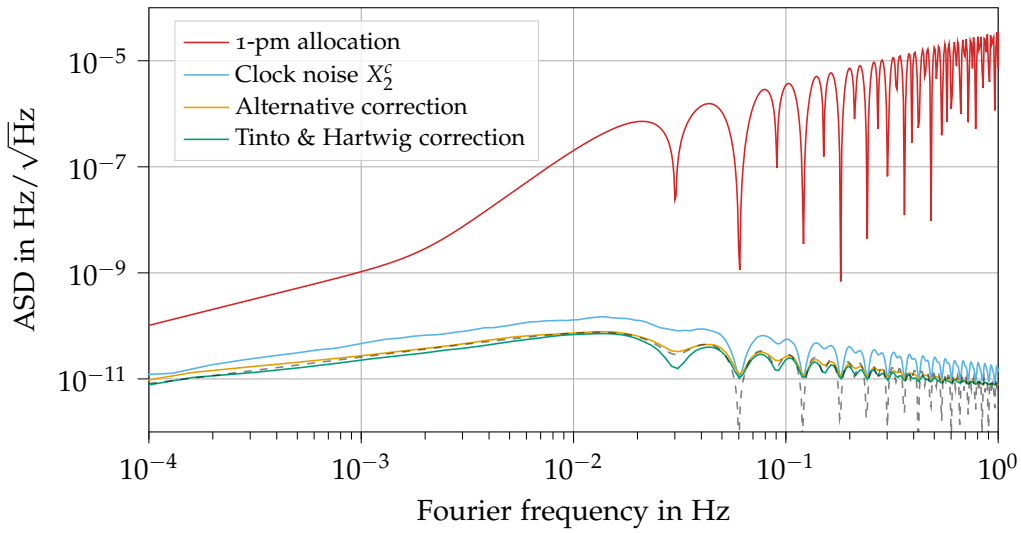

FIGURE 13.3: Comparison of the residual clock noise obtained with the reduction algorithm proposed in section 13.3.1 (in blue), the alternative algorithm proposed in section 13.3.3.5 (in orange), and the algorithm previously proposed in the literature [86] (in green). Overlayed the analytical model shown in eq. (13.66). The usual 1 pm-noise allocation curve is shown in red.

allow for laser noise reduction, they are automatically sufficiently small to not significantly impact the clock noise reduction.

13.3.3.5 *Comparison to other algorithms*

In fig. 13.3, we compare the performance of our clock-noise reduction algorithm (blue curve) against that from [86] (plotted in green). In our notation system and replacing delay operators by their Doppler-delay counterparts, the former algorithm is given by

$$X_2^c = X_2 - (1 - \dot{\mathbf{D}}_{12131}) K_{X_1} \,, \tag{13.56}$$

where K_{X_1} is the correcting expression for the first-generation Michelson,

$$\begin{aligned} K_{X_1} = &-\frac{b_{12}}{2}\Big[(1-\dot{\mathbf{D}}_{121})(r^c_{13}+\dot{\mathbf{D}}_{21}r^c_{31}) \\ &\quad + (1-\dot{\mathbf{D}}_{131})(r^c_{12}+\dot{\mathbf{D}}_{12}r^c_{21})\Big] \\ &+ a_{12}(r^c_{13}+\dot{\mathbf{D}}_{13}r^c_{31}) - a_{13}(r^c_{12}+\dot{\mathbf{D}}_{12}r^c_{21}) \\ &+ a_{21}[r^c_{13} - (1-\dot{\mathbf{D}}_{131})r^c_{12} + \dot{\mathbf{D}}_{13}r_{31}] \\ &- a_{31}[r^c_{12} - (1-\dot{\mathbf{D}}_{121})r^c_{13} + \dot{\mathbf{D}}_{12}r^c_{21}] \,. \end{aligned} \tag{13.57}$$

We see that the former algorithm performs slightly better than the one proposed above, by about a factor of two in amplitude.

This difference in the performance is explained by the factorization used to build the second-generation correction from the first-generation version. The factorized delays are applied to the whole first generation expression, which partly accounts for the the time-varying beatnote frequencies, leading to a lower residual. This is only valid under the assumption that Doppler-delay operators can be commuted. In our setup, this assumption is only an approximation, but the residual due to this effect (i.e., terms scaled by the commutator of two delay operators) is smaller than that due to time-varying

beatnotes (i.e., arising from the commutator of beatnote frequencies and delay operators).

A first solution to achieve the same performance in the framework of this paper is to build the clock-noise correction for the first-generation Michelson X_1 combination under the same assumptions, and then apply the same factor $(1 - \dot{\mathbf{D}}_{12131})$. Our simulations show that we exactly recover the same levels of residual clock noise.

A second, more general solution is to observe that beatnote frequencies always appear directly to the left of the clock noise terms in eq. (13.20). Going to eq. (13.21), we commuted the $\mathbf{P}_{ij}$ with all beatnote frequencies. A more conservative approach would be to construct expressions $R_{ij}^{a_{ij}}$ which evaluate to

$$R_{ij}^{a_{ij}} = \mathbf{P}_{ij} a_{ij} q_i \,, \tag{13.58}$$

and similarly for the other terms in eq. (13.20), such that they can be used directly in that equation. This can be approximated by directly rescaling all r_{ij} by a_{ij} before constructing R_{ij}. Inspecting our correction variable in eq. (13.23), one of the clock-noise terms always appears attached to a delay operator. This leaves us with a single delay-beatnote commutator in each r_{ij} term, due to the physical propagation delay.

In detail, we compute

$$\mathrm{TDI}^c = \mathrm{TDI} - \sum_{i,j,k \in \mathcal{I}_3^+} R_{ij}^{b_{jk}} - R_{ij}^{a_{ij}} - R_{ik}^{b_{ij}} - R_{ik}^{a_{ik}} + \mathbf{P}_{ij}(b_{jk} r_{ij}^c) \,. \tag{13.59}$$

In the example of the second generation Michelson variable, we would for example have

$$\begin{aligned} R_{12}^{b_{23}} &= -(1 - \dot{\mathbf{D}}_{131})(b_{23} r_{12} + \dot{\mathbf{D}}_{12} b_{23} r_{21}) \\ &\quad + (2 - \dot{\mathbf{D}}_{121} - \dot{\mathbf{D}}_{12131})(b_{23} r_{13} + \dot{\mathbf{D}}_{13} b_{23} r_{31}) && \text{(13.60a)} \\ &= \mathbf{P}_{12} b_{23} q_1 - (1 - \dot{\mathbf{D}}_{131})\big(\big[b_{23}, \dot{\mathbf{D}}_{12}\big] q_2 + \dot{\mathbf{D}}_{12}\big[b_{23}, \dot{\mathbf{D}}_{21}\big] q_1\big) \\ &\quad + (2 - \dot{\mathbf{D}}_{121} - \dot{\mathbf{D}}_{12131})\big(\big[b_{23}, \dot{\mathbf{D}}_{13}\big] q_3 + \dot{\mathbf{D}}_{13}\big[b_{23}, \dot{\mathbf{D}}_{31}\big] q_1\big) \,, && \text{(13.60b)} \\ &\equiv \mathbf{P}_{12} b_{23} q_1 + R_{12}^{[b_{23}]} && \text{(13.60c)} \end{aligned}$$

where we introduced an error term $R_{12}^{[b_{23}]}$ accounting for the commutators, and used that

$$b_{23} r_{12} = b_{23}(\dot{\mathbf{D}}_{12} q_2 - q_1) = (\dot{\mathbf{D}}_{12} b_{23} q_2 - b_{23} q_1) + \big[b_{23}, \dot{\mathbf{D}}_{12}\big] q_2 \,, \tag{13.61}$$

and similar for the other combinations of beatnote frequency and r_{ij}. We observe that $R_{12}^{b_{23}}$ now consists of our desired expression $\mathbf{P}_{12} b_{23} q_1$ and the new error term $R_{12}^{[b_{23}]}$.

The residual clock noise in any TDI variable can therefore be approximated as

$$\mathrm{TDI}^{c,res} = \sum_{i,j,k \in \mathcal{I}_3^+} R_{ij}^{[b_{jk}]} - R_{ij}^{[a_{ij}]} - R_{ik}^{[b_{ij}]} - R_{ik}^{[a_{ik}]} + \mathbf{P}_{ij}\big(\big[b_{jk}, \dot{\mathbf{D}}_{ij}\big] q_j\big) \,. \tag{13.62}$$

In the frequency domain, we get using eq. (13.39),

$$\begin{aligned}\mathcal{F}\left[R_{12}^{[b_{23}]}\right](\omega) \approx d\dot{b}_{23}e^{-i\omega d}\big[&((e^{-i\omega 2d}-1)(\mathcal{F}[q_2]+e^{-i\omega d}\mathcal{F}[q_1]) \\ &+(2-e^{-i\omega 2d}-e^{-i\omega 4d})(\mathcal{F}[q_3]+e^{-i\omega d}\mathcal{F}[q_1])\big] \end{aligned} \tag{13.63}$$

$$\equiv d\dot{b}_{23}e^{-i\omega d}\tilde{R}_{12}^{q} \tag{13.64}$$

for a single residual term, where $\tilde{R}_{12}^{q}$ collects the complex exponentials and clock noise terms in the above equation. Overall, this gives

$$\begin{aligned}\mathrm{TDI}^{c,res} \approx de^{-i\omega d}\sum_{i,j,k\in\mathcal{I}_3^+}&(\dot{b}_{jk}-\dot{a}_{ij})\tilde{R}_{ij}^{q}-(\dot{b}_{ij}+\dot{a}_{ik})\tilde{R}_{ik}^{q} \\ &+\dot{b}_{jk}\widetilde{\mathbf{P}}_{ij}\mathcal{F}[q_j]\ .\end{aligned} \tag{13.65}$$

If we again assume that all three clocks are uncorrelated and have the same PSD $S_{\dot{q}}$, we need to collect all their contributions individually, and finally get

$$\begin{aligned}S_{\mathrm{TDI}^{c,res}}(\omega) = \Big[&3\left[(\dot{a}_{12}+\dot{a}_{21})^2+(\dot{a}_{13}+\dot{a}_{31})^2\right]\cos(2d\omega) \\ &-\big[\dot{a}_{12}(\dot{a}_{21}+2\dot{a}_{31}-3\dot{b}_{12})+\dot{a}_{13}(2\dot{a}_{21}+\dot{a}_{31}) \\ &\quad-\dot{b}_{12}(3\dot{a}_{21}+2(\dot{a}_{31}+\dot{b}_{12}))+2(\dot{a}_{21}+\dot{a}_{31})^2\big]\cos(4d\omega) \\ &+\dot{a}_{12}(2\dot{a}_{13}+9\dot{a}_{21}+4(\dot{a}_{12}+\dot{a}_{31})-3\dot{b}_{12}) \\ &+\dot{a}_{13}(4(\dot{a}_{13}+\dot{a}_{21})+9\dot{a}_{31})+6\left(\dot{a}_{21}^2+\dot{a}_{21}\dot{a}_{31}+\dot{a}_{31}^2\right) \\ &-\dot{b}_{12}(3\dot{a}_{21}+2\dot{a}_{31}+2\dot{b}_{12})\Big]8d^2\sin^2(d\omega)S_{\dot{q}}\,.\end{aligned} \tag{13.66}$$

Note that although we computed the residual here for the example of the Michelson X combination, the general approach can be applied to any TDI combination.

The results of this alternative scheme for X_2 are presented in fig. 13.3 as the orange line, overlayed by our analytical model. We don't recover the exact zeros from [86] as they are related to the factor $(1-\dot{\mathbf{D}}_{12131})$, but otherwise achieve a very similar residual noise level.

13.4 NUMERICAL VERIFICATION OF CLOCK CORRECTION WITH TOTAL FREQUENCY

We have argued in section 13.1 that in principle, we can include the correction for the desynchronization between the different clocks in the main laser noise reduction step. However, as discussed in section 13.2 this requires very high numerical precision, and we suggested to instead detrend variables given in total frequency to work with smaller numbers. This implies that clock noise is no longer automatically reduced while constructing the variable, requiring an additional clock noise reduction step, which we derived in section 13.3. There, we showed simulations of just the frequency fluctuations to check our analytical models of the achievable laser noise reduction.

We now want to verify numerically how these results translate to the more realistic case of having an input variable expressed in total frequency, and

show that TDI still works if the clocks including large offsets and drifts. In addition, we will include ranging noise in the MPRs, and show that it can be sufficiently suppressed using a combination of a polynomial fit and the sideband measurements.

For this, we simulate 10^5 s of data using `LISANode`, with the usual ESA provided orbits. We enable laser-, clock- and ranging noise, and use the usual locking scheme N1-LA12, while disabling all other noises. The MPRs then measure the clock time differences at the events of emission and reception of the beams, plus a stochastic ranging noise at $1\,\mathrm{m}/\sqrt{\mathrm{Hz}}$.We want to stress that the MPRs thus include all imperfections from the clocks of the two spacecraft involved in each link. For the clocks, we include the deterministic drifts given in appendix D.8, in addition to initial timer offsets of 1 s, 0.1 s and -0.7 s for spacecraft 1, 2 and 3, respectively. We also include the random clock jitters as given in appendix D.8, but do not simulate modulation noise.

Relative to their respective proper time.

For all cases, we compute both the second generation Michelson X and Y variables. With our locking scheme, all non-locking beatnotes entering in X are actually recorded on spacecraft 1, according to the same clock. This is not the case for Y, where we have to use non-locking beatnotes from spacecraft 1, 2, and 3, such that we expect potentially different behaviour for these two variables.

Since we are using the total frequency, we expect numerical quantization noise due to the large varibles to be a significant contributor to the final noise spectrum. To keep track of these effects, we run another simulation with identical parameters, but *all* noises disabled. All variables still carry their numerical quantization noise, and other numerical errors due to, e.g., the Lagrange interpolation, will still appear in the result.

13.4.1 *TDI using total frequency*

We first compute the TDI variables directly using the total frequencies as input, without any detrending. As delays, we use the MPRs, and apply the Doppler correction as outlined in section 12.4. We recall that for applying the Doppler correction, we have to compute the derivative of the delays applied in TDI. Any error in these Doppler factors will be scaled by the large beatnote frequencies, such that they have to be determined with great precision. Errors in the delays themselves, however, are less important, since beatnote frequencies are changing relatively slowly.

We can compute an accurate estimate of the MPR derivative by utilizing the sideband measurements. Following the definitions in chapter 6, we can define similar variables to the r_{ij} used in section 13.3:

$$\dot{\rho}_{12} = \frac{\mathrm{isc}_c - \mathrm{isc}_{sb} + 1\,\mathrm{MHz}}{2.401\,\mathrm{GHz}}, \tag{13.67a}$$

$$\dot{\rho}_{13} = \frac{\mathrm{isc}_c - \mathrm{isc}_{sb} - 1\,\mathrm{MHz}}{2.4\,\mathrm{GHz}}, \tag{13.67b}$$

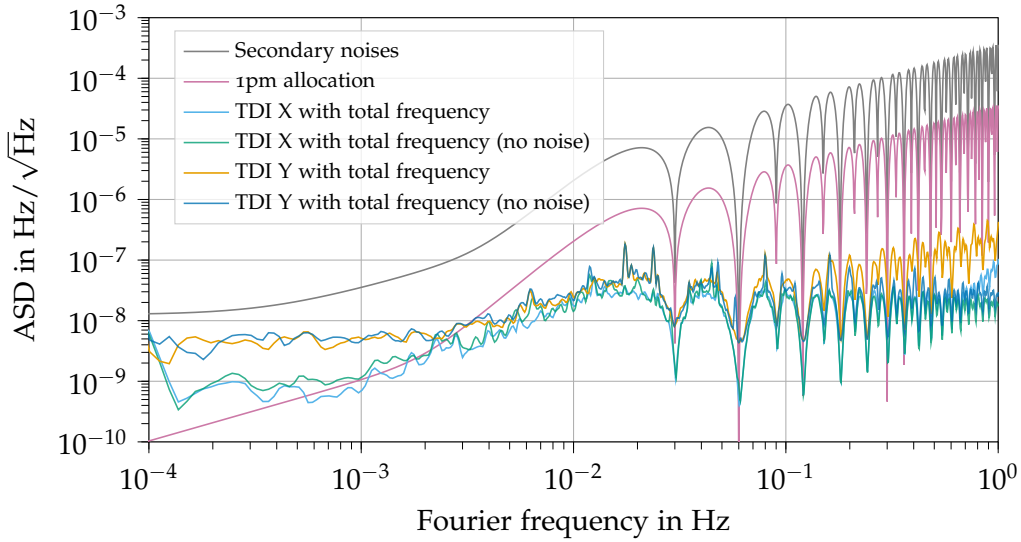

FIGURE 13.4: TDI X_2 and Y_2 constructed using variables in total frequency, including laser and clock noise, as well as large deterministic clock drifts and offsets. Laser noise is still reduced, but numerical artifacts due to the large dynamic range of the variables become significant. Simulation results without any noises enabled shown as comparison. The usual 1 pm-noise allocation curve is shown in red.

and cyclic for the other spacecraft. The main difference between these equations and eq. (13.22) is that we compensate for the 1 MHz beatnote frequency offsets of the sidebands wrt. the carrier.

For the actual time shifts, we use the MPRs, but apply a polynomial fit to remove any in-band fluctuations from them. The small fluctuations correcting for clock noise are accounted for in the Doppler correction, for which we use the $\dot{\rho}_{ij}$ as the delay derivatives. We use interpolation order 65 in order to not be limited at high frequencies. We then estimate the spectrum using the LPSD algorithm[10].

We compute the TDI variable X_2 (and its cyclic permutations) in multiple steps. Following [83], X_2 can be factorized as

$$\begin{aligned} X_2 = (1 - \dot{\mathbf{D}}_{13121})\overbrace{\left((\dot{\eta}_{12} + \dot{\mathbf{D}}_{12}\dot{\eta}_{21}) + \dot{\mathbf{D}}_{121}(\dot{\eta}_{13} + \dot{\mathbf{D}}_{13}\dot{\eta}_{31})\right)}^{A} \\ - (1 - \dot{\mathbf{D}}_{12131})\underbrace{\left(\dot{\mathbf{D}}_{131}(\dot{\eta}_{12} + \dot{\mathbf{D}}_{12}\dot{\eta}_{21}) + (\dot{\eta}_{13} + \dot{\mathbf{D}}_{13}\dot{\eta}_{31})\right)}_{B} . \end{aligned} \tag{13.68}$$

We first construct the one-arm roundtrip variables,

$$(\dot{\eta}_{12} + \dot{\mathbf{D}}_{12}\dot{\eta}_{21}), \quad (\dot{\eta}_{13} + \dot{\mathbf{D}}_{13}\dot{\eta}_{31}) , \tag{13.69}$$

followed by the two-arm roundtrips labelled A and B in eq. (13.68), to which we then finally apply the delay differences $(1 - \dot{\mathbf{D}}_{13121})$ and $(1 - \dot{\mathbf{D}}_{12131})$.

Besides being computationally less expensive, this method also has the advantage that any numerical noise present in A and B gets suppressed towards low frequencies by the delay differences[11], which act like a first derivative.

We only need to apply a total of 6 high-order interpolations, compared to 14 when using the fully expanded version of X_2.

The result is plotted in fig. 13.4. We observe that both laser and clock noise are indeed significantly suppressed in both X and Y, but not to the level

10 With the following parameters: `bmin=1, Lmin=0, Jdes=2000, Kdes=100, order=1, win=np.kaiser, psll=240`.

11 We thank M. Staab for suggesting to use this factorization in order to reduce the numerical noise in these variables!

previously observed. One limiting effect we expected in section 13.2 is numerical noise. To verify this, we overlay simulation results with all noises disabled (in green and dark blue), which agree well with our simulation results with laser and clock noise enabled (in sky-blue and orange) across most of the frequency band. At high frequencies, we see a small increase in Y. A possible explanation could be that the polynomial fit introduces a small bias in the delays, which following section 12.3 should affect Y more significantly than X with our locking scheme. We also observe that our usual 1 pm allocation curve is not met at low frequencies, with a larger discrepancy for Y than for X.

However, the 10 pm optical metrology system (OMS) allocation curve given in eq. (8.1) (from which we derived our 1 pm allocation) is quite stringent at low frequencies, and almost an order of magnitude below the expected level of test-mass acceleration noise at a Fourier frequency of 10^{-4} Hz. In fact, the numerical noise in our variable is significantly below the expected test-mass acceleration noise level, as shown by the grey curve labeled 'secondary noises' in fig. 13.4.

This is the same curve shown in fig. 9.1, where it agreed well with our simulation results when all effects are enabled.

13.4.2 *TDI using detrended total frequency*

As discussed in section 13.2, an alternative to using the total frequency is to first detrend all time series, and then compute the TDI variables using the detrended data. This has the advantage that the delays need to be known at much lower precision. The disadvantage is that this requires an additional clock correction step, as described in section 13.3.

We therefore detrend our data by applying a polynomial fit to each variable, using the same methods already described in chapter 8. We then compute the TDI variables using the fit residuals as input, and afterwards apply the clock correction procedure described in section 13.3. We also apply a fit to the MPRs, and use its result as our input delay series to reduce any numerical noise in the MPR themselves. We apply the Doppler correction as outlined in section 12.4, again using the $\dot{\rho}_{ij}$ introduced in section 13.4.1 to not couple any ranging noise, and use the same interpolation order 65. We then estimate the spectrum using the LPSD algorithm, with the same parameters as before.

The result is plotted in fig. 13.5. We included the previously achieved results from fig. 13.5 as a comparison, and see that we indeed achieve a lower noise floor when using detrended variables, at least for Y. The 1 pm-noise allocation curve is now almost met at very low frequencies, such that the additional numerical noise is far below the expected test-mass acceleration noise level. The steep increase at the very lowest frequencies is an artifact from the spectral estimation.

The results in this section demonstrate that it is possible to reduce both laser and clock noise without any relation to a global or common reference frame.

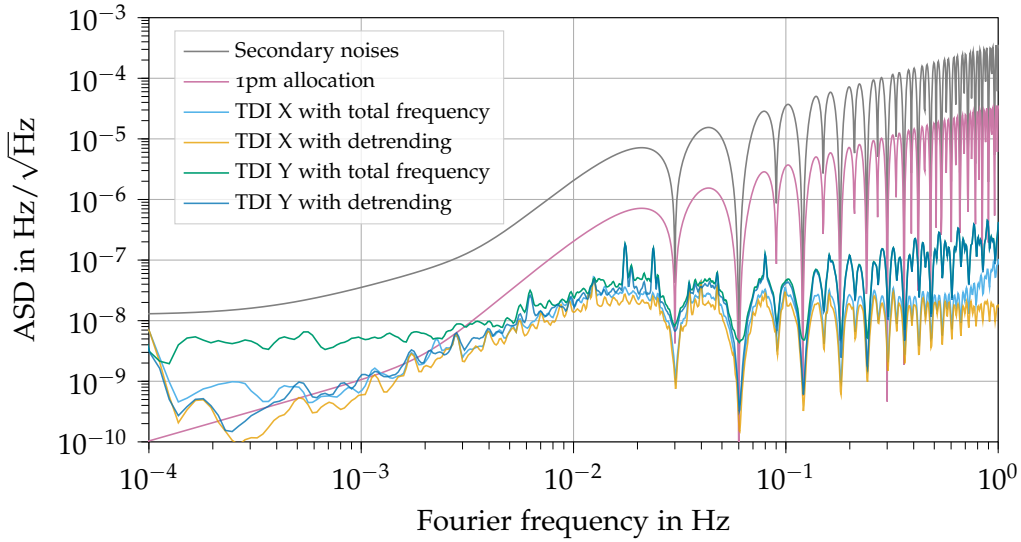

FIGURE 13.5: TDI X_2 and Y_2 constructed using fit residuals of variables in total frequency, including laser and clock noise, as well as large deterministic clock drifts and offsets. Laser noise is reduced, and numerical artifacts due to the large dynamic range of the variables are smaller than when directly using the total frequency. The usual 1 pm-noise allocation curve is shown in red.

13.5 OUTLOOK: RANGING PROCESSING AND SYNCHRONIZATION TO TCB

We showed in section 13.4 that both clock and laser noise can be reduced to match the 1 pm allocation curve in most of the frequency band when using data provided in total frequency, even in the presence of significant clock offsets and drifts, as well as random ranging measurement noise.

Except for a small violation at the smallest frequencies around 10^{-4} Hz, where this allocation curve is unnecessarily stringent.

However, we still neglected the final processing step of shifting the resulting variables to a common time frame, like the TCB. This requires accurate knowledge of all 3 clock offsets wrt. TCB. These clock offsets are encoded in the MPRs, where they appear entangled with the delay due to the inter-spacecraft propagation.

One way to disentangle this information is to use a Kalman filter, similar to what has been described in [96]. Such a filter can use information on the expected dynamical behaviour of the different components making up the MPRs, for example due to the orbital dynamics and statistically expected evolution of the clock fluctuations, in combination with additional interferometric measurements and ground based observations to provide an accurate estimate of the individual clock offsets and the physical light propagation times as seperate variables. Designing these filters is non-trivial, and multiple versions are currently under development inside the LISA consortium. Final results on their performance using realistic simulations are not yet available.

Depending on how well the clock offsets can be determined, one could also first transform all variables to a common reference frame, either one of the spacecraft clocks or even TCB, and then construct the TDI variable using, for example, light travel times computed in the TCB. Compared to the approach presented in this thesis, this might offer the advantage that we can use the additional information entering the Kalman filter to achieve overall better performance. However, as described in section 13.2, any timeshift applied

before TDI needs to fulfill stringent timing requirements, which might be difficult to achieve for synchronization to TCB.

Synchronizing the variables after laser noise has been reduced is much less critical, since the time shifts can be applied to the in-band fluctuations, which are several orders of magnitude smaller than the original MHz beatnotes.

Another effect we neglected in section 13.4 are large deterministic biases in the MPRs, for example due to processing or cable delays affecting the PRN measurements. Ideally, these should be characterized on-ground before launch, such that they can be simply compensated in a calibration step. In case this is not possible, or that these biases turn out to be time-varying, they could be determined using time-delay interferometric ranging (TDI-R). The basic idea behind TDI-R is that in order to fully suppress laser and clock noise, the delays applied in TDI have to be identical to the ones present in the actual data. Any errors in the delays will cause an increased noise level, such that one can use the noise level in the TDI variables to monitor how far the applied delays deviate from the true ones. The basic idea of TDI-R is discussed in [87].

SUMMARY AND CONCLUSION

In this thesis, we modeled the interferometric measurements produced by the Laser Interferometer Space Antenna (LISA), and explored different aspects of the initial noise-reduction pipeline (INREP) for LISA.

The INREP is designed to suppress otherwise overwhelming primary noise sources, such as laser frequency noise and clock noise, and produce variables which can be used for astrophysical data analysis.

We show both analytically and by means of numerical simulations that the main noise sources included in our simulations can be suppressed below the level of secondary noises, even when that simulation includes previously neglected effects such as de-synchronized clocks, large frequency offsets due to Doppler shifts and laser locking control loops. We derived a detailed simulation model, in an effort to produce simulated data streams which are more representative of the data expected from the real mission, including ancillary data streams needed for clock noise correction. These simulations are the basis for developing and testing the algorithms used in the INREP. The raw measurements produced by the simulation are given as the total frequency of the MHz interferometric beatnotes, in which gravitational wave signals would appear as µcycle phase fluctuations. We show that double precision variables are sufficient to facilitate this large dynamic range.

The core algorithm used in the INREP is time-delay interferometry (TDI), which is designed to construct virtual equal-arm interferometers out of the raw LISA measurements, in which laser noise is naturally suppressed. In essence, TDI functions by forming linear combinations of the individual measurements recorded on the different spacecraft. By applying appropriate timeshifts while constructing such a linear combination, it is possible to significantly suppress laser noise in the final variable. TDI is usually formulated in terms of laser phase noise, assuming that all interferometric measurements are given according to a global time scale such as TCB.

In this thesis, we show that such TDI variables can also be constructed directly out of the raw LISA measurements, which are sampled according to the three un-synchronized spacecraft clocks, and that no prior synchronization to a common timescale is required. In this scheme, the clock synchronization is applied as part of the time shifts which are an integral part of constructing any TDI combination. Such time-shifts can be recovered to sufficient accuracy by combining the dedicated pseudo random noise (PRN) and clock-sideband measurements, even when the PRN measurement carries significant ranging measurement noise. We argue that this result is basically valid regardless of if the raw measurements are given as total phase or frequency.

However, working with frequency instead of phase requires a slight adjustment to the TDI algorithm, as Doppler shifts of the laser beams during

propagation need to be taken into account. We show analytically that this adjustment can be naturally included in the formulation of TDI, and perform simulations to verify that we achieve the same noise suppression one would expect without considering Doppler shifts in the simulated data.

In addition, TDI variables can be constructed using just frequency fluctuations, which can be recovered from the total frequency by subtracting a simple polynomial fit. This has the advantage of significantly reducing the dynamic range of the variables, which eases the impact of numerical artifacts during processing such as TDI. A downside is that clock noise can no longer be compensated by the time-shifts applied in TDI, and instead needs to be subtracted in an extra processing step. While such clock noise correction algorithms where already known, we contributed to their generalization from so-called first generation TDI variables to second generation TDI, and showed for the first time simulations which demonstrate this clock noise suppression. In addition, we derived a generalized formulation of such a clock correction algorithm, which can be applied to any second generation TDI variable.

We also modeled the residual clock noise levels achievable after the correction, as well as how additional noise in the sideband measurements used for clock correction couple into the final TDI variable. These results are directly applicable to the ongoing effort in the LISA consortium to develop a detailed performance model for the mission, which relies on these kinds of analytical and numerical studies to verify that the scientific objectives can be achieved in the presence of realistic instrument noise.

Besides modeling the residual clock noise, we also derived several new models for different effects limiting the achievable laser noise suppression. This includes the effect of interpolation errors, as well as updated versions of the previously known residual laser noise levels due to the so-called flexing filtering coupling and systematic ranging biases, which we now compute taking the laser locking conditions into account. The laser locking breaks the usual triangular symmetry, such that the three Michelson variables X, Y and Z can contain different levels of residual laser noise. In addition, we briefly discuss why the laser locking does not significantly impact any non-suppressed effects, such as secondary noises or the gravitational wave signal, and again verify these arguments with numerical simulations.

Finally, we explored the space of possible second generation TDI combinations, following the approach of geometric TDI known from the literature. During this work, we identified additional variables of 14 links which were previously missed. The full space of second generation TDI combinations is large, but can be reduced by removing duplicates which are related to each other by an internal symmetry. This leads to a set of 34 core combinations up to a length of 16 links.

We show analytically that this set of core-combinations can be further related to the set of four generators of first generation TDI, and show simulation results that this relationship can be – at least approximatively – extended to the second generation variables. For this, we identify that multiple variables can act as second-generation variants of the fully symmetric Sagnac combination

ζ, all of which suppress laser noise to a significantly lower level then the previously known second generation versions of ζ.

Future work could concern the INREP processing steps which we neglected in this thesis. Although we showed that laser noise can be reduced below the requirements without synchronizing all measurements to TCB, such a synchronization still has to be performed on the final variables to allow the observations to be coordinated with electromagnetic and earth-based GW observatories. To achieve this, the very precise on-board measurements could be combined with ground-based observation of the spacecraft positions in a Kalman-like optimal filter to recover independent estimates of the offsets between the three spacecraft clocks and TCB. Assuming this procedure works with sufficient precision, this would also allow to bring all measurements to TCB before constructing the TDI variable – it would be very interesting to compare the performance of these different approaches to combine clock synchronization with TDI.

Furthermore, we completely ignored a major noise source which might require on-ground calibration, tilt-to-length (TTL) coupling. It describes any coupling of angular tilts into a longitudinal pathlength change. To simulate TTL couplings, our simulation needs to be enhanced to include variables representing those angular tilts, such that we can compute the additional pathlength changes. In addition, we can only correct for TTL couplings if both the beam angles and the coupling coefficients for how these angles cause a pathlength error are known. The angles can be determined using the DWS measurments, which we should add as an additional simulation outputs. The coupling coefficients then need to be determined in a calibration procedure, the details of which are currently under development in the LISA consortium.

And finally, most of the results presented in this thesis are based solely on analytical studies and numerical experiments. While the simulations are useful to rule out errors in the analytical models presented in part iii, any error in the model underlying the simulation will not be caught. It is therefore imperative to cross-check the results presented here with real experiments, such as the Hexagon experiment being developed at the AEI, wherever possible. While the full LISA measurement chain, including large optical delays, can probably not be reproduced on ground, such experiments can still verify our models for, e.g., the coupling of clock noise, and its suppression.

Part IV

APPENDIX

A

CONVENTIONS

A.1 INDEX CONVENTIONS

We will need to distinguish many different elements onboard or conceptually attached to the three LISA spacecraft. These include hardware components, such as the spacecraft themselves, MOSAs, and optical benches, but also physical quantities such as the noise time series of a laser, or the delay of a laser beam propagating between the spacecraft.

Our notation will be guided by the following principles, which are largely based on the proposed unified conventions of the LISA consortium [21]:

- Each of the spacecraft is identified by one index out of the set $\{1, 2, 3\}$.
- Each element which exists only once onboard a spacecraft, such as the unique USO, is indexed by that spacecrafts index.
- Each element uniquely associated to one of the two MOSAs, such as the optical benches, test-masses, etc., will be indexed by two indices. The first one is that of the spacecraft the MOSA is mounted, while the second index is that of the spacecraft the MOSA is pointing to.
- Quantities which describe a process that involves the propagation between two of the spacecraft will be interpreted as being associated to the spacecraft in which the quantity is measured, or in whose frame it is naturally expressed. For example, the gravitational wave signal observed in the interferometer on MOSA 12 will be indexed with the same indices 12. The same convention applies to the delay of a beam arriving on spacecraft 1 from spacecraft 2, which will be labelled by the indices 12.

This is summarized in fig. A.1.

Note that this notation uniquely identifies each element using just the spacecraft indices. LISA is an almost equilateral triangle, with most components of interest in this thesis being present twice on each spacecraft, attached to the MOSAs pointing to each of the other two spacecraft. As such, most of these components have 6 versions, which need to be uniquely identified.

This 6-fold symmetry is very closely related to the symmetry group of an equilateral triangle, which indeed has six elements. The vertices of the triangle, which represent spacecraft indices in our case, can be subject to either of these transformations:

- The identity $\mathcal{I}$,

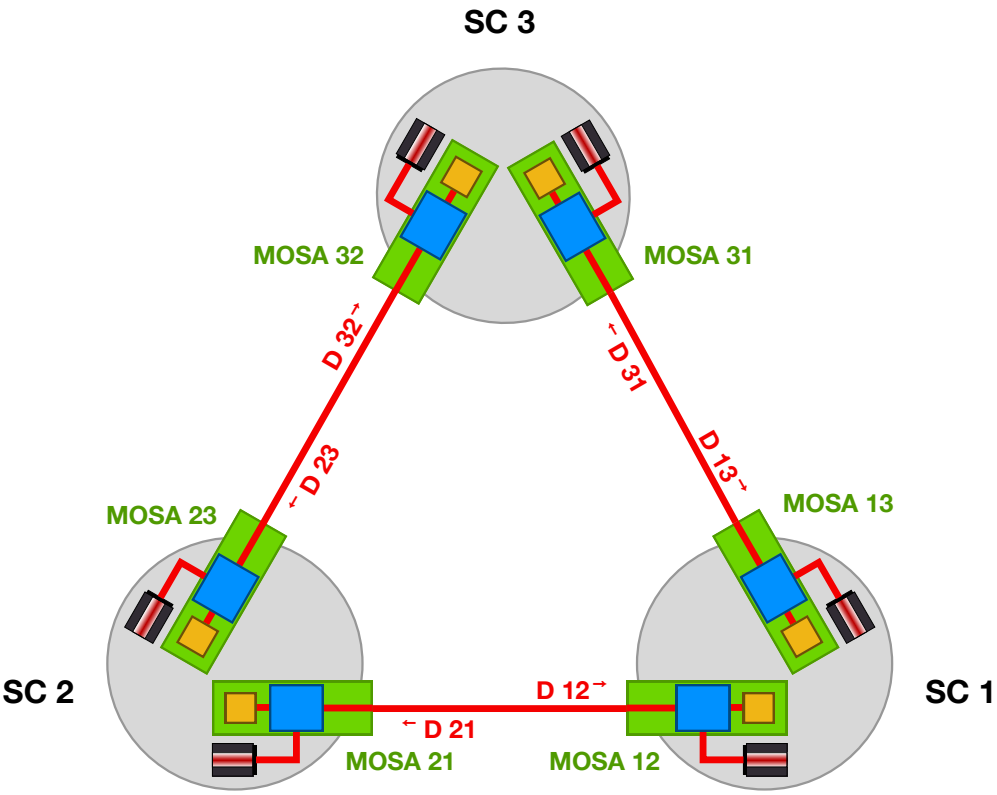

FIGURE A.1: Labelling conventions used for spacecraft, light travel times, lasers, MOSAs, and interferometric measurements. From [23].

- two circular permutations, $\mathcal{C}_1 = \{1 \to 2, 2 \to 3, 3 \to 1\}$ and $\mathcal{C}_2 = \{1 \to 3, 3 \to 2, 2 \to 1\}$,
- or a reflection along the axis seperating two of the spacecraft, exchanging two of the indices and leaving the third one unchanged; so either $\mathcal{M}_1 = \{2 \leftrightarrow 3\}$, $\mathcal{M}_2 = \{1 \leftrightarrow 3\}$, or $\mathcal{M}_3 = \{1 \leftrightarrow 2\}$.

Note that any of these symmetries can be written as multiple applications of one of the circular permutations and up to one mirror symmetry. In detail, we have

$$\mathcal{I} = \mathcal{C}_1^3, \quad \mathcal{C}_2 = \mathcal{C}_1^2, \quad \mathcal{M}_2 = \mathcal{M}_1\mathcal{C}_1, \quad \mathcal{M}_3 = \mathcal{M}_1\mathcal{C}_1^2\,. \tag{A.1}$$

By choosing a notation which uniquely identifies each element using just the spacecraft indices, we can write most equations in this thesis for just one of the six cases, and then apply these rules for exchanging the indices to directly get the 5 other versions of these equations.

A.2 MAPPING BETWEEN CONVENTIONS

Traditionally, many different notations have been used to describe the LISA instrument and in particular TDI. Table A.1 gives the mapping between the double-index conventions used in the article, and a previously very popular alternative using primed indices, used in, e.g., [24, 20, 64, 66]. We give the correspondence for optical bench and associated subsystems and quantities, and that for light TTs and their derivatives.

Double-index	Primed indices for optical benches	Primed indices for light TTs
12 (e.g., ν^{isc}_{12} or d_{12})	1 (e.g., ν^{isc}_{1})	3 (e.g., d_3)
23 (e.g., ν^{isc}_{23} or d_{23})	2 (e.g., ν^{isc}_{2})	1 (e.g., d_1)
31 (e.g., ν^{isc}_{31} or d_{31})	3 (e.g., ν^{isc}_{3})	2 (e.g., d_2)
13 (e.g., ν^{isc}_{13} or d_{13})	$1'$ (e.g., $\nu^{\text{isc}}_{1'}$)	$2'$ (e.g., $d_{2'}$)
32 (e.g., ν^{isc}_{32} or d_{32})	$3'$ (e.g., $\nu^{\text{isc}}_{3'}$)	$1'$ (e.g., $d_{1'}$)
21 (e.g., ν^{isc}_{21} or d_{21})	$2'$ (e.g., $\nu^{\text{isc}}_{2'}$)	$3'$ (e.g., $d_{3'}$)

TABLE A.1: Conversion between index convention in this thesis and those used in [64].

A.3 TIME COORDINATE AND REFERENCE SYSTEMS

The following time coordinate are used in this document. They are largely based on [21].

- The Barycentric Coordinate Time (TCB), denoted t,
- the spacecraft proper time (TPS) of each of the three spacecraft, denoted τ_1, τ_2, and τ_3,
- the on-board clock time (THE) of each of the three spacecraft, containing instrumental clock noise, denoted $\hat{\tau}_1$, $\hat{\tau}_2$, and $\hat{\tau}_3$.

Signals are, whenever possible, expressed in their proper or *natural* time coordinate. E.g., local laser beam phases are expressed in the TPS of the spacecraft housing the laser, and inter-spacecraft PPRs computed in the Barycentric Celestial Reference System (BCRS) are expressed in TCB coordinate.

It is sometimes useful to express a signal in a different time coordinate. Mathematically, this is equivalent to defining a new function of time. To prevent confusion while highlighting that the function describes the same physical quantity, we will use the same symbol but add a superscript denoting the time coordinate. For example, a phase ϕ could be expressed as function of the TCB, writing $\phi^t(x)$, or it could be expressed as function of the spacecraft proper time of spacecraft i, writing $\phi^{\tau_i}(x)$, or as function of the clock time of that spacecraft, writing $\phi^{\hat{\tau}_i}(x)$. Note that the symbol used for the function argument is arbitrary, and does not specify the reference frame. We will often use τ without subscripts as a generic function argument for functions of TPS or THE.

Conversions between time coordinates can easily be expressed with these conventions. One can simply give the time expressed in one time coordinate as a function of the time expressed in a different coordinate. For example, $\tau_i^t(x)$ is the TPS as a function of the TCB time. Trivially,

$$t^t(x) = \tau_i^{\tau_i}(x) = \hat{\tau}_i^{\hat{\tau}_i}(x) = x\,. \tag{A.2}$$

It is often useful to model the deviation of one time scale with respect to another one. For any two time scales A, B, we adopt the notation

$$A^B(x) = x + \delta A^B(x)\,, \tag{A.3}$$

such that, for example in

$$\tau_i^t(x) = x + \delta\tau_i^t(x)\,, \tag{A.4}$$

$\delta\tau_i^t(x)$ is the offset of the spacecraft proper time of spacecraft i with respect to TCB.

One important class of signals we study are phases ϕ of electromagnetic waves. As scalar quantities, these are invariant under coordinate transformations, such that they transform from one time frame to another using a simple time shift:

$$\phi^{\tau_i}(\tau) = \phi^t(t^{\tau_i}(\tau)) = \phi^{\hat{\tau}_i}(\hat{\tau}_i^{\tau_i}(\tau))\,. \tag{A.5}$$

This is not correct for frequencies. Since the frequency is defined as the time derivative of the phase, is inherently depends on the time scale of an observer.

In order to reduce the number of symbols for equations expressed in frequency, we will adopt the 'dot' notation for the derivative. As such, the time derivative of any function f^τ will be written as

$$\dot{f}^\tau = \frac{\mathrm{d}f^\tau}{\mathrm{d}\tau}. \tag{A.6}$$

Note that this derivative is always with respect to the function's natural reference frame. In some cases, for example for nested functions where the chain rule should be applied, we will continue to use the $\mathrm{d}/\mathrm{d}\tau$ notation.

A.4 TIME SHIFT OPERATORS

One important set of mathematical operators used in this thesis are time shift operators. They act on a time dependent function by evaluating it at another time. The most important application in this thesis is to model the propagation of signals between the different spacecraft, either in the simulation or when applying TDI.

We thus define the following notations related to time-shift operators and TDI combinations:

- $\mathbf{D}_{ij}x(\tau) = x(\tau - d_{ij}(\tau))$: Delay operator.

  At time of reception τ of a beam from spacecraft i, gives x evaluated at time of emission at spacecraft j, which we write as $\tau - d_{ij}(\tau)$. Depending on in what frame $x(\tau)$ is given, the computation of d_{ij} can include a change in reference frames, and clock offsets. Example: for data given in the TCB, d_{ij} is the relativistic light travel time computed in the TCB. For data given according to the on-board clocks, d_{ij} has to compensate for reference frame conversions and clock imperfections. In cases where there is chance of confusion, we include a superscript indicating which reference frame is being used. For example, dij^t is the light travel time in the TCB, d_{ij}^τ is the PPR used in chapter 5, and $d_{ij}^{\hat{\tau}}$ is the MPR, including clock offsets of $\hat{\tau}_i$ and $\hat{\tau}_j$ wrt. τ_i and τ_j.

- $\mathbf{D}_{\overline{ij}}x(\tau) = x(\tau + a_{ij}(\tau))$: Advancement operator.

  At time of emission τ of a beam from spacecraft i, gives x evaluated at time of reception at spacecraft j, $\tau + a_{ij}(\tau)$. Fulfills $\mathbf{D}_{ij}\mathbf{D}_{\overline{ji}}x(t) = \mathbf{D}_{\overline{ji}}\mathbf{D}_{ij}x(t) = x(t)$.

- $\dot{\mathbf{D}}_{ij}x(\tau) = (1 - \dot{d}_{ij})x(\tau - d_{ij}(\tau))$: Doppler delay.

  To be used with variables expressed as frequencies.

- $\dot{\mathbf{D}}_{\overline{ij}}x(\tau) = (1 + \dot{a}_{ij})x(\tau + a_{ij}(\tau))$: Doppler advancements.

  To be used with variables expressed as frequencies.

- $\mathbf{D}_{12;21;\overline{13};\overline{31}} = \mathbf{D}_{12}\mathbf{D}_{21}\mathbf{D}_{\overline{13}}\mathbf{D}_{\overline{31}}$: Nested delay/advancement operator.

  Any single adjacent delays or advancements can be concatenated to a list of delays/advancements, seperated by ;.

- $\mathbf{D}_{\overline{121};131} = \mathbf{D}_{\overline{12};\overline{21};13;31}$: Photon path delay operator.

  Decomposes into nested delay for photon paths indicated by indices. Whenever there is a change in direction of the photon path, a new path must be attached, seperated by ;.

  - Physical interpretation of $\mathbf{D}_{ijkl}$: Given a time of reception at i, what was the time of emission at l, for a beam that traveled from l to k to j to i?
  - Physical interpretation of $\mathbf{D}_{\overline{ijkl}}$: Given a time of emission at i, what will be the time of reception at l, for a beam that travels from i to j to k to l?
  - Physical interpretation of $\mathbf{D}_{\overline{ijkl};lmno}$: Given a time of emission at i, what will be the time of reception at l for a beam traveling from i to j to k to l? Given that time as time of reception at l, what is time of emission at o for a beam that traveled from o to n to m to l?

  Useful as short hand notation. Example: Laser noise residual in 1st generation Michelson can be written

$$(\mathbf{D}_{\overline{12131};12131} - 1)p_1 = (\mathbf{D}_{\overline{12};\overline{21};\overline{13};\overline{31};12;21;13;31} - 1)p_1 \tag{A.7}$$

  with advancements, or

$$(\mathbf{D}_{12131} - \mathbf{D}_{13121})p_1 = (\mathbf{D}_{12;21;13;31} - \mathbf{D}_{13;31;12;21})p_1 \tag{A.8}$$

  without. Note that the order of delays in the expression without advancement gets reversed.
  This translates to the notation used in [92] for photon paths in the following way:

$$(\mathbf{D}_{\overline{12131};12131} - 1)p_1 \equiv \overrightarrow{3'322'}\overleftarrow{33'2'2}\,, \tag{A.9}$$

  so indices with a bar are traversed forward in time (with the beam direction), and un-bared indices are traversed backwards in time (against the beam direction).

The fundamental one-link delays $\mathbf{D}_{ij}$ and advancements $\mathbf{D}_{\overline{ij}}$, as well as the nested variant, are fully compatible with this notation; they just start each individual link as new photon path which is added to the overall loop.

- $\mathcal{D}_{ij}x(t) = x(t - \tilde{d}_{ij}(t))$: offline delay.

  Delays applied in offline/on-ground processing. Like propagation delay, but using a measured/processed estimate of d_{ij} instead of the real value. All notations defined for $\mathbf{D}_{ij}$ carry over to $\mathcal{D}_{ij}$, and can be combined in any way; For example, we could use something like $\dot{\mathcal{D}}_{\overline{12131};123;\overline{3231}}$.

- $\mathbf{D}_A x(t) = x(t - d_A(t))$: single index delay.

  We sometimes need to study the general properties of single delay operators, which are not related to specific spacecraft. In this case, the two indices hurt readability, which is why we use a single index notation in parallel. To avoid confusion, single index delays $\mathbf{D}_A$ will be labelled with upper case latin letters, starting at $A, B, \ldots$, or using another lower identifying index, like $A_1, A_2, \ldots$. These are never replaced with single spacecraft indices, and are not uniquely related to any specific delay, but can be evaluated as spacecraft index pairs. For example, if we derive a condition for the commutator of two delays, $\mathbf{D}_A\mathbf{D}_B - \mathbf{D}_B\mathbf{D}_A$, we could evaluate it replacing A, B with any spacecraft index pair, like $\mathbf{D}_{12;23} - \mathbf{D}_{23;12}$.

- $\mathbf{D}_{A_1A_2\ldots A_n} \equiv \mathbf{D}_{A_1}\mathbf{D}_{A_2}\ldots\mathbf{D}_{A_n}$: Nested single index delay.

B

INTERPOLATION WITH LAGRANGE POLYNOMIALS

Most of our analytical formulations are expressed in continous time, such that we can evaluate all functions at arbitrary times. However, as described in chapter 7, the real data available on ground will be a digital time series sampled at a fixed sampling rate. Time shifting by non-integer time intervals requires interpolation between the samples. This has been first proposed for TDI in LISA in [76], and different interpolation methods have been analyzed in detail in [41].

Both the TDI implementations in `LISANode` and `PyTDI` implement fractional delay filters using a Lagrange interpolation scheme as described in [41].

Each interpolation comes with the potential of interpolation errors, which is why it is advisable to avoid multiple interpolations of the same time series. Therefore, nested delays are usually implemented by first computing the overall delay to be applied to the η_{ij} variables, which is then only interpolated once.

Note that the computation of the delay itself is much less sensitive to interpolation errors, since the delays are very smooth functions which are in addition filtered to remove any high-frequency content, cf. section 13.5. Therefore, it is sufficient to use a low interpolation order when computing the overall delay.

This is in stark contrast to the main variables η_{ij}, which require high interpolation orders to achieve sufficient laser noise suppression[1], see section 12.3.2.2.

B.1 LAGRANGE INTERPOLATION COEFFICIENTS

Offline delays are implemented using fractional delay filters. They consist of an integer delay $\mathcal{D}^0_{ij}$ delaying the time series to the nearest sample, followed by a non-casual FIR filter $\mathcal{D}^\epsilon_{ij}$ whose filter coefficients are computed by constructing a Lagrange interpolating polynomial around the point of interest. Consequently, we decompose the overall delay d_{ij} to be applied into an integer part and a fractional part,

Meaning that the fractional part of the delay uses samples both in the past and future of the point of interest. Assuming that the integer delay is sufficiently large, the overall fractional delay filter is causal, i.e., it requires only samples in the past.

$$d_{ij} = d^0_{ij} + d^\epsilon_{ij}\,, \tag{B.1}$$

with $d^0_{ij} = N/f_s$, f_s as the sampling rate, and N an integer.

1 In `LISANode`, the default values for the interpolation orders of the η variables and the travel times are 31 and 3, respectively, while in `PyTDI`, they are set to 31 and 5.

In all generality, we can write

$$\mathcal{D}_{ij} = \mathcal{D}^{\epsilon}_{ij}\mathcal{D}^{0}_{ij}\,, \tag{B.2}$$

where the integer delay $\mathcal{D}^{0}_{ij}$ acts on a time series $x[n]$ as

$$\mathcal{D}_{ij}x[n] = x[n-N]\,, \tag{B.3}$$

while the fractional delay $\mathcal{D}^{\epsilon}_{ij}$ acts as a non-causal FIR filter,

$$\mathcal{D}^{\epsilon}_{ij}x[n] = \sum_{k=-p+1}^{p} c^{\epsilon}_{k}x[n+k]\,, \tag{B.4}$$

with $p = \frac{\text{order}+1}{2}$ as the half-point count.

B.1.1 *Lagrange coefficients in* `LISANode`

In `LISANode`, following [20], the integer number of samples N and the fractional number of samples ϵ are computed as

$$N = \text{ceil}\big(d_{ij}f_s\big) - 1\,, \tag{B.5}$$
$$\epsilon = 1 + N - d_{ij}f_s\,. \tag{B.6}$$

With these definitions, we have

$$d^{0}_{ij} = \frac{N}{f_s}\,, \qquad d^{\epsilon}_{ij} = \frac{1-\epsilon}{fs}\,. \tag{B.7}$$

By defining the following ϵ dependent variables,

$$A = \frac{1}{p}\prod_{i=1}^{p-1}\left(1+\frac{\epsilon}{i}\right)\left(1+\frac{1-\epsilon}{i}\right), \tag{B.8}$$
$$B = 1-\epsilon\,, \tag{B.9}$$
$$C = \epsilon\,, \tag{B.10}$$
$$D = \epsilon(1-\epsilon)\,, \tag{B.11}$$
$$E[j] = (-1)^{j}\frac{(p-1)!}{(p-1-j)!}\frac{p!}{(p+j)!}\,, \tag{B.12}$$
$$F[j] = j+\epsilon\,, \tag{B.13}$$
$$G[j] = j+(1-\epsilon)\,, \tag{B.14}$$

the filter coefficients can be computed as

$$c^{\epsilon}_{0} = AC\,, \tag{B.15}$$
$$c^{\epsilon}_{1} = AB\,, \tag{B.16}$$
$$c^{\epsilon}_{j} = AD\frac{E[j]}{F[j]} \qquad \forall j > 1\,, \tag{B.17}$$
$$c^{\epsilon}_{j} = AD\frac{E[j]}{G[j]} \qquad \forall j < 0\,. \tag{B.18}$$

B.1.2 *Lagrange coefficients in* `PyTDI`

`PyTDI` uses a slightly different formulation for the variable fractional delay filter. Note that this formulation yields equivalent results to the one in `LISANode`.

In particular, the integer number of samples N and the fractional number of samples ϵ are now defined as

$$N = \mathrm{floor}\left(d_{ij} f_s\right), \tag{B.19}$$

$$\epsilon = d_{ij} f_s - N. \tag{B.20}$$

With these definitions, we have

$$d^0_{ij} = \frac{N}{f_s}, \qquad d^\epsilon_{ij} = \frac{\epsilon}{f_s}. \tag{B.21}$$

Confer to the in-code documentation for the definitions of the coefficients in this case. The actual resultant coefficients c^ϵ_k are identical in both implementations, down to the numerical limit.

B.2 INTERPOLATION ERRORS

We want to study the error we make when interpolating a time series when compared to a perfect delay[2]. It is useful to do this analysis in the frequency domain. For this, we need to compute the Fourier transform of

$$\Delta_{ij} = \left(\mathcal{D}_{ij} - \mathbf{D}_{ij}\right). \tag{B.22}$$

We have

$$\mathcal{F}\left[\mathcal{D}^0_{ij} x(t)\right](\omega) = e^{-i\omega d^0_{ij}} \mathcal{F}\left[x\right](\omega) \tag{B.23}$$

for the integer delay,

$$\mathcal{F}\left[\mathcal{D}^\epsilon_{ij} x(t)\right](\omega) = \sum_{k=-p+1}^{p} c^\epsilon_k e^{i\omega k/f_s} \mathcal{F}\left[x\right](\omega) \tag{B.24}$$

for the fractional delay and

$$\mathcal{F}\left[\mathbf{D}^\epsilon_{ij} x(t)\right](\omega) = e^{-i\omega(d^0_{ij} + d^\epsilon_{ij})} \mathcal{F}\left[x\right](\omega) \tag{B.25}$$

for the perfect delay. Overall, this gives

$$\mathcal{F}\left[\Delta_{ij} x(t)\right] = e^{-i\omega d^0_{ij}} \left[\left(\sum_{k=-p+1}^{p} c^\epsilon_k e^{i\omega k/f_s}\right) - e^{-i\omega d^\epsilon_{ij}}\right] \mathcal{F}\left[x\right](\omega) \tag{B.26}$$

2 We thank M. Lilley for useful discussions regarding this topic, and for cross-checking most of the results presented in this section!

for the difference between the offline and perfect delay. For the purpose of estimating the PSD, we are interested in the squared magnitude of this quantity, which is given as

$$\left|\mathcal{F}\left[\Delta_{ij}x(t)\right]\right|^2 = \left|\left(\sum_{k=-p+1}^{p} c_k^\epsilon e^{i\omega k/f_s}\right) - e^{i\omega d_{ij}^\epsilon}\right|^2 \left|\mathcal{F}\left[x\right](\omega)\right|^2 . \tag{B.27}$$

The integer part of the delay cancels, and we are left with an expression depending only on the fractional delay ϵ. This expression can be computed numerically for estimating a PSD.

As mentioned above, depending on how the coefficients are computed, we either have $d_{ij}^\epsilon = (1-\epsilon)/f_s$ or $d_{ij}^\epsilon = \epsilon/f_s$.

Alternatively, we can compute it analytically. In general, we have $|x-y|^2 = |x|^2 + |y|^2 - xy^* - x^*y$ for any two complex numbers x, y. In our case, we get

$$\begin{aligned}\left|\left(\sum_{k=-p+1}^{p} c_k^\epsilon e^{i\omega k/f_s}\right) - e^{i\omega d_{ij}^\epsilon}\right|^2 &= \left|\sum_{k=-p+1}^{p} c_k^\epsilon e^{i\omega k/f_s}\right|^2 + \left|e^{i\omega d_{ij}^\epsilon}\right|^2 \\ &\quad - \sum_{k=-p+1}^{p} c_k^\epsilon \left(e^{i\omega(k/f_s - d_{ij}^\epsilon)} + e^{-i\omega(k/f_s - d_{ij}^\epsilon)}\right) \\ &= \left|\sum_{k=-p+1}^{p} c_k^\epsilon e^{i\omega k/f_s}\right|^2 + 1 \\ &\quad - 2\sum_{k=-p+1}^{p} c_k^\epsilon \cos\left(\omega(k/f_s - d_{ij}^\epsilon)\right) .\end{aligned} \tag{B.28}$$

The first term contains mixed terms for the different coefficients. We can write

$$\begin{aligned}\left|\sum_{k=-p+1}^{p} c_k^\epsilon e^{i\omega k/f_s}\right|^2 &= \left(\sum_{k=-p+1}^{p} c_k^\epsilon e^{i\omega k/f_s}\right)\left(\sum_{l=-p+1}^{p} c_l^\epsilon e^{-i\omega l/f_s}\right) \\ &= \sum_{k=-p+1}^{p}\sum_{l=-p+1}^{p} c_k^\epsilon c_l^\epsilon e^{i\omega(k-l)/f_s} .\end{aligned} \tag{B.29}$$

It is useful to split up the double sum into three components, $k = l$, $k < l$ and $l < k$. This gives us

$$\begin{aligned}\left|\sum_{k=-p+1}^{p} c_k^\epsilon e^{i\omega k/f_s}\right|^2 &= \sum_{k=-p+1}^{p} c_k^{\epsilon 2} + \sum_{k=-p+1}^{p}\sum_{l=k+1}^{p} c_k^\epsilon c_l^\epsilon e^{i\omega(k-l)/f_s} \\ &\quad + \sum_{l=-p+1}^{p}\sum_{k=l+1}^{p} c_k^\epsilon c_l^\epsilon e^{i\omega(k-l)/f_s}\end{aligned} \tag{B.30}$$

We can then rename the indices $k \leftrightarrow l$ in the third sum to combine the last two terms, so we have in total

$$\begin{aligned}\left|\sum_{k=-p+1}^{p} c_k^\epsilon e^{i\omega k/f_s}\right|^2 &= \sum_{k=-p+1}^{p} c_k^{\epsilon 2} + \sum_{k=-p+1}^{p}\sum_{l=k+1}^{p} c_k^\epsilon c_l^\epsilon \left(e^{i\omega(k-l)/f_s} + e^{-i\omega(k-l)/f_s}\right) \\ &= \sum_{k=-p+1}^{p} c_k^{\epsilon 2} + 2\sum_{k=-p+1}^{p}\sum_{l=k+1}^{p} c_k^\epsilon c_l^\epsilon \cos(\omega(k-l)/f_s)\,.\end{aligned} \tag{B.31}$$

This means finally, we get

$$\begin{aligned}\left|\left(\sum_{k=-p+1}^{p} c_k^\epsilon e^{i\omega k/f_s}\right) - e^{i\omega d_{ij}^\epsilon}\right|^2 &= 1 + \sum_{k=-p+1}^{p} c_k^{\epsilon 2} \\ &\quad - 2\sum_{k=-p+1}^{p} c_k^\epsilon \cos\Big(\omega(k/f_s - d_{ij}^\epsilon)\Big) \\ &\quad + 2\sum_{k=-p+1}^{p}\sum_{l=k+1}^{p} c_k^\epsilon c_l^\epsilon \cos(\omega(k-l)/f_s)\,.\end{aligned} \tag{B.32}$$

However, it turns out that this expression is less useful in practice than eq. (B.27). The reason is that at low frequencies, the interpolation errors cancel down to the numerical limit. In eq. (B.27), this cancellation happens in amplitude, and we square the expression afterwards; small numerical errors thus get strongly suppressed in the final PSD. In eq. (B.32), however, the cancellation happens in power, such that numerical errors in the computation show up with their full magnitude in the PSD.

This effect is clearly visible in fig. B.1, where the noise floor of the PSD expression is twice as high as that of the square of the complex expression (on a logarithmic axis), which is itself in agreement with the expected numerical limit.

As can be seen in fig. B.1, the interpolation errors are mostly relevant at high frequencies close to the Nyquist rate, and highly depend on the interpolation order and the fractional delay. Indeed, in the limit $\epsilon = 0$, the Lagrange interpolation collapses to a simple integer delay, which of course does not introduce any errors.

We present in section 12.3.2.2 how these interpolation errors couple into the final output of our TDI variables.

B.3 NESTED DELAYS

A naive approach to compute a nested delay $\mathcal{D}_{A_1 \ldots A_n} x(t)$ would be to simply interpolate the time series $x(t)$ n times, once for each delay. However, as mentioned above, this has the potential of introducing large numerical errors.

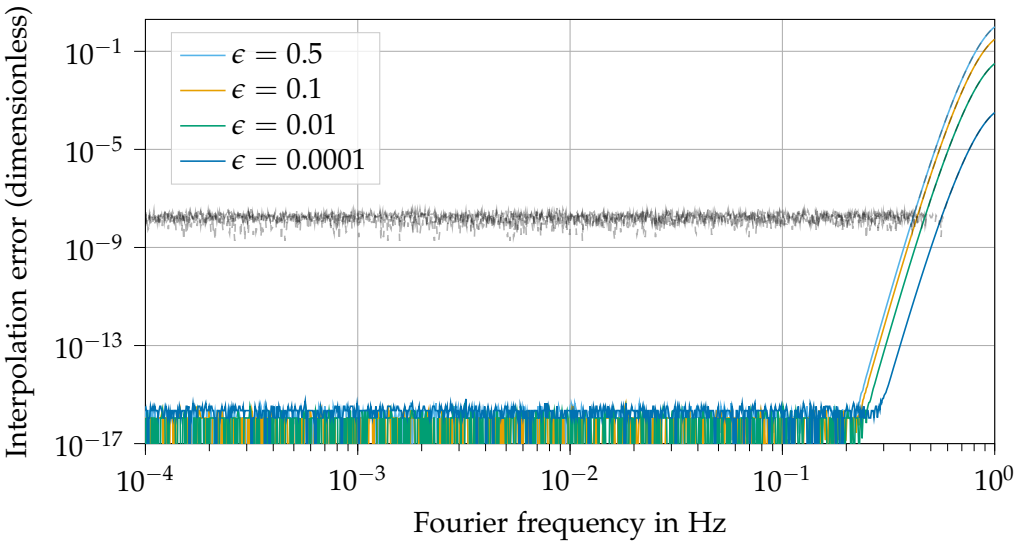

FIGURE B.1: Interpolation error magnitude at different fractional delays ϵ, expressed as fraction of an integer delay. Colored curves are computed numerically from eq. (B.27), while grey dotted curves use analytical model given in eq. (B.32). The latter has a higher numerical noise floor. We plot the square-root of both expressions.

To circumvent this problem, we first compute the overall delay to be applied to a time series, and then only interpolate it once. Note that this approach is also more in-line with our interpretation of TDI combinations in chapter 10, where each η_{ij} is evaluated at the time associated to one specific spacetime event, and the nested delay is simply computing that time with respect to the current timestamp.

In detail, a nested delay applied to an arbitrary function can be written as

$$\mathcal{D}_{A_1 \dots A_n} x(t) = x(t - \underbrace{d_1(t) - \mathcal{D}_{A_1} d_2(t) - \dots - \mathcal{D}_{A_1 \dots A_{n-1}} d_n(t)}_{d_{\text{total}}}) \,, \tag{B.33}$$

with each individual delay acting as $\mathcal{D}_{A_i} x(t) = x(t - d_i)$.

Following [20], the total delay d_{total} can thus be computed iteratively:

$$d_{\text{total}} = \sum_{k=1}^{n} z_k \,, \tag{B.34}$$

with

$$z_1 = d_1(t) \tag{B.35}$$

$$z_i = d_i \left(t - \sum_{k=1}^{i-1} z_k \right) \,. \tag{B.36}$$

The delays applied in the computation of the z_i themselves are also implemented using Lagrange interpolation. However, since these are typically very smooth functions with no high-frequency content, a low interpolation order is sufficient here.

B.4 COMPUTATION OF FORWARD TIME SHIFTS

As stated in section 6.3, the quantity we directly measure with the dedicated ranging measurement in LISA is the delay $\mathbf{D}_{ij}$. However, in order to apply the more general multi-beam TDI algorithm given in section 11.1.1, we need to compute advancements $\mathbf{D}_{\overline{ij}}$ out of the delays.

What we measure is actually a pseudo range, containing clock offsets in addition to the physical light travel time. Assuming ranging noise is sufficiently suppressed, these can be directly used as input to TDI, see chapter 13.

The starting point for this is eq. (11.2), which evaluated at a given coordinate time reads

$$\mathbf{D}_{\overline{ji}}\mathbf{D}_{ij}x(t) = \mathbf{D}_{\overline{ji}}x(t - d_{ij}(t)) = x(t + a_{ij}(t) - d_{ij}(t + a_{ij}(t))) \equiv x(t)\,. \tag{B.37}$$

This immediately gives an implicit equation for the time series of advancements a_{ij}:

$$a_{ij}(t) = d_{ij}(t + a_{ij}(t))\,. \tag{B.38}$$

We can solve this equation iteratively by computing

$$\begin{aligned} a^0_{ij}(t) &= d_{ij}(t)\,, \\ a^{n+1}_{ij}(t) &= d_{ij}(t + a^n_{ij}(t))\,, \end{aligned} \tag{B.39}$$

This procedure has been implemented in `LISANode`[3] and `PyTDI`[4]. In `PyTDI`, the iteration is stopped once the residual error $a^n_{ij} - a^{n+1}_{ij}$ is less then 1 ps, whereas the implementation in `LISANode` always stops after 4 cycles.

3 Together with M. Muratore and J.-B. Bayle
4 Implemented by M. Staab. and J.-B. Bayle.

C

DIFFERENT MODELS FOR FREQUENCY STABILITY

C.1 INTRODUCTION

The content of this chapter is based on an internal technical note for the geoQ Sonderforschungsbereich, see [42].

The main observable in LISA is the interferometric signal detected in the different channels onboard each spacecraft. There are different options for how to represent these signals, which have different trade-offs in terms of processing complexity and information content. In this appendix, we review the mathematical framework used in this thesis to describe periodic signals. In particular, we utilize it to describe the beatnotes measured in the various interferometers of LISA (c.f. section 5.4), at frequencies between 5 MHz and 25 MHz. In addition, electromagnetic fields produce by the lasers are also described using the same framework (c.f. section 5.2.1), at much higher frequencies of around 282 THz.

We will also review the different quantities used to describe frequency stability both in the time- and frequency domain.

C.1.1 *Literature*

As this is supposed to be a technical overview, most of the information in this document can also be found in other documents or textbooks with similar topics. Therefore, most of the basic definitions are given without reference.

Particularly relevant references are [29] for the theoretical background in section C.2 as well as [49] for practical considerations. [70] and [2] are good references for time domain stability analysis of oscillators, here discussed in section C.3. They also contain some information on the topic discussed in section C.4, the conversion between time and frequency domain measures of oscillator stability.

C.1.2 *Periodic signals*

We consider periodic signals $V(\tau)$ which can be represented by

$$V(t) = A\cos(\Phi(t)) = A\cos(2\pi\nu_0 t + \phi(t))\,, \tag{C.1}$$

with A as the possibly time varying amplitude, here assumed constant. $\Phi(t)$ is the total phase in radian[1], ν_0 as the constant nominal frequency of the signal in Hertz, and $\phi(t)$ as the phase deviations, also in radian. Since the cosine is periodic, the total phase and the phase deviations are only defined up to arbitrary integer multiple of 2π.

Alternatively to the total phase $\Phi(t)$, one can also use the instantaneous frequency,

$$\nu(t) = \frac{1}{2\pi}\dot{\Phi}(t) = \nu_0 + \frac{1}{2\pi}\dot{\phi}(t)\,, \tag{C.2}$$

to get

$$V(t) = A\cos\left(2\pi\int_0^t \nu(t')\,\mathrm{d}t'\right) = A\cos(2\pi\nu_0 t + \phi(t))\,. \tag{C.3}$$

If the signal frequency is fairly stable, it is sometimes easier to describe it using the timing jitter $x(t)$ in seconds or the dimensionless fractional frequency deviations $y(t)$,

$$x(t) = \frac{\phi(t)}{2\pi\nu_0} \quad \text{and} \quad y(t) = \frac{\nu(t)-\nu_0}{\nu_0} = \frac{\dot{\phi}(t)}{2\pi\nu_0} = \dot{x}(t)\,, \tag{C.4}$$

so that we have

$$\nu(t) = \nu_0(1+y(t)) \quad \text{and} \quad \Phi(t) = 2\pi\nu_0(t+x(t))\,. \tag{C.5}$$

Because phase deviations $\phi(t)$ are only defined up to an integer multiple of 2π, the timing jitter $x(t)$ is itself defined up to a multiple of $1/2\pi\nu_0$. To define the latter unambiguously, we often choose $\phi(t)$ such that for some point in time t_0, $\phi(t_0) \in [0, 2\pi[$. For example, t_0 could be the time at which we start tracking the phase of an interferometric beatnote.

C.1.3 *Relationship to displacement, velocity and acceleration*

Since most of our simulation model concerns the propagation of EM waves, which propagate at the speed of light c, a timing jitter $x(t)$ can easily be related to a path length change l in meters. Consequently, fractional frequency variations $y(t)$ are related to velocities v, and the derivative of $y(t)$ to the acceleration a, respectively:

$$l(t) = c \cdot x(t) \tag{C.6a}$$
$$v(t) = c \cdot y(t) \tag{C.6b}$$
$$a(t) = c \cdot \dot{y}(t) \tag{C.6c}$$

As derivatives of one another, positions, velocities and acceleration are closely related. However, it is important to point out that the integration constant (the

1 Note that we choose to use cycles instead of radian for most of this thesis, to have a simple relationship between phase and frequency. The conversion is simply given by $\Phi[\text{rad}] = 2\pi\Phi[\text{cycles}]$. We use radian in this appendix to reflect the standard notation used in the literature.

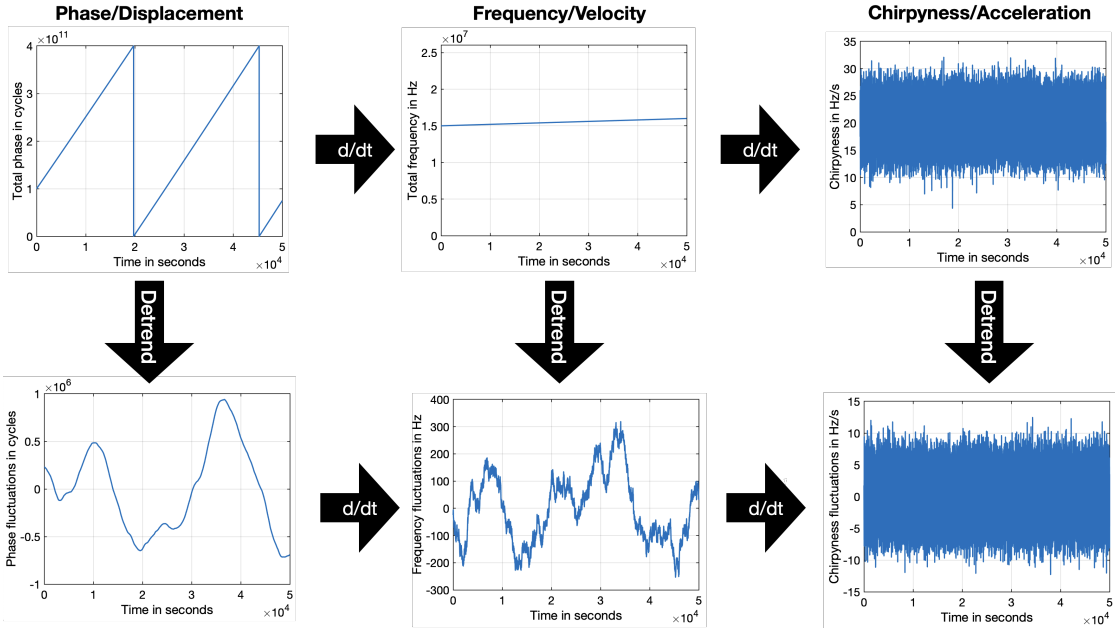

FIGURE C.1: Example for expressing the same signal in total phase, frequency or chirpyness, or in the respective fluctuations. For illustrative purposes, we assumed a signal with a constant offsets plus some white noise in chirpyness. The white noise (f^0 in terms of PSD) becomes a random walk (f^{-2}) in frequency and finally a random run (f^{-4}) in phase.

total phase for $\Phi(t)$ or the total frequency for $\nu(t)$) is lost when performing derivatives. As such, the total phase $\Phi(t)$ in principle contains more information than the instantaneous frequency. In many situations, however, the total phase is only physically meaningful up to a constant, such that phase and frequency are often seen as equivalent in the context of interferometry.

The acceleration still contains less information than either of them, so it is unsuitable in situations where the absolute frequency of the signal is important. Due to this, $\dot{\nu}(t)$ is not widely used to describe periodic functions. However, since acceleration is widely used to describe the test mass behaviour in LISA Pathfinder and LISA, it is worthwhile to mention the relationship in this section.

Since a signal of time varying frequency is often called a chirp, $\dot{\nu}(t)$ is called the chirpyness.

C.1.4 *Deterministic behaviour*

Many oscillators display deterministic deviations from their nominal frequency, such as a linear frequency drift or a constant frequency offset.

Such deterministic effects can heavily skew the results of the methods for estimating frequency stability described below, masking actual random fluctuations. It is therefore common practice to subtract deterministic trends before performing a stability analysis.

Notice that equation eq. (C.2) implies that a frequency offset corresponds to a linear ramp in the phase data whereas a frequency drift leads to quadratic behaviour in the phase data.

C.2 FREQUENCY STABILITY IN THE FREQUENCY DOMAIN

C.2.1 *The power spectral density*

In the frequency domain, a stochastic process V is usually described by the power spectral density (PSD), S_V. It can be defined as the Fourier transform[2] of the autocorrelation function R:

$$S_V^{II}(f) = \int_{-\infty}^{\infty} R(t) e^{-i2\pi ft} dt. \tag{C.7}$$

The superscript ^{II} indicates that this is a two-sided PSD, defined for both positive and negative frequencies. Assuming the process under investigation is wide-sense stationary and ergodic, the autocorrelation function is given by

$$R(\tau) = \lim_{T\to\infty} \frac{1}{T} \int_{-T/2}^{T/2} V(t)V(t+\tau) dt. \tag{C.8}$$

Further details on the autocorrelation function can be found in appendix C.8.

In most practical applications, the PSD needs to be estimated from a finite time series using the periodogram[3]. Assume that we have recorded a real signal $V(t)$ over a time period T. The periodogram of that signal is than defined as

$$P_T(f) = \frac{1}{T} \left|\tilde{V}_T(f)\right|^2, \tag{C.9}$$

where $\tilde{V}_T$ is the Fourier transform of the truncated signal V_T:

$$V_T(t) = \begin{cases} V(t) & \text{for} -T/2 < t < T/2 \\ 0 & \text{elsewhere} \end{cases} \tag{C.10}$$

such that

$$\tilde{V}_T(f) = \int_{-T/2}^{T/2} V(t) e^{-i2\pi ft} dt. \tag{C.11}$$

One can than show [29] that the periodogram P_T converges to the PSD for $T \to \infty$, i.e.,

$$S_V^{II}(f) = \lim_{T\to\infty} \frac{1}{T} \left|\tilde{V}_T(f)\right|^2. \tag{C.12}$$

However, the variance of this estimate does not necessarily converge to zero, meaning that the estimate does not necessarily get better when one uses a longer time series. Instead, increasing T leads to a finer frequency resolution. The variance can be reduced by first splitting the time series

2 Assuming the Fourier transform of the autocorrelation function exists.

3 In contrast to the PSD, the periodogram can always be calculated for a finite time series, regardless of whether the Fourier transform of the autocorrelation function exists.

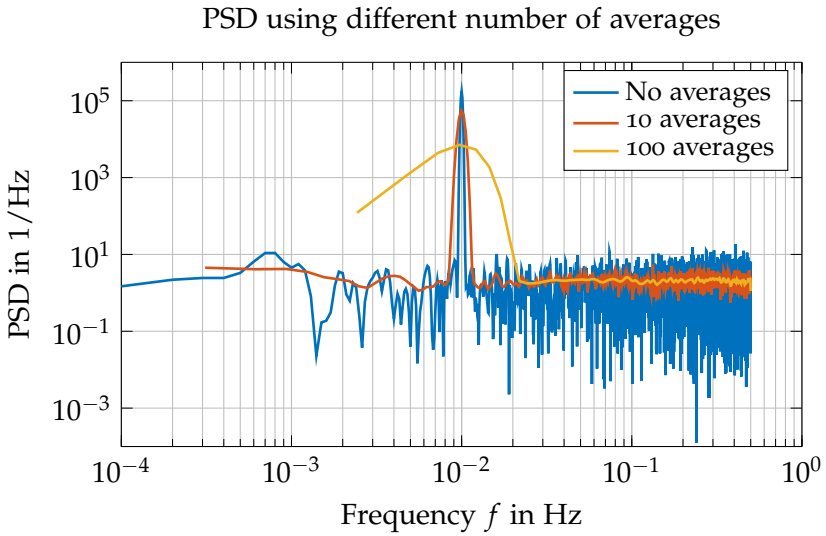

FIGURE C.2: PSD of white noise plus a sharp peak at 10mHz. The PSD is estimated from a finite time series by means of the periodogram using no, 10 or 100 averages. Notice that averaging decreases the variance as well as the frequency resolution, thereby widening the peak and limiting the lowest resolvable frequencies.

into shorter segments. One can then calculate the periodograms for these shorter segments and then average the results; however, since the individual segments are shorter, this reduces the frequency resolution. Thus, assuming that the measurement time T is fixed, one has to consider a tradeoff between the desired frequency resolution and the acceptable variance of the estimate. This effect is demonstrated in figure C.2.

Truncating the signal as in equation eq. (C.10) might be the simplest way to truncate a time series; however, it might not yield the most accurate result. In general, it is advisable to apply a so-called window function to the truncated time series before calculating the periodogram; this reduces an effect known as spectral leakage, which spreads power from frequencies in one frequency bin into adjacent frequency bins. Directly using eq. (C.10) is also called a box-shaped window in this context, which is rarely optimal. An in-depth discussion of the influence of different window functions as well as other notes on practical considerations when calculating power spectral densities can be found in [49].

C.2.2 *Related quantities*

Notice that equation eq. (C.9) returns an estimate for the two-sided power spectral density, with positive and negative frequency values. Real valued signals yield a PSD that is an even function of the frequency, $S_V^{II}(f) = S_V^{II}(-f)$, which means that the information in the negative frequency part is redundant. This is why experimentalists usually work with the one-sided power spectral density,

$$S_V^I(f) = 2S_V^{II}(f), \tag{C.13}$$

which is only defined for positive frequencies. The factor of 2 is used to ensure that the one-sided power spectral density still relates to the same total signal power. The rest of this document will always refer to the one sided

PSD (except when explicitly stated otherwise), and the superscript $(\,)^I$ will be omitted.

The PSD of a real-valued signal with units of [signal] has units of [signal]^2/Hz, which intuitively translates to signal power[4] in a unit bandwidth. Consequently, the total power of the signal is given by the integral

$$P = \int_0^\infty S_V^I(f)\,\mathrm{d}f\,. \tag{C.14}$$

This relation follows from Parseval's theorem,

$$\int_{-\infty}^{\infty} |V(t)|^2\,\mathrm{d}t = \int_{-\infty}^{\infty} \left|\tilde{V}(2\pi f)\right|^2\,\mathrm{d}f\,, \tag{C.15}$$

where the left hand side gives the total energy of the signal. Dividing this equation by the measurement time T yields the average signal power on the left, whereas the right hand side yields the integral over the PSD, using equation eq. (C.9).

If the PSD is estimated from a discrete time series recorded at a certain sampling frequency f_s, the Nyquist–Shannon sampling theorem states that the highest resolvable signal frequency is $f_s/2$ (Nyquist frequency). Signals at a higher frequency are 'aliased' into the frequency band $[1/T, f_s/2]$, such that

$$P = \int_{1/T}^{f_s/2} S_V^I(f)\,\mathrm{d}f \tag{C.16}$$

is the total signal power[5].

In the case of white noise S_V^I is constant, so $P = \frac{f_s}{2} S_V^I$; since the power of the signal is a physical quantity that should not depend on the sampling rate of our measurement apparatus, the value of the PSD has to depend on the sampling frequency (assuming that the noise bandwidth is larger than $f_s/2$). This problem can be circumvented by low-pass filtering the measured signal before sampling it, discarding noise power at frequencies above $\frac{f_s}{2}$.

Instead of working with the PSD, it is sometimes more convenient to look at the linear- or amplitude spectral density (ASD), in units [signal]$/\sqrt{\text{Hz}}$, which is simply defined as

$$\mathrm{ASD}_V(f) = \sqrt{S_V(f)}. \tag{C.17}$$

Other common notations to denote an ASD are

$$\mathrm{ASD}_V(f) = S_V^{1/2}(f) = \tilde{V}(f), \tag{C.18}$$

Here, $\tilde{V}$ is *not* the Fourier transform of V.

4 Using a generalized notion of $[power] = [signal]^2$, which does not have to correspond to a physical power with units of Watts. In the case of an electrical signal in Volts, the power is given by $[power] = V^2/R$; so the formula holds for voltage through a resistor with $R = 1\Omega$.

5 The lower bound of $1/T$ stems from the fact that $f = 0$ would correspond to an infinitely long measurement.

C.2.3 *Measures of oscillator stability*

Power spectral densities can be calculated for arbitrary observable quantities. In our situation, all of the variables mentioned above (ϕ, x, ν, y) could be used to describe the stability of an oscillator. We usually estimate the PSD using a version of eq. (C.12), which contains the square of the Fourier transform. Since derivatives become multiplications with $2\pi f$ in the frequency domain, the PSDs of phase and frequency fluctuations can easily be converted into one another[6]:

$$S_y(f) = (2\pi f)^2 S_x(f), \qquad S_\phi(f) = (2\pi\nu_0)^2 S_x(f), \qquad S_\nu(f) = \nu_0^2 S_y(f), \tag{C.19}$$

so in total we have

$$S_y(f) = (2\pi f)^2 S_x(f) = \frac{f^2}{\nu_0^2} S_\phi(f) = \frac{1}{\nu_0^2} S_\nu(f). \tag{C.20}$$

Another measure for stability that is usually provided for high Fourier frequencies is the single sideband (SSB) phase noise, which is nowadays defined as

$$\mathcal{L} = \frac{1}{2} S_\phi(f). \tag{C.21}$$

It is typically expressed in units dBc/Hz, utilizing

$$\mathcal{L}\,[\mathrm{dBc/Hz}] = 10 \log_{10}\left(\frac{1}{2} S_\phi[\mathrm{rad^2/Hz}] \cdot 1\mathrm{Hz}\right) \tag{C.22}$$

or equivalently

$$\mathcal{L}\,[\mathrm{rad^2/Hz}] = 10^{\frac{\mathcal{L}[\mathrm{dBc/Hz}]}{10}} \mathrm{rad^2/Hz}. \tag{C.23}$$

The unit dBc/Hz stands for 'dB below the carrier in a 1Hz bandwidth'. It was historically computed from the power spectrum of the signal V(t), by comparing the power in a 1Hz bandwidth at a given offset f from the carrier with the total signal power. One disadvantage of this procedure is that both amplitude and phase noise influence the signal's power spectrum, which is one of the reasons that eq. (C.21) was adopted as the modern definition.

Note that phase noise (S_ϕ and $\mathcal{L}$) is defined with respect to a carrier frequency. Its numerical value can be made arbitrarily small by using frequency dividers[7] to produce a lower frequency signal; however, this does not make the oscillator more stable. Therefore, the reference frequency has to be stated in addition to the phase noise itself in order to get a physically meaningful quantity. The same is true for absolute frequency fluctuations S_ν.

It is thus advisable to use S_y or S_x for comparing the performance of different oscillators.

6 Notice that y and ν also differ by a constant offset. This would only affect the PSD for a Fourier frequency of oHz, which is usually omitted, c.f. [49]

7 Frequency dividers convert a signal to a lower frequency, conserving the timing jitter of the original signal. This is in contrast to mixers and interferometers, which conserve phase errors instead.

C.2.4 *Colors of noise*

Many noise processes have PSDs that follow a power law of the kind

$$S(f) \sim f^{\alpha}, \tag{C.24}$$

where α is an integer. This behaviour can also be restricted to a limited bandwidth, or a mixture of different power laws might be present, such that

$$S(f) = \sum_{\alpha} h_{\alpha} f^{\alpha}, \qquad h_{\alpha} \in \mathbb{R} \tag{C.25}$$

Some power laws must be band limited, since the total power should be a finite quantity; depending on the value of α, the integral eq. (C.16) might not converge if the lower and upper bounds f^{-} and f^{+} approach 0 or $+\infty$, respectively. Noise of these types therefore has to be band limited to some frequency range. In practice, however, the upper and lower frequency limits that can be measured are given by the achievable sampling rate and the available measurement time, which are both finite.

High values of α indicate that most of the signal's power is located at high frequencies whereas the opposite is true for low values of α. Due to this, these power laws are often named by color, in analogy to the visible light spectrum. There, light of different colors correspond to light at different frequencies, such that light with a spectral composition dominated by low or high frequencies appears red or blue, respectively. These names, however, are not standardized across the literature and should only be used as rough guidelines. Some of the most commonly encountered power laws are:

- $\alpha = -2$: One speaks of red noise, random walk noise or brownian noise (random particle movement). As the name suggests, this kind of noise can be generated by integrating a series of uncorrelated random values, i.e., following a path of random steps. The total power converges for $f^{+} \to \infty$, but not for $f^{-} \to 0$.
- $\alpha = -1$: Known as pink noise, shot noise or flicker noise. It is characterised by having an equal amount of noise power in each decade on a logarithmic scale. The total power diverges for both $f^{+} \to \infty$ and $f^{-} \to 0$.
- $\alpha = 0$: a flat spectral distribution, also called white noise. It has an equal amount of noise power in equally spaced frequency intervals. Corresponds to a series of uncorrelated random values. The total power converges for $f^{-} \to 0$, but not for $f^{+} \to \infty$.
- $\alpha = +1$: Blue noise. One also speaks of flicker phase noise when encountered in a spectrum of frequency measurements, in analogy to the conversion between phase and frequency PSDs eq. (C.19). The total power converges for $f^{-} \to 0$, but not for $f^{+} \to \infty$.
- $\alpha = +2$: Violet noise. Also called white phase noise when encountered in a spectrum of frequency measurements, again in analogy to eq. (C.19). The total power converges for $f^{-} \to 0$, but not for $f^{+} \to \infty$.

C.2.5 *Integrating and differentiating noises*

Take two time series $g(t)$ and $p(t)$ that fulfill $g(t) = \frac{\mathrm{d}p}{\mathrm{d}t}$. Due to properties of the Fourier transform, the PSD of g can be derived from the PSD of p by multiplying with $(2\pi f)^2$, such that

$$S_g(f) = (2\pi f)^2 S_p(f). \tag{C.26}$$

Conversely, one can also integrate noise with $\alpha = n$ to get noise with $\alpha = n + 2$. These principles are often used to simulate noises with spectral densities of the form $f^{\alpha \pm 2n}$, by successively integrating or differentiating a given noise with spectrum f^{α}. Notice that you cannot use this method to generate noise with uneven values for α (starting from white noise), though there are other methods to generate noise with arbitrary noise shapes, see for example [45].

C.3 FREQUENCY STABILITY IN THE TIME DOMAIN

Another way to characterise noise is to look at statistical measures in the time domain. For this section, we will assume that we have discrete a time series y_k for the fractional frequency deviations and x_k for the timing errors, respectively. We will further denote samples from a time series derived by averaging over a time interval τ by $\bar{y}_i$, where τ must be a multiple of the basic measurement interval $\tau_0 = 1/f_s$.

In this discrete case, the derivative in eq. (C.4) translates to a difference, meaning

$$y_i = \frac{\Delta(x_i)}{\tau_0} = \frac{x_{i+1} - x_i}{\tau_0}. \tag{C.27}$$

Notice that N frequency samples correspond to $N' = N + 1$ phase samples; we need the initial phase x_0 to reconstruct the phase data from the frequency data:

$$x_{i+1} = \tau_0 y_i + x_i = \tau_0 \sum_{k=0}^{i} y_k + x_0, \qquad i < N. \tag{C.28}$$

C.3.1 *Standard variance*

The most common way of describing the statistical properties of a random process Y is the standard variance. It is defined as

$$\tilde{\sigma}_Y^2 = E[(Y - E[Y])^2] = E[Y^2] - E[Y]^2, \tag{C.29}$$

where $E[\cdot]$ is the statistical expectation. Given N samples y_k of the random process, one can estimate the standard variance by computing the sample variance, such that

$$\tilde{\sigma}_y^2 = \frac{1}{N-1} \sum_{k=1}^{N} [y_k - \langle y \rangle_N]^2, \qquad \langle y \rangle_N = \frac{1}{N} \sum_{k=1}^{N} y_k \tag{C.30}$$

Unfortunately, this is not very useful in the presence of divergent noise ($S_y(f) \sim f^\alpha, \alpha < 0$), because the mean over all samples (and hence the value of $\tilde{\sigma}_y^2$) will not converge when $N \to \infty$. Since these kinds of noises are often encountered when studying frequency stability, other types of variances were defined to remedy this problem.

C.3.2 *Allan variance*

The Allan variance σ_y^2 is the most common way of quantifying frequency stability in the time domain. Instead of estimating the average deviations from the mean as is done by the standard variance, it is defined as the expectation of the squared difference of adjacent samples after averaging the time series over a certain time interval τ.

Introduce $\bar{y}_i$ as the fractional frequency values averaged over the time $\tau = m\tau_0$:

$$\bar{y}_i = \frac{1}{m} \sum_{k=im}^{(i+1)m-1} y_k, \tag{C.31}$$

which implicitly depend on τ. Then the Allan variance is defined as

$$\tilde{\sigma}_y^2(\tau = m\tau_0) = \frac{1}{2} E\left[(\bar{y}_{i+1} - \bar{y}_i)^2\right] \tag{C.32}$$

The factor one half is introduced such that the Allan variance coincides with the standard variance for white noise.

The Allan variance has the advantage that it converges for most common clock noises. In practice, the statistical expectation is estimated by the sample mean, such that we have

$$\sigma_y^2(\tau) = \frac{1}{2(M-1)} \sum_{i=1}^{M-1} [\bar{y}_{i+1} - \bar{y}_i]^2, \tag{C.33}$$

where M is the length of the series $\bar{y}_i$. If the original time series has N samples, the averaged series has $M = N/m$ samples, rounded towards the next lower integer value.

Due to the fundamental relationship between phase and frequency eq. (C.27), one can also calculate the Allan variance out of timing data x_k:

$$\sigma_y^2(\tau) = \frac{1}{2(M'-2)\tau^2} \sum_{i=1}^{M'-2} [x_{(i+2)m} - 2x_{(i+1)m} + x_{im}]^2, \tag{C.34}$$

where $M' = M + 1$. Notice that the x_k are *not* averaged in this case. This can be seen by inspecting the difference of two adjacent samples of the averaged series $\bar{y}_i$:

$$\bar{y}_{i+1} - \bar{y}_i = \frac{1}{m}\left(\sum_{k=(i+1)m}^{(i+2)m-1} y_k - \sum_{k=im}^{(i+1)m-1} y_k\right) \tag{C.35}$$

$$= \frac{1}{m}\left(\sum_{k=im}^{(i+1)m-1} y_{k+m} - y_k\right) \tag{C.36}$$

$$= \frac{1}{m\tau_0}\left(\sum_{k=im}^{(i+1)m-1} \Delta(x_{k+m}) - \Delta(x_k)\right) \tag{C.37}$$

$$= \frac{1}{\tau}\left(x_{(i+2)m} - 2x_{(i+1)m} + x_{im}\right), \tag{C.38}$$

using the general property of the difference Δ that $\sum_{i=i_0}^{i_1} \Delta(a_i) = a_{i_1+1} - a_{i_0}$ for any ordered series a_i.

For white noise, the Allan deviation satisfies $\sigma_y(\tau) = \tilde{\sigma}_{\bar{y}}$ (i.e. the standard deviation of the time series after averaging blocks of m samples is the same as the Allan deviation for $\tau = m\tau_0$).

C.3.2.1 *Overlapping Allan variance*

The original definition of the Allan variance in equation eq. (C.33) uses the sample mean over $M - 1$ realisations of the squared differences of averaged frequency data,

$$[\bar{y}_{i+1} - \bar{y}_i]^2, \tag{C.39}$$

to estimate the true statistical expectation of this difference.

Here, the averages are computed such that each sample is used only once, i.e., there is no overlap between adjacent averages. This means that not all possible ways of computing the squared difference eq. (C.39) are utilised.

Instead, one can form every possible average over a time interval τ by allowing the ranges of samples to overlap:

$$\bar{y}'_i = \frac{1}{m}\sum_{k=i}^{i+m-1} y_k. \tag{C.40}$$

Using this notation, $(\bar{y}_{i+1} - \bar{y}_i)^2$ translates to $(\bar{y}'_{i+m} - \bar{y}'_i)^2$. This now yields $N - 2m$ possible realisations of eq. (C.39), significantly increasing the statistical certainty of the resulting Allan variance:

$$\sigma_y^2(\tau) = \frac{1}{2(N-2m+1)}\sum_{j=1}^{N-2m+1} [\bar{y}'_{i+m} - \bar{y}'_i]^2 \tag{C.41}$$

$$= \frac{1}{2m^2(N-2m+1)}\sum_{j=1}^{N-2m+1}\left(\sum_{i=j}^{j+m-1} [y_{i+m} - y_i]\right)^2. \tag{C.42}$$

Due to the double summation, directly applying this formula to large data sets can lead to prohibitively long computation times. Luckily, computing the overlapping Allan variance out of phase data is much more efficient:

$$\sigma_y^2(\tau) = \frac{1}{2(N'-2m)\tau^2} \sum_{i=1}^{N'-2m} [x_{i+2m} - 2x_{i+m} + x_i]^2, \tag{C.43}$$

so it is usually preferable to convert frequency data into phase data to use the more efficient formula. $N' = N + 1$ is the number of available phase samples.

In general, using overlapping averages is the preferred way of estimating the Allan variance.

C.3.2.2 *Certainty of the estimated Allan variance*

As mentioned above, the 'true' Allan variance corresponding to the process under investigation is estimated from a finite time series in all practical applications. The certainty of this estimate is often assumed to be given by $\pm 1\sigma$ error bars at $\pm\sigma_y(\tau)/\sqrt{M}$, where M is the number of non-overlapping average frequency samples used to calculate $\sigma_y(\tau)$ for a given τ. Although this is an easy way to equip a computed Allan variance with error bars, it is usually not quite correct, because the certainty depends on the correlation between the used samples, i.e., the underlying power law. It is also not applicable to the overlapping Allan variance. If the power law is known, the former can be corrected by multiplying the error bars with a factor k_α [70]:

α	-2	-1	0	1	2
k_α	0.75	0.77	0.87	0.99	0.99

This assumes a PSD of the form $S_y(f) \sim f^\alpha$. Instead of using this simple formula, one can also determine error bars using χ^2 statistics, cf. [2, 70] for further information.

C.3.2.3 *Deterministic effects*

Since the Allan variance is calculated from differences of adjacent frequency samples, it is invariant under frequency offsets, which are equivalent to linear drifts in the phase data.

A linear frequency drift leads to quadratic behaviour in the Allan variance. This can be seen by considering equation eq. (C.32): for a linear drift and no additional random behaviour, the difference is equal to the drift rate y_d times the timespan between the samples, which is just τ after averaging the time series. Notice that the normalisation factor $1/2$ in equation eq. (C.32) implies that if the frequency drifts with

$$y(t) = y_0 + y_d \cdot t, \tag{C.44}$$

we get

$$\sigma_y^2(\tau) = \frac{y_d^2}{2} \cdot \tau^2 \tag{C.45}$$

for the Allan variance.

C.3.3 *Modified Allan variance*

The Allan variance has the disadvantage that it does not discriminate between white and flicker phase noise; they both lead to $\sigma_y \sim \tau^{-1}$, making it impossible to infer the underlying power law from the Allan variance alone. The so called modified Allan variance solves this problem by performing an additional averaging operation on the phase data:

$$\operatorname{mod} \sigma_y^2(\tau) = \frac{1}{2\tau^2 m^2 (N-3m+1)} \sum_{j=1}^{N-3m+1} \left[\sum_{i=j}^{m+j-1} (x_{i+2m} - 2x_{i+m} + x_i) \right]^2 . \tag{C.46}$$

Naively implementing this formula can become computationally expensive, again, due to the double summation; this can be remedied by pre-computing the second differences in the inner sum.

C.3.4 *Other variances*

The Allan variance and the modified Allan variance are not the only time domain measures used to describe oscillator stability, but they are the most frequently encountered ones. Therefore, this document will only consider these two variances. For a more complete overview over other variances, see [2, 70].

C.4 DOMAIN CONVERSIONS

In general, the aforementioned measures of frequency stability in the time and frequency domain are not equivalent; in particular, it is not possible to convert arbitrary Allan deviations into corresponding power spectral densities.

C.4.1 *Standard variance for a given PSD*

In the simplest case of white noise, the Allan variance is closely related[8] to the standard variance and can be uniquely converted to a PSD. Remember

8 As argued above, we have $\sigma_{\bar{y}}^2(\tau) = \tilde{\sigma}_{\bar{y}}^2$ in this case.

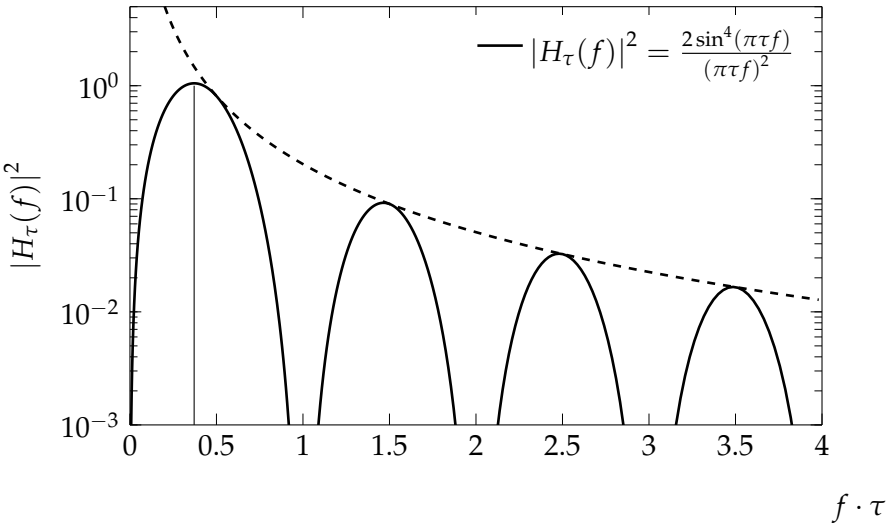

FIGURE C.3: Transfer function of the regular Allan deviation. The higher frequency contributions are suppressed with $1/f^2$, indicated by the dotted line. The first peak is at $f \approx 0.3710/\tau$.

that the PSD is the Fourier transform of the auto correlation function. This means that we can use the inverse Fourier transform to write

$$\tilde{\sigma}^2 = R(0) = \int_0^\infty S(f)df. \tag{C.47}$$

For band-limited white noise, $S(f)$ is equal to a constant S or zero, so we get $\tilde{\sigma}^2 = S \cdot \text{Bandwidth}$. The bandwidth where the PSD is known is often limited by the Nyquist frequency, such that

$$\tilde{\sigma}^2 = \frac{f_s}{2} \cdot S. \tag{C.48}$$

This relation can be used to simulate noise with a given PSD and sampling rate by utilising a random number generator. A given series of random numbers with variance $\tilde{\sigma}$ can be rescaled with $2/f_s$ to represent white noise with a PSD of S in the aforementioned bandwidth.

C.4.2 *Integral formulas*

The calculation of the different variances for a given τ can be understood as the application of a digital filter, which can be described in the frequency domain by applying the corresponding transfer function $H_\tau(f)$ to the PSD. The value of $\sigma_y^2(\tau)$ is then interpreted as the power of the filtered signal, which is computed in the frequency domain by integrating the PSD:

$$\sigma_y^2(\tau) = \int_0^{f_h} S_y(f) \left|H_\tau(f)\right|^2 df \tag{C.49}$$

Notice that this integral is not guaranteed to converge for $f_h \to \infty$. If it diverges, the result of this conversion strongly depends on the chosen cutoff frequency f_h.

In practice, the PSD itself is also estimated by some numerical algorithm, which often involves some level of processing like removing a DC offset or a

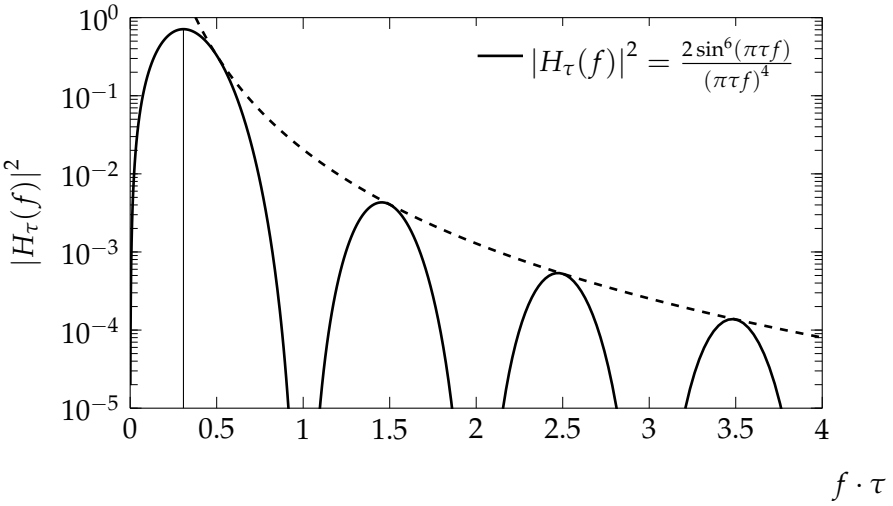

FIGURE C.4: Transfer function of the modified Allan deviation. The higher frequency contributions are suppressed with $1/f^4$, indicated by the dotted line. The first peak is at $f \approx 0.3079/\tau$.

linear trend. This can cause disparities when comparing Allan deviations directly computed from frequency or phase data with Allan deviations obtained from converted power spectral densities.

C.4.2.1 *PSD to Allan variance*

The transfer function of the Allan variance is [2]

$$|H_\tau(f)|^2 = \frac{2\sin^4(\pi\tau f)}{(\pi\tau f)^2}, \tag{C.50}$$

which is plotted in fig. C.3. This means we can calculate the Allan variance using

$$\sigma_y^2(\tau) = 2\int_0^{f_h} S_y(f)\frac{\sin^4(\pi\tau f)}{(\pi\tau f)^2}df, \tag{C.51}$$

where f_h is the high frequency cutoff of the measurement device. It is apparent that this integral does not converge for $f_h \to \infty$ if $S_y(f) \sim f^{\alpha>1}$, i.e., in the presence of significant phase noise.

C.4.2.2 *PSD to modified Allan variance*

The analogue to equation eq. (C.51) for the modified Allan variance is [2]

$$\operatorname{mod}\sigma_y^2(\tau) = \frac{2}{m^4}\int_0^{f_h} S_y(f)\frac{\sin^6(\pi\tau f)}{(\pi\tau_0 f)^2\sin^2(\pi\tau_0 f)}df \tag{C.52}$$

$$\approx 2\int_0^{f_h} S_y(f)\frac{\sin^6(\pi\tau f)}{(\pi\tau f)^4}df, \tag{C.53}$$

where f_h is the high frequency cutoff of the measurement device and $\tau = m\tau_0 = m/f_s$. The integral in eq. (C.52) quickly converges to the one in eq. (C.53) for $m \to \infty$ [72], such that

$$|H_\tau(f)|^2 \approx \frac{2\sin^6(\pi\tau f)}{(\pi\tau f)^4}. \tag{C.54}$$

This transfer function is plotted in figure C.4.

The modified Allan variance is less dependent on the cutoff frequency f_h since contributions from high frequencies are suppressed with $1/f^4$ instead of $1/f^2$ in the case of the regular Allan variance, which allows the integral to still converge for more divergent PSDs.

C.4.3 *Parametric conversion for power laws*

The integral formula connecting Allan variance and power spectral density can be analytically solved for power spectral densities following a simple power law, leading to Allan variances following a different power law. This allows for simple conversion formulas for the most often encountered types of frequency instabilities[9] [72]:

Noise Type:	RW FM	Flicker FM	White FM	Flicker PM	White PM
$S_y(f) =$	$h_{-2}f^{-2}$	$h_{-1}f^{-1}$	$h_0 f^0$	$h_1 f^1$	$h_2 f^2$
$\sigma_y^2(\tau) =$	$A \cdot h_{-2}\tau^1$	$B \cdot h_{-1}\tau^0$	$C \cdot h_0 \tau^{-1}$	$D \cdot h_1 \tau^{-2}$	$E \cdot h_2 \tau^{-2}$
mod $\sigma_y^2(\tau) =$	$A' \cdot h_{-2}\tau^1$	$B' \cdot h_{-1}\tau^0$	$C' \cdot h_0 \tau^{-1}$	$D' \cdot h_1 \tau^{-2}$	$E' \cdot h_2 \tau^{-3}$

Here, the coefficients are given by

$$A = \tfrac{2\pi^2}{3}, \qquad B = 2\ln 2, \qquad C = \tfrac{1}{2}, \quad D = \tfrac{1.038+3\ln 2\pi f_h \tau}{4\pi^2}, \quad E = \tfrac{3f_h}{4\pi^2},$$

$$A' = 0.824\tfrac{2\pi^2}{3}, \quad B' = \tfrac{27}{20}\ln 2, \quad C' = \tfrac{1}{4}, \quad D' = 0.084, \qquad E' = \tfrac{3f_h\tau_0}{4\pi^2}.$$

Notice that the Allan variance coefficients for white and flicker phase noise depend on the cut-off frequency f_h, as expected, and that the corresponding Allan variances both are (almost) proportional to τ^{-2}. This makes it difficult, if not impossible, to determine the coefficients h_1 and h_2 from Allan deviation plots alone.

If data on high frequency phase noise (S_ϕ or $\mathcal{L}$) is available in addition to Allan deviations for the long term stability, one can also try to fit a power law to the high frequency data and extrapolate it to lower frequencies to determine h_1 and h_2. One can than still use the Allan deviation to determine h_{-2}, h_{-1} and h_0.

It should be noted that [2] cautions against using these conversion formula when more than one kind of power law is present.

C.4.4 *Numerical approximation of the PSD*

Although the integral equations in section C.4.2 are, in general, not invertible, one can still attempt to find an approximate numerical solution to the inverse problem of finding a power spectral density from given values of the Allan

9 RW = Random Walk, FM = Frequency Modulation, PM = Phase Modulation.

variance. We attempt here to develop such a method to estimate either the regular or the modified Allan deviation.

The integral equation eq. (C.49) is given in continuous time. In practice, however, one only has discrete values for the Allan deviation σ_i for times τ_i and seeks discrete values for the power spectral density P_j at frequencies f_j. This allows to rewrite eq. (C.49) into a matrix equation of the form

$$\sigma = H \cdot P, \tag{C.55}$$

i.e.,

$$\sigma_i = \sum H_{ij} P_j, \qquad H_{ij} = \int_{f_j - \delta_j^-}^{f_j + \delta_j^+} |H_{\tau_i}(f)|^2 \, df, \tag{C.56}$$

where the frequency spacing is assumed to be in such a way that the PSD is approximately constant in each frequency interval $[f_j - \delta_j^-, f_j + \delta_j^+]$, and the δ's are chosen such that

$$\sum_j H_{ij} = \int_0^{f_h} |H_{\tau_i}(f)|^2 \, df. \tag{C.57}$$

The matrix H is usually not invertible and has to be 'regularised' in order to solve the matrix equation eq. (C.55). One possible approach to achieve this is to introduce an approximation of H (let's call it $\bar{H}$) that is guaranteed to be invertible and then solve the matrix equation

$$\sigma = ((1-\lambda)H + \lambda \bar{H})P, \tag{C.58}$$

by inverting $((1-\lambda)H + \lambda\bar{H})$. The parameter $\lambda \in [0,1]$ should be as small as possible, but large enough to make the matrix invertible.

One possible choice for $\bar{H}$ is inspired by the transfer function of the Allan variance and by the idea that each value of σ_i should correspond to one value of P_j at a frequency f_j that is reciprocal to the averaging time τ_i. That is, the transfer function in figure C.3 is replaced with a sharp peak located at the first maximum of the original transfer function, 'forgetting' the contributions from the higher frequency lobes. This peak is not at exactly $0.5/\tau$, since its location is affected by the enveloping $1/f^2$ dependence. For the regular Allan deviation, the first maximum is at $f_i \approx 0.3710/\tau_i$ while it is at $f_i \approx 0.3079/\tau_i$ for the modified Allan deviation. The corresponding matrix has the form

$$\bar{H} = \begin{pmatrix} 0 & \dots & 0 & 0 & \eta_1 \\ 0 & \dots & 0 & \eta_2 & 0 \\ \vdots & & \iddots & & \vdots \\ 0 & \eta_{n-1} & 0 & \dots & 0 \\ \eta_n & 0 & 0 & \dots & 0 \end{pmatrix}, \qquad \eta_i = \sum_j H_{ij}. \tag{C.59}$$

In the case of the regular Allan variance, this procedure only works if the PSD is at most proportional to $f^{\alpha<1}$, since the side lobes contribute too much to

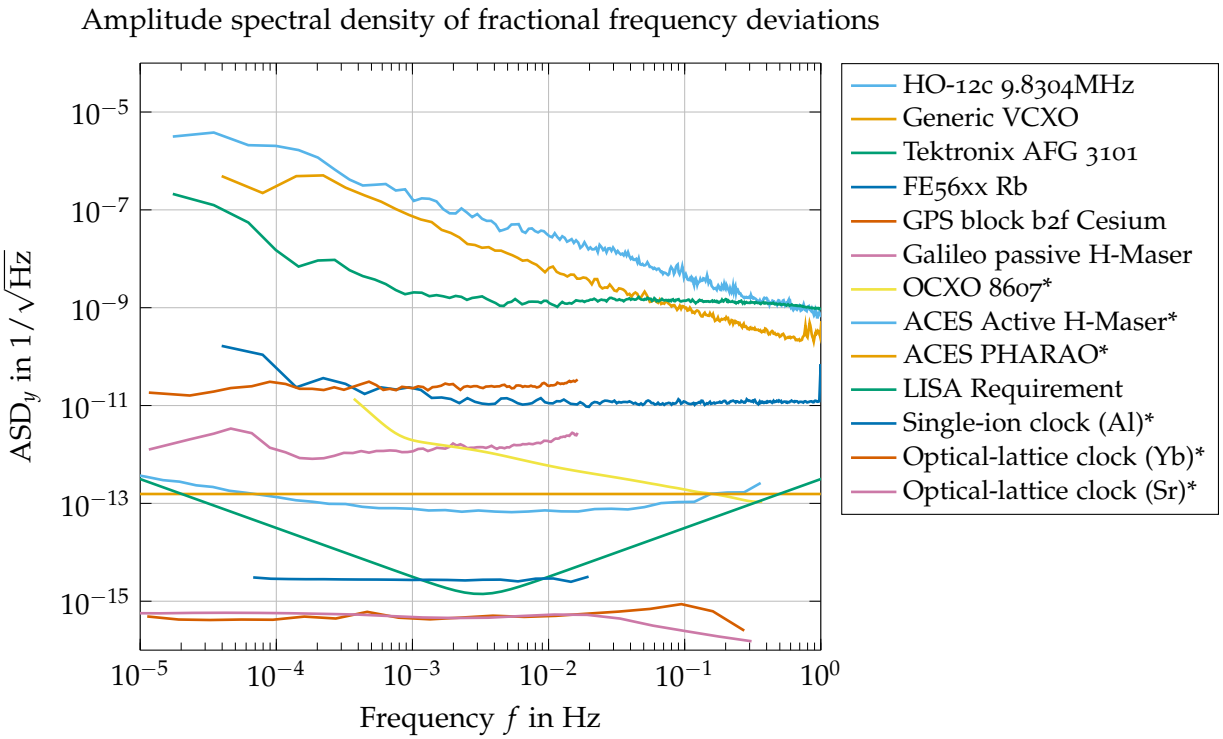

FIGURE C.5: Overview of the frequency stability of different oscillators in terms of ASD$_y$. Plots marked with an * are converted from an Allan deviation. The ordering in the legend corresponds to the order in which the curves appear in the plot.

the value of the Allan variance otherwise, making the conversion non-reliable. It is more stable in the case of the modified Allan variance, since the higher frequency parts are suppressed with $1/f^4$ instead of $1/f^2$; here, it yields reasonable results for all common clock noise types. Appendix C.7 contains some examples.

C.5 EXAMPLES

Figures figs. C.5 to C.7 show measured stability values for different commercial oscillators as well as some values taken from external sources in terms of amplitude spectral density, Allan deviation and modified Allan deviation. Since long term stability is commonly expressed using the Allan deviation, manufacturers usually do not provide power spectral density plots at frequencies below 1Hz. The ASD plots in figure C.5 were either directly computed from the raw frequency/phase data or they were converted from Allan variances using the algorithm described in section C.4.4. Similarly, some of the plots in figure C.7 where obtained by first converting an Allan deviation to a PSD and then back to a modified Allan deviation. Notice that these conversions are somewhat inaccurate for the highest and lowest frequencies. Deterministic trends where removed from the raw data before calculating Allan deviations and PSDs such that these plot only show the random fluctuations; the downward trend for the largest τ in figures C.6 and C.7 observed for some of the quartz oscillators is an artefact of this drift removal.

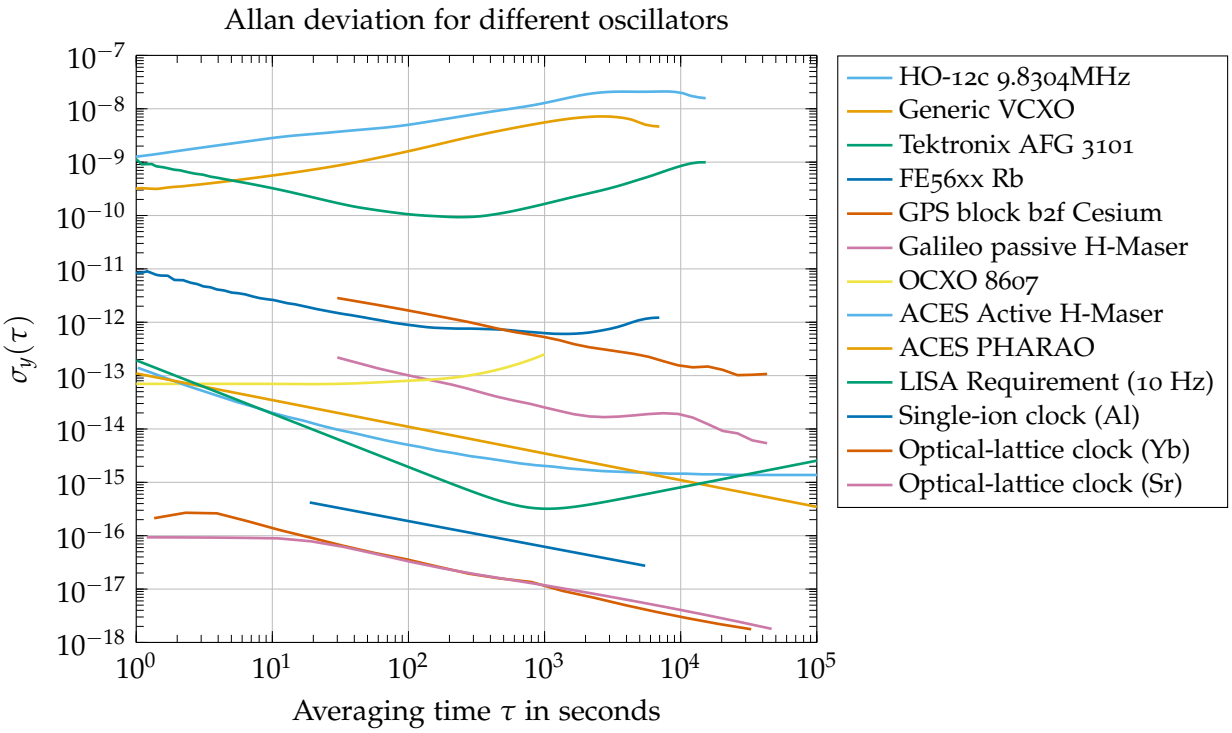

FIGURE C.6: Overview over frequency stability of different oscillators in terms of Allan deviation.

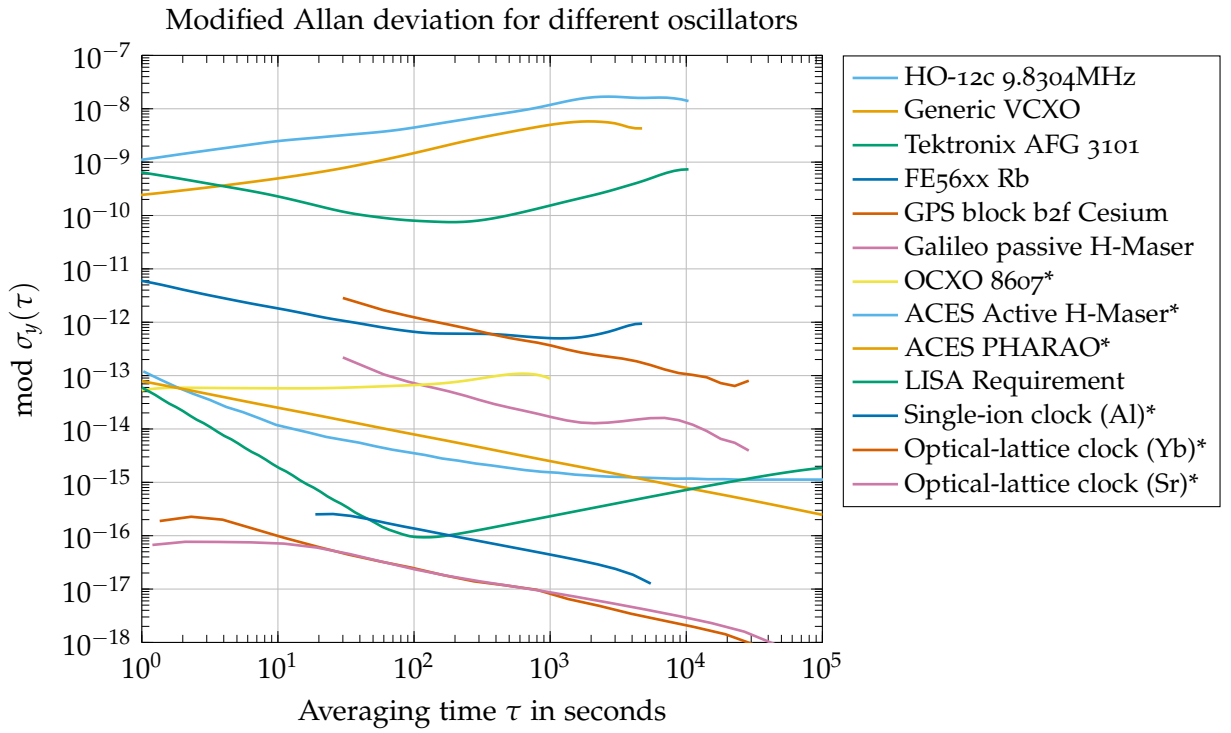

FIGURE C.7: Overview over frequency stability of different oscillators in terms of modσ_y. Plots marked with an * are converted from an Allan deviation by first converting it to a PSD.

C.5.1 *LISA requirement*

One area of interest for characterising frequency stability in the context of this thesis is inter-satellite interferometry, as it will be utilised by LISA, which will measure relative distances between spacecraft with picometer accuracy. It achieves this accuracy using heterodyne laser interferometry; in this scheme, the path length change introduces a phase shift in the laser light from the remote spacecraft, which is combined with a local laser on the receiving spacecraft to get a low frequency beat note at around 20 MHz. This electrical signal is then digitised using an analog to digital converter; this is where the clock noise of the onboard oscillator enters the signal, since variations in its sample rate are indistinguishable from actual phase variations in the signal.

Ideally, the on-board oscillator should be so stable that the noise introduced this way is smaller than the required picometer accuracy.

LISA will use lasers at a wavelength of 1064 nm, which means that 1 pm $\sqrt{\text{Hz}}^{-1}$ corresponds to a phase variation of $\phi = 2\pi\,\mu\text{rad}\,\sqrt{\text{Hz}}^{-1}$. These are translated into phase variations in the 20 MHz beat note, which corresponds to a timing jitter of

$$\text{ASD}_x = \frac{2\pi\,\mu\text{rad}\,\sqrt{\text{Hz}}^{-1}}{2\pi \times 20\,\text{MHz}} = \frac{50\,\text{fs}}{\sqrt{\text{Hz}}}. \tag{C.60}$$

This can be converted into fractional frequency stability using eq. (C.19), the result of which is plotted in figure C.5 in comparison with other oscillators. Here, following [64], it was assumed that the frequency dependence of the requirement is

$$\text{ASD}_x = \sqrt{S_x(f)} = \frac{50\,\text{fs}}{\sqrt{\text{Hz}}}\sqrt{1 + \left(\frac{3\,\text{mHz}}{f}\right)^4}. \tag{C.61}$$

Notice that the mission requirement for the on-board clock cannot be fulfilled by any space-qualified clock available today. The optical lattice clocks described in [57] would be stable enough, however, they achieve this performance as large laboratory experiments, not as flight-ready hardware. This is why clock noise correction schemes have been developed for LISA, as discussed in chapters 6 and 13 of this thesis.

Also notice the discrepancy between figures C.5 and C.6. In figure C.5, the curve for the LISA requirement intersects with the one from the single-ion clock, whereas the two curves do not intersect in figure C.6. Here, it becomes apparent that the Allan deviation is not a good measure of frequency stability in the presence of white phase noise, since it depends on the high frequency cutoff f_h, which was assumed to be at 10Hz in this case. Choosing a different value significantly influences the resultant LISA requirement in figure C.6. The modified Allan deviation shown in figure C.7 instead yields results which are consistent with the spectral density in figure C.5.

C.5.2 *Quartz oscillators*

A quartz oscillator is a very common and versatile electrical component that produces a periodic signal derived from the mechanical vibrations of a quartz crystal which is coupled to an electrical circuit via the piezoelectric effect of the quartz material. High quality quartz oscillators can be very stable, although the crystals resonance frequency has a slight dependence on temperature, which limits the long term stability. In addition, the resonance frequency tends to slowly change with time regardless of temperature, a process called aging. They are often tuneable in a limited frequency range by applying a voltage to a capacitance diode connected to the crystal, which can be used to compensate for temperature fluctuations; alternatively (or additionally), one can install the oscillator in a temperature stabilised housing (called oven), which in turn allows to tune the frequency by adjusting the temperature. Usual abbreviations for these different concepts are:

- XO - crystal oscillator
- VCXO - voltage controlled crystal oscillator
- TCXO - temperature compensated crystal oscillator
- OCXO - oven controlled crystal oscillator

The upper two curves in the comparison figure C.5 where recorded for free-running VCXOs at room temperature. The slightly better performing Tektronix AFG 3101 is an arbitrary function generator, which contains a good quartz oscillator as reference clock. The significantly more stable OCXO 8607 is, as the name suggests, a high quality oven controlled crystal oscillator. It's Allan deviation was taken from the manufacturers data sheet and converted to an ASD.

Since quartz oscillators generally have good short term stability and can be easily adjusted in frequency, they are often combined with a reference signal that is known to have good long term stability, such as the timing data provided by Global Positioning System (GPS) or an atomic frequency standards (AFSs). This is also known as 'disciplining', and can be realized in practice by steering the frequency of the oscillator with a low bandwidth control loop to follow the more stable reference at low Fourier frequencies.

C.5.3 *Atomic frequency standards*

AFSs use the electronic or optical transition frequencies of atoms as a reference to provide a very stable clock signal. These devices are in general larger and much more complicated than simple quartz oscillators, but deliver unmatched longterm frequency stability.

C.5.3.1 *Ground based AFS*

FE 5680A The FE 5680A is a commercial rubidium frequency standard. The frequency stability data shown was obtained by comparing a FE 5680A with an FE 5650, which is a very similar device by the same company that mainly differs by its form factor. As can be seen in figure C.5, its performance is somewhat comparable to spaceborne AFS used in, for example, GPS satellites.

LABORATORY CLOCKS State-of-the-art laboratory clocks can achieve much better frequency stability than the commercial devices studied above. [57] contains a performance comparison between different optical lattice clocks, again in terms of Allan deviations, which were converted to ASDs for figure C.5.

C.5.3.2 *Spaceborne AFS*

GNSS Global Navigation(al) Satellite Systems (GNSSs) need very stable clocks in order to provides accurate ranging information. The multi-GNSS experiment of the international GNSS service [61] provides clock performance data for different satellite constellations in terms of timing deviations, which can be used to compute their frequency stability. Notice that this is an estimate of the actual performance of the on-board atomic clocks, not the accuracy achievable with a GPS receiver on ground. The constellations under consideration are:

- GPS - Global Positioning System, USA. Different Blocks correspond to different generations of satellites, using Rubidium or Cesium AFS.
- GLONASS - Globalnaja nawigazionnaja sputnikowaja sistema, Russia. Uses Cesium AFS.
- BeiDou Navigation Satellite System, China. Uses Rubidium AFS.
- Galileo, EU. Uses Rubidium AFS and passive hydrogen masers on each satellite.

Different satellites within the same constellation/generation can show significantly different performance. Figure C.8 shows the averaged performance of each constellation for GPS week 1929 after removing particularly bad outliers. The specific data set used in this analysis is provided by Deutsches GeoForschungsZentrum (GFZ) Potsdam [90] and is available at [1]. Figures C.5 to C.7 only contain traces representing the best and worst performing constellations for the sake of better readability. Figure C.8 shows all of the different GNSS constellations in comparison.

Note that GNSS is only available close to earth, such that it is not an option for missions like LISA.

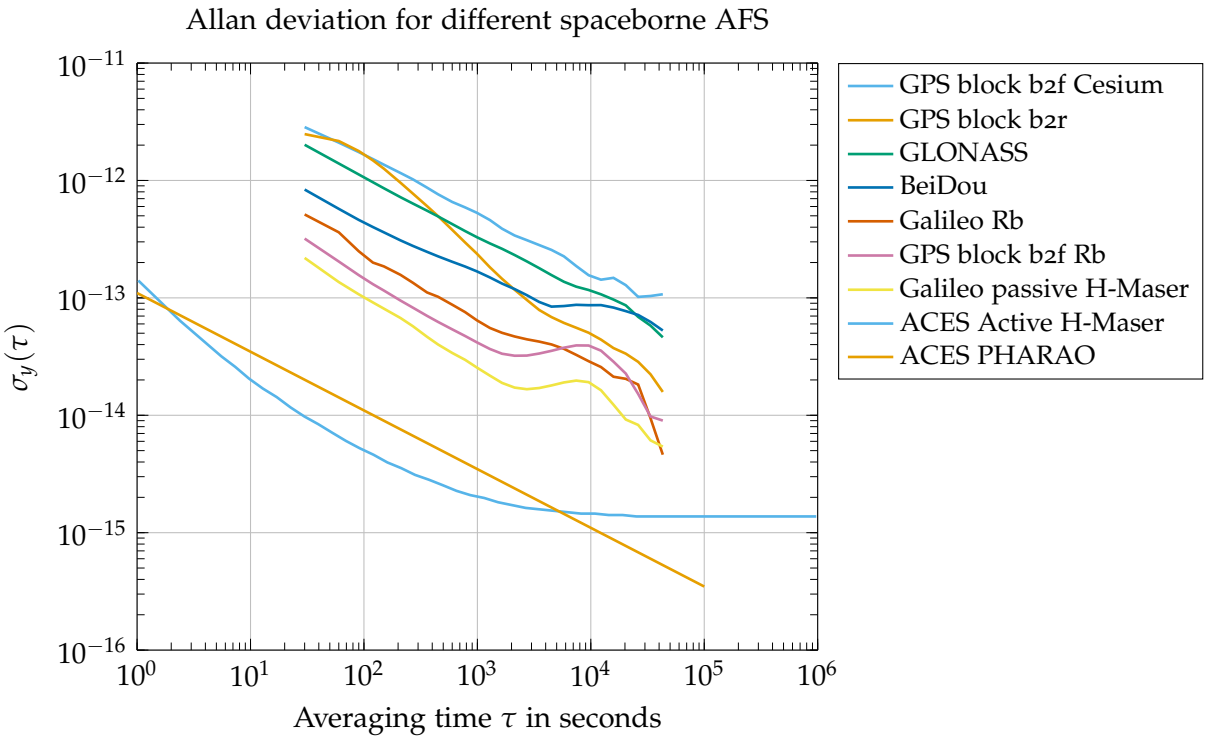

FIGURE C.8: Overview of the frequency stability of different spaceborne AFS. Expected In-flight performance of the ACES clocks.

ACES The Atomic Clock Ensemble in Space (ACES) is an ESA project scheduled to be launched to the International Space Station (ISS) in 2021, which contains two atomic clocks: a cesium laser cooled atomic fountain clock, PHARAO, for long-term stability and an active hydrogen maser, SHM, for short-term stability. The estimated in-flight performance shown here was given in [26] as an Allan deviation.

C.6 METHODS OF FREQUENCY DETERMINATION

So far, we have introduced different ways of quantifying noise present in a given time series of phase or frequency data. Acquiring such data for a given oscillator always requires a reference device to which you can compare your device under test (DUT). In the simplest case, this reference would be another oscillator that is known to have much better performance than the DUT, such that the inherent noise of the reference is negligible. If no such stable reference is available, one can instead compare two devices of the same type with each other, such that the noise present in the final signal is proportional to $\sqrt{2} \times$ [noise of DUT]. The factor $\sqrt{2}$ follows from the assumption that the noise in both devices is uncorrelated.

C.6.1 *Principle of measurement*

The simplest experimental setup used to determine the phase noise of two identical oscillators is shown in fig. C.9. In this setup, the two oscillators

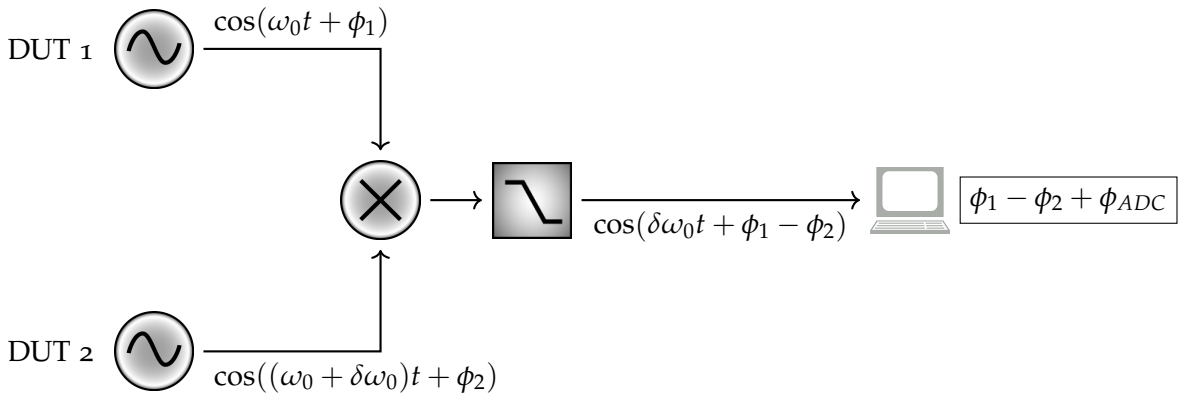

FIGURE C.9: Experimental setup for determination of differential phase deviations between two oscillators. Here, the signals are given using the angular frequency $\omega = 2\pi\nu$ for brevity. ϕ_{ADC} is the phase error introduced due to timing variations in the sampling clock used to digitise the signal.

are operated with a slight frequency offset $\delta\nu_0$, also called the heterodyne frequency. Their respective electrical signals are combined using an electrical mixer, which multiplies them. Thus, the resultant signal is of the form[10]

$$\begin{aligned}\cos(2\pi\nu_0 t + \phi_1(t)) \times \cos(2\pi(\nu_0 + \delta\nu)t + \phi_2(t)) \\ = \cos(4\pi\nu_0 t + 2\pi\delta\nu t + \phi_1(t) + \phi_2(t)) \\ + \cos(2\pi\delta\nu_0 t + \phi_1(t) - \phi_2(t)).\end{aligned} \tag{C.62}$$

Notice that both the high frequency component at twice the carrier frequency and the low frequency component at the heterodyne frequency $\delta\nu_0$ contain the phase noise information we want to measure. Typical carrier frequencies of electrical signals[11] are in the range of MHz, whereas the heterodyne frequency can be adjusted to be of the order of a few kHz, which is more convenient for digitisation. Therefore, the high frequency component of the mixed signal is removed by a low pass filter prior to conversion to the digital domain by an analog-to-digital converter (ADC). This digital representation can then be used to determine the phase of the signal using a suitable algorithm.

One problem with this approach is that the ADC is triggered by a sampling clock, which also introduces its own phase noise[12]. This can be circumvented by a more advanced setup, which is depicted in fig. C.10. Here, both devices under test are operated at the same frequency. They are then mixed with a third oscillator at $\nu_{ref} = \nu_0 + \delta\nu$, here called the local oscillator (LO). The LO is also used to generate the sampling clock[13] which is used to trigger the ADC.

10 Using the basic trigonometric identity $2\cos(x)\cdot\cos(y) = \cos(x-y) + \cos(x+y)$.

11 The principle described here is also used in heterodyne laser interferometers. There, the mixing happens when the laser light at frequencies of a few hundred THz interferes to create a beatnote in the MHz range.

12 Although it should be noted that the mixer preserves phase noise, not timing jitter, thus the required timing stability of the sampling clock is reduced by the ratio of sampling frequency to carrier frequency.

13 To track a signal at a frequency of $\delta\nu$, the Nyquist-Shannon theorem states that the sampling rate must be at least $2\delta\nu$. It is usually chosen with some additional margin, such that the sampling clock might operate around $4\delta\nu$, which is still orders of magnitude lower than the carrier frequency.

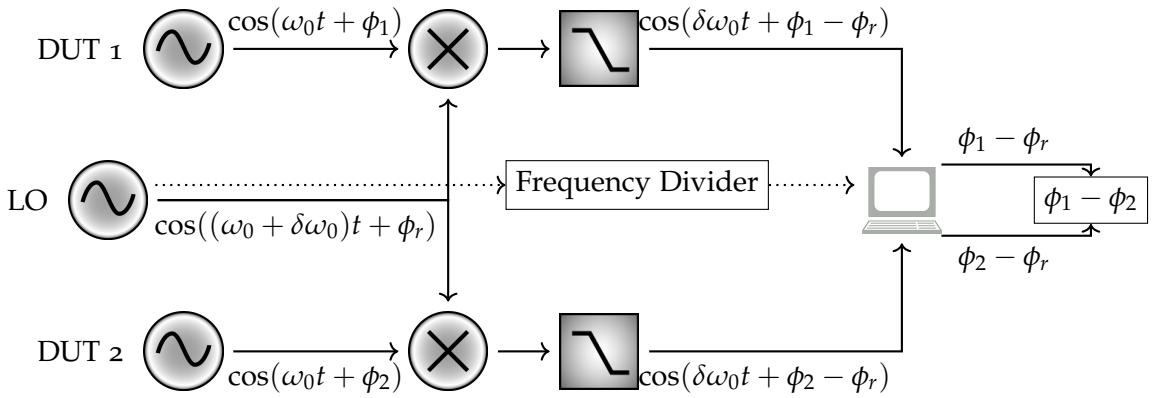

FIGURE C.10: Experimental setup for determination of differential phase deviations between two oscillators, DUT 1 and DUT 2, by mixing them with a third device operated at an offset frequency. The local oscillator LO is used both for mixing and to create the sampling clock which triggers the ADC, which operates at a much lower frequency.

The mixing yields two seperate beatnotes which both contain the differential phase noise of the LO and one of the DUTs. Tracking the phase of both of them yields two time series of phase data which can be subtracted to get a single time series which is free of the LOs phase noise. Therefore, the LO does not need to be as stable as the DUTs but can be a more convenient device such as an arbitrary function generator which can be easily adjusted in frequency.

This scheme has the additional advantage that it can be used to determine the performance of oscillators that always operate at exactly the same frequency.

C.6.2 *Algorithms for frequency determination*

One of the last steps in the measurement scheme described above is the determination of instantaneous phase/frequency deviations of the mixed signal using the digital representation of the signal recorded by the ADC. Different algorithms can be used to achieve this, some of which will be sketched in the following.

C.6.2.1 *Zero-Crossing counter*

One of the simplest and fastest algorithms to determine the frequency of a signal is by counting cycles. This can be done by interpolating the time stamp z_i of each ascending zero-crossing and using these values to calculate the length of each period $T_i = z_{i+1} - z_i$, such that the frequency series is simply given by $f_i = 1/T_i$. The accuracy of the algorithm can be improved by computing the average period length over many cycles, i.e., $\langle T_i \rangle_N = (z_{i+N} - z_i)/N$. However, it still remains very susceptible to noise since only the sample points near the zero crossings are used for the analysis.

C.6.2.2 *Constant frequency demodulation*

This method is similar in principal to the electronic mixing used to get a beat note between two oscillators. The digitised signal

$$V(t) = \sin(2\pi\nu_0 t + \phi(t)) \tag{C.63}$$

is multiplied with a perfect sine and a cosine at the assumed nominal frequency, yielding the so-called in-phase and quadrature components of the signal:

$$\begin{aligned} I_c(t) &= \sin(2\pi\nu_0 t + \phi(t)) \cdot \sin(2\pi\nu_0 t) && \text{(C.64a)} \\ &= \frac{1}{2}(\cos(\phi(t)) - \cos(4\pi\nu_0 t + \phi(t)))\,, && \text{(C.64b)} \\ Q_c(t) &= \sin(2\pi\nu_0 t + \phi(t)) \cdot \cos(2\pi\nu_0 t) && \text{(C.64c)} \\ &= \frac{1}{2}(\sin(\phi(t)) + \sin(4\pi\nu_0 t + \phi(t)))\,. && \text{(C.64d)} \end{aligned}$$

The high frequency component can be removed by a digital low-pass filter. The simplest implementation of such a filter would be to take the average over some timespan $T \gg 1/\nu_0$ to get

$$\begin{aligned} \bar{I}_c(t) &= \frac{1}{2}\cos(\phi(t))\,, && \text{(C.65a)} \\ \bar{Q}_c(t) &= \frac{1}{2}\sin(\phi(t)). && \text{(C.65b)} \end{aligned}$$

This assumes that the phase noise changes slowly compared to T. $\phi(t)$ can than be recovered using

$$\phi(t) = \operatorname{atan2}(\bar{I}_c, \bar{Q}_c). \tag{C.66}$$

The arctangent2 utilises two arguments to give a unique result for $\phi \in (-\pi, \pi]$, instead of $\phi \in (-\pi/2, \pi/2]$ for the regular arctangent or the arcsine. However, since it always returns a value $\phi \in (-\pi, \pi]$, a steadily growing phase (such as from a slight frequency offset) leads to periodic phase jumps which have to be detected and removed by the implemented algorithm.

This method also requires that the frequency of the signal under investigation is known and reasonably constant. Otherwise, the demodulation happens at the wrong frequency, e.g. $\nu_0 + \delta\nu_0$,such that we get

$$\begin{aligned} I_c(t) &= \sin(2\pi\nu_0 t + \phi(t)) \cdot \sin(2\pi(\nu_0 + \delta\nu_0)t) && \text{(C.67a)} \\ &= \frac{1}{2}(\cos(2\pi\delta\nu_0 t + \phi(t)) - \cos(4\pi\nu_0 t + 2\pi\delta\nu_0 t + \phi(t)))\,, && \text{(C.67b)} \\ Q_c(t) &= \sin(2\pi\nu_0 t + \phi(t)) \cdot \cos(2\pi(\nu_0 + \delta\nu_0)t) && \text{(C.67c)} \\ &= \frac{1}{2}(\sin(2\pi\delta\nu_0 t + \phi(t)) + \sin(4\pi\nu_0 + 2\pi\delta\nu_0 t + \phi(t)))\,. && \text{(C.67d)} \end{aligned}$$

Thus, we would no longer have a DC term, but instead an oscillation at $\delta\nu_0$. If $\delta\nu_0$ is large enough, the low-pass filter will remove this part as well, such that $\bar{I}_c = \bar{Q}_c = 0$.

C.6.2.3 *Digital PLL*

A digital phase-locked loop (DPLL) is similar in concept to the aforementioned demodulation with constant frequency. The difference is that instead of just tracking the phase deviations relative to a digital reference as described above, a feedback loop is implemented. It adjust the digital references phase such that the phase deviations vanish. Once the loop is locked, this procedure creates a digital replica of the analog signal from which the desired phase is readily available. One of the advantages of this approach is that a DPLL can track the phase of a signal which varies in frequency. We describe DPLLs in more detail in section 3.5 of this thesis.

C.6.2.4 *Kalman filter*

A Kalman filter is an algorithm which combines a-priori information about the behaviour of a signal and the expected noise levels with actual measurements to obtain an estimate of the true process, modelled by a state vector. Since Kalman filtering is used in many subject areas, numerous introductory textbooks exist on the topic, among them [78].

The classical Kalman filter is formulated for linear system models, where it can be shown to be the optimal filter for this application. In the case of frequency determination, the underlying process is non-linear, requiring a generalised formulation known as the extended Kalman filter (EKF). We use the discrete time formulation.

One approach to using an EKF for frequency determination can be found in [40], although this particular formulation is designed to deal with large amplitude fluctuations, which is unnecessary in our application. Therefore, we used a modified state vector of the form

$$x_k = \begin{pmatrix} x_k[0] \\ x_k[1] \\ x_k[2] \\ x_k[3] \end{pmatrix} = \begin{pmatrix} I_k \\ Q_k \\ \omega_k \\ A_k \end{pmatrix} = \begin{pmatrix} \cos(\omega k + \phi) \\ \sin(\omega k + \phi) \\ \omega_k \\ A_k \end{pmatrix}, \tag{C.68}$$

which consists of the in-phase and quadrature components I and Q, the angular frequency ω and the amplitude A of the signal. Here, we assumed that ω is normalised to the sampling frequency such that the time step between two samples Δt corresponds to a unit time interval.

The assumed dynamical behaviour of the process is modelled by the evolution equation, which relates the state vector at the last time step to the current time step:

$$x_k = f(x_{k-1}) + \text{noise}. \tag{C.69}$$

Here, the function $f(x_k)$ is given by

$$f(x_k) = \begin{pmatrix} x_k[0]\cos(\omega) - x_k[1]\sin(\omega) \\ x_k[0]\sin(\omega) + x_k[1]\cos(\omega) \\ \omega \\ A \end{pmatrix}. \tag{C.70}$$

The measurement equation relates the measurements y_k we take to our state vector x_k. In our case, we only take one scalar measurement at each time step, which is simply

$$y_k = h_k(x_k) + \text{noise} = A \cdot I_k + \text{noise} = x_k[0]x_k[3] + \text{noise}. \tag{C.71}$$

This model fits the description of the discrete time EKF found in the literature, e.g., in [78].

The filter assumes that the measurement as well as ω and A are contaminated with white gaussian noise at each time step, whose variance has to be stated beforehand in addition to starting values for I, Q, ω and A. Finding reasonable values for these variances can be quite challenging and severely influences the overall performance of the algorithm.

Advantages of this approach are that each new sample provides new information, making it ideal for real time applications.

C.7 TEST OF CONVERSION ALGORITHM

Some of the PSDs shown in the overview figure C.5 were converted from a given Allan deviation using the conversion algorithm described in section C.4.4. To justify these result, the algorithm was tested by computing both PSDs and Allan deviations directly from measured time series of frequency fluctuations of some oscillators and then compare the results of the conversion with the directly computed values. As can be seen in figure C.11, the conversion yields results in the right order of magnitude for most common clock noises, with the exception of white phase noise, as expected. Figure C.12 shows the same calculation done using the modified Allan deviation, which yields consistent result for phase noise as well.

C.8 STOCHASTIC PROCESSES

This appendix is meant to give a short overview on the most common statistical quantities. For a more detailed discussion, see e.g. [29].

Noise is a stochastic process. It causes random fluctuations in the deterministic results produced by an experiment, such that different realisations of the same experiment yield different results. Likewise, the magnitude of these deviations might change over time, e.g. due to changes in environmental factors like temperature or ageing of the materials used to build the experiment. Since

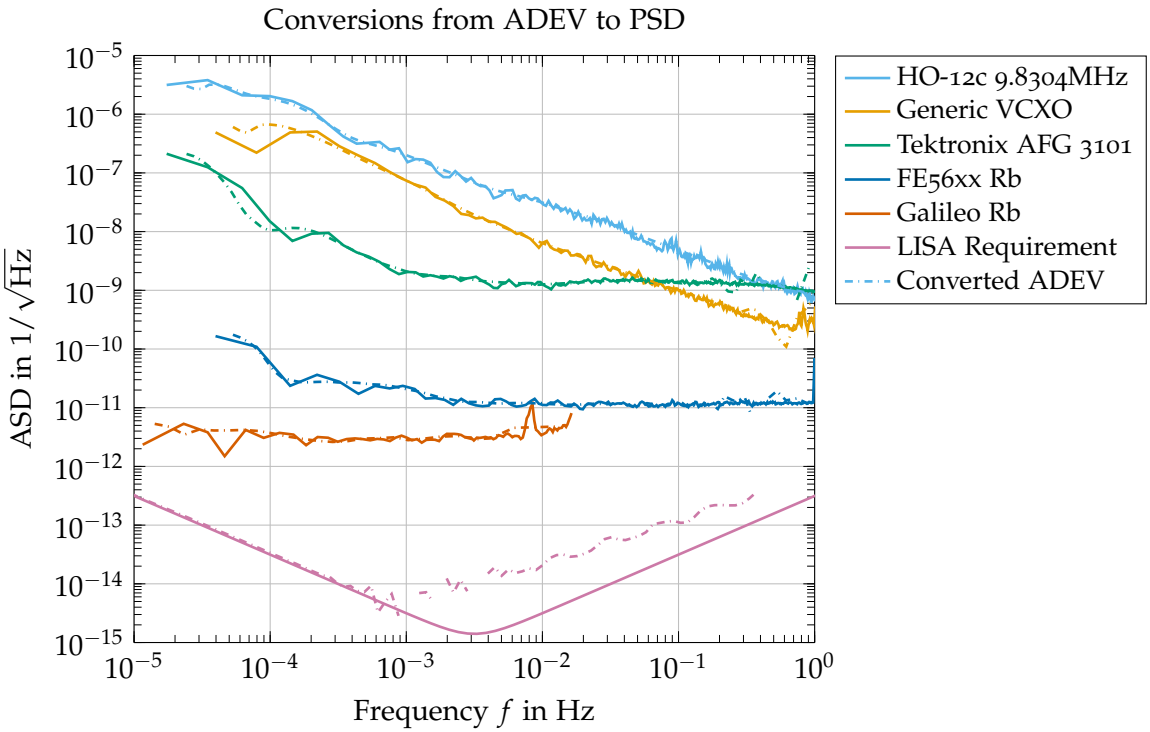

FIGURE C.11: Comparison between PSD directly computed from frequency data and converted Allan variance for some selected oscillators. The free parameter was chosen to be $\lambda = 0.3$.

the deviations are random, one can only describe their average behaviour by using statistical quantities.

Given N realisations $x_i(t)$ of a stochastic process $x(t)$, the sample mean is defined as

$$\langle x(t) \rangle_N = \frac{1}{N} \sum_{i=1}^{N} x_i(t). \tag{C.72}$$

It is often used to estimate the statistical expectation $E[x(t)]$ of the process.

Similarly, the time average of a single realisation $x_i(t)$ over an interval $[-T/2, T/2]$ is given by

$$\bar{x}_i = \frac{1}{T} \int_{-T/2}^{T/2} x_i(t)\, \mathrm{d}t \tag{C.73}$$

If time average and sample mean converge to the same value for $T \to \infty$ and $N \to \infty$, respectively, the process is called *ergodic*. The mean $E[x(t)]$ is also called the first moment of the stochastic process. The second moment is the auto correlation function

$$R(t, \tau) = E[x(t)x(t+\tau)], \tag{C.74}$$

which can be estimated using the sample mean.

If both mean and autocorrelation are time independent, the autocorrelation only depends on the time difference, i.e. $R(t, \tau) = R(\tau)$. In this case, the

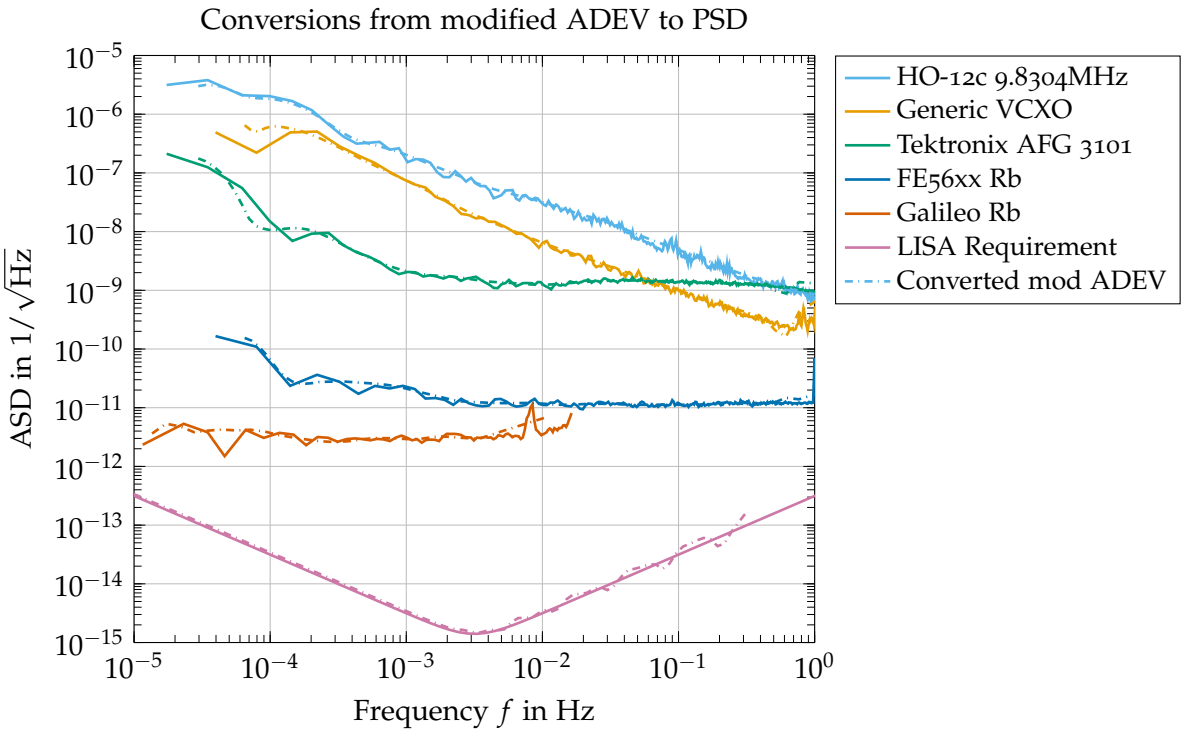

FIGURE C.12: Comparison between PSD directly computed from frequency data and converted modified Allan variance for some selected oscillators. The free parameter was chosen to be $\lambda = 0.3$.

process is called wide sense stationary (WSS). If it is also ergodic, we can calculate $R(\tau)$ using the time average. We then get

$$R(\tau) = \lim_{T\to\infty} \frac{1}{T} \int_{-T/2}^{T/2} x(t)x(t+\tau)\,\mathrm{d}t \tag{C.75}$$

for the autocorrelation function.

One can also define higher moments as the statistical expectation of higher powers of $x(t)$, which can also be time-dependent. If all of them are static, the process under investigation is called stationary.

C.9 (UN-)CORRELATED NOISE

Usually, the total noise in a signal has different physical origins, such that the total signal can be written as the sum of two or more signals:

$$V(t) = V_1(t) + V_2(t), \tag{C.76}$$

where $V_1(t)$ and $V_2(t)$ are both contaminated with their own noise, described by the PSDs S_{V_1} and S_{V_2}. Now the question arrises how the PSD S_V is related to S_{V_1} and S_{V_2}. The PSD is defined as the Fourier transform of the autocorrelation function R. We have

$$R_V(\tau) = \lim_{T\to\infty} \frac{1}{T} \int_{-T/2}^{T/2} V(t)V(t+\tau)\,\mathrm{d}t \tag{C.77}$$

$$= \lim_{T\to\infty} \frac{1}{T} \int_{-T/2}^{T/2} (V_1+V_2)(t)(V_1+V_2)(t+\tau)\,\mathrm{d}t \tag{C.78}$$

$$= \lim_{T\to\infty} \frac{1}{T} \Big(\int_{-T/2}^{T/2} V_1(t)V_1(t+\tau)\,\mathrm{d}t + \int_{-T/2}^{T/2} V_2(t)V_2(t+\tau)\,\mathrm{d}t + \int_{-T/2}^{T/2} V_1(t)V_2(t+\tau)\,\mathrm{d}t + \int_{-T/2}^{T/2} V_2(t)V_1(t+\tau)\,\mathrm{d}t \Big) \tag{C.79}$$

$$= R_{V_1} + R_{V_2} + R_{V_1,V_2} + R_{V_2,V_1}, \tag{C.80}$$

where

$$R_{V_1,V_2} = \lim_{T\to\infty} \frac{1}{T} \int_{-T/2}^{T/2} V_1(t)V_2(t+\tau)\,\mathrm{d}t \tag{C.81}$$

is defined to be the cross correlation function[14] of V_1 and V_2. Using this in conjunction with the definition of the PSD eq. (C.7), we get

$$S_V = S_{V_1} + S_{V_2} + S_{V_1,V_2} + S_{V_2,V_1} \tag{C.82}$$

for the PSD of the total signal. S_{V_1,V_2} is the so-called cross spectral density (CSD), defined as the Fourier transform of the cross correlation function.

Since R_{V_1,V_2} is not necessarily an even function, the cross spectral density (CSD) S_{V_1,V_2} is not guaranteed to be real. One can show, though, that

$$S_{V_1,V_2}(f) = S^*_{V_2,V_1}(f), \tag{C.83}$$

such that $S_{V_1,V_2} + S_{V_2,V_1}$ is indeed real. In fact, we can write

$$S_V = S_{V_1} + S_{V_2} + 2\,\mathrm{Re}\left[S_{V_1,V_2}\right] = S_{V_1} + S_{V_2} + 2\,\mathrm{Re}\left[S_{V_2,V_1}\right], \tag{C.84}$$

as argued in [29].

If V_1 and V_2 are uncorrelated, their CSD vanishes, such that we simply have

$$S_V = S_{V_1} + S_{V_2} \tag{C.85}$$

for the combined signal.

Some care must be taken when using the ASD instead of the PSD, since eq. (C.85) implies that

$$\mathrm{ASD}_V = \sqrt{S_V} = \sqrt{S_{V_1} + S_{V_2}} = \sqrt{\mathrm{ASD}_{V_1}^2 + \mathrm{ASD}_{V_2}^2}, \tag{C.86}$$

again assuming uncorrelated noise. This is often abbreviated by saying that noise adds quadratically.

14 Assuming that both V_1 and V_2 are real valued and wide-sense stationary.

D

NOISE MODELS

In this appendix, we describe the different noise sources that we simulate within `LISANode`. In particular for each noise, we give a short description and its mathematical expression. That includes spectral shapes in the form of their PSD for stochastic terms, as well as any deterministic effects.

The noise models are derived from allocations or current best estimates (CBEs) given in the performance model [39], where applicable. They are expressed originally in terms of acceleration, displacement or frequency fluctuations. We give explicitly the conversion to the units used in this document, i.e., timing jitter for all pathlength fluctuation noises, and phase for laser noise.

We give here a continuous description of these noise models; however, they are actually implemented as discrete noise sources at f_s^{phy}.

This appendix is adapted from [16], and was written in close collaboration with J.-B. Bayle.

We remark that some of the noise sources are not matching the CBE given in [39], and need to be updated.

D.1 LASER NOISE

Laser noise describes the optical phase fluctuations in the electromagnetic field of a free-running laser stabilized to a cavity.

Laser noise is given in [39][1] by the allocation for the *laser frequency stability* in units of frequency,

$$S_{\dot{N}^p}(f) = \left(30\,\text{Hz}/\sqrt{\text{Hz}}\right)^2 \left[1 + \left(\frac{2\times 10^{-3}\,\text{Hz}}{f}\right)^4\right]. \tag{D.1}$$

In the current simulation, we neglect the $1/f^4$ term, and approximate the now constant laser frequency stability to $28.2\,\text{Hz}/\sqrt{\text{Hz}}$, which corresponds to a fractional frequency stability of exactly 10^{-13}. In terms of phase noise N^p, this equates to

$$S_{N^p}(f) = \left(4.49\,\text{Hz}/\sqrt{\text{Hz}}\right)^2 f^{-2}. \tag{D.2}$$

This should be updated in a future version of the simulation.

1 In [39], laser noise is called $\tilde{s}_\nu$.

D.2 MODULATION NOISE

Modulation noise describes any mismatch in the phase of the modulation sidebands which are transmitted to the distant spacecraft and the pilot tone used as a local timing reference. For more information on the technical details of the frequency distribution system, cf. section 3.7 and chapter 6, or the literature, e.g. [14].

Both the 2.4 GHz and the 2.401 GHz sideband signals used for modulation are generated from the local USO. The pilot tone is derived from the electrical 2.4 GHz signal using a series of low noise frequency dividers. As such, the 2.4 GHz signal has lower noise with respect to the pilot tone then the 2.401 GHz signal. We will not model the noise of the frequency dividers, and at the moment assume that all modulation noises have the same spectral shape. The optical modulation is performed using an EOM followed by a fibre amplifier.

According to [14], the fiber amplifier is the dominating part. We fit a rough model to the blue curve in fig. 5.13 in [14] to obtain a timing jitter power spectral density of

$$S_M(f) = \left(1 \times 10^{-14}\,\mathrm{s}/\sqrt{\mathrm{Hz}}\right)^2 \left[1 + \left(\frac{1.5 \times 10^{-2}\,\mathrm{Hz}}{f}\right)^2\right]. \tag{D.3}$$

We remark that this is an *underestimate* compared to the more recent measurements presented in chapter 6. The reason for this discrepancy is that the blue curve in fig. 5.13 in [14] corresponds to a 1 W fibre amplifier, allowing lower noise levels. This noise level should be updated in a future version of the simulation.

D.3 TEST-MASS ACCELERATION NOISE

Test-mass acceleration noise describes the optical pathlength variations due to the test-mass motion away from its nominal position inside its housing.

The acceleration of the test mass is given in [39][2] by the allocation value for the *single test-mass acceleration noise* in acceleration units,

$$\left(2.4 \times 10^{-15}\,\mathrm{ms}^{-2}/\sqrt{\mathrm{Hz}}\right)^2 \left[1 + \left(\frac{0.4 \times 10^{-3}\,\mathrm{Hz}}{f}\right)^2\right] \left[1 + \left(\frac{f}{8 \times 10^{-3}\,\mathrm{Hz}}\right)^4\right]. \tag{D.4}$$

The equivalent pathlength fluctuation picks up a factor two in order to account for the beam reflection onto the test mass. In the simulation, we neglect high-frequency components since they are far smaller than the OMS displacement noise, c.f. appendix D.5. Moreover, we whiten the noise at below 10^{-14} Hz to prevent numerical overflow.

2 In [39], the acceleration of the test mass is called S_g.

Converting to timing jitter using a factor $1/(2\pi f)^4 c^2$, we get

$$S_{N^\delta}(f) = \left(\frac{4.05\times10^{-25}\,\mathrm{s}^{-1}/\sqrt{\mathrm{Hz}}}{f^2}\right)^2\left[1+\left(\frac{0.4\times10^{-3}\,\mathrm{Hz}}{f}\right)^2\right]. \quad \text{(D.5)}$$

Note that this is an this is an out-of-loop value, ignoring the coupling of test-mass to spacecraft motion introduced by DFACS. This is to be updated and consolidated once spacecraft dynamics are properly implemented in the simulation.

D.4 BACKLINK NOISE

Beams are transmitted between adjacent optical benches using optical fibres. During this transmission, the beams can pick up an additional phase noise term. We model only the non-reciprocal noise terms, i.e., the difference between the phase shift of a beam propagating from optical bench i to i' vs. that of the beam propagating from i' to i.

Backlink noise is given in [39][3] by the allocation for the *reference backlink* in displacement,

$$S_{N^{\mathrm{bl}}}(f) = \left(3\times10^{-12}\,\mathrm{mHz}^{0.5}\right)^2\left[1+\left(\frac{2\times10^{-3}\,\mathrm{Hz}}{f}\right)^4\right]. \quad \text{(D.6)}$$

Contrary to what is present in [39], we use the same value for both the test-mass and the reference interferometers. The equivalent timing jitter power spectral density $S_{N^{\mathrm{bl}}}(f)$ can be computed by dividing by c, and reads

$$S_{N^{\mathrm{bl}}}(f) = \left(1\times10^{-20}\,\mathrm{sHz}^{0.5}\right)^2\left[1+\left(\frac{2.0\times10^{-3}\,\mathrm{Hz}}{f}\right)^4\right]. \quad \text{(D.7)}$$

D.5 READOUT NOISE

We summarize as readout noise N^{ro} the equivalent positional readout error in meters due to technical noise sources such as shot noise. For it's value, we use the overall entry for OMS displacement noise in [39].

OMS displacement noise is given in [39] as the allocation value for the *long-arm noise*, *test-mass ifo noise* and *reference noise* in terms of displacement, by a power spectral density of the form

$$S_{N^{\mathrm{ro}}}(f) = A^2\left[1+\left(\frac{2\times10^{-3}\,\mathrm{Hz}}{f}\right)^4\right], \quad \text{(D.8)}$$

where A depends on the interferometer,

- inter-spacecraft interferometer carrier: $A = 6.35\times10^{-12}\,\mathrm{m}/\sqrt{\mathrm{Hz}}$,

3 In [39], the backlink noise is called $\tilde{s}_{\mathrm{Ref,back}}$.

- inter-spacecraft interferometer sideband: $A = 1.25 \times 10^{-11}\,\mathrm{m}/\sqrt{\mathrm{Hz}}$,
- test-mass interferometer: $A = 1.42 \times 10^{-12}\,\mathrm{m}/\sqrt{\mathrm{Hz}}$.
- reference interferometer carrier: $A = 3.32 \times 10^{-12}\,\mathrm{m}/\sqrt{\mathrm{Hz}}$,
- reference interferometer sideband: $A = 7.90 \times 10^{-12}\,\mathrm{m}/\sqrt{\mathrm{Hz}}$,

In `LISANode`, we simulate both carriers and sideband. Since there are no values given for the sideband beatnotes, we approximate them using $\epsilon = 0.15$ instead of $\epsilon = 0.85$ in the shot noise formula in [39] to account for the lower power level.

We converted to timing jitter by dividing by c, to get:

- inter-spacecraft interferometer carrier: $A = 2.12 \times 10^{-20}\,\mathrm{s}/\sqrt{\mathrm{Hz}}$,
- inter-spacecraft interferometer sideband: $A = 4.17 \times 10^{-20}\,\mathrm{s}/\sqrt{\mathrm{Hz}}$,
- test-mass interferometer: $A = 4.73 \times 10^{-21}\,\mathrm{s}/\sqrt{\mathrm{Hz}}$,
- reference interferometer carrier: $A = 1.11 \times 10^{-20}\,\mathrm{s}/\sqrt{\mathrm{Hz}}$,
- reference interferometer sideband: $A = 2.63 \times 10^{-20}\,\mathrm{s}/\sqrt{\mathrm{Hz}}$.

Note that the OMS displacement noise as given in [39] summarizes multiple noise sources, some of which are already otherwise accounted for, such as backlink noise. Therefore, these values should be updated in a future version of the simulation.

D.6 OPTICAL BENCH PATHLENGTH NOISE

Optical bench pathlength noise N^{ob} summarizes different optical pathlength noises due to, for example, jitters of optical components in the path of the different beams. It is modelled as a optical pathlength change in meters, with values based on [39].

Optical bench pathlength noise in terms of displacement is given by a power spectral density of the form

$$S_{N^{\mathrm{ob}}}(f) = A^2\,, \tag{D.9}$$

where A depends on the beam,

- local beams in the test-mass interferometers: $A = 4.24 \times 10^{-12}\,\mathrm{m}/\sqrt{\mathrm{Hz}}$,
- local beams in the reference interferometers: $A = 2 \times 10^{-12}\,\mathrm{m}/\sqrt{\mathrm{Hz}}$,
- all other beams: $A = 1 \times 10^{-15}\,\mathrm{m}/\sqrt{\mathrm{Hz}}$.

We converted to timing jitter by dividing by c, to get:

- local beams in the test-mass interferometers: $A = 1.4 \times 10^{-20}\,\mathrm{s}/\sqrt{\mathrm{Hz}}$,
- local beams in the reference interferometers: $A = 6.7 \times 10^{-21}\,\mathrm{s}/\sqrt{\mathrm{Hz}}$,
- all other beams: $A = 3.3 \times 10^{-24}\,\mathrm{m}/\sqrt{\mathrm{Hz}}$.

D.7 RANGING NOISE

Pseudo-ranging is performed by correlating local and distant PRN signals, c.f. section 6.3. Ranging noise describes the imperfection of the overall ranging measurement scheme in a single link.

Pseudo-ranging is given by an ad-hoc model, combining a systematic bias $N_i^{R,o}$ and a zero-mean stochastic Gaussian white noise $N_i^{R,\epsilon}(\tau_i)$,

$$N_i^R(\tau_i) = N_i^{R,o} + N_i^{R,\epsilon}(\tau_i)\,, \tag{D.10}$$

with default values of $S_{N^{R,\epsilon}} = 3 \times 10^{-9}\,\mathrm{s}/\sqrt{\mathrm{Hz}}$ (or $0.9\,\mathrm{m}/\sqrt{\mathrm{Hz}}$), and $N_i^{R,o} = 0\,\mathrm{s}$.

D.8 CLOCK NOISE

USOs on each spacecraft act as central time references for all onboard systems, and therefore represent clocks ticking according to the on-board clock time (THE), c.f. section 6.1.1. Clock noise models any deviations of these clocks from the corresponding spacecraft proper time (TPS).

Clock noise is given by the model described in [81], expressed in terms of fractional frequency deviations as the sum

$$\dot{q}_i(\tau) = \dot{N}_i^q(\tau) + y_{0,i} + y_{1,i}\tau + y_{2,i}\tau^2\,. \tag{D.11}$$

with

$$y_0 \approx 5 \times 10^{-7}\,\mathrm{s\,s^{-1}}, \quad y_1 \approx 1.6 \times 10^{-14}\,\mathrm{s\,s^{-2}}, \quad y_2 \approx 9 \times 10^{-23}\,\mathrm{s\,s^{-3}}\,. \tag{D.12}$$

These values should be seen as orders of magnitude, and will be different for all 3 USOs.

We use

- $\dot{N}_i^q(\tau)$ is a random jitter, generated as a flicker noise with a PSD between $10^{-5}\,\mathrm{Hz}$ and $f_s^{\mathrm{phy}}/2 = 1.5\,\mathrm{Hz}$ given by

$$S_{\dot{N}_i^q}(f) = \left(6.32 \times 10^{-14}\right)^2 f^{-1}\,, \tag{D.13}$$

- $y_{0,i}$ a constant deterministic frequency offset, by default set to 5×10^{-8}, 6.25×10^{-7}, and -3.75×10^{-7} for the 3 spacecraft clocks,
- $y_{1,i}$ a constant frequency linear drift, by default set to $8 \times 10^{-16}\,\mathrm{s^{-1}}$, $1 \times 10^{-14}\,\mathrm{s^{-1}}$, and $-6 \times 10^{-15}\,\mathrm{s^{-1}}$ for the 3 spacecraft clocks, and
- $y_{2,i}$ a constant frequency quadratic drift, by default set to $3 \times 10^{-24}\,\mathrm{s^{-2}}$, $2.25 \times 10^{-23}\,\mathrm{s^{-2}}$, and $-3.75 \times 10^{-23}\,\mathrm{s^{-2}}$ for the 3 spacecraft clocks.

Expressed as a timing jitter, clock noise reads

$$q_i(\tau) = N_i^q(\tau) + y_{0,i}\tau + \frac{1}{2}y_{1,i}\tau^2 + \frac{1}{3}y_{2,i}\tau^3\,, \tag{D.14}$$

with $N_i^q(\tau)$ now a random timing jitter with a PSD of

$$S_{N_i^q}(f) = \left(1 \times 10^{-14}\right)^2 f^{-3}. \tag{D.15}$$

ACKNOWLEDGMENTS

First, I want to thank Prof. Dr. Karsten Danzmann as director of the AEI, for having created a fantastic work environment, as well as for his enthusiastic lectures which first brought my attention to his institute. I'm equally grateful to apl. Prof. Dr. Gerhard Heinzel for giving me the opportunity to join his space interferometry group, despite the fact that I knew very little about interferometry before starting my Ph.D. His insights, kindness and patience have taught me invaluable lessons.

I also want to thank Maître de Conférences Dr. Antoine Petiteau and Dr. Martin Hewitson for co-supervising my thesis, and Prof. Dr. Guido Müller for agreeing to act as referee alongside Gerhard and Antoine. I'm also grateful to Prof. Dr. Klemens Hammerer, who agreed to chair my defense on short notice!

LISA is a large international collaboration, such that I had the opportunity to work closely with people from all over the world while developing this thesis – this has been a truly great experience. I want to thank all the members of the LISA Instrument and Data Processing groups for the countless discussions, and in particular, I want to thank those with whom I've had the pleasure to collaborate on publications (or am in the process of doing so).

Special thanks to Jean-Baptiste for our close collaboration over most of my Ph.D., and his inexplicable ability to turn barely readable equations and sometimes *very* rough ideas into beautiful presentations and fully functional python programs.

I also want to thank all the members of the AEI, in particular the space interferometry group. It is a great place to do a Ph.D., from the excellent lecture week program and plentiful social events to the overall friendly, positive but also professional work environment.

I'm especially grateful to Vitali for introducing me to the AEI space interferometry group, and teaching me many things about laser interferometery, signal processing, programming and experimental work.

To all the people who agreed to read parts of my thesis, and provided invaluable comments and corrections – Jean-Baptiste, both Martin S. and H., Marc, Martina, Niklas, Thomas and Vitali, thank you! I would have never caught all the errors you found.

Before joining the AEI, many people have of course left impressions without whom I would have not arrived at this point – too many to list. I want to extend special thanks to my family for always supporting me, and to my brother, whose genuine passion for physics and science always inspired me. I'm incredibly grateful to Martina, who gave me the strength to not lose my

sanity in the final years of the PhD, and made the otherwise so turbulent year 2020 a time I can think back to with a smile.

I gratefully acknowledge support by the Max-Planck Society and the Deutsches Zentrum für Luft- und Raumfahrt (DLR), with funding from the Bundesministerium für Wirtschaft und Technologie. I'm also grateful for the opportunity to spend a few weeks in China during my Ph.D., supported by the Max-Planck-Society within the LEGACY ("Low-Frequency Gravitational Wave Astronomy in Space") collaboration.

CURRICULUM VITÆ

PERSONAL INFORMATION

Name	Olaf Hartwig
Born	November 15th, 1985 in Osnabrück, Germany
Email	olaf.hartwig@aei.mpg.de

EDUCATION

2016-2021	Ph.D. candidate in physics Max-Planck Institute for Gravitational Physics, Hannover, Germany Thesis: *Instrumental modelling and noise reduction algorithms for the Laser Interferometer Space Antenna*
2015	M. Sc. in physics Universität Hannover, Germany Thesis: *Yang-Mills Theory on Coset Spaces with antisymmetric Torsion*
2012	B. Sc. in physics Universität Hannover, Germany Thesis: *Der klassische Limes in der Quantenmechanik*
2005	General qualification for university entrance (Abitur) Gymnasium Langenhagen

PUBLICATIONS

2021	*Adapting time-delay interferometry for LISA data in frequency* Jean-Baptiste Bayle, Olaf Hartwig and Martin Staab, accepted for publication in Phys. Rev. D.
2021	*Clock-jitter reduction in LISA time-delay interferometry combinations* Olaf Hartwig and Jean-Baptiste Bayle, Phys. Rev. D 103, 123027 – Published 28 June 2021
2018	*Time-delay interferometry and clock-noise calibration* Massimo Tinto and Olaf Hartwig, Phys. Rev. D 98, 042003 – Published 21 August 2018

BIBLIOGRAPHY

[1] Clock product from the multi-gnss experiment provided by the gfz potsdam, hosted at the crustal dynamics data information system (cddis). ftp://cddis.gsfc.nasa.gov/gnss/products/mgex/1929/.

[2] Standard definitions of physical quantities for fundamental frequency and time metrology–random instabilities, 2009.

[3] J. Aasi et al. Advanced LIGO. *Class. Quant. Grav.*, 32:074001, 2015.

[4] B. P. Abbott et al. A First Targeted Search for Gravitational-Wave Bursts from Core-Collapse Supernovae in Data of First-Generation Laser Interferometer Detectors. *Phys. Rev. D*, 94(10):102001, 2016.

[5] B. P. Abbott et al. Observation of gravitational waves from a binary black hole merger. *Phys. Rev. Lett.*, 116:061102, Feb 2016.

[6] B. P. Abbott et al. Prospects for Observing and Localizing Gravitational-Wave Transients with Advanced LIGO, Advanced Virgo and KAGRA. *Living Rev. Rel.*, 21(1):3, 2018.

[7] B. P. Abbott et al. GWTC-1: A Gravitational-Wave Transient Catalog of Compact Binary Mergers Observed by LIGO and Virgo during the First and Second Observing Runs. *Phys. Rev. X*, 9(3):031040, 2019.

[8] R. Abbott et al. GWTC-2: Compact Binary Coalescences Observed by LIGO and Virgo During the First Half of the Third Observing Run. 10 2020.

[9] Klaus Abich, Alexander Abramovici, Bengie Amparan, Andreas Baatzsch, Brian Bachman Okihiro, David C. Barr, Maxime P. Bize, Christina Bogan, Claus Braxmaier, Michael J. Burke, Ken C. Clark, Christian Dahl, Katrin Dahl, Karsten Danzmann, Mike A. Davis, Glenn de Vine, Jeffrey A. Dickson, Serge Dubovitsky, Andreas Eckardt, Thomas Ester, Germán Fernández Barranco, Reinhold Flatscher, Frank Flechtner, William M. Folkner, Samuel Francis, Martin S. Gilbert, Frank Gilles, Martin Gohlke, Nicolas Grossard, Burghardt Guenther, Philipp Hager, Jerome Hauden, Frank Heine, Gerhard Heinzel, Mark Herding, Martin Hinz, James Howell, Mark Katsumura, Marina Kaufer, William Klipstein, Alexander Koch, Micah Kruger, Kameron Larsen, Anton Lebeda, Arnold Lebeda, Thomas Leikert, Carl Christian Liebe, Jehhal Liu, Lynette Lobmeyer, Christoph Mahrdt, Thomas Mangoldt, Kirk McKenzie, Malte Misfeldt, Phillip R. Morton, Vitali Müller, Alexander T. Murray, Don J. Nguyen, Kolja Nicklaus, Robert Pierce, Joshua A. Ravich, Gretchen Reavis, Jens Reiche, Josep Sanjuan, Daniel Schütze, Christoph Seiter, Daniel Shaddock, Benjamin Sheard, Michael Sileo, Robert Spero, Gary Spiers, Gunnar Stede, Michelle Stephens, Andrew Sutton, Joseph

Trinh, Kai Voss, Duo Wang, Rabi T. Wang, Brent Ware, Henry Wegener, Steve Windisch, Christopher Woodruff, Bernd Zender, and Marcus Zimmermann. In-orbit performance of the grace follow-on laser ranging interferometer. *Phys. Rev. Lett.*, 123:031101, Jul 2019.

[10] Pau Amaro-Seoane et al. Laser Interferometer Space Antenna. Technical report, ESA, February 2017.

[11] M.-C. Angonin, J.-B. Bayle, O. Hartwig, Aurélien Hees, Marc Lilley, C. Le Poncin-lafitte, and P. Wolf. LISA Orbit, Time and Frequency Transfer Simulation Model. Technical report, 2020.

[12] M. Armano, H. Audley, J. Baird, P. Binetruy, M. Born, D. Bortoluzzi, E. Castelli, A. Cavalleri, A. Cesarini, A. M. Cruise, K. Danzmann, M. de Deus Silva, I. Diepholz, G. Dixon, R. Dolesi, L. Ferraioli, V. Ferroni, E. D. Fitzsimons, M. Freschi, L. Gesa, F. Gibert, D. Giardini, R. Giusteri, C. Grimani, J. Grzymisch, I. Harrison, G. Heinzel, M. Hewitson, D. Hollington, D. Hoyland, M. Hueller, H. Inchauspé, O. Jennrich, P. Jetzer, N. Karnesis, B. Kaune, N. Korsakova, C. J. Killow, J. A. Lobo, I. Lloro, L. Liu, J. P. López-Zaragoza, R. Maarschalkerweerd, D. Mance, N. Meshksar, V. Martín, L. Martin-Polo, J. Martino, F. Martin-Porqueras, I. Mateos, P. W. McNamara, J. Mendes, L. Mendes, M. Nofrarias, S. Paczkowski, M. Perreur-Lloyd, A. Petiteau, P. Pivato, E. Plagnol, J. Ramos-Castro, J. Reiche, D. I. Robertson, F. Rivas, G. Russano, J. Slutsky, C. F. Sopuerta, T. Sumner, D. Texier, J. I. Thorpe, D. Vetrugno, S. Vitale, G. Wanner, H. Ward, P. J. Wass, W. J. Weber, L. Wissel, A. Wittchen, and P. Zweifel. Lisa pathfinder platform stability and drag-free performance. *Phys. Rev. D*, 99:082001, Apr 2019.

[13] S. Babak, A. Petiteau, A. Sesana, P. Brem, P. A. Rosado, S. R. Taylor, A. Lassus, J. W. T. Hessels, C. G. Bassa, M. Burgay, R. N. Caballero, D. J. Champion, I. Cognard, G. Desvignes, J. R. Gair, L. Guillemot, G. H. Janssen, R. Karuppusamy, M. Kramer, P. Lazarus, K. J. Lee, L. Lentati, K. Liu, C. M. F. Mingarelli, S. Osłowski, D. Perrodin, A. Possenti, M. B. Purver, S. Sanidas, R. Smits, B. Stappers, G. Theureau, C. Tiburzi, R. van Haasteren, A. Vecchio, and J. P. W. Verbiest. European Pulsar Timing Array limits on continuous gravitational waves from individual supermassive black hole binaries. *Monthly Notices of the Royal Astronomical Society*, 455(2):1665–1679, January 2016.

[14] Simon Barke. *Inter-Spacecraft Frequency Distribution for Future Gravitational Wave Observatories*. PhD thesis, Gottfried Wilhelm Leibniz Universität Hannover, 2015.

[15] Simon Barke, Nils Brause, Iouri Bykov, Esteban Delgado, Juan Jose, Anders Enggaard, Oliver Gerberding, Gerhard Heinzel, Joachim Kullmann, Sören Möller Pedersen, et al. Lisa metrology system-final report. 2014.

[16] J.-B. Bayle and O. Hartwig. Lisa simulation model. Technical report, LISA Consortium TN, 2020.

[17] J.B. Bayle. Lisa instrument. `https://gitlab.in2p3.fr/lisa-simulation/instrument`, 2021.

[18] J.B. Bayle, O. Hartwig, M. Lilley, and A. Petiteau. Lisanode. `https://gitlab.in2p3.fr/j2b.bayle/LISANode`, 2021.

[19] J.B. Bayle, A. Hees, and M. Lilley. Lisa orbits. `https://gitlab.in2p3.fr/lisa-simulation/orbits`, 2020.

[20] Jean-Baptiste Bayle. *Simulation and Data Analysis for LISA: Instrumental Modeling, Time-Delay Interferometry, Noise-Reduction Performance Study, and Discrimination of Transient Gravitational Signals*. PhD thesis, Université de Paris, October 2019.

[21] Jean-Baptiste Bayle et al. Reference Systems, Conventions, and Notations for LISA. Technical report, 2020.

[22] Jean-Baptiste Bayle, Olaf Hartwig, and Antoine Petiteau. Time-delay interferometry – update on the ongoing studies. Presentation at the LISA Consortium Meeting 2019, Gainesville, 2019.

[23] Jean-Baptiste Bayle, Olaf Hartwig, and Martin Staab. Adapting time-delay interferometry for LISA data in frequency. *Phys. Rev. D (accepted)*, 2021.

[24] Jean-Baptiste Bayle, Marc Lilley, Antoine Petiteau, and Hubert Halloin. Effect of filters on the time-delay interferometry residual laser noise for LISA. *Phys. Rev.*, D99(8):084023, 2019.

[25] Joachim M. Bestenlehner, Paul A. Crowther, Saida M. Caballero-Nieves, Fabian R. N. Schneider, Sergio Simón-Díaz, Sarah A. Brands, Alex de Koter, Götz Gräfener, Artemio Herrero, Norbert Langer, Daniel J. Lennon, Jesus Maíz Apellániz, Joachim Puls, and Jorick S. Vink. The R136 star cluster dissected with Hubble Space Telescope/STIS - II. Physical properties of the most massive stars in R136. *Monthly Notices of the Royal Astronomical Society*, 499(2):1918–1936, December 2020.

[26] Luigi Cacciapuoti. Atomic clock ensemble in space mission status, 03 2017. Talk at Rencontres de Moriond 2017 - Gravitation, La Thuile.

[27] NASA Goddard Space Flight Center. The gravitational wave spectrum, sources and detectors. `http://science.gsfc.nasa.gov/663/research/index.html`. Accessed: 2021-04-17.

[28] The Consortium, P. Seoane, Sofiane Aoudia, H. Audley, Georgia Auger, Svitlana Babak, J. Baker, E. Barausse, Simon Barke, Massimo Bassan, Volker Beckmann, Matthew Benacquista, P. Bender, E. Berti, P. Binétruy, J. Bogenstahl, C. Bonvin, D. Bortoluzzi, N. Brause, and Peter Zweifel. The gravitational universe : a white paper on the gravitationnal waves detection and characterization in space using million kilometers laser interferometry. *http://arxiv.org/abs/1305.5720*, 05 2013.

[29] Wilbur B.jun. Davenport and William L. Root. *Introduction to the theory of random signals and noise. Repr.* Piscataway, NJ: IEEE, repr. edition, 1987.

[30] Glenn de Vine, Brent Ware, Kirk McKenzie, Robert E. Spero, William M. Klipstein, and Daniel A. Shaddock. Experimental demonstration of time-delay interferometry for the laser interferometer space antenna. *Phys. Rev. Lett.*, 104:211103, May 2010.

[31] Vladimir Dergachev and Maria Alessandra Papa. Results from the First All-Sky Search for Continuous Gravitational Waves from Small-Ellipticity Sources. *Phys. Rev. Lett.*, 125(17):171101, 2020.

[32] S. V. Dhurandhar, K. Rajesh Nayak, and J.-Y. Vinet. Algebraic approach to time-delay data analysis for lisa. *Phys. Rev. D*, 65:102002, May 2002.

[33] Albert Einstein. Über Gravitationswellen. *Sitzungsber. Preuss. Akad. Wiss. Berlin (Math. Phys.)*, 1918:154–167, 1918.

[34] Juan Jose Esteban Delgado. *Laser Ranging and Data Communication for the Laser Interferometer Space Antenna*. PhD thesis, Gottfried Wilhelm Leibniz Universität Hannover, January 2012.

[35] Ewan Fitzsimons. Lisa-ukob-inst-tn-004: Lisa tilt-to-length and optical alignment analysis. Technical report, 2020.

[36] Oliver Gerberding. *Phase readout for satellite interferometry*. PhD thesis, Gottfried Wilhelm Leibniz Universität Hannover, 2014.

[37] Domenico Giulini. Differentialgeometrie für physiker. `https://qig.itp.uni-hannover.de/~giulini/papers/Skript-Differentialgeometrie.pdf`, June 2020.

[38] Domenico Giulini and Claus Kiefer. *Gravitationswellen*. 01 2017.

[39] LISA Performance Working Group. Lisa performance model and error budget (lisa-lcst-inst-tn-003). Technical report, June 2018.

[40] Habib Hajimolahoseini, Mohammad Reza Taban, and Hamid Soltanian-Zadeh. Extended kalman filter frequency tracker for nonstationary harmonic signals, 01 2012.

[41] H. Halloin. Note on decimation and interpolation filters for lisa simulation. Technical report, 2018.

[42] Olaf Hartwig. Different measures of frequency stability. Technical report, Max-Planck Institute for Gravitational Physics (Albert Einstein Institute), 2017.

[43] Olaf Hartwig and Jean-Baptiste Bayle. Clock-jitter reduction in lisa time-delay interferometry combinations. *Phys. Rev. D*, 103:123027, Jun 2021.

[44] G. Heinzel. Laser interferometry, 2014. Lecture at the University of Hannover.

[45] Gerhard Heinzel. Generation of random time series with prescribed spectra. 2006.

[46] Gerhard Heinzel. Lisa frequency planning. Technical report, Max-Planck Institute for Gravitational Physics (Albert Einstein Institute), 2018.

[47] Gerhard Heinzel. Lisa data rates. Technical report, Max-Planck Institute for Gravitational Physics (Albert Einstein Institute), 2020.

[48] Gerhard Heinzel, Miguel Dovale Álvarez, Alvise Pizzella, Nils Brause, and Juan José Esteban Delgado. Tracking length and differential-wavefront-sensing signals from quadrant photodiodes in heterodyne interferometers with digital phase-locked-loop readout. *Phys. Rev. Applied*, 14:054013, Nov 2020.

[49] Gerhard Heinzel, Albrecht Rüdiger, and Roland Schilling. Spectrum and spectral density estimation by the discrete fourier transform (dft), including a comprehensive list of window functions and some new flat-top windows. 2002.

[50] Gerhard Heinzel, Albrecht Rüdiger, and R Schilling. Spectrum and spectral density estimation by the discrete fourier transform (dft), including a comprehensive list of window functions and some new flat-top windows. *Max Plank Inst*, 12, 01 2002.

[51] Ronald W. Hellings. Elimination of clock jitter noise in space born laser interferometers. *Phys. Rev.*, D64:022002, 2001.

[52] Martin Hewitson. Lisa-lcst-inst-tn-012: Analytical ttl models for lisa. Technical report, 2021.

[53] Sergei Klioner, Robin Geyer, Hagen Steidelmüller, and Alexey Butkevich. Data timing, time transfer and on-board clock monitoring for space astrometry with gaia. *Space Science Reviews*, 212, 11 2017.

[54] M Laporte, H Halloin, E Bréelle, C Buy, P Grüning, and P Prat. Status of the LISA on table experiment: a electro-optical simulator for LISA. *Journal of Physics: Conference Series*, 840:012014, may 2017.

[55] LISA Instrument Group. LISA Payload Definition Document. Technical Report 2.1, 2018.

[56] LISA Science Study Team. LISA Science Requirements Document. Technical Report 1.0, ESA, May 2018. `https://www.cosmos.esa.int/web/lisa/lisa-documents/`.

[57] Andrew D Ludlow, Martin M Boyd, Jun Ye, Ekkehard Peik, and Piet O Schmidt. Optical atomic clocks. *Reviews of Modern Physics*, 87(2):637, 2015.

[58] Charles W. Misner, K. S. Thorne, and J. A. Wheeler. *Gravitation*. W. H. Freeman, San Francisco, 1973.

[59] Shawn J. Mitryk, Guido Mueller, and Josep Sanjuan. Hardware-based demonstration of time-delay interferometry and tdi-ranging with spacecraft motion effects. *Phys. Rev. D*, 86:122006, Dec 2012.

[60] Peter J. Mohr, David B. Newell, and Barry N. Taylor. Codata recommended values of the fundamental physical constants: 2014. *Rev. Mod. Phys.*, 88:035009, Sep 2016.

[61] Oliver Montenbruck, Peter Steigenberger, Lars Prange, Zhiguo Deng, Qile Zhao, Felix Perosanz, Ignacio Romero, Carey Noll, Andrea Stürze, Georg Weber, Ralf Schmid, Ken MacLeod, and Stefan Schaer. The multi-gnss experiment (mgex) of the international {GNSS} service (igs) – achievements, prospects and challenges. *Advances in Space Research*, 59(7):1671 – 1697, 2017.

[62] Martina Muratore. *Time delay interferometry for LISA science and instrument characterization*. PhD thesis, University of Trento, 2021.

[63] Martina Muratore, Daniele Vetrugno, and Stefano Vitale. Revisitation of time delay interferometry combinations that suppress laser noise in LISA. *Classical and Quantum Gravity*, 37(18):185019, aug 2020.

[64] Markus Otto. *Time-Delay Interferometry Simulations for the Laser Interferometer Space Antenna*. PhD thesis, Gottfried Wilhelm Leibniz Universität Hannover, December 2015.

[65] Huisheng Peng, Daoyong Chen, Jian Huang, Satish Chikkannanavar, Jens Hänisch, Menka Jain, Dean Peterson, S Doorn, Yunfeng Lu, Yuntian Zhu, and Quanxi Jia. Strong and ductile colossal carbon tubes with walls of rectangular macropores. *Physical review letters*, 101:145501, 11 2008.

[66] Antoine Petiteau, Gerard Auger, Hubert Halloin, Olivier Jeannin, Eric Plagnol, Sophie Pireaux, Tania Regimbau, and Jean-Yves Vinet. LISACode: A Scientific simulator of LISA. *Phys. Rev. D*, 77:023002, 2008.

[67] Stephane Plaszczynski. Generating long streams of $1/f^{\alpha}$ noise. *Fluct. Noise Lett.*, 7:R1–R13, 2007.

[68] K Rajesh Nayak, S Koshti, S V Dhurandhar, and Jean-Yves Vinet. On the minimum flexing of LISAs arms. *Class. Quant. Grav.*, 23:1763–1800, February 2006.

[69] K. Rajesh Nayak and J. Y. Vinet. Algebraic approach to time-delay data analysis for orbiting LISA. 11 2004.

[70] W.J. Riley, Physics Laboratory (U.S.). Time, and Frequency Division. *Handbook of Frequency Stability Analysis*. NIST special publication. U.S. Department of Commerce, National Institute of Standards and Technology, 2008.

[71] Joseph D. Romano and Neil J. Cornish. Detection methods for stochastic gravitational-wave backgrounds: a unified treatment. *Living Rev. Rel.*, 20(1):2, 2017.

[72] Enrico Rubiola. *Phase noise and frequency stability in oscillators*. Cambridge University Press, 2008.

[73] Bernard F. Schutz. *A FIRST COURSE IN GENERAL RELATIVITY*. Cambridge Univ. Pr., Cambridge, UK, 1985.

[74] Thomas S. Schwarze, Germán Fernández Barranco, Daniel Penkert, Marina Kaufer, Oliver Gerberding, and Gerhard Heinzel. Picometer-stable hexagonal optical bench to verify lisa phase extraction linearity and precision. *Phys. Rev. Lett.*, 122:081104, Feb 2019.

[75] Alberto Sesana. Prospects for Multiband Gravitational-Wave Astronomy after GW150914. *Phys. Rev. Lett.*, 116(23):231102, 2016.

[76] D. A. Shaddock, B. Ware, R. E. Spero, and M. Vallisneri. Postprocessed time-delay interferometry for lisa. *Phys. Rev. D*, 70:081101, Oct 2004.

[77] Benjamin Sheard, G Heinzel, Karsten Danzmann, Daniel Shaddock, William Klipstein, and William Folkner. Intersatellite laser ranging instrument for the grace follow-on mission. *Journal of Geodesy*, 86:1083–1095, 2012.

[78] Dan Simon. *Optimal State Estimation*. John Wiley & Sons, Inc., jan 2006.

[79] Robert Spero, Brian Bachman, Glenn de Vine, Jeffrey Dickson, William Klipstein, Tetsuo Ozawa, Kirk McKenzie, Daniel Shaddock, David Robison, Andrew Sutton, and Brent Ware. Progress in interferometry for LISA at JPL. *Classical and Quantum Gravity*, 28(9):094007, apr 2011.

[80] B. Steltner, M. A. Papa, H. B. Eggenstein, B. Allen, V. Dergachev, R. Prix, B. Machenschalk, S. Walsh, S. J. Zhu, and S. Kwang. Einstein@Home All-sky Search for Continuous Gravitational Waves in LIGO O2 Public Data. *Astrophys. J.*, 909(1):79, 2021.

[81] The SYRTE Theory and Metrology group. Modeling for lisa. Technical report, 2020.

[82] Massimo Tinto and J. W. Armstrong. Cancellation of laser noise in an unequal-arm interferometer detector of gravitational radiation. *Phys. Rev. D*, 59:102003, 1999.

[83] Massimo Tinto and Sanjeev Dhurandhar. Time-delay interferometry. *Living Reviews in Relativity*, 24, 12 2021.

[84] Massimo Tinto, F. B. Estabrook, and J. W. Armstrong. Time delay interferometry for LISA. *Phys. Rev.*, D65:082003, 2002.

[85] Massimo Tinto, Frank B. Estabrook, and J. W. Armstrong. Time delay interferometry with moving spacecraft arrays. *Phys. Rev.*, D69:082001, 2004.

[86] Massimo Tinto and Olaf Hartwig. Time-delay interferometry and clock-noise calibration. *Phys. Rev. D*, 98:042003, Aug 2018.

[87] Massimo Tinto, Michele Vallisneri, and J. W. Armstrong. Time-delay interferometric ranging for space-borne gravitational-wave detectors. *Phys. Rev. D*, 71:041101, Feb 2005.

[88] Toray Composite Materials America, Inc. *T1100S - Intermediate Modules Carbon Fibre*, 5 2019. Rev. 3.

[89] Michael Tröbs and Gerhard Heinzel. Improved spectrum estimation from digitized time series on a logarithmic frequency axis. *Measurement*, 39:120–129, 02 2006.

[90] Maik Uhlemann, Gerd Gendt, Markus Ramatschi, and Zhiguo Deng. Gfz global multi-gnss network and data processing results, 2015.

[91] Wikimedia user Inductiveload. Psr b1913+16 period shift graph, 2010. Data from J. M. Weisberg and J. H. Taylor, Relativistic Binary Pulsar B1913+16: Thirty Years of Observations and Analysis, July 2004.

[92] Michele Vallisneri. Geometric time delay interferometry. *Phys. Rev.*, D72:042003, 2005. [Erratum: Phys. Rev.D76,109903(2007)].

[93] Michele Vallisneri. Synthetic LISA: Simulating time delay interferometry in a model LISA. *Phys. Rev. D*, 71:022001, 2005.

[94] Jean-Yves Vinet. Some basic principles of a "lisa". *Comptes Rendus Physique*, 14(4):366–380, 2013. Gravitational waves / Ondes gravitationnelles.

[95] Pauli Virtanen, Ralf Gommers, Travis E. Oliphant, Matt Haberland, Tyler Reddy, David Cournapeau, Evgeni Burovski, Pearu Peterson, Warren Weckesser, Jonathan Bright, Stéfan J. van der Walt, Matthew Brett, Joshua Wilson, K. Jarrod Millman, Nikolay Mayorov, Andrew R. J. Nelson, Eric Jones, Robert Kern, Eric Larson, C J Carey, İlhan Polat, Yu Feng, Eric W. Moore, Jake VanderPlas, Denis Laxalde, Josef Perktold, Robert Cimrman, Ian Henriksen, E. A. Quintero, Charles R. Harris, Anne M. Archibald, Antônio H. Ribeiro, Fabian Pedregosa, Paul van Mulbregt, and SciPy 1.0 Contributors. SciPy 1.0: Fundamental Algorithms for Scientific Computing in Python. *Nature Methods*, 17:261–272, 2020.

[96] Yan Wang. *On inter-satellite laser ranging, clock synchronization and gravitational wave data analysis*. PhD thesis, Gottfried Wilhelm Leibniz Universität Hannover, 2017.

[97] Gudrun Wanner and Nikolaos Karnesis and. Preliminary results on the suppression of sensing cross-talk in LISA pathfinder. *Journal of Physics: Conference Series*, 840:012043, may 2017.

[98] J. M. Weisberg and J. H. Taylor. The Relativistic Binary Pulsar B1913+16: Thirty Years of Observations and Analysis. In Fred A. Rasio and Ingrid H. Stairs, editors, *Binary Radio Pulsars*, volume 328 of *Astronomical Society of the Pacific Conference Series*, page 25, July 2005.

[99] J. M. Weisberg, J. H. Taylor, and L. A. Fowler. Gravitational waves from an orbiting pulsar. *Scientific American*, 245:74–82, October 1981.

[100] E. W. Weisstein. Jacobi-anger expansion. https://mathworld.wolfram.com/Jacobi-AngerExpansion.html, May 2021. From MathWorld–A Wolfram Web Resource.

[101] Norbert Wex. Testing relativistic gravity with radio pulsars. 02 2014.

[102] Clifford M. Will. *Theory and Experiment in Gravitational Physics*. Cambridge University Press, 1993.

[103] Andrzej Wolski. Theory of electromagnetic fields. In *CERN Accelerator School: Course on RF for Accelerators*, 11 2011.

EIGENSTÄNDIGKEITSERKLÄRUNG

Hiermit versichere ich, die vorliegende Arbeit selbstständig verfasst und keine anderen als die angegebenen Quellen und Hilfsmittel benutzt sowie die Zitate deutlich kenntlich gemacht zu haben.

Hannover, im Juli 2021

Olaf Hartwig

COLOPHON

This document was typeset using a modified version of the `classicthesis` LaTeX package developed by André Miede and Ivo Pletikosić.

Plots and figures were rendered using the LaTeX packages `pgfplots` and `tikz`. The exceptions are figs. 2.2 and C.1, which were created with `Blender` and `Matlab`, respectively.

Most figures utilize the component library developed by A. Franzen, available at `gwoptics.org/ComponentLibrary/`. Plots were first generated using either `Matlab` or the python package `matplotlib`, and then exported to `tikz` using either the `Matlab` script `matlab2tikz` or the python package `tikzplotlib`, available at `github.com/matlab2tikz/` and `pypi.org/project/tikzplotlib/`, respectively.

Figures not created by the author are marked as such, with references provided in their caption.

The present version of this manuscript contains minor changes relative to the version handed in to the referees. The referees spotted several typographical errors, which were corrected. They also suggested clearer formulations and some additional clarifying statements for selected paragraphs, which did not significantly alter the content of this thesis but improved its presentation. In addition, the referees suggested slight adjustments to fig. 3.11 and fig. 6.1 to be more representative of the expected hardware design for LISA. Figure C.1 was updated to show that the three bottom plots are related by derivatives.

Additional references were added on pages 130, 167 and 211. The acknowledgements were updated.